Development of Novel Monitors for Early Detection of Fouling in Reverse Osmosis Systems

Sim Siang Tze Victor

School of Civil and Environmental Engineering

2014

Development of Novel Monitors for Early Detection of Fouling in Reverse Osmosis systems

Sim Siang Tze Victor

School of Civil and Environmental Engineering

Singapore Membrane Technology Centre

A thesis submitted to the Nanyang Technological University in fulfillment for the degree of Doctor of Philosophy

2014

ACKNOWLEDGMENT

First and foremost, I would like to express my deep appreciation to my supervisor Professor Dr. Anthony Fane, and my unofficial supervisor, Professor Dr. William Krantz, for their encouragement, guidance and support. I am also grateful for the wide connections within the Singapore Membrane Technology Centre (SMTC) that enabled me to learn much from experts such as Associate Professor Dr. Wang Rong, Associate Professor Dr. Tang Chuyang, Professor Dr. Hans-Curt Flemming, and Professor Dr. Hans Coster. I am really fortunate to have this opportunity to learn from such well-known figures in membrane science.

Special thanks go to Dr. Chong Tzyy Haur for his invaluable help and critical comments. Huge credit goes to him for my smooth progress in my research. I like to thank Stanislaus Suwarno and Amir Taheri for the collaborative work on the new patent filed for the enhanced acoustic technique for the detection of biofilm, and the work on the dead-end filtration work on the study of metastability of colloidal foulants together with the work on high pressure filtration experiments for fouling prediction, respectively. I would also like to acknowledge the opportunity to assist in the company, Membrane Instruments and Technology (MINT).

My heart-felt gratitude goes to my wife *Tan Li Yan Julie* for her constant moral support, perseverance and encouragement. I am eternally grateful to my son *Jowen* for being the best motivation to continue working hard for my family.

Lastly, I would like to thank all the colleagues, staffs and my friends for their help and providing great and friendly atmosphere in Singapore Membrane Technology Centre (SMTC).

Contents

ABSTRACT

Today, the leading technology for new desalination installations uses reverse osmosis (RO) membranes. The current generation of RO membranes is of sufficiently high permeability that further significant improvement in RO membrane permeability is less likely to be the primary driver for a major reduction in the cost of desalination but should arise from a variety of other process improvements. As the primary energy use in an RO system is the power required for the high pressure to pump the feed water and is directly related to the feed pressure and flow rate, savings can come in the energy costs in pre-empting fouling problems.

In this project, a novel sensor has been developed to provide more reliable information for process monitoring based on a side-stream RO fouling monitor cell simulating flows in the plant termed the ‘canary cell’. The canary cell is found to be representative of the spiral wound module (SWM), which is the most commonly used configuration in the water desalination industry that can serve as an early warning system. Using a non-invasive method of Ultrasonic Time Domain Reflectometry (UTDR), foulants on the RO membrane can be detected. The UTDR sensor applies an acoustic signal that reflects from interfaces such as membrane and fouling layer in the cell. The method can detect changes in properties over a few microns and are well suited for integration with the ‘canary cell’ to detect incipient fouling.

The UTDR sensor has been shown to monitor colloidal fouling in-situ, in real-time and non-destructively that provides evidence for the metastability of colloidal fouling. Various operational parameters are further evaluated to understand and potentially control the onset of metastability. With the usage of acoustic enhancers, the UTDR sensor was further adapted for the detection of the biofouling, which would otherwise be incapable of reflecting the ultrasound wave for detection due to insufficient difference in acoustic impedance since the bulk of biofilms are water medium. The combination with another online sensor, the Feed Fouling Monitor (FFM), further

expanded the application of the UTDR sensor to predicting RO fouling through the measurements of foulant thickness and mass-based specific cake resistance. FFM is an adaptation of the Integrity Sensor (IS) that operates by measuring the transmembrane pressure (TMP) across a membrane of a low hydraulic resistance relative to a reference pressure differential.

<u>Publications</u>:

1. **Sim S.T.V.**, Chong T.H., Krantz W.B., Fane A.G. (2012), "Monitoring of colloidal fouling and its associated metastability using Ultrasonic Time Domain Reflectometry", <u>Journal of Membrane Science</u>, **401-402**: 241-253.
2. **Sim S.T.V.**, Jie C., Chong T.H., Yeo P.S.A., Krantz W.B., Coster H.G.L., Fane A.G. (2012), "Development of Novel Monitors for Early Detection of Fouling in Reverse-Osmosis Systems", in: <u>International Desalination Association (IDA) Journal</u>, Vol. 4, Numb. 3.
3. **Sim S.T.V.**[1], Suwarno S.R.[1], Chong T.H., Krantz W.B., Fane A.G. (2013), "Monitoring membrane biofouling via ultrasonic time-domain reflectometry enhanced by silica dosing", <u>Journal of Membrane Science</u>, 428: 24-37.
4. **Sim S.T.V.**, Wang R., Miao T., Fane A.G. (2013), "Membranes for Osmotic Power" In: Hoek E.M.V., Tarabara V.V. (Eds.), <u>Encyclopedia of Membrane Science and Technology</u>, John Wiley & Sons, New Jersey, United States.
5. **Sim S.T.V.,** Wang R., Fane A.G. (2013), "Blue Energy" In: Drioli E., Giorno L. (Eds.), <u>Encyclopedia of Membranes</u>, Springer.
6. **Sim S.T.V.**, She Q., Chong T.H., Tang C.-Y., Fane A.G., Krantz W.B. (2013), "Strategic co-locations in a Hybrid Process involving desalination and Pressure Retarded Osmosis (PRO)", <u>Membranes</u>, 3: 98-125.
7. Taheri A.H.[1], **Sim S.T.V.**[1], Sim L.N., Chong T.H., Krantz W.B., Fane A.G. (2013), "Development of a new technique to predict reverse osmosis fouling", <u>Journal of Membrane Science</u>, 448: 12-22.
8. **Sim S.T.V.**[1], Taheri A.H.[1], Chong T.H., Krantz W.B., Fane A.G. (2013), "Colloidal Fouling and its Metastability – Effects of Crossflow Velocity, Salinity and Colloids Concentration", <u>Journal of Membrane Science</u>, *Submitted*.

---

[1] These authors contributed equally to the work.

9. **Sim S.T.V.**, Krantz W.B., Chong T.H., Fane A.G. (2013), "Novel Monitor for the Reverse Osmosis Spiral Wound Module - Development of the Canary Cell", Desalination, *Submitted*.

Patents:

1. Maung N.W., Tan E.K., Wong F.-S., Yeo P.S.A., Krantz W.B., Fane A.G., **Sim S.T.V.** (2010), "A Membrane Sensor and Method of Detecting Fouling in a Fluid", Patent WO/2012/060778 filed on 1 November 2010.
2. **Sim S.T.V.**, Suwarno S.R., Chong T.H., Krantz W.B., Fane A.G. (2011). Enhanced Acoustic Diagnostic Tool for Fouling in Membrane Processes, Patent WO/2013/066268 filed on 31 October 2011.
3. Tang C.-Y., She Q., Ma N., Wei J., **Sim S.T.V.**, Fane A.G. (2012), "Reinforced Membranes for Producing Osmotic Power in Pressure Retarded Osmosis", Patent Application PCT/SG2013/000350 filed on 15 August 2012.

Conference proceedings:

1. Krantz W.B., Yeo P.S.A., **Sim S.T.V.,** Fane A.G. (2010), "The Integrity Sensor – A Novel Instrument for Assessing the Performance of Pre-filtration Membranes", in: American Institute of Chemical Engineers Annual Meeting (AIChE 2010), Salt Lake City, Utah, United States.
2. Yeo P.S.A., Lin S.C., Ching S.Y.P., **Sim S.T.V.,** Krantz W.B., Fane A.G. (2011), "An On-line instrument for Assessing the Integrity of Pre-filtration Membranes", in: International Congress on Membranes and Membrane Processes (ICOM 2011), Amsterdam, Netherlands.
3. **Sim S.T.V.** (2011), "Ultrasonic Time Domain Reflectometry (UTDR) as Fouling Sensor", in: How sensors can improve the membrane plant performance, Singapore International Water Week, Singapore.
4. **Sim S.T.V.**, Jie C., Chong T.H., Yeo P.S.A., Krantz W.B., Coster H.G.L., Fane A.G. (2011), "Development of Novel Monitors for Early Detection of Fouling in Reverse-

Osmosis Systems", in: International Desalination Association (IDA) World Congress 2011, Perth, Australia – *Awarded Best Oral Presentation, Young Leader Award.*

5. Taheri A.H., **Sim S.T.V.**, Chong T.H., Sim L.N., Krantz W.B., Fane A.G. (2012), "Development of new techniques to predict reverse osmosis fouling", in: International Conference on Membranes in Drinking and Industrial Waste Production, Leeuwarden, Netherlands.

6. **Sim S.T.V.**, Suwarno S.R., Chong T.H., Yeo P.S.A., W.B. Krantz, Fane A.G. (2012), "Ultrasonic Time Domain Reflectometry: Acoustic Radar for Early Detection of Fouling in Reverse-Osmosis Systems", in: Singapore International Water Week (SIWW) 2012, Singapore – *Poster*.

7. **Sim S.T.V.**, Suwarno S.R., Lim Y.X.S., Lim W.X.J., Chong T.H., Fane A.G (2012), "Development of novel acoustic sensor for early detection of biofouling in reverse-osmosis systems", in: Euromembrane 2012, London, United Kingdom.

8. **Sim S.T.V.** (2012), "A view inside the black box made possible with Ultrasonic Time Domain Reflectometry", in: Membrane Fouling and Monitoring Workshop 2012, Oxford, United Kingdom.

9. Chong T.H., **Sim S.T.V.**, Suwarno S.R., Taheri A.H., Krantz W.B., Fane A.G. (2013), "Detection of Fouling and Cleaning of Reverse Osmosis Membranes by Acoustic Method", in: 7th International Water Association (IWA) Specialized Membrane Technology Conference and Exhibition for Water and Wastewater Treatment and Reuse, Toronto, Canada.

10. **Sim S.T.V.**, Taheri A.H., Chong T.H., Sim L.N., Yeo A.P.S., Krantz W.B., Coster H.G.L., Fane A.G. (2013), "Long Term Sustainability of Desalination becomes more achieveable with Novel Sensors", in: International Desalination Association (IDA) World Congress 2013, Tianjin, China – *Poster*.

11. **Sim S.T.V.**, Chong T.H., Krantz W.B., Fane A.G. (2013), "Development of the Canary Cell – A Surrogate to the Reverse Osmosis Spiral Wound Module (RO SWM) System", in: International Membrane Science & Technology Conference (IMSTEC), Melbourne, Australia – *Awarded The Patron Prize (Best Oral Paper Presentation).*

Awards:

1. NRF (EWT) PhD Scholarship 2010-2014: Awarded by Singapore's National Research Foundation (NRF), through the Environment & Water Industry Development Council (EWI) to develop experts in Environment and Water Technologies (EWT).
2. IDA Scholarship 2010/2011 & 2011/2012: Channabasappa Memorial Scholarship.
3. Best Oral Presentation, Young Leader Award 2011: Paper entitled "Development of Novel Monitors for Early Detection of Fouling in Reverse-Osmosis Systems" awarded for superior technical content and style of presentation in the International Desalination Association (IDA) World Congress 2011 in Perth, Australia.
4. Green Talents Competition 2011: 20 young scientists selected for the 'Green Talents' competition organized by the German Federal Ministry of Education and Research (BMBF).
5. Singapore – Netherlands Sustainability Award 2011/2012: Winning proposal entitled "Pressure Retarded Osmosis for Marina Barrage & Sustainable Brine Disposal" for the Singapore – Netherlands Water Challenge.
6. 2nd Prize, Shell Inter-varsity Student Paper Presentation (S-SPEC) 2012: Postgraduate oral paper presentation on the paper entitled "Pressure Retarded Osmosis for Desalination and Sustainable Brine Disposal".
7. A.T. Kearney Scholarship 2013: Top 100 below 35 years old selected globally to share their scientific breakthroughs at the Falling Wall Labs in Berlin, Germany.
8. The Patron Prize 2013: Paper entitled "Development of the Canary Cell – A Surrogate to the Reverse Osmosis Spiral Wound Module (RO SWM) System" awarded for best oral presentation in the International Membrane Science & Technology Conference (IMSTEC) 2013 in Melbourne, Australia.
9. System Engineering Essay Competition 2013 (Merit Award): Paper entitled "Innovative Strategic Co-Location for More Efficient Production of Industrial Water" selected by Temasek Defense Systems Institute (TDSI) for the development of ideas and insights into systems engineering in the field of water resource management, environment and energy.

LIST OF TABLES

LIST OF FIGURES

LIST OF SYMBOLS

A	Amplitude of wave (V)
c	Speed of sound in material (ms^{-1})
C_b	Concentration of solute in bulk solution (gL^{-1} or kgm^{-3})
C_g	Concentration of solute at cake or gel layer (gL^{-1} or kgm^{-3})
C_P	Concentration of solute in permeate solution (gL^{-1} or kgm^{-3})
CP	Concentration polarization (dimensionless)
C_w	Concentration of solute on membrane surface (gL^{-1} or kgm^{-3})
Δd	Distance between reflecting interface and ultrasonic transducer (m)
d_f	Diameter of spacer filament (m)
d_h	Hydraulic diameter (m)
D	Solute diffusivity (m^2s^{-1})
D_{eff}	Effective diffusion coefficient of solute (m^2s^{-1})
D_f	Solute diffusion in the cake layer (m^2s^{-1})
D_m	Diffusion coefficient of solute due to Brownian diffusion (m^2s^{-1})
D_s	Diffusion coefficient of solute due to shear (m^2s^{-1})

h Channel height (m)

h_{sp} Height of channel spacer (m)

J_{cc} Volumetric permeation flux in the canary cell (LMH or $m^3m^{-2}s^{-1}$)

J_{Crit} Critical flux (LMH or $m^3m^{-2}s^{-1}$)

J_{ss} Steady state flux or critical flux (LMH or $m^3m^{-2}s^{-1}$)

J_{SWM} Volumetric permeation flux in the spiral wound module (LMH or $m^3m^{-2}s^{-1}$)

J_v Permeate flux (LMH or $m^3m^{-2}s^{-1}$)

k_{eff} Effective mass transfer coefficient (ms^{-1})

k_m Mass transfer coefficient in unfouled membrane channel (ms^{-1})

k_f Mass transfer coefficient in the cake layer (ms^{-1})

L Channel length (m)

L_{cc} Canary cell length (m)

l_m Mesh size (m)

L_{SWM} Spiral wound module length (m)

m_f Mass of foulant deposit per unit area (kgm^{-2})

ΔP Difference in applied pressure across membrane (Pa or bar)

Q Crossflow volumetric flow rate (m^3s^{-1})

Q_f Solvent on the feed side (m^3s^{-1})

Q_{Fresh} Fresh water flow rate (m^3s^{-1})

Q_0 Solvent on the outlet side (m^3s^{-1})

ΔQ_{PRO} Transported water flow rate through PRO membrane (m^3s^{-1})

Q_{Saline} Saline water flow rate (m^3s^{-1})

Re Reynolds Number (dimensionless)

R_f Foulant layer resistance (m^{-1})

R_m Membrane resistance (m^{-1})

r_p Radius of particle (m)

t Time required for wave to travel from a reflecting interface (s)

T Temperature of solute (K)

TMP Transmembrane pressure (pa)

TMP_0 Initial transmembrane pressure (pa)

v Crossflow velocity (ms^{-1})

v_f Crossflow velocity in the feed side (ms^{-1})

v_0 Crossflow velocity in the outlet side (ms^{-1})

W Channel width (m)

W_{cc} Canary cell width (m)

W_{SWM} Spiral wound module width (m)

Z Acoustic impedance of material (Nsm^{-3})

Greek Letters

$1/\kappa$ Debye length (nm)

Φ Volume fraction of particles (dimensionless)

Φ_c Critical volume fraction of particles (dimensionless)

θ Fractional deposition factor (dimensionless)

θ_{sp} Angle between adjacent spacer filaments (°)

β Sticking potential of the foulant (dimensionless)

ε Foulant layer porosity (dimensionless)

ε_{app} Apparent foulant layer porosity (dimensionless)

ε_{sp} Channel voidage (dimensionless)

λ Friction coefficient (dimensionless)

$\Delta\pi_w$ Osmotic pressure difference (pa)

δ_c Foulant layer thickness (m)

δ Thickness of concentration polarization layer (m)

ρ Density of material/liquid (kgm^{-3})

ρ_p Density of particle (kgm^{-3})

μ Dynamic viscosity of solution (Pa.s)

κ Boltzmann constant, 1.38 x 10^{-23} (JK^{-1})

α_f Specific cake resistance of the foulant layer (mkg^{-1})

α_{RO} Specific cake resistance of the foulant layer in RO (mkg^{-1})

α_0 Reference specific cake resistance of the foulant layer (mkg^{-1})

ζ_{Si} Zeta potential of colloidal silica (mV)

ζ_{R} Reference zeta potential of colloidal silica (mV)

σ^* Finite distance at which the inter-particle potential is zero (nm)

σ_{Silica} Lennard-Jones potential of silica (nm)

σ_{Water} Lennard-Jones potential of water (nm)

CHAPTER 1 : INTRODUCTION

1.1 Problem Statement

Water is abundant everywhere but most is not potable water as only 0.8% is considered freshwater. The sources of fresh water are contributed by more than 60% from surface water, 36.3% by groundwater and only <0.5% from desalination and water reuse (Gleick, 1996; Kolodziejski and Gasson, 2005). The increase of developing economies and population numbers in recent decades has increased water demand and caused accelerating global depletion of groundwater. The rate of groundwater depletion has more than doubled between 1960 and 2000, causing the amount of groundwater lost to increase from 126 to 283 km^3 of water per year (Wada *et al.*, 2010). The latter figure is equivalent to a hefty 28 times the global installed capacity of water reuse plants in 2009 (GWI, 2009) or 10 times the current global installed capacity of desalination plants (IDA, 2012). Hence, it is widely expected that the contribution from desalination and water reuse will increase in the years to come (Pearce, 2008). By 2016, desalination capacity is forecast to increase to 88.9 million m^3 per day while water reuse capacity is expected to grow to 79.5 million m^3 per day (GWI, 2009). To put this into perspective, the total combined capacity of desalination and water reuse by 2016 is approximately the entire annual renewable freshwater supply of either Egypt or South Africa (Gleick and Cooley, 2009).

Today, the prevalent desalination process as well as for new desalination installations uses reverse osmosis (RO) membranes (Elimelech and Philip, 2011; Lee *et al.*, 2011; Lattemann *et al.*, 2010; Greenlee *et al.*, 2009). The current generation of RO membranes is of sufficiently high permeability that further significant improvement in permeability is less likely to be the primary driver for a major reduction in the cost of desalination. This could arise from a variety of other process improvements that include, but are not limited to, optimization of process configuration and process schemes (Zhu *et al.*, 2009). Moreover, recent empirical evidence suggests that it may be difficult to further increase water permeability without putting membrane selectivity as a trade off (Geise *et al.*, 2011).

A significant 53% of the total operation and maintenance costs for RO desalination comes from energy consumption based on the breakdown of the operating and maintenance (O&M) costs for a typical 0.19 million m^3/d (50 mgd) ground water desalting plant utilizing RO system (Bartels *et al.*, 2005). Therefore, savings can potentially come from reduced energy consumption. The average production cost of desalinated seawater using RO is around US \$0.50/m^{-3} to US \$0.70/m^{-3} with energy demand accounting for 50% of the total production costs as shown in Figure 1.1 that gives the breakdown of the operation costs of RO seawater desalination process (GWI, 2007; Dore, 2005). As the primary energy use in an RO system is the power required for the high pressure to pump the feed water and is directly related to the feed pressure and flow rate (Wilf and Klinki, 2001), significant savings can come in the energy costs in pre-empting fouling problems. For example, it is estimated that the global overall costs for biofilms caused by downtime in desalination is significantly high (Flemming, 2011a) and using seawater desalination as an illustration, the annual potential savings for an early warning of biofouling for an average 10,000 m^3 seawater RO plant can be significant up to 2 million dollars (Vrouwenwelder *et al.*, 2011).

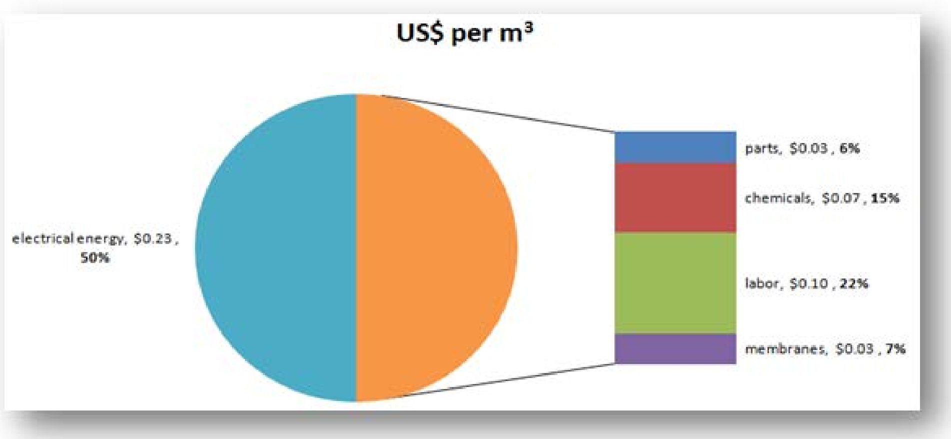

Figure 1.1: Operation costs in US$ of RO desalination process (GWI, 2007).

Once the RO process is in operation, there are two avenues to pre-empt fouling problems. Firstly, the fouling propensity of the water can be measured and allowed for. However, the commonly used technique for this, Silt Density Index (SDI), is empirical and potentially unreliable (Schippers and Verdouw, 1980, Lipp *et al.*, 1990; Yiantsios and Karabelas, 2002; Boerlage *et al.*, 2003).

The other approach is through more sensitive monitoring of the 'state of the process' using novel monitors on a side-stream cell simulating the RO elements in the main plant. This could have benefits compared to measurements of pressures and flows on the main plant that may fail to detect incipient fouling (Moody *et al.*, 1983) since they are integral measurements over the whole system.

In this thesis, a non-invasive method, known as Ultrasonic Time Domain Reflectometry (UTDR) has been improved and evaluated to provide reliable information for process monitoring in real-time to understand fouling mechanisms in-situ and non-invasively. UTDR operates by applying an acoustic signal that reflects from interfaces such as membrane and fouling layer in the cell (Mairal *et al.*, 1999; Mairal *et al.*, 2000; Sanderson *et al.*, 2002; Xiu *et al.*, 2002; Chai *et al.*, 2007; Krantz and Greenberg, 2008; Sim *et al.*, 2012a; Sim *et al.*, 2012b; Sim *et al.*, 2013b). The method is well studied to detect changes in properties over a few microns (Sim *et al.*, 2012a; Sim *et al.*, 2013b; Chen *et al.*, 2004c), and is suited for integration into a fouling simulation cell. This is called a 'canary cell' and is a side-stream cell that simulates the flow and flux within a spiral wound RO module and acts as an early detection fouling monitor. The term 'canary' is analogous to the canaries taken by miners in coal mines to warn of dangerous gases.

1.2 Objectives

The general objective of this research is to utilize a sensor for monitoring the fouling state of the membrane process that provides signals for process control to reduce fouling in RO systems. The main technology used in the sensor is UTDR that is integrated with the ‘canary cell’, a side-stream cell simulating the flow within a spiral wound RO module, to act as an early detection fouling monitor system for incipient fouling. Specific directives are to detect and characterize membrane fouling by colloids and biofilms and its mechanisms, using UTDR. An additional objective is to combine UTDR with another in-house developed feed fouling monitor (FFM) based on the design of a patented membrane integrity sensor (Maung *et al.*, 2010) for the development of a new technique to predict RO fouling.

1.3 Structure of the Thesis

Based on the objectives highlighted in Section 1.2, the main tasks are:

- A critical review of the available literature on fouling in RO, non-invasive fouling detection methods, and fouling monitors (Chapter 2).
- Development of experimental procedures and design considerations for crossflow, dead-end, low pressure ultrafiltration (UF), high pressure RO, spiral wound modules, filtration models, UTDR equipment and methodology, calibration measurements for UTDR, and ex-situ membrane autopsies. Models for filtration theory and hydrodynamics characterization are also described (Chapter 3).
- Detailed analysis of UTDR waveforms for low pressure UF, and high pressure RO experiments (Chapter 4).
- Adaptation and demonstration of UTDR to detect a selected foulant that exhibits interesting rheological behavior and a fundamental fouling study of the foulant based on hydrodynamics, flux and salinity conditions (Chapter 5).
- Extension of UTDR beyond the traditional detection for inorganic deposits to biofouling (Chapter 6).
- Combining UTDR with the feed fouling monitor (FFM) to predict RO fouling (Chapter 7).
- Correlating the response of the ‘canary cell’ to the performance of the spiral wound RO module and establishing the conditions necessary for the ‘canary cell(s)’ to behave as an early warning system for incipient fouling (Chapter 8).

- Recommendations for future work based on the findings of this thesis (Chapter 9).

In summary, Chapter 2 presents the literature review required to appreciate the different topics in the thesis while Chapter 3 summarizes the design considerations, various materials and apparatuses, and theories for the subsequent chapters. Chapter 4 introduces the analysis of acoustic waveforms for the various set-ups and explains how non-invasive UTDR can monitor the fouling in-situ, in real-time and non-destructively. Chapter 5 present the evidence that metastability of colloidal fouling occurs complemented by the usage of UTDR before evaluating various operational parameters to understand and potentially control the onset of metastability. Metastability of colloidal suspensions refers to the transformation of the colloidal suspensions from a fluid- to solid-like behavior. More details of metastability of colloidal suspensions is covered in section 2.2.1.1 of Chapter 2. Chapter 6 illustrates how biofouling detection by UTDR is possible with the usage of acoustic enhancers and shows that additional information can be obtained by the new technique. Chapter 7 shows how UTDR combined with FFM can be used to predict RO fouling and explain what important considerations of UTDR needs to be considered. Chapter 8 demonstrates how the canary cell can be representative of the SWM and can provide an early warning system. The last chapter, Chapter 9, concludes by elaborating on future work for improvements of the UTDR and the canary cell concept.

In addition, there are a number of complementary studies done related to improving the economics of desalination that are highlighted outside the main body of the thesis in the Special Appendix. These include (i) new hybrid designs involving pressure retarded osmosis (PRO) that could result in significant savings in terms of energy consumption and capital costs for desalination, (ii) a short research project in IWW Zentrum Wasser, Germany that enabled exposure to an optical fouling monitor known as the OptiQuad®, and (iii) the initial development work on a patented membrane integrity sensor (IS). An adaptation of the IS has been the FFM described in Chapter 7.

CHAPTER 2 : LITERATURE REVIEW

Membrane processes have progressed significantly over during the past few years. This chapter provides the literature related to the operation of reverse osmosis, fouling, non-invasive fouling detection methods, state-of-the-art UTDR, and fouling monitors.

2.1 Fundamentals of Reverse Osmosis

Osmosis is a natural phenomenon where water (solvent) passes through a semi-permeable membrane from the side of lower solute concentrations (higher chemical potential of the water) to the side of higher solute concentration (lower chemical potential) until the two solutions become equal in concentration or the pressure of the more concentrated solution increases to match the difference in osmotic pressure. In reverse osmosis (RO), a pressure greater than the osmotic pressure difference is applied to the more concentrated solution side in order to reverse the flow. Today, the leading desalination technology is RO (Elimelech and Philip, 2011; Lee *et al.*, 2011; Lattemann *et al.*, 2010; Greenlee *et al.*, 2009). The reduction in energy consumption from >15 $kWhm^{-3}$ in the 1970s to less than 2 $kWhm^{-3}$ in 2006 is the combined result of fouling and concentration polarization minimization and improved membrane permeability and energy recovery (Elimelech and Philip, 2011; Lee *et al.*, 2011).

The RO membrane has a selective layer that retains solutes such as ions but allows water molecules to pass through. Permeate flux, J_v is defined as the permeate flow rate per unit membrane area and is given by

$$J_v = \frac{TMP - \Delta\pi_w}{\mu R_m} \tag{2.1}$$

Where TMP is the trans-membrane pressure, μ is the viscosity of permeate, R_m is the resistance of membrane, and $\Delta\pi_w$ is the osmotic pressure difference across the membrane influenced by the effect of concentration polarization that will be further explained in Section 2.1.3.

2.1.1 Membrane Modules and Module Configurations

Thin film composite (TFC) polyamide membranes dominate the RO membrane market. TFC membranes consist of three layers: a structural support by a polyester web of about 120 – 150 μm, a microporous interlayer of about 40 μm, and a very thin seperation barrier layer on the surface of about 0.2 μm (Peterson, 1990). As the membrane must be strong enough to withstand the high operating pressure that can reach up to 70 bars for seawater desalination, the support layer is optimized for maximum strength and resistance to compression while the selective layer is optimized for maximum solvent flux and retention of solute (Peterson, 1993). A large number of different module configurations are mentioned in the literature. However, most commercially available membrane module systems can be classified into four main types (Baker, 2004; Wagner, 2001; Nishimura and Koyama, 1992):

- Plate-and-frame
- Hollow-fiber
- Tubular
- Spiral-wound

In Figure 2.1, a schematic of the spiral wound module is shown. The spiral wound module (SWM) is the most commonly used configuration in the water desalination industry because of several advantages over other modules. It allows a high productivity per unit volume due to its large surface to volume ratio and the concentration polarization can be kept low due to the feed channel spacer that also makes the module less susceptible to fouling.

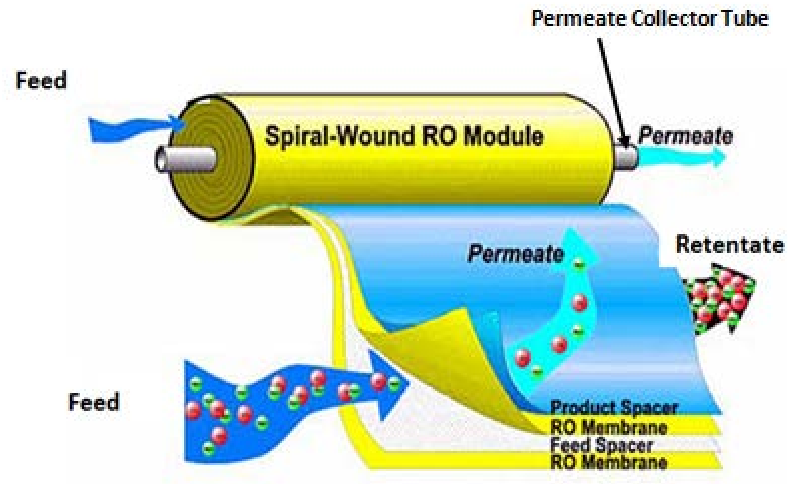

Figure 2.1: Schematic of the SWM in operation (modified from www.water-technology.net).

2.1.2 Operation mode (Constant Flux vs Constant TMP)

There are two modes of operation of RO systems; under constant transmembrane pressure (TMP) or under constant flux. In the constant TMP operation mode, the flux varies according to the apparent resistance of the membrane and if fouling occurs, the flux declines over time. For this reason, commercial RO systems are operated at constant flux to maintain a constant production rate. In the fixed flux operation mode, the TMP will vary according to the apparent resistance of the membrane and if fouling occurs, the TMP will rise over time in order to keep the flux constant through a higher feed pressure. There is an important difference in the way fouling occurs under these two modes. Fouling tends to be flux driven. Therefore, the fouling rate in constant TMP operation mode is 'self-limiting' while the fouling rate in constant flux operation mode can toggle between 'self-accelerating' and 'steady continuum' depending on the properties of the foulant and operating environment. The two operation modes are illustrated in Figure 2.2.

Under constant TMP operation mode, the flux continues to drop over time as fouling progresses but the rate of deposition of foulant that is dependent on the driving force caused by the flux decreases in tandem with the decrease in flux. Under a constant flux operation mode, the driving force caused by the flux is constant over time and that leads to a constant deposition of foulant layer that should result in a constant increase in TMP with time. However, there are observations in the literature where the TMP jumps even for 'model' solutions of only one foulant dispersed in appropriate buffer solutions (Su *et al.*, 2000; Metsämuuronen *et al.*, 2002) that is associated with metastability of colloidal foulants and this is further discussed in Section 2.2.1.1. In addition, the build-up of the foulant cake layer, especially for applications of reverse osmosis, leads to a process called cake enhanced osmotic pressure (CEOP). This is also known to be responsible for a 'self-accelerating' TMP behavior as the back diffusion of the solute through the foulant cake is hindered (Hoek *et al.*, 2002; Chong *et al.*, 2008). CEOP is further discussed in Section 2.1.3.1.

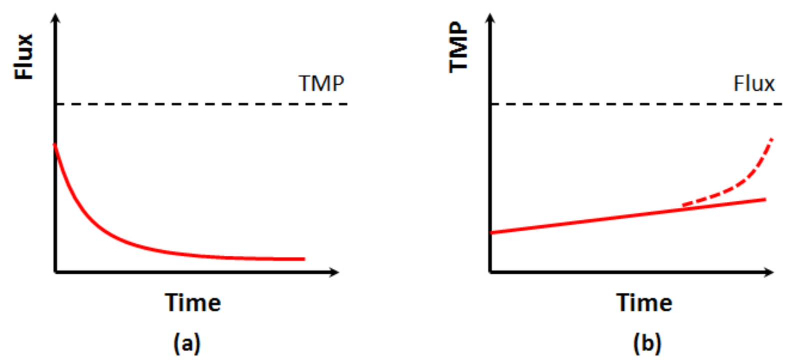

Figure 2.2: Schematic of TMP and flux profile, (a) constant pressure operation, and (b) constant flux operation

2.1.3 Concentration Polarization

When solute is rejected by the membrane due to the natural consequence of membrane selectivity, the concentration of the solute increases near the membrane surface. However, the convective flow of the solute to the membrane surface is balanced by back diffusion of solute to the bulk feed solution. This gradual build up in solute concentration towards the membrane surface is termed concentration polarization (CP). Figure 2.3 is a schematic diagram of the CP process.

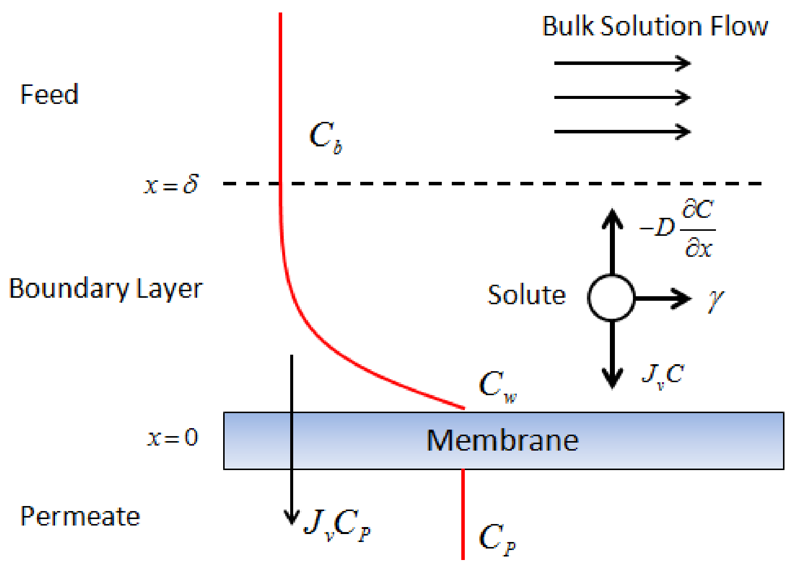

Figure 2.3: Concentration Polarization within a Membrane Module

At steady-state conditions, the flux of solute to the membrane, J_vC, the flux of solute through the membrane, J_vC_P, and the back diffusion of the solute, $-D\frac{\partial C}{\partial x}$, are in equilibrium with the following assumptions of Fickian diffusion, no chemical reaction, negligible concentration gradient parallel to the membrane, constant density, and diffusion coefficient independent of solute concentration. The process can be written mathematically as the convective-diffusion equation (Bird *et al.*, 1960; Field, 2010):

$$J_vC_P = J_vC - D\frac{\partial C}{\partial x} \tag{2.2}$$

Integration of Equation 2.2 with the following boundary conditions taken into account,

$x = 0$ $\qquad\qquad\qquad$ $C = C_w$

$x = \delta$ $\qquad\qquad\qquad$ $C = C_b$

yields

$$CP = \frac{C_w - C_P}{C_b - C_P} = \exp(\frac{J_v}{D/\delta}) = \exp(\frac{J_v}{k_m}) \tag{2.3}$$

Where D is the solute diffusivity, δ is the thickness of the CP layer, and k_m is the mass-transfer coefficient which is equal to D/δ only when flux tends to zero but is used as a common assumption. For an ideal membrane that totally rejects the solute, the solute concentration in the permeate is zero that gives

$$CP = \frac{C_w}{C_b} = \exp(\frac{J_v}{k_m}) \tag{2.4}$$

Various studies have confirmed that concentration polarization is controlled by the mass transfer at the membrane surface (Porter, 1972; Song and Elimelech, 1995; Koutsou *et al.*, 2009). The mass-transfer coefficient for flow through a flat-sheet membrane channel in the absence of feed spacers can be assumed as flow through a flat rectangular channel and can be obtained from the Gratez-Lévêque equation (Porter, 1972) for laminar flow conditions:

$$k_m = 0.816\left(\frac{6QD_{eff}{}^2}{h^2wL}\right)^{1/3} \tag{2.5}$$

Where Q is the crossflow volumetric flowrate, h is the channel height, w is the channel width, L is the channel length, and D_{eff} is the effective diffusion coefficient. D_{eff} is due to both the Brownian motion molecular diffusion coefficient, D_m and the shear-induced hydrodynamic diffusion coefficient, D_s (Lee and Clark, 1998) and can be obtained by Equation 2.6:

$$D_{eff} = D_m + D_s = \frac{\kappa T}{6\pi\mu r_p} + 0.03{r_p}^2\gamma \tag{2.6}$$

Where κ is the Boltzmann constant, T is the temperature, r_p is the radius of particle, μ is the dynamic viscosity of solution and γ is the shear rate. For sub-micron particles (typically < 100 nm), Brownian motion molecular diffusion is predominant over shear-induced hydrodynamic diffusion and $D_{eff} \approx D_m$.

The mass transfer at the membrane surface can also be described by the dimensionless Peclet number, which is the product of the Schmidt number and the Reynolds number (Brodkey and Hershey, 1988). Due to the dimensionless nature of the Peclet number, it is useful in evaluating the canary cell, which is a crossflow cell to simulate the spiral wound module (SWM), as described in Chapter 8. For a specified solute, and operation under the same feed source and flux conditions, the Schmidt number will be a constant for both the canary cell and the SWM. This results in concentration polarization being primarily a function of hydrodynamic characteristics that can be characterized by the Reynolds number. Therefore, matching the Reynolds number for the canary cell to that of the SWM should provide similar average mass transfer at the membrane surface.

Though concentration polarization (CP) is inevitably caused by the selectivity of the membrane, it is still undesirable for a number of reasons. Firstly, the increased osmotic pressure near the membrane surface will require additional driving force to maintain a constant flux through the membrane and leads to additional pressure being applied. Secondly, CP causes a greater concentration gradient to occur across the membrane that facilitates solute passage across the membrane, which increases as CP worsens. Lastly, CP promotes fouling (Matthiasson and Sivik, 1980). All of these reasons reduce the efficiency of the membrane based separation process. Equation 2.3 shows an exponential relationship between flux, diffusion coefficient and concentration polarization. The concentration polarization can be minimized through decreasing flux, maintaining a smaller boundary layer thickness (by increasing Reynolds Number) and higher diffusion coefficient.

2.1.3.1 Cake Enhanced Osmotic Polarization (CEOP)

In the presence of a foulant cake layer, the back transport of solute is hindered (Hoek *et al.*, 2002) and is given by

$$CP = \exp(\frac{J_v}{k_{eff}}) \tag{2.7}$$

with

$$\frac{1}{k_{eff}} = \frac{1}{k_m} + \frac{1}{k_f} \tag{2.8}$$

where k_{eff} is the effective mass transfer coefficient that is the net effect of the mass transfer, k_m in an un-fouled membrane channel and the mass transfer in the cake layer, k_f. k_f is a function of the cake layer thickness, δ_c, and the solute diffusion in the cake layer, D_f, and is represented by Equation 2.9:

$$k_f = \frac{D_f}{\delta_c} \tag{2.9}$$

D_f is related to the cake porosity, ε, and can be estimated by (Boudreau, 1996)

$$D_f = D(\frac{\varepsilon}{1 - ln\varepsilon^2}) \tag{2.10}$$

From Equation 2.10, CP due to ions retained by the RO membrane will experience a decrease in the effective mass transfer coefficient, k_{eff}, in the presence of a build-up of foulant cake over time that therefore leads to a 'self-accelerating' TMP rise during constant flux operation mode.

2.2 Membrane Fouling

Membrane fouling is the deposition of undesirable material on the membrane surface or into the pores that causes an unwanted decline in flux under constant pressure operation or increases in transmembrane pressure (TMP) under constant flux operation. Unlike concentration polarization that is reversible with an elimination of TMP, membrane fouling is a build-up of material on the membrane surface that may only be partially reversible.

Fouling may take various forms: physicochemical adsorption from solution, precipitation of sparingly soluble salts, growth of biofilms, and deposition of suspended matter onto and into the membrane. Fouling occurs when the critical flux is exceeded such as under suppression of charge interactions in a high salinity environment in applications of reverse osmosis. Critical flux refers to the flux level below which no fouling occurs and above which a membrane is fouled (Field *et al.*, 1995) and describes the controlling step in membrane fouling. There are five main sources of fouling, namely particulates, microbial cells, colloids, organics and inorganic ions (Boerlage *et al.*, 1998; Fane *et al.*, 2009) that can be further broken down into categoies of fouling:

- Cake and Pore fouling
- Scaling
- Biofouling

Factors that aggravate fouling are lack of sufficient pretreatment, lack of sufficient fluid management in terms of hydrodynamic environment, high flux and unsuitable membrane properties (Fane *et al.*, 2009).

The types of fouling occurring in RO are reported as organic cake fouling, biological fouling, and scaling, of which biofouling is often the most serious problem in the operation of RO plants (Uemura and Henmi, 2008). Fouling by colloids is also viewed as the most persistent problem in the use of membrane processes in potable water applications (Boerlage *et al.*, 1998). Fouling is further complicated because the fouling phenomenon in a commerical plant evolves differently from that at the smaller laboratory scale. Fouling in the plant presents itself in terms of fouling maldistribution along the module length and width of a single module that develops into a ‘fouling creep’ phenonmenon in a train or stage consisting of multiple modules arranged in series. It is therefore of interest to highlight fouling by colloids, biofouling and fouling evolution in commerical settings in more detail during sections 2.2.1, 2.2.2 and 2.2.3 respectively.

2.2.1 Fouling by Colloids

Colloids are usually characterized by a large surface area to volume ratio due to their inherent small diameter (typically < 1 μm). When a colloid is in contact with a solution of ions, there will be a distribution of ions around the colloids where the combined system of the surface charge of a colloid and its counter-ions in solution is termed as the electrical double layer (EDL). The EDL is made up of the Stern layer and a diffuse layer whose characteristic length or ‘thickness’ is known as the Debye length, $1/\kappa$. At 25°C, the Debye length of an aqueous solution for 1:1 electrolyte e.g. NaCl, can be estimated by (Israelachvili, 1992)

$$1/\kappa = \frac{0.304}{\sqrt{[NaCl]}} nm \tag{2.11}$$

Colloidal fouling is the formation of a colloidal deposit cake layer on the membrane surface. Colloidal dispersions commonly present on membrane surfaces during water treatment include inorganic foulants such as aluminum silicate minerals, silica, iron oxides, and organic macromolecular foulants that are also colloidal in nature such as polysaccharides, proteins, and natural organic material (Ning *et al.*, 2005; Yiantsios *et al.*, 2005; Tran *et al.*, 2007; Her *et al.*, 2007)

Other than the fact that many foulants are colloidal in nature, colloidal fouling has also been of much interest due to the inherent size range of colloids (1 nm – 1 μm) (Tang *et al.*, 2010) that makes them cause membrane fouling (Stumm, 1993; Buffle and Leppard, 1995). Particles larger than colloids can be removed via shear-induced diffusion or lateral migration while solutes in the molecular size range can be removed from the membrane surface via molecular (Brownian) diffusion (Bacchin *et al.*, 2006). Intermediate sized colloids ($\sim$ 0.1 μm) may have low Brownian diffusion and low shear-induced diffusion; this makes them more fouling prone.

2.2.1.1 Metastability of Colloidal Suspensions

Colloid dispersions exhibit unique characteristics by displaying both fluid- and solid-like behavior with the transition between these regimes taking different forms (Segrè *et al.*, 2001). A hard sphere-type behavior occurs when colloidal particles experience a repulsive interaction on contact due to volume exclusion. The hard spheres exhibit fluid-like behavior at low concentrations but as the volume fraction, Φ increases, the particles become increasingly crowded until at $\Phi \approx 0.58$, a glass transition to a disordered solid takes place (Pusey and Megen, 1987; Megen and Underwood, 1994). Colloidal particles that have an attractive interparticle energy undergo a transformation from fluid- to solid-like behavior occurring at lower critical volume fractions, where Φ_c <0.58 (Chen and Russel, 1991) whose range of values depends on the magnitude of the attractive energy on contact. Gelling even at arbitrarily low volume fractions (Carpineti and Giglio, 1992) is possible at very large interaction energy and that leads to the formation of fractal clusters from irreversible diffusion-limited aggregation (Weitz and Oliveria, 1984). Colloidal silica has been found to be metastable in nature (Sim *et al.*, 2012a) and experiences a glass transition region (Trompette *et al.*, 2005) and is therefore a suitable model foulant to be used for the study of metastability of colloids.

2.2.2 Biofouling

Biofouling is a biofilm phenomenon (Flemming, 2011a). Biofilms can be loosely defined as “microbial aggregates that usually accumulate at a solid–liquid interface and are encased in a matrix of highly hydrated extracellular polymeric substances (EPS)” (Flemming and Wingender, 2010). In most biofilms, the biofilm cells account for less than 10% of the dry mass and are embedded in the remaining > 90% matrix that is the extracellular material produced mostly by the organisms themselves. It consists of a conglomeration of different types of EPS, which forms the support of the biofilm and is responsible for adhesion to surfaces and for cohesion in the biofilm (Flemming and Wingender, 2010). Characterization shows that biofilms mainly consists of > 90% moisture content, > 50% organic content of dried deposit and $>10^6$ CFU/cm^2 of high microbiological counts (Baker and Dudley, 1998). Therefore, water constitutes the largest component of the biofilm matrix (Flemming, 2011b).

A common phenomenon, biofouling is a costly problem. Over billions of years, biofilm organisms have evolved to develop multiple effective defense strategies against a multitude of stresses such as irradiation, biocides, antibiotics, and host immune systems. Antifouling efforts may provide initial success but it tends to be time dependent and not permanent as all surfaces will be colonized by microbial biofilms overtime (Flemming, 2011a). In 1994, Flemming *et al.* estimated the costs of biofouling accounted for 30% of the operating costs in a membrane application at Water Factory 21, Orange County (Flemming *et al.*, 1994). This was about $750,000 per year at that time. The rate has not changed much since and it is estimated that the global overall costs for biofilms caused by downtime in desalination is significantly high (Flemming, 2011a). As an illustration, the annual potential savings for an early warning of biofouling of an average 10,000 m^3 seawater RO plant can be significant at 2 million dollars (Vrouwenwelder *et al.*, 2011).

The basis of biofouling is organic fouling (Ivnitsky *et al.*, 2005; Kimura *et al.*, 2005) so good pretreatment only limits biofouling in RO processes (Semiat and Hasson, 2009) but is unable to prevent it. Continuous chlorine dosing to seawater feed with sodium bisulfate dosing prior to the RO process is a common method to prevent biofouling. Unfortunately, thin film composite polyamides are the materials of most RO membranes today and these can be oxidized in the presence of chlorine that deteriorates the membrane performance over time (Uemura and Henmi, 2008). It is also recognized that the steps of chlorination/dechlorination may often be ineffective as the bacteria that survive have an increased supply of nutrient so that biofouling is exacerbated. Hence, the preferred approach could be to accept the existence of biofilms but learn how to reduce efficiently their effects below an acceptable level of interference (Flemming, 2011a). The appropriate strategies require the selection of better cleaners, strategic cleaning protocols, foulant deposits monitoring, early warning systems, cleaning-friendly system designs, easy-to-clean membranes, and minimization of nutrients availability.

2.2.3 Fouling Evolution in Commercial Settings

As highlighted in Section 2.1.1, the SWM is the most commonly used configuration in the water desalination industry. Due to the distributions of flux and crossflow velocities along a single SWM element's membrane length and width (Schwinge *et al.*, 2002; Schwinge *et al.*, 2004; Alexandis *et al.*, 2007), there would be foulant maldistribution (uneven foulant distribution) in the SWM. Autopsies have shown that the foulant deposition decreases from the inlet or the feed side to the outlet, and from the side close to the permeate collector tube to the closed end of the permeate channel. In addition, the fouling evolves by a 'fouling creep' phenomenon (Chen *et al.*, 2004a; Hoek *et al.*, 2008) along a train or stage that consists of multiple SWM elements arranged in series. The fouling creep is characterized by the initial fouling of the first few SWM elements followed by a shift to the relatively less fouled regions along the length of the train or stage to compensate for the loss of upstream permeability. This is a major reason why measurements of pressures and flows on the plant fail to detect incipient fouling (Moody *et al.*, 1983) since they are integral measurements over the whole system. On the other hand, a small simulation cell of relatively short length operating in a side-stream would be more sensitive since it would not experience fouling creep. This is the basis of the canary cell (Chapter 8) that could potentially mimic the plant's performance with the desirable option of evaluating the local fouling phenomenon in every SWM module of the plant.

2.3 Non-Invasive Fouling Detection Methods

The study of membrane performance has interest in three different regions: (i) the membrane, (ii) the fluid boundary layer that includes the membrane-fluid interface and a cake or fouling layer, and (iii) the bulk feed in the membrane module (Chen *et al.*, 2004c). Most experimental work on membrane performance has focused on measurement of macroscopic, indirect, and integral parameters such as flux, solute rejection and pressure drop and this is a limitation to elucidate the microscopic processes and mechanistic theories of membrane performance. There are not many studies available that have observed microscopic processes happening in-situ during filtration in order to substantiate theories and models. Novel non-invasive, in-situ and rigorous quantification of processes affecting membrane performance is essential for breakthroughs in the understanding of membrane performance (Chen *et al.*, 2004b).

Reviews of non-invasive observations methods for in-situ real-time monitoring of membrane processes were based on the following characteristics for comparisons: truly non-invasiveness that has minimal interference with membrane performance, truly real-time to observe dynamic phenomena, device specific with specially designed cells or modules, region specific to the three different regions of membrane performance, the resolution and sample space of the methods, calibration of the technique using a model based on a number of assumptions, and complexity for the degree of specialization involved in application and the level of infrastructure needed (Chen *et al.*, 2004b; Chen *et al.*, 2004c). The various methods described can be separated into two main categories, optical and non-optical. Optical methods are truly real-time and are very sensitive but they usually require a specially designed membrane cell and some require use of specific membranes. However, optical methods usually require an optical window, the resolution is also limited to sub-micron scale, and they are unable to study opaque and concentrated samples. Non-optical methods are capable of improving resolution down to the angstrom scale such as small-angle neutron scattering, SANS, and specie differentation such as NMR imaging, radio labelling and computer aided tomography. However, most non-optical methods rely on complicated signal processing where data acquisition times and data interpretation are issues. Both approaches face the challenge of providing sufficient resolution and data acquistion speed without disrupting significantly the velocity and concentration profiles (Chen *et al.*, 2004c).

To study membrane performance in RO plants, the necessity of an optical window for optical methods presents a safety and technical concern due to the high pressure requirements in RO processes. The use of optical fibres may overcome this. Non-optical methods are less limited and a particular method, ultrasonic time domain reflectometry (UTDR) stand out in terms of its sub-micron resolution and ability to study at least two of the three regions affecting membrane processes; the membrane and the fluid boundary layer that includes the membrane-fluid interface and a cake or fouling layer. This method is used in this thesis and is reviewed in the following section.

2.4 UTDR State-of-the-Art

2.4.1 Fundamentals of UTDR

An ultrasonic wave provides information on the media through which it travels. Its velocity c is a property of the material through which it is being transmitted with c increasing with increasing density of the material, ρ. Δd, the distance between the reflecting interface and the transducer, determines the time t for a waveform to travel through a medium based on the velocity, c, and is given by (Krantz and Greenberg, 2008)

$$t = \frac{2\Delta d}{c} \qquad (2.12)$$

When an ultrasonic wave encounters an interface between two media, reflection, transmission, and mode conversion such as change of phase (i.e., of the wave form) can occur. The magnitude of the reflected and transmitted waves is a function of the difference between the acoustic impedances of the media, $Z_2 - Z_1$, where $Z_i \equiv \rho_i c_i$ and the subscripts 1 and 2 denote the media from which and into which, respectively, the wave is propagating. The amplitude A of the reflected wave relative to the incident wave perpendicular to an interface is given by (Krantz and Greenberg, 2008)

$$A = \frac{Z_2 - Z_1}{Z_2 + Z_1} \qquad (2.13)$$

A plot of the instantaneous voltage of the UTDR waveform shown schematically in Figure 2.4 provides information on (a) the media being studied with (b) the corresponding time-domain responses for the arrival time, amplitude, and phase modulation of the reflected waves. A new peak C distinct from peak B, which is the membrane/feed solution interface, will be generated if a foulant layer thickness is within the UTDR spatial resolution determined by the transducer frequency. If the spatial resolution, which is a function of the frequency and speed of sound wave through the media, is limiting, the fouling layer will not create a distinct peak. However, this will cause the arrival time of peak B to decrease, shown in Figure 2.4 (b) as peak C', which is the reflected wave from the fouling layer/membrane interface. Using any stationary reference point, i.e., reflection A in this case, the arrival times of peaks B and C (or C') permit determination of the thickness of the foulant layer or the membrane (at filtration time for fouling = 0 min). By superimposing the waveforms, the difference between the reference and test waveforms can be compared with suitable software and signal analysis; the resolution of UTDR for the thickness measurement is dependent on the frequency of the transducer and is typically between 100 - 750 nm (Li *et al.*, 2005a).

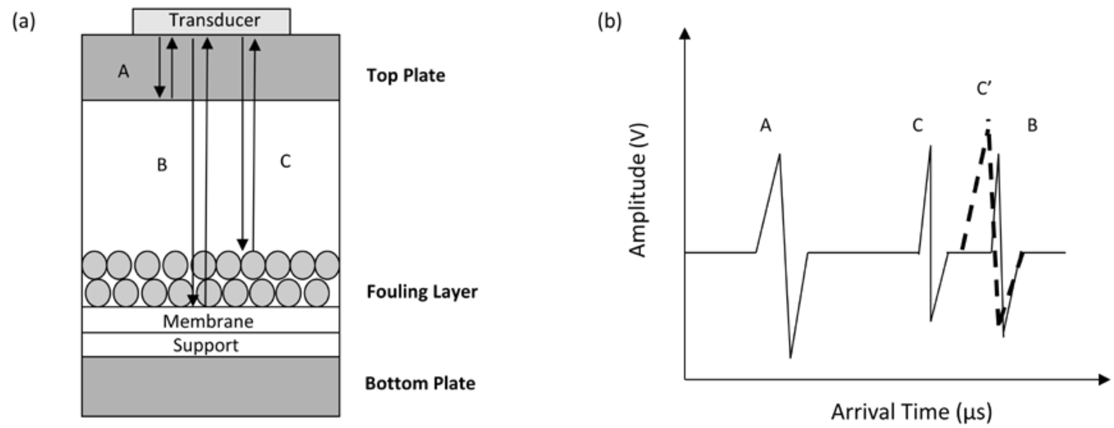

Figure 2.4: (a) Schematic representation of the principle of UTDR measurements in a flat-sheet module and (b) corresponding time-domain responses for configuration in (a).

2.4.2 Successful Applications of UTDR for Membrane Processes

UTDR has been successfully used to study membrane processes for more than a decade. Measurement of thickness changes has been proven for various processes such as the evaporative casting of polymeric films (Kools *et al.*, 1998), membrane compaction owing to high-pressure (Peterson *et al.*, 1998; Aerts *et al.*, 2001), and cake layer growth of various foulants (Mairal *et al.*, 1999; Mairal *et al.*, 2000; Sanderson *et al.*, 2002; Li *et al.*, 2002a; Li *et al.*, 2002b; Li and Sanderson, 2002; Xiu *et al.*, 2002; Li *et al.*, 2005b; Chai *et al.*, 2007; Li *et al.*, 2007; Silalahi *et al.*, 2009; Chai *et al.*, 2012; Li *et al.*, 2012; Lu *et al.*, 2012; Mizrahi *et al.*, 2012; Sim *et al.*, 2012a; Sim *et al.*, 2013b; Taheri *et al.*, 2013). Non-invasive measurement of membrane fouling and cleaning has also been done using UTDR (Mairal *et al.*, 1999; Mairal *et al.*, 2000; Li and Sanderson, 2002; Sanderson *et al.*, 2002; Chai *et al.*, 2007; Lu *et al.*, 2012; Mizrahi *et al.*, 2012; Sim *et al.*, 2012a; Sim *et al.*, 2013b; Chai *et al.*, 2012). Large scale applications have been demonstrated by using UTDR to study commerical spiral wound RO modules (Chai *et al.*, 2007; Chai *et al.*, 2012). Hence, UTDR possess the potential to observe fouling in-situ, in real-time and non-destructively.

Although ultrasonic reflectometry in the frequency domain has been demonstrated for the characterization of foulant growth, in particular biofilm growth on membrane coupons exposed in a bioreactor (Fonseca, 2002; Kujundzic *et al.*, 2007), it required the use of immersion transducers that are not designed for high pressure applications. Moreover, the capability to predict RO fouling is governed by the ability to model the phenomenon of cake enhanced osmotic pressure that is dependent on the thickness of the foulant layer (Taheri *et al.*, 2013). Other phyiscal properties of the foulant layer are also dependent on the thickness measurement such as the determination of yield stress (Sim *et al.*, 2012a) and the inhomogenity of biofilms (Sim *et al.*, 2013b). Therefore, the usage of ultrasonic reflectometry in the time domain is preferred.

2.6 Fouling Monitors

Currently, membrane fouling studies at the pilot and industrial scale use a trial and error approach. Typically, production parameters such as pressure drop or flux decline and product quality are used as indicators of the fouling. Together with destructive membrane studies (autopsies), these indicators are used as diagnostic tools for fouling (Vrouwenvelder *et al.*, 2006b). Using biofouling as an illustration, this is the most expensive way to monitor fouling (Flemming *et al.*, 1998) because by the time (bio)fouling is detected, it is in a very late phase (Flemming, 2003) due to the production parameters being integral measurements of either the entire membrane module, stage or train. It would save much time, material and money to know earlier the development and extent of (bio)fouling and to design anti-fouling measures (Flemming *et al.*, 1996). There is a need for better tools and measurements for early warning systems where microscopic observations of the fouling affecting membrane processes can be monitored in-situ, in real-time and non-destructively that can subsequently allow specific countermeasures (Flemming *et al.*, 1998; Flemming, 2003). It is possible to function as an early warning system if proper and extensive calibrations of the signals from the non-invasive detection methods can be done to match the extent of fouling affecting membrane processes (Flemming, 2003).

For the ideal fouling monitor, there are several requirements such as (1) be representative of the membrane element, (2) be accurate and reproducible, (3) allow the assessment of membrane performance, (4) allow the assessment of fouling either in-situ, in real-time and non-destructively or through analysis of membrane samples, (5) be user friendly and (6) have low or modest costs. In summary, the fouling monitor needs to be representative of a spiral wound RO module by having the same material in terms of membrane and spacers, the same spatial dimensions in terms of channel height and product spacer channels, and the same hydrodynamics in terms of pressure drop, flow rate, and product spacer channels. Secondly, the measurements from the fouling monitor need to be accurate and reproducible to allow the collection of a database that facilitates the interpretation of data collected under different hydrodynamic conditions of the spiral wound RO module and/or at different locations of a RO stage or train. Finally, the monitor needs to be able to monitor the fouling quantitatively through (i) operational parameters like pressure and flux profile, or (ii) in-situ, real-time and non-destructive observations such as signals from non-invasive fouling detection methods, or (iii) allow the analysis of membrane coupons in the monitor (Vrouwenvelder *et al.*, 2006b).

There are a few fouling monitors described in the literature. They are the Membrane Fouling Simulator (MFS) developed by Vrouwenvelder's group in the Netherlands (Vrouwenvelder *et al.*, 2006a; Vrouwenvelder et al., 2006b; Vrouwenvelder et al., 2007; Vrouwenvelder et al., 2010; Vrouwenvelder *et al.*, 2011). This was followed by the high pressure optical membrane module and the external membrane monitor (MeMo) developed by Hoek's group (Subramani and Hoek, 2008; Huang *et al.*, 2010) and Cohen's group (Uchymiak *et al.*, 2007; Bartman *et al.*, 2011; Gu *et al.*, 2013), respectively, in the United States. Both the MFS and the high pressure optical membrane module allow the quantification and characterization of biofouling in-situ and in real-time with non-invasive detection methods such as magnetic resonance imaging (MRI) for the MFS (Vrouwenvelder et al., 2010) and an optical microscope equipped with a reflected fluorescence system for the new high pressure optical membrane module (Huang *et al.*, 2010). Similarly with in-situ, real-time with non-invasive detection, the MeMo allowed the characterization of membrane scaling through the use of optical microscopy with near dark-field illumination (Gu *et al.*, 2013).

The MFS was shown to be representative of a spiral wound membrane module in terms of the development of channel pressure drop. However, the MFS appears to be operated at low pressure and without flux, so it provides only partial simulation (Vrouwenvelder et al., 2006a; Vrouwenvelder et al., 2006b; Vrouwenvelder et al., 2007; Vrouwenvelder et al., 2010; Vrouwenvelder *et al.*, 2011). Although Hoek's high pressure optical membrane module is capable of operating up to 83 bars of pressure (Subramani and Hoek, 2008; Huang *et al.*, 2010), the representative nature of the new high pressure optical membrane module for a spiral wound membrane module has yet to be shown. On the other hand, the Membrane Monitor (MeMo) is capable of operating at high pressure and has shown to appropriately represent a custom-made miniaturized spiral wound membrane module. However, it is not clear if the usage of spacers in commercial spiral wound membrane module could be utilized in MeMo without obstructing the imaging technique (Gu *et al.*, 2013). Chong *et al.* developed a high pressure RO crossflow cell that was used with and without feed spacers (Chong *et al.*, 2008; Chong, 2008). Fouling was monitored by pressure rise as well as UTDR (Chong *et al.*, 2007; Chong, 2008). The canary cell developed in this thesis is based on the high pressure cell of Chong *et al.* and has been compared with the performance of a SWM in Chapter 8.

2.7 Concluding Remarks

This chapter has provided a basic review of the principles of RO membrane processes, fundamentals of concentration polarization and membrane fouling, followed by a more comprehensive review of colloidal fouling, biofouling and fouling evolution in commercial settings. The various non-invasive fouling detection methods, together with state-of-the-art UTDR have been reviewed. Finally, fouling monitors and the requirements for an early warning system for the applications of reverse osmosis have been described.

A key concern for the control of fouling in RO membrane processes is the need for an appropriate early warning system that can provide plant operators with sufficient information to make economic decisions for strategic countermeasures. This requires the integration of non-invasive fouling detection methods with fouling monitors that can allow the monitoring of membrane fouling to detect fouling in-situ, in real-time and non-destructively under the high pressure operating environment for applications of reverse osmosis.

A non-invasive fouling detection method, UTDR, stands out in terms of its resolution, and capabilities to monitor the membrane and the fluid-boundary layer. There are however problems associated with UTDR that need further development for its integration into a fouling monitor. The difficulty in UTDR detecting biofouling, which is the most important problem for applications of reverse osmosis, without the usage of immersion transducers needs to be resolved. In addition, the fouling monitor needs to be representative of a spiral wound RO module in terms of materials, spatial dimensions, and hydrodynamics, and should also be carefully characterized with model foulants in terms of its accuracy and reproducibility under different conditions that simulate the operating conditions of different locations of the spiral wound RO elements. With the integration of UTDR, the fouling monitor should be capable of monitoring the fouling quantitatively and allow in-situ, in real-time and non-destructive observations. Combining the UTDR measurements with other online data would ideally provide methods of fouling prediction; this approach is addressed in Chapter 7 of the thesis.

CHAPTER 3 : EXPERIMENTAL DESIGN CONSIDERATIONS, MATERIALS AND METHODS, MEMBRANE AUTOPIES AND MODELS

This chapter summarizes the various design considerations for the experiments in terms of control of fouling behaviour, concentration polarization, module design and equipment, and UTDR equipment and methodology. Based on the design considerations, the UTDR system, model foulants, types of membranes, background electrolyte, filtration set-ups, and ex-situ membrane autopsies using various analytical techniques such as scanning electron microscopy (SEM), confocal laser scanning microscopy (CLSM), and inductively-coupled plasma optical emission spectrometer (ICP-OES) are then chosen. In the conclusion of this chapter, two models are developed that are used to obtain various experimental properties such as the average porosity of the foulant layer, foulant concentration along the membrane length, effects of fouling propensity of foulants, and the Reynolds Number characterising the hydrodynamics.

3.1 Design Considerations

Prior to summarizing the materials and apparatus used, the design considerations will be discussed for the fouling conditions, filtration experiments, and UTDR equipment and methodology. There are two types of fouling experiments, colloidal silica fouling and biofouling that require different approaches. Separate considerations for the canary cell experiments are also required for the correlation of the canary cell to the SWM.

3.1.1 Control of Fouling Behaviour and Concentration Polarization

As highlighted in section 2.2.1.1, colloidal particles can be destabilized. Operation at constant flux rather than constant pressure was adopted to achieve a constant rate of foulant deposition rather than an uncontrolled fouling rate to study the occurrence of destabilization of the colloidal particles within the foulant layer. Varying the flux and foulant concentration can be used to control the concentration polarization as well as the foulant layer structure; prior studies have shown that filtration at higher fluxes and at higher foulant concentrations forms a denser foulant layer (Boerlage *et al.*, 2003; Sim *et al.*, 2011). Carrying out the filtration at different salinities is also known to alter the foulant layer; a prior study has shown that filtration at higher salinity forms a denser foulant layer due to a reduction of the repulsive forces (Faibish *et al.*, 1998). In order to differentiate between the effects of effective volume fraction, which is characterized by the average porosity of the foulant layer, and membrane surface concentration caused by concentration polarization on the metastability of colloidal suspensions, experiments can be done at different fluxes, crossflow velocities, salinity and foulant concentration. A doubling of either the salinty or foulant concentration at different fluxes will permit determining whether the effective volume fraction or concentration polarization has more influence on the occurrence of metastability. To calculate the average porosity of the foulant layer, a filtration model is developed in Section 3.4.1 from the the use of the TMP profile.

Low pressure UF experiments do not retain the salt used as the background electrolyte. Therefore, low pressure UF experiments would not have concentration polarization of the salt as experienced by high pressure RO experiments. The difference between the salinities caused by the salt concentration polarization effect needs to be accounted for in filtration models. Other than concentration polarization, the higher concentration of salinity near the membrane surface can also influence the foulant particles electric double layer interactions and affect the foulant layer properties, such as average porosity. To account for this, the effect of salt concentration on the specific cake resistance and cake porosity needs to be investigated.

3.1.2 Filtration Module Design and Equipment

Certain considerations need to be met for the choice of flowrate, crossflow filtration module design, and equipment. Appropriate consideration of the module dimensions is required to achieve crossflow velocities of at least 0.1 m/s (Sim *et al.*, 2012a). The volume of permeate flow relative to the feed flow also needs to be less than 5% to maintain an effectively constant bulk concentration (Sim *et al.*, 2012a). However, the recovery may be higher in a typical SWM. Fortunately, the change for the bulk concentration can be accounted for in section 3.4.1. The transmembrane pressure (TMP) needs to be allowed to increase to maintain constant flux for experimental run times amounting to hours or days at a time. This requires an automated increase of inlet pressure with a constant permeate backpressure or the automated decrease of permeate backpressure with a constant inlet pressure. A pressure surge supressor or pulse dampener can be installed to minimise pressure fluctuations with the size of equipment appropriate for the flowrate and pressure required since most pressure pumps create pressure fluctuations in the inlet. Since all membrane modules tend to foul unevenly due to local flux variations, it is appropriate to keep the membrane length short to minimise the effect of these flux variations and to ensure a more even foulant layer.

Controlled biofouling studies would require prescribed amounts of a well-characterized bacterium under conditions of constant biomass deposition, which would require constant flux conditions. The bacteria load can also be more consistent if resting bacteria cells do not proliferate (Sandiford and Wooldridge, 1931) so the bacteria stock solution needs to be prepared in batch and replenished daily. Also, no excess nutrient should be introduced into the feed as the batch prepared bacteria stock solution will have its nutrient content completely removed in the harvesting step. There is also need to characterize the biofilm formed through common parameters such as bacteria counts and extra polymeric substances (EPS) and thickness by confocal laser scanning microscopy (CLSM).

For the canary cell experiments, it is important to understand that the canary cell is a plate-and-frame design and the spiral wound module has a different configuration. Therefore, the flow rates and fluxes of both the canary cell and the SWM have to be allowed to be controlled independently. Achieving crossflow velocities of 0.07 - 0.20 m/s is recommended based on inventory of feed flows used in practice (Vrouwenvelder *et al.*, 2009). As SWMs in RO plants are arranged in trains and are tied by a fixed throughput, operation at constant flux rather than constant pressure was adopted to run the SWM to simulate closer to a real plant situation. To corroborate whether the canary cell represents the SWM, ex-situ membrane autopsies for the amount of deposited foulant have to be performed to complement use of the traditional operating parameter of TMP.

Replicates were performed at the same conditions to account for experimental reproducibility for all experiments. To ensure accurate observation and analysis of trends, a replicate set of at least three different conditions was performed.

For the ideal canary cell, there are several requirements already highlighted in section 2.6. It is noted that the canary cell developed in this thesis does have lower channel pressure drop than a SWM. The channel pressure drop, ΔP_{ch}, is proportional to the length of the channel (Vrouwenvelder *et al.*, 2009) and is given by

$$\Delta P_{ch} = \lambda \frac{\rho v^2}{2} \frac{L}{d_h} \tag{3.1}$$

Where λ is the friction coefficient, ρ is the specific liquid density, v is the average crossflow velocity, L is the length of the channel and d_h is the hydraulic diameter.

The canary cell is intentionally designed to be significantly shorter than a commercial SWM, which is approximately 1 meter in length. A similar cell design to the canary cell found the channel pressure drop to be relatively less sensitive to fouling as compared to fouling of the membrane (Suwarno *et al.*, 2012). The assumption in the canary cell concept is that membrane fouling is dominant over spacer fouling. This is clearly correct for colloids, and our previous work (Suwarno *et al.*, 2012) suggests it is a reasonable assumption for biofouling.

3.1.3 UTDR Equipment and Methodology

3.1.3.1 UTDR Equipment

The ultrasonic transducers, signal pulser and receiver, and storage oscilloscope or electronic digitizer form the three main components of the UTDR equipment. Through vibrations of piezoelectric crystals excited by the electrical energy emitted from the signal pulser and receiver, the transducers are used for generating and receiving the ultrasound waveforms. Depending on the requirements of the experiments, the selection of frequency and the need for focused or divergent transducers are then considered. Focused transducers can provide higher sensitivity and higher resolution but at the expense of higher signal attentuation while higher frequency allows greater lateral resolution (Sim *et al.*, 2012a). The storage oscilloscope, or electronic digitizer, is used to transform the received ultrasound waves from the transducers into observable waveforms of signal voltages and allows the recording and storage of the waveforms for post analysis,. The oscilloscope or digitizer adds to the limitations of the UTDR system's sensitivity through its acquistion time intervals and voltage sensitivity (Sim *et al.*, 2012a).

3.1.3.2 Methodology

To adapt the UTDR for monitoring of membrane processes requires special considerations. To avoid unnecessary attentuation of the sound waves and allow their proper propagation through the medium, the surface of the membrane module where the transducers are mounted needs to be smooth and appropriately coupled (Sim *et al.*, 2012a). Peaks of interest such as the membrane and the feed solution interface, and the fixed plate and the feed solution interface are important to indicate the stability of the UTDR configuration and to use the arrival time data to determine thickness measurements from the waveform analysis (Sim *et al.*, 2012a). It is important to know where to place the transducers. They should not be placed near the inlet or the outlet ports of the membrane module to allow the correct monitoring of foulant layer growth in fully developed hydrodynamic flow established under crossflow conditions (Sim *et* *al.*, 2012a). It is of value to use standard off-line techniques such as scanning electron microscopy (SEM) or in the case of biofouling, confocal laser scanning microscopy (CLSM) to corroborate the UTDR measurements and confirm its accuracy since the application of UTDR to monitor membrane processes is not the conventional method of measurement (Sim *et al.*, 2012a; Sim *et al.*, 2013b).

To detect biofouling noninvasively in real-time using UTDR, it is necessary to increase the acoustic impedance difference at the biofilm/water and membrane/biofilm interfaces (Sim *et al.*, 2012b). The 'acoustic enhancer' should not affect the biofilm development, which requires a need for a toxicity test (Sim *et al.*, 2012b). Studying biofouling in both low and high pressure membrane processes under conditions of controlled hydrodynamics should be applied using UTDR (Sim *et al.*, 2012b). In particular, whether the acoustic enhancers affect the fouling phenomenon would be more of a consideration when the biofouling is studied in low pressure processes because the contribution from the fouling layer to the TMP will be larger relative to that for high pressure processes (Sim *et al.*, 2012b). Biofouling detection using UTDR is described in Chapter 6.

3.2 Materials and Apparatuses

In this section, materials and apparatuses based on the above design considerations are chosen. Detail procedures of the experiments are highlighted in the relevant chapters.

3.2.1 UTDR System

The choice of transducer is detailed in section 3.1.3.1. In all experiments, an unfocused transducer of 5 MHz frequency was chosen. This provided a theoretical spatial resolution of the UTDR system used of approximately 72 μm to 144 μm, which is a quarter to a half of the wavelength of the sound waves, assuming 1500 m/s as the speed of sound wave through the media, which is predominantly water. The resolution allowed observation of the top and bottom of the UF membrane layer (Sim *et al.*, 2012a; Sim *et al.*, 2012b; Sim *et al.*, 2013b), and the top of the membrane layer and the top of the lower membrane module plate for the high pressure RO experiments (Taheri *et al.*, 2013) and fitted the experimental needs. This was because the thickness of the UF membrane was around 220 μm as specified by the membrane manufacturer while the thickness of the RO membrane (Dow, BW-30) was around 120 μm after compaction (Peterson *et al.*, 1998). Although a focused transducer would provide higher resolution and sensitivity, it is only available commercially as an immersion type and is unable to withstand pressure and would not fulfill the requirements of the pressurized filtration experiments. As a result, the UTDR system consisted of a 5 MHz transducer (Olympus Model Videoscan, V-109RM), a 300 MHz digitizer (National Instruments, Model PCI-5152) with a sensitivity of 0.5 ns/div and 39 mv/div, and a pulser-receiver (Panametrics 5058PR). The transducer was externally mounted on the cell using silicone oil as the acoustic couplant. Depending on the filtration mode, the position of the transducers was either placed on top of the membrane module in the crossflow filtration mode or placed at the bottom of the membrane module in the dead-end filtration mode as illustrated in Figures 3.2 to 3.6 in sections 3.2.3 and 3.2.4.

3.2.2 Model Foulant, Background Electrolyte and Membrane Type

Colloidal silica (Sigma-Aldrich, Ludox TMA) was used as model fouling agent that exhibited interesting rheological behavior (Trompette *et al.*, 2005; Sim et al., 2012a). The silica was supplied in the form of a 34 wt% suspension in deionised water at pH 6. No significant change in pH was detected upon the addition of silica to the test solution. The colloidal silica has a nominal particle diameter of 20 nm based on data provided by the manufacturer. Milli-Q water (Millipore) was used to prepare the silica and sodium choride solutions for all tests. Sodium chloride (Sigma-Aldrich) was used as the background electrolyte solution. The sodium chloride solution was filtered (0.2 μm Nalgene, Model 597-4520) before use. For biofouling experiments, *Pseudomonas aeruginosa* bacteria were chosen because this strain has been commonly used in other biofilm studies (Nickel *et al.*, 1985; O'Toole and Kolter, 1998; Hentzer *et al.*, 2002; Suwarno *et al.*, 2012).

A polyethersulfone ultrafiltration membrane with a nominal molecular weight cut-off of 30 kDa (Pall Omega) was used in the low pressure ultrafiltration experiments to ensure retention of the silica particles and the bacteria but not accumulation of the sodium chloride. A thin film composite (TFC) polyamide membrane (Dow, BW-30) was used in the high pressure RO experiments with the exception of the canary cell experiments that uses a similar TFC polyamide membrane (Dow, TW-30)[2]. For correlation of the canary cell to the SWM experiments, a 2.5 inch thin film composite polyamide membrane spiral wound module (Dow, TW30-2540) with a nominal membrane surface area of 2.52 m^2 (0.90 m x 0.70 m) was used. The permeate spacer, feed spacers and membranes for the canary cell were obtained from an identical spiral wound module. For biofouling experiments, the membranes were wetted and soaked in 70% ethanol for 10 hours before use. Otherwise, the membranes were wetted and soaked in Milli-Q water for 10 hours before use.

3.2.3 Crossflow Filtration Apparatuses

The crossflow filtration experiments were carried out at either high pressure or low pressure depending on the type of membranes used. For high pressure crossflow filtration experiments, the placement of flowmeters and conductivity meters were required to be after the back pressure regulator as they were not designed for high pressure usage. Separately, the biofouling and colloidal fouling experiments required slightly different apparatuses. As highlighted in section 3.1.1 for biofouling experiments, a constant biomass deposition was desired that required a controlled injection of bacteria through a valve and metering pump. This was complemented with

[2] The manufacturer has clarified that both TW30 and BW30 are the same membranes. The different labels of TW and BW are for easy referencing to the packaging of the SWM, tapered-wound and fiberglass-bounded, respectively

filters deliberately installed downstream of the crossflow cell to filter out undeposited bacteria and prevent the feed tank from becoming a bioreactor.

The low pressure experiments employed a rectangular parallel plate crossflow cell (Ying Kwang Trading, custom-made) that had a membrane area of 0.0054 m^2 (0.18 m x 0.03 m) and a channel height of 1 mm. A separate acrylic cross-flow membrane cell with an effective membrane area of 0.0012 m^2 (0.06 m x 0.03 m) was used for the low pressure experiments in a new technique to predict RO fouling through the combination of the UTDR and FFM in Chapter 7. The high pressure experiments including the canary cell experiments done to correlate the canary cell to the SWM, employed a rectangular parallel plate crossflow cells (AR Engineering, custom-made) that had a membrane area of 0.0186 m^2 (0.31 m x 0.06 m) and a channel height of 0.8 mm. Figure 3.1 shows a photo of the canary cell.

Figure 3.1: Top-down view of the canary cell.

For the low pressure experiments, the feed was delivered from a continuously stirred 10L tank by a gear pump (Cole-Palmer, Model 74013-45) and by a positive displacement pump for the high pressure experiments (CAT PUMP Model 227). For the canary cell experiments, the feed was delivered from a continuously stirred 30L tank by a positive displacement pump (HYDRA-CELL, Model D10E). The temperature of the feed for all experiments was kept constant with cooling water from chillers. For continuous injection of bacteria stock solution or silica particles as acoustic enhancers for the biofilm detection (Sim *et al.*, 2012b), a valve and metering pump (ELDEX, Model 5979-OptosPump 2HM) was used. The permeate flux was held constant by mass flow controllers (Brooks Instrument, Model 5882 for the low pressure experiments, the BW-30 and the canary cell; Bronkhorst Cori-Tech, Model M55AAD55OS for the SWM). The TMP was measured using pressure transducers (Ashcroft, Model 2174 and Bourdon Haenni, Model E913). The salt concentration of the feed and permeate was determined using conductivity meters. For the biofouling experiments, the retentate was continuously filtered to prevent bacteria from entering the feed tank. Figures 3.2-3.5 show the different schematics of the crossflow filtration apparatus with integration of UTDR.

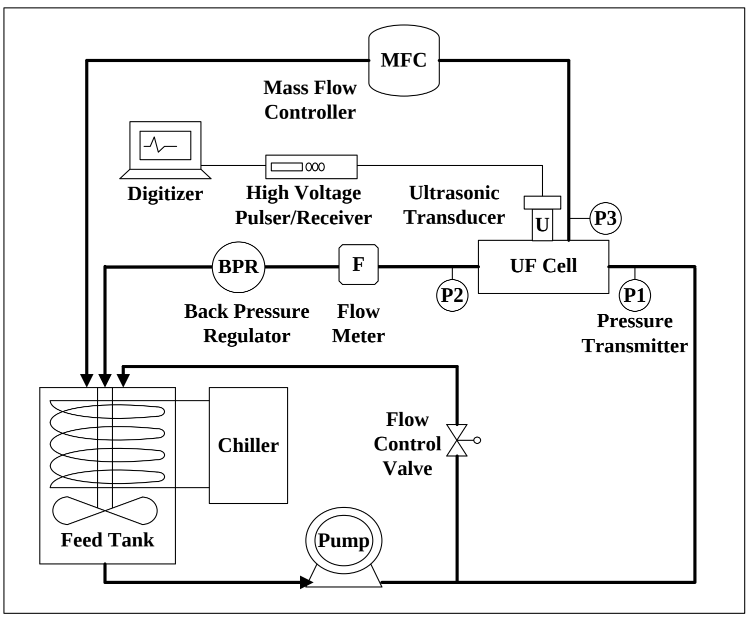

Figure 3.2: Schematic of Low Pressure UF Crossflow Filtration Apparatus with UTDR.

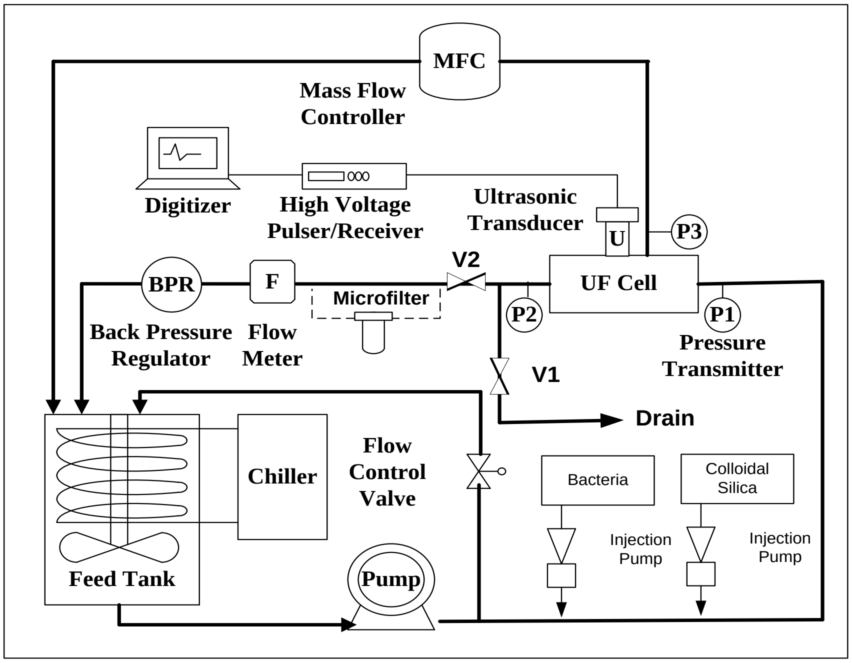

Figure 3.3: Schematic of the Biofouling Experiments using the Low Pressure UF Crossflow Filtration Apparatus with UTDR.

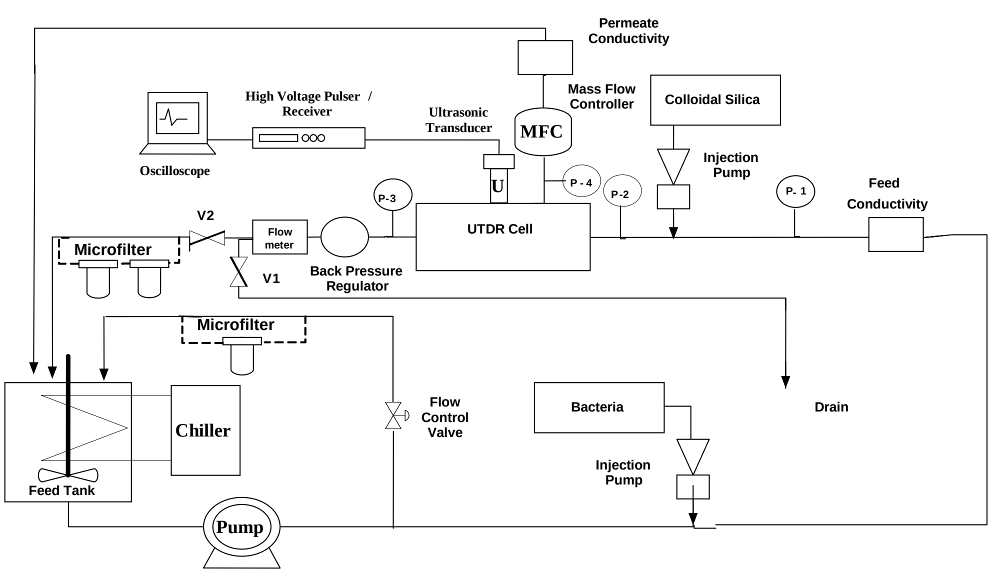

Figure 3.4: Schematic of the Biofouling Experiments using the High Pressure Crossflow Filtration Apparatus with UTDR.

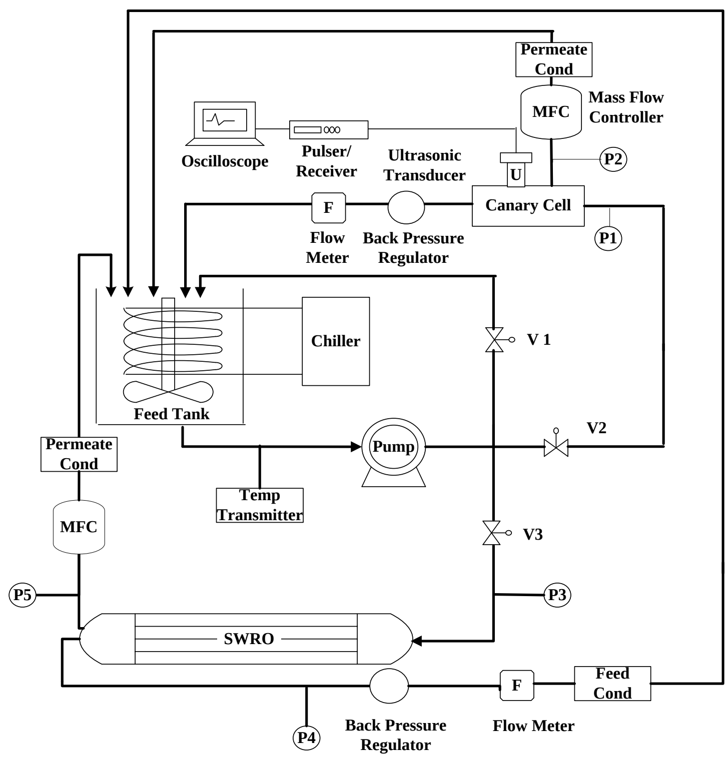

Figure 3.5: Schematic of the SWM Apparatus and the Canary Cell with UTDR.

3.2.4 Dead-end Filtration Apparatus

The unstirred dead-end filtration cell (AR Engineering, custom-made) with a volume of 120 mL and an active membrane area of 0.00126 m^2 (circular diameter of 40 mm) was connected to a nitrogen gas cylinder to supply the required pressure. For the constant flux experiments, the feed cell was pressurized to 210 kPa with nitrogen gas. A mass flow controller (Brooks Instrument, Model 5882) fixed the flux by controlling the flow. The TMP was measured using two pressure transducers (Cole Parmer, Model 206). The dead-end filtration cell was used specifically on occassions required to eliminate the phenonmeon of ‘fractional deposition’ that has been observed by several investigators (Zhang *et al.*, 2010; Chong *et al.*, 2008). The fractional deposition of foulant is thought to arise due to the inefficiency of deposition on membrane surfaces that reduces the net rate of foulant accumulation. It appears to be caused by the presence of a fluid foulant layer as observed by various studies using independent methods of UTDR (Sim *et al.*, 2012a) and nuclear magnetic resonance (NMR) measurements (Airey *et al.*, 1998). This factor has been found experimentally to strongly correlate with the crossflow velocity (Zhang *et al.*, 2010; Chong *et al.*, 2008). Investigation using dead-end filtration mode eliminates the deposition factor phenomenon introduced by the cross-flow filtration mode. Figure 3.6 shows the schematic of the dead-end filtration apparatus with integration of UTDR

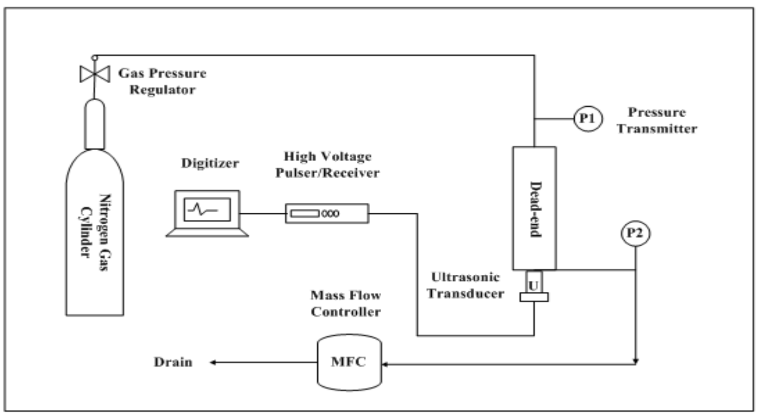

Figure 3.6: Schematic of the Dead-end Filtration Apparatus with UTDR.

3.3 Membrane Autopsies

As highlighted in sections 3.1.2 and 3.1.3.2, membrane autopsies were performed primarily for three purposes; biofilm characterization including CLSM to corroborate the UTDR measurement of the biofilm and toxicity test to ensure the silica particles are safe to use as ‘acoustic enhancers’, SEM to corroborate the UTDR measurement of the silica foulant layer, and ICP-OES to corroborate the representativeness of the canary cell to the SWM.

3.3.1 Biofilm Characterization

For the low pressure experiments, the fouled membranes were removed from the low pressure cell for autopsy that involved a bacterial plate count and EPS analysis. The membrane was cut into three 3 x 5 cm segments labeled 1 through 3 from the feed inlet to outlet as shown in Figure 3.7. Coupons 1 and 3 were then soaked in 50 mL tubes containing sterilized Milli-Q having the same salinity as the experiments. The tubes were sonicated (Fisher Scientific, Model FB15068) for one minute to detach the biofilm from the membrane. Each tube was then stirred with a vortex (Velp Scientifica, Model RX3) for 10 seconds after which 1 mL was withdrawn for bacterial plate counts. Then 1 mL of 1.0 mol of sodium hydroxide solution was added to the tube and left in the refrigerator at $4^{o}C$ for 24 hours before being analyzed for EPS content.

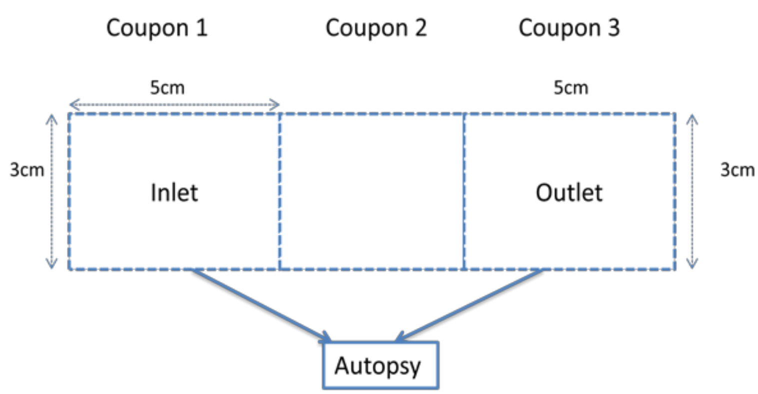

Figure 3.7: Schematic of Membrane Coupons for Autopsies for Biofilm Characterization.

3.3.1.1 EPS Analysis

EPS consists primarily of polysaccharides and proteins. Polysaccharides were analyzed by the calorimetric method (Dubois *et al.*, 1956) where 5 mL of concentrated H_2SO_4 and 1 mL of 5 wt% phenol solution were added to 2 mL of sample solution and left to cool for 10 minutes. Using glucose as the standard, the polysaccharides concentration was determined using absorbance at 490 nm. A commercial Bicinchoninic Acid (BCA) Assay Kit (Pierce, product #23225) was used to determine the protein concentration. 2 ml of working reagent was mixed with 1 mL of sample solution and was left for two hours in the dark. Using bovine serum albumin (BSA) as the standard, it was then measured using absorbance at 562 nm.

3.3.1.2 Bacterial Count Analysis

The serial dilution method was performed for the bacterial analysis to obtain 1 mL samples. A mixture of 2 g/L of sodium chloride and 5 g/L nutrient broth (NB) solution was autoclaved and used for the dilution. 100 µL of diluted solution was then poured on to agar plates. The autoclaved agar solution was prepared with a concentration of 8 g/L of NB and 14 g/L of agar (Beckton-Dickinson, Bacto agar).

3.3.1.3 CLSM Analysis

As the biofilm morphology could be changed from the sample preparation and high vacuum involved in techniques such as scanning electron microscopy, confocal laser scanning microscopy (CLSM) was used as the off-line measurement technique. Moreover, the usefulness of CLSM for characterizing biofilms has been demonstrated in prior studies (Battin *et al.*, 2003; Chen *et al.*, 2013; Suwarno *et al.*, 2012). Membrane samples (1.3 cm from the top and bottom of the membrane, and 8.5 cm between the feed inlet and outlet near the UTDR transducer location) were cut and separated as shown in Figure 3.8 to be representative of the biofilm thickness as measured by the UTDR method. The membrane samples were prepared for CLSM (Zeiss, Model LSM710) by staining using LIVE/DEAD BacLight Bacterial Viability Kits (Molecular Probes, L7012) in accordance with the manufacturer's specifications.

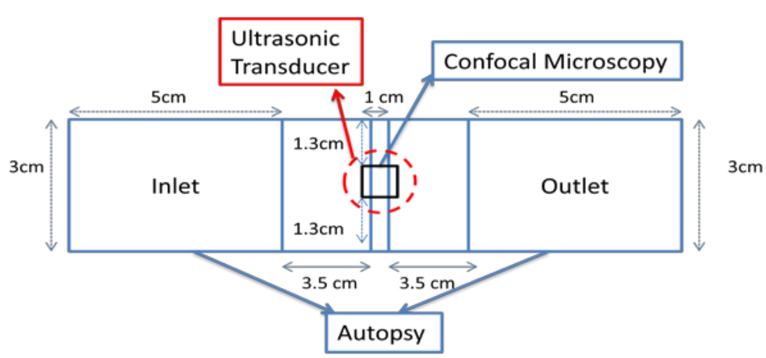

Figure 3.8: Schematic of Membrane Sample for the CLSM analysis for Biofilm Characterization.

3.3.1.4 Silica Toxcity Assessment

Various concentrations of silica (0, 0.2, 1.0, 6.0 g/L) in aqueous solutions containing 2 g/L of sodium chloride and 5 g/L NB were used to conduct a toxicity test to determine if the silica used as the acoustic enhancers (Sim *et al.*, 2013b) in Chapter 6 had any detrimental effects on the viability of the bacteria. After an induction process of 24 hours for each condition, the colony-forming units left from the bacteria grown in the aqueous solutions containing different concentrations of silica were measured.

3.3.2 Scanning Electron Microscopy (SEM) Measurements

An SEM (Zesis, Model EVO 50) was used to analyze the fouled membrane cross-sections. Using a sharp blade (Vidyut, Super-Max), the membranes were first cut before gold sputter-coated (Emitech, model SC7620) for 60 seconds with argon gas as the ionising plasma. Using new blades each time, the membrane samples were carefully cut near the locations of the placement of the ultrasound transducers. To limit damage to the membrane samples from prolonged exposure to the electron gun during SEM analysis, precautions were taken. This was done through keeping the Extra High Tension (EHT) gun setting at an acceptable 15 kV to prevent sample charging and limiting the time of the electron beam focusing on any particular membrane area to typically less than 20 minutes (Sim *et al.*, 2012a). EHT refers to the voltage with which the electrons hit the sample.

3.3.3 Representativeness of Canary cell to SWM

Inductively-Coupled Plasma Optical Emission Spectrometer (ICP-OES) (PerkinElmer, Optima 8000) was used as the ex-situ measurement technique as it is able to detect the elemental silica foulant that has aggregated on the membrane surface. Studies have shown that the foulant layer is made up of two contiguous layers; a loosely bound outer layer (Airey *et al.*, 1998) and a residual tightly bound bottom portion of the foulant layer caused by the metastability of the colloidal silica (Sim *et al.*, 2012a). For the

SWM, each membrane sheet was divided into 9 equal regions as depicted by Figure 3.9 to determine the foulant distribution across the membrane sheet. The dimension of each region was same as the dimension of the membrane in the canary cell for comparative study. Two 2 cm x 2 cm square of membrane samples (indicated by red boxes) were then taken from each region and the membrane of the canary cell according to dimensions reflected in Figure 3.10. The membrane samples were then placed into 15 ml centrifuge tubes containing 13 ml of sodium hydroxide solution of pH 12 for at least 48 hours to extract the silica foulant from the membrane. A solution of pH 12 was chosen as the solubility of silica has been shown to increase rapidly in solutions of pH 9 or greater (Krauskopf *et al.*, 1956). Beyond 48 hours, additional tests showed that there was no further increase in the detection of the elemental silica. It should be noted that during the process of transferring the membrane samples for the extraction process in sodium hydroxide solutions, the labile upper layers of the deposit may have become lost or displaced. The aggregated lower layers were more robust and remained intact, and were more reliable in ex-situ membrane autopsies (Sim *et al.*, 2012a).

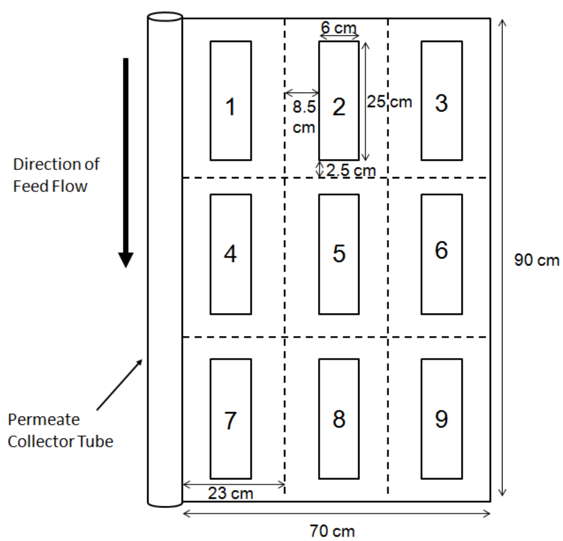

Figure 3.9: Dimensions of regions autopsied on a membrane sheet in a SWM.

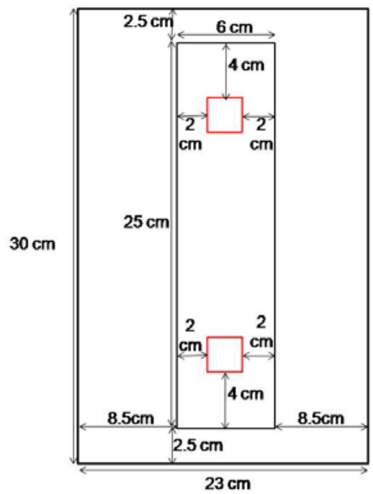

Figure 3.10: Closed-up dimensions of a region autopsied in a SWM.

3.4 Models

This section develops models to obtain various experimental properties such as the average porosity of the foulant layer, foulant concentration along the membrane length, effects of fouling propensity of foulants, and the Reynolds Number that charactizes the hydrodynamics.

3.4.1 Filtration Model

A filtration model is derived here to obtain the average porosity of the foulant layer structure from the transmembrane pressure, ΔP, profile that in turn gives an indication of the effective volume fraction of the foulant layer. Premeate flux, J_v, is given by Darcy's law:

$$J_v = \frac{\Delta P}{\mu\left(R_m + R_f\right)} \tag{3.2}$$

Where R_m is the membrane resistance and R_f is the foulant layer resistance.

The foulant layer resistance, R_f, which increases in time owing to an increasing foulant layer thickness (Sim *et al.*, 2012a) is defined by Equation 3.3:

$$R_f = (J_v - J_{Crit})\alpha_f C_b t \tag{3.3}$$

Where α_f is the mass-based specific cake resistance, J_v is the permeate flux (volumetric flow per unit area), J_{Crit} is the critical flux, t is the filtration time and C_b is the concentration of particles per unit volume of filtrate, V.

If the solute is totally retained by the membrane and the removal of solute by crossflow or stirring that causes a loss of foulant layer resistance, R_f is assumed to be constant, $J_{Critical}$ is equivalent to the steady state flux under the critical flux concept (Bacchin *et al.*, 2006) and is defined by Equation 3.4 as the flux caused by convective-diffusion through the concentration polarization boundary layer (Chudacek and Fane, 1984; Porter, 1972). It should be noted that the critical fluxes were measured experimentally in Section A.1 of Appendix and the steady state flux was used to corroborate the accuracy of the measurements is given by

$$J_{ss} = k \ln \frac{C_g}{C_b} \tag{3.4}$$

The mass-transfer coefficient k can be obtained from the Graetz-Lévêque equation for flat rectangular channels (Porter, 1972) and is given by Equation 3.5:

$$k = 0.816\left(\frac{6QD_{eff}{}^{2}}{h^2wL}\right)^{1/3} \tag{3.5}$$

Where Q is the crossflow volumetric flowrate, h is the channel height, w is the channel width and L is the channel length.

The effective diffusion coefficient, D_{eff} is due to both the Brownian motion molecular diffusion coefficient, D_m and the shear-induced hydrodynamic diffusion coefficient, D_s (Lee and Clark, 1998) and gives

$$D_{eff} = D_m + D_s = \frac{\kappa T}{6\pi\mu r_p} + 0.03 r_p^{\ 2}\gamma \tag{3.6}$$

Where κ is the Boltzmann constant, T is the temperature, r_p is the radius of particle, μ is the dynamic viscosity of solution and γ is the shear rate.

However, the shear-induced hydrodynamic diffusion coefficient, D_s becomes relatively insignificant for submicron particles. Since this model is primarily designed for colloidal solutions, D_{eff} can be assumed to be equal to D_m (Trettin and Doshi, 1980). Rearranging Equation 3.2 gives

$$\Delta P = J_v \mu R_m + J_v \left(J_v - J_{ss}\right)\mu\alpha_f C_b t \tag{3.7}$$

Equation 3.7 assumes that the bulk foulant concentration along the length of the membrane remains unchanged during the deposition. This assumption needs to be validated since the deposition of foulant on the membrane could change its concentration in the bulk fluid. A schematic of the crossflow cell under constant flux operation is shown in Figure 3.11.

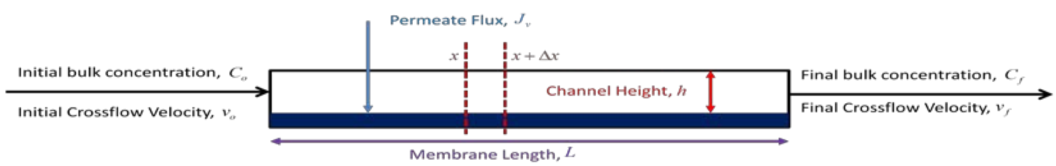

Figure 3.11: Schematic of the crossflow cell under constant flux operation.

A differential mass balance for the foulant over an increment of membrane area $dA = wdx$ is given by Equation 3.8:

$$\left(vhwC\right)\Big|_{x} - \left(vhwC\right)\Big|_{x+\Delta x} = \left(J_v - J_{Crit}\right) wC\Delta x \tag{3.8}$$

where C is the foulant concentration in the cell expressed as mass per unit volume, w is the width of the cell, v is the average axial velocity of the liquid on the feed side of the cell. Taking the limit of Equation 3.8 as $\Delta x \to 0$ gives the following:

$$\frac{d\left(vC\right)}{dx} = -\frac{\left(J_v - J_{Crit}\right)C}{h} \tag{3.9}$$

A differential mass balance on the permeating liquid (i.e., water) is given by

$$\left(vhw\right)\Big|_{x} - \left(vhw\right)\Big|_{x+\Delta x} = J_v w\Delta x \tag{3.10}$$

Taking the limit of Equation 3.10 as $\Delta x \to 0$ gives the following:

$$\frac{dv}{dx} = -\frac{J_v}{h} \tag{3.11}$$

Expanding Equation 3.9 gives

$$v\frac{dC}{dx} + C\frac{dv}{dx} = -\frac{\left(J_v - J_{Crit}\right)C}{h} \tag{3.12}$$

Substituting Equation 3.11 into Equation 3.12 gives

$$\frac{dC}{dx} = \frac{J_{Crit}C}{vh} \tag{3.13}$$

Integrating and applying the boundary condition that $C = C_0$ at $x = 0$, where C_o is the concentration of the foulant at the upstream end of the cell, gives

$$C = C_0 e^{\frac{J_{Crit}x}{vh}} \tag{3.14}$$

Hence, if the critical flux is not zero, the concentration on the feed side will increase exponentially with axial distance along the membrane. However, the maximum increase in concentration along the membrane is less than 2% based on the module channel dimensions given in Section 3.2.3, the critical flux values in Table A.1 of Section A.1 in the Appendix, and the conditions of the crossflow velocity in Chapter 5. Therefore, it is reasonable to assume a constant concentration along the membrane for all experiments.

An important improvement to Equation 3.7 includes a semi-empirical term that is the fractional deposition factor, θ. This incorporates the sticking potential of the foulant, β. As highlighted earlier in section 3.4.2 the reason for the use of dead-end filtration mode is that deposited particles remain in the cake. In crossflow mode, the deposition on membrane surfaces due to the presence of a shear-induced fluid foulant layer reduces the net rate of foulant accumulation. This was observed by various studies using independent methods of UTDR (Sim *et al.*, 2012a) and nuclear magnetic resonance (NMR) measurements (Airey *et al.*, 1998). Moreover, this effect was found experimentally to strongly correlate with the crossflow velocity (Zhang *et al.*, 2010; Chong *et al.*, 2008). Membrane fouling is known to be dependent on the foulant structure and thickness (Lee *et al.*, 2004) and controlled by foulant-fouled membrane interactions (Wang *et al.*, 2011a; Wang *et al.*, 2011b). It is believed these factors affect the fractional deposition factor, θ, and are accounted for by the fouling potential of the foulant, β, which is a measure of the tendency of the foulant particles to stick to each other. It is a function of the foulant-fouled membrane interaction (zeta potential of the foulant), foulant structure (molecular shape), size (molecular weight, MW) as well as other parameters that characterize the ability of the foulant particles to adhere to each other; that is,

$$\beta \equiv f(\zeta^{-1}) \times f(\text{shape}) \times f(\text{MW}) \times \ldots \qquad (3.15)$$

It is beyond the scope of this thesis to determine the explicit functionality of β for the wide spectrum of foulants.

Several authors (Chong *et al.*, 2008; Taheri *et al.*, 2013) had found the empirical rate of accumulation for colloidal silica to be only 5% – 10% of what would have theoretically accumulated on the membrane based solely on Equation 3.7. Unlike critical flux that has a simple physical relationship between the back diffusion force caused by concentration polarization and the drag force caused by the convection of the solute towards the membrane, the mechanism behind the rate of foulant accumulation on the membrane is not well understood. Hence in this study, the rate of accumulation is conservatively assumed to have a theoretical value of 0.10 for all crossflow experiments except in Chapter 7 where the best empirical fit is when θ is equivalent to a value of 0.05. The fractional deposition factor, θ, would be influenced by the fouling potential of foulant, β, and this is allowed for in the following equation:

$$\theta = 0.10\beta \qquad (3.16)$$

Where the fouling potential of foulant is assumed in this study to be equal to 1, i.e., $\beta = 1$ for all experiments except those involving changes in salinity. This is reasonable since this thesis involves only colloidal silica as the model foulant except in biofouling experiments for which the particle-particle interactions should be similar for the same salinity, foulant structure, size and other parameters that affect the ability of the foulant particles to adhere to each other. Although salinity was varied in the dead-end experiments, both θ and β are equivalent to one since there is no crossflow to dislodge the foulant.

To account for changes in salinity, the fouling potential is calculated using the zeta potential of silica , ζ_{Si} , as shown in Table 3 in section A.2 of the Appendix, , as a percentage of the reference zeta potential of colloidal silica, ζ_{R} ; that is, at the electrolyte background of 2 g/L sodium chloride solution. The fouling potential of the foulant due to changes in salinity is corrected with $\beta = \frac{\zeta_R}{\zeta_{Si}}$. A higher zeta potential relative to the reference zeta potential implies a stronger repulsive force between the foulant particles and hence stronger repulsive foulant-fouled membrane interactions and a lower sticking tendency that result in a lower value of the fouling potential, β. The values of β are then used to calculate the fractional deposition factor, θ, using Equation 3.16.

Therefore, Equation 3.7 assumes the following form for crossflow mode:

$$\Delta P = J_v \mu R_m + \theta J_v \left(J_v - J_{Crit} \right) \mu \alpha_f C_b t \tag{3.17}$$

For the unstirred dead-end filtration mode, the effects of solute back-diffusion and the fractional deposition phenomenon can be neglected, i.e., $J_{Crit} \approx 0$ (Chudacek and Fane, 1984) and $\theta = 1$. Therefore, Equation 3.17 becomes:

$$\Delta P = J_v \mu R_m + J_v^{\ 2} \mu \alpha_f C_b t \tag{3.18}$$

The specific cake resistance, α_f (provided $J_{Critical}$ is known), can be determined from the slope of the linear region of a plot of ΔP versus time using Equations 3.17 and 3.18.

3.4.1.1 Determination of Porosity and Thickness

The cake-average porosity, ε, of the foulant layer can be estimated from α_f using the Carman-Kozeny equation (Carman, 1937):

$$\alpha_f = \frac{180\left(1-\varepsilon\right)}{\rho_p d_p^{\ 2} \varepsilon^3} \tag{3.19}$$

where ρ_p is the particle density and d_p is the particle diameter. The cake layer thickness, δ_c can then be determined from:

$$\delta_c = \frac{m_f(t)}{\rho_p(1-\varepsilon(t))} \tag{3.20}$$

where m_f is the mass of foulant deposited per unit area. For dead-end mode,

$$m_f = J_v C_b t \tag{3.21}$$

3.4.2 Hydrodynamics Characterization

The characterization of the hydrodynamics is chosen to be described by the Reynolds number. However, different flow regimes result from the usage of feed spacers and the loss of permeate through the large membrane surface area of the SWM. This section first derives the effect of feed spacer on the effective crossflow velocity before accounting for the Reynolds Number dependence on the module dimensions and flux conditions for both the canary cell and the SWM.

3.4.2.1 Effect of Feed Spacers

The presence of the feed channel spacer reduces the average channel cross-sectional area for the feed water to flow both in the canary cell and the SWM. The effective crossflow velocity, v, is given by the total flow rate, Q, divided by the effective total cross sectional area (Da Costa *et al.*, 1994):

$$v = \frac{Q}{\varepsilon_{sp} h_{sp} w} \tag{3.22}$$

where ε_{sp} is the channel voidage, w is the channel width and h_{sp} is the height of the spacer used (equal to the feed spacer thickness provided by manufacturer). Figure 3.12 shows a schematic of the rhomboid type spacers used in the SWM, ε_{sp} is defined by

$$\varepsilon_{sp} = 1 - \frac{\pi d_f^2}{2 l_m h_{sp} \sin\theta_{sp}} \tag{3.23}$$

where d_f the diameter of spacer filaments, l_m is mesh size, and θ_{sp} is the angle defined by Figure 3.12.

A digital light microscope (KEYENCE, Model VH-Z100R) was used to measure the dimensions of the spacer and using an average of four measurements, l_m and d_f are equivalent to 2.53 mm and 0.40 mm, respectively. The angle θ of the spacer is 90°.

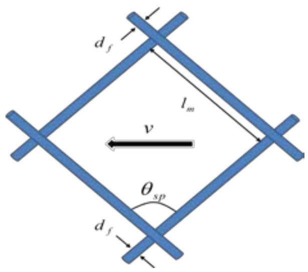

Figure 3.12: Schematic of the rhomboid spacer used.

3.4.1.2 Derivation of the Reynolds Number

Figure 3.13 shows a schematic of the canary cell under constant flux operation.

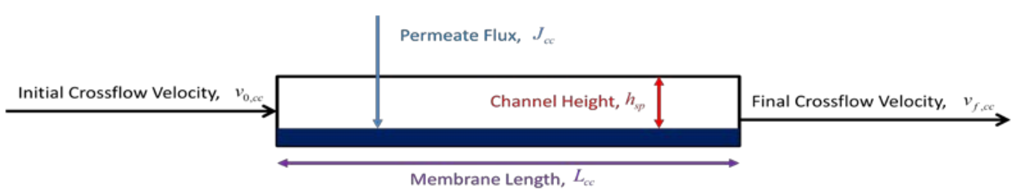

Figure 3.13: Schematic of the canary cell under constant flux operation.

The mass balance for the solvent in the canary cell is described by Equation 3.24:

$$Q_{f,cc} = Q_{0,cc} - J_{cc} L_{cc} w_{cc} \tag{3.24}$$

where $Q_{f,cc}$ and $Q_{0,cc}$ are the amounts of solvent on the feed and outlet side, respectively, of the canary cell, w_{cc} is the width of the canary cell, L_{cc} is the length of the canary cell and J_{cc} is the volumetric permeation flux in the canary cell.

Note that Equation 3.24 divided by cross-sectional area of the canary cell implies that

$$v_{f,cc} = v_{0,cc} - \frac{J_{cc} L_{cc}}{\varepsilon_{sp} h_{sp}} \tag{3.25}$$

where $v_{f,cc}$ and $v_{0,cc}$ are the effective linear velocities of the liquid on the feed and outlet side, respectively, of the canary cell.

Figure 3.14 shows the schematic of the feed channel between two membrane sheets in a spiral wound module under constant flux operation.

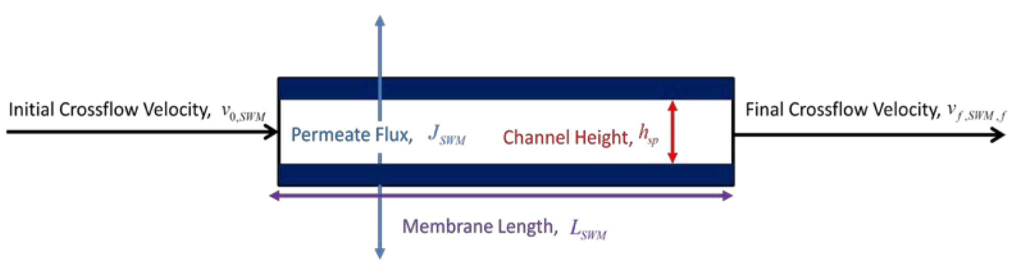

Figure 3.14: Schematic of a channel sandwiched between two membrane sheets in a spiral wound module under constant flux operation.

The mass balance for the solvent in the SWM is described by Equation 3.26:

$$Q_{f,SWM} = Q_{0,SWM} - 2nJ_{SWM} L_{SWM} w_{SWM} \tag{3.26}$$

where $Q_{f,SWM}$ and $Q_{0,SWM}$ are the amounts of solvent on the feed and outlet side, respectively, of the SWM, w_{SWM} is the leaf width of the SWM, L_{SWM} is the length of the SWM, n is the number of membrane leaves in the SWM and J_{SWM} is the volumetric permeation flux in the SWM.

Note that Equation 3.26 divided by cross-sectional area of the SWM implies that

$$v_{f,SWM} = v_{0,SWM} - \frac{2nJ_{SWM}L_{SWM}}{\varepsilon_{sp}h_{sp}} \tag{3.27}$$

where $v_{f,SWM}$ and $v_{0,SWM}$ are the effective linear velocity of the liquid on the feed and outlet side, respectively, of the SWM.

The Reynolds Numbers is given by Equation 3.28,

$$\mathrm{Re}_i = \frac{d_h \rho \left(v_{0,i} + v_{f,i} \right)}{2\mu} \tag{3.28}$$

Where the subscript i refers to either the canary cell or spiral wound module and d_h is the hydraulic diameter.

In the presence of feed channel spacer, the hydraulic diameter can be described by (Da Costa *et al.*, 1994),

$$d_h = \frac{4\varepsilon_{sp}}{\dfrac{2}{h_{sp}} + \dfrac{4(1-\varepsilon_{sp})}{d_f}} \tag{3.29}$$

Substituting Equation 3.25 into Equation 3.28 gives the Reynolds Number for the canary cell,

$$\mathrm{Re}_{cc} = \frac{d_h \rho L_{cc}}{\varepsilon_{sp} h_{sp} \mu} \left(\frac{Q_{0,cc}}{w_{cc} L_{cc}} - \frac{J_{cc}}{2} \right) \tag{3.30}$$

Substituting Equation 3.27 into Equation 3.28 gives the Reynolds Number for the SWM,

$$\mathrm{Re}_{SWM} = \frac{d_h \rho L_{SWM}}{\varepsilon_{sp} h_{sp} \mu} \left(\frac{Q_{SWM,0}}{n w_{SWM} L_{SWM}} - J_{SWM} \right) \tag{3.31}$$

3.5 Concluding Remarks

This chapter helps to appreciate the basis on how the experiments were set-up, which materials and apparatus were chosen, why membrane autopsies were done, what kind of analytical techniques were used, and how to derive the average porosity of the foulant layer and calculation of the Reynolds Number. Therefore, subsequent chapters only provide detailed information on how the experiments were carried out with the details on the experimental set-up, membrane autopsies, and modeling work being referenced back to the appropriate sections in this chapter.

CHAPTER 4 : ANALYSIS OF UTDR WAVEFORMS FOR VARIOUS EXPERIMENTS

UTDR was used to characterize fouling in both crossflow and dead-end filtration modes. In the dead-end filtration mode, only low pressure UF experiments were run. However, there were three types of experiments in the crossflow filtration mode; low pressure UF experiments without the use of feed spacers, high pressure RO experiments with and without the use of feed spacers. The usage of feed spacers was only done for the canary cell experiments since the canary cell had to be representative of the SWM in terms of flow channel hydrodynamics. This chapter provides the information required to decipher the data in order to isolate the peaks of interest reflected from the interfaces such as fixed plate/permeate support, permeate support/membrane, and membrane/feed solution.

To assist interpretation of the signals, the thickness of the various materials used needs to be specified. The nominal thickness of the UF membrane was stated to be 220 μm by the manufacturer. The thickness of the RO membrane after compaction was assumed to be about 120 μm as reported by other authors (Peterson *et al.*, 1998). The permeate support used for all experiments was the product spacer with a thickness of about 0.2 mm used in a spiral wound reverse osmosis module. The foulant layer thickness was calculated using Equation 2.12 in section 2.4.1 of Chapter 2 for which the sound velocity was assumed to be 1500m/s similar to that of water (Sim *et al.*, 2012a; Chai *et al.*, 2012).

It should be noted that the hardware allows arrival time resolution of up to 1 ns, and this allows measurement of the changes in thickness of around 0.75 μm that is similar to the resolution claimed by other authors using similar arrival time resolution

(Peterson *et al.*, 1998). Using higher magnification[3] during the analysis, the peaks almost always spread across a number of data points so a simple time averaging algorithm was used to locate the 'exact' arrival time of the peaks. This improves the resolution down to 0.5 ns, half of the 1 ns time interval that gives an error uncertainty of 50%. As a result, the resolution determined with this software algorithm and hardware system is able to achieve 0.75 +/- 0.38 μm. The identification of peaks of interest is done by comparing the absolute values of the arrival time with theoretical expected peak values as highlighted in the following sections 4.1 and 4.2. This is further complimented by artificially manipulating the operational flux to confirm the identified peak as the membrane peak of interest. Figure 4.1 shows the plots of the amplitude of the acoustic wave response in volts for a RO membrane as a function of the arrival time in microseconds for a contact time at 1 hour under consecutive runs of different fluxes. It is clear from Figure 4.1 the arrival time of peak A, which corresponds to the theoretical expected peak value of the membrane/feed solution interface, shifted to the right due to a higher transmembrane pressure (TMP) for a higher flux of 42.1 L/m^{2}h. This minor compaction of the membrane was reversible when the flux was lowered back from the recovery of the arrival time of peak A thereby supporting the initial identification of peak A to be the membrane/feed solution interface. Separately, an alternative method of normalization is also used in the subsequent chapters by deducing the arrival time with respect to the common peak of interest that corresponds to the membrane/feed solution interface. This method is performed for better visualization of the difference in the arrival times of adjacent peaks of interests such as the membrane/permeate support and the permeate support/plate interfaces that allows for a quick verification of the approximate membrane thickness based on the known values.

---

[3] Higher magnification involves systematically arranging the data points in decreasing order of amplitude over a range of 100 ns in order to perform the time averaging algorithm.

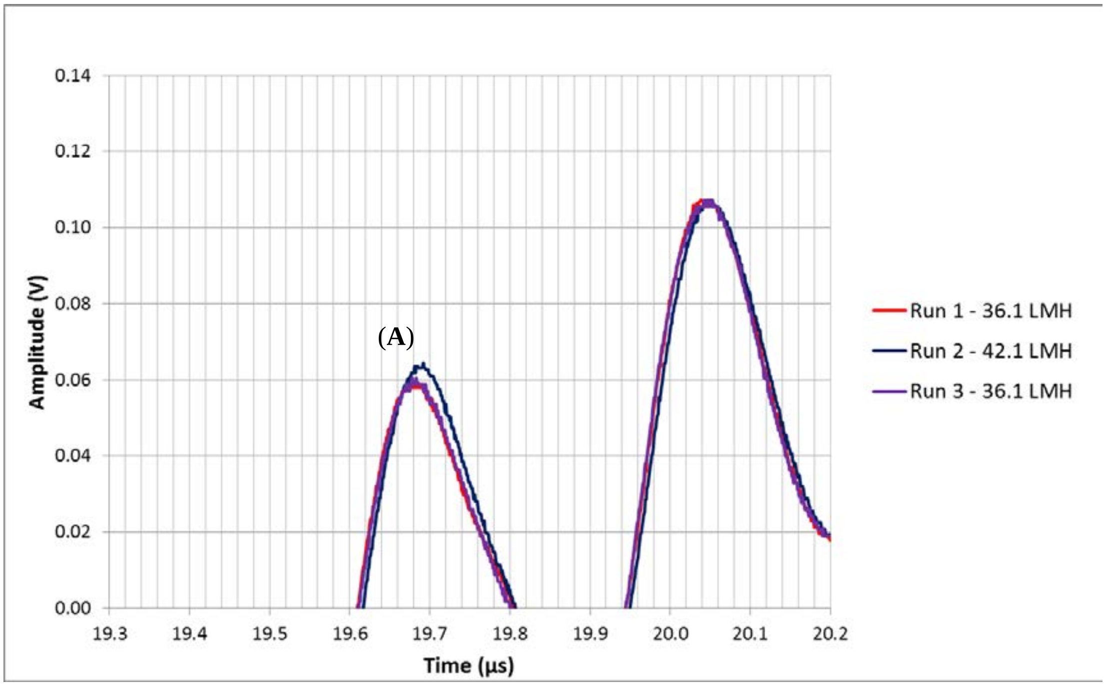

Figure 4.1: Peak Amplitude versus arrival time for a RO membrane under a crossflow velocity of 0.10 m/s for an aqueous solution containing 2 g/L of sodium chloride at consecutive constant fluxes of 36.1 L/m^{2}h, 42.1 L/m^{2}h and 36.1 L/m^{2}h for contact times of 1 hour. Peak (A) is the reflection from the fixed top plate/feed solution interface, Peak (B) is the reflection from the permeate support/fixed bottom plate interface

4.1 Dead-end Experiments

The peaks of interest for the dead-end experiments are peaks A, B, and C corresponding to the reflected acoustic wave generated from the following interfaces; (i) fixed bottom plate/permeate support, (ii) permeate support/membrane, and (iii) membrane/feed solution, respectively. In order to calculate the theoretical arrival time of the peaks of interest using Equation 2.12 in section 2.4.1, the following sound velocities are assumed for the materials; 1500 m/s for water, membrane material and permeate support. For the cell material (Perspex), the value was measured as 2900 m/s using the arrival time of the interface of the fixed top plate/feed solution and the measured thickness. Therefore, the theoretical arrival time of peaks A, B, and C are calculated to be 10.97 μs, 11.23 μs, and 11.53 μs, respectively, which are in close agreement with the actual arrival times of peaks A, B, and C in Figure 4.3 (ii). At a contact time of 0 hr with no introduction of foulant, the difference in arrival times for peaks B and C corresponds to the thickness of the unfouled membrane. When the silica is added at a contact time > 0 hours, the difference in arrival times then corresponds to the combined thicknesses of the membrane and the foulant layer.

Figure 4.2 shows a partial schematic of the dead-end filtration module and the ultrasonic transducer. Figure 4.3 shows the plots of the amplitude of the acoustic wave response in volts for peaks A, B and C of interest as a function of the arrival time in microseconds for a contact time at 0 hours: (i) full reflected signals of the cell and (ii) enlarged region for peaks A, B and C.

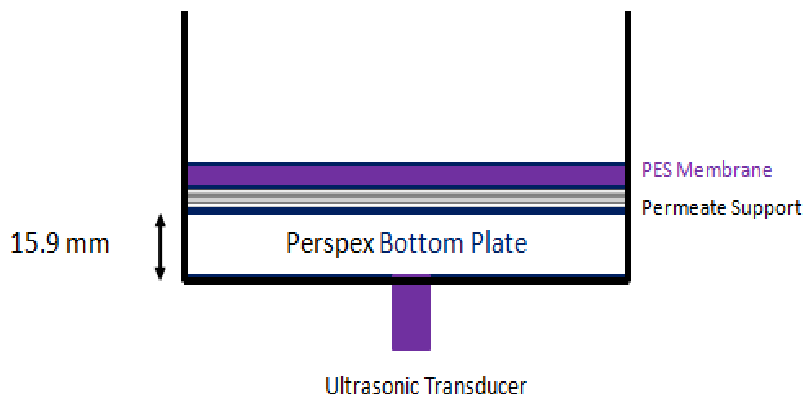

Figure 4.2: Partial schematic of dead-end filtration module with ultrasonic transducer.

(i)

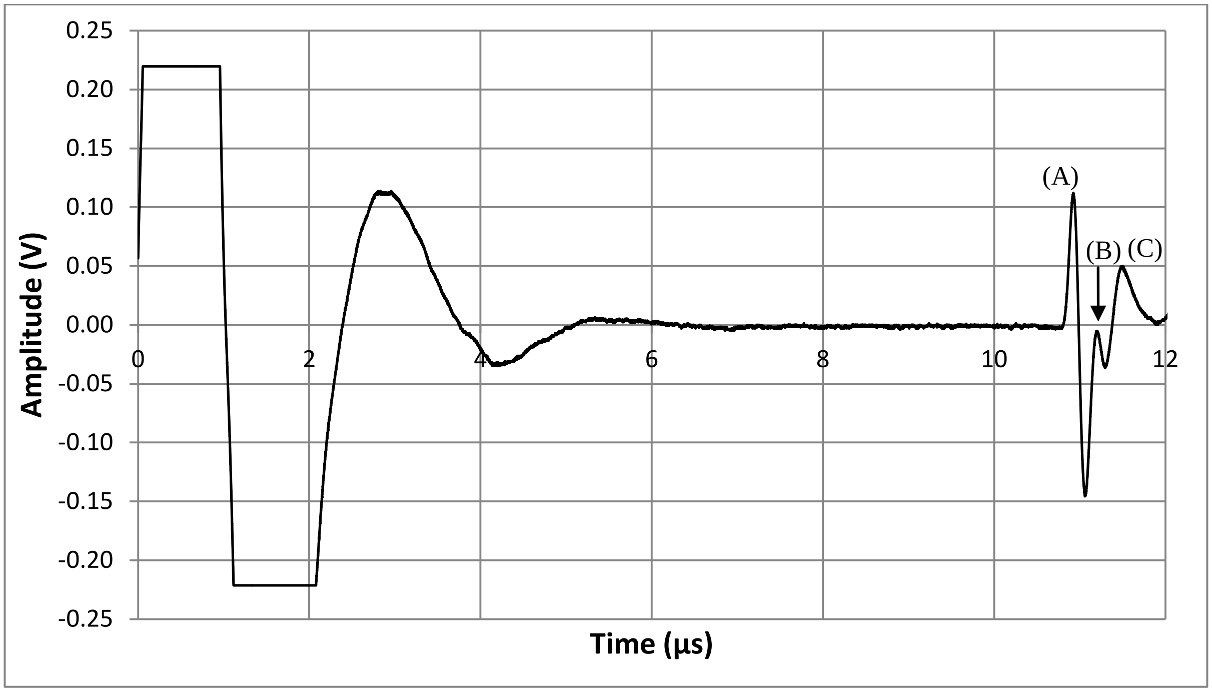

(ii)

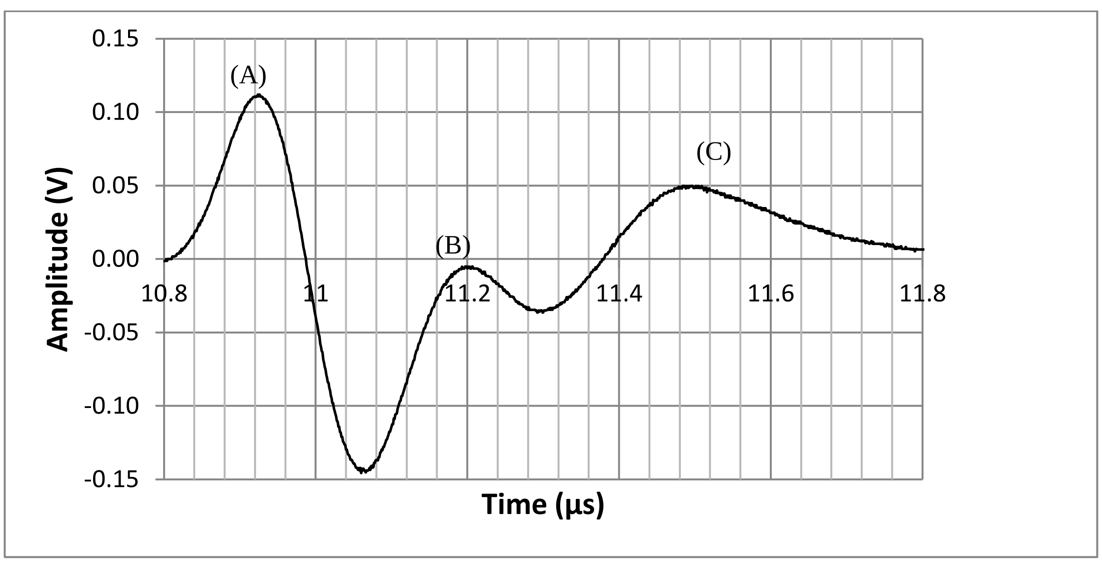

Figure 4.3: Peak Amplitude versus arrival time for an aqueous solution containing 2 g/L of sodium chloride and 0.4 g/L of silica at a constant flux of 80 L/m^{2}h under dead-end filtration mode for contact times of 1, 3 and 5 minutes: (i) full reflected signals of the cell and (ii) peaks

A, B, and C of interest. Peak (A) is the reflection from the fixed bottom plate/permeate spacer interface, Peak (B) is the reflection from the permeate spacer/membrane interface, and Peak (C) is the reflection from the membrane with foulant/feed solution interface.

4.2 Crossflow Experiments

To calculate the theoretical arrival time of the peaks of interest using Equation 2.12 in Section 2.4.1, the following sound velocities are assumed for the materials; 1500 m/s for water, membrane material and permeate spacer. For the cell material (Perspex), the value was measured as 2800 m/s using the arrival time of the interface of the fixed top plate/feed solution and the measured thickness. For experiments using RO membranes, a sound velocity of 2000 m/s is assumed for the polymeric membrane material (Chai *et al.*, 2012) due to the relatively lower water permeability of RO membranes compared to UF membranes. It should be noted that for RO experiments, the permeate spacer/membrane interface could not be resolved due to the frequency of the transducer used but is instead replaced by the fixed permeate spacer/bottom plate interface. This limitation does not affect the calculation of the foulant layer thickness as explained in Sections 4.2.2 and 4.2.3.

4.2.1 UF Membrane

The peaks of interest are peaks A, B and C corresponding to the reflected acoustic wave generated from the following interfaces; (i) fixed top plate/feed solution, (ii) feed solution/membrane, and (iii) membrane/permeate support, respectively. Therefore, the theoretical arrival time of peaks A, B and C are calculated to be 14.29 μs, 15.62 μs and 15.91 μs, respectively, which are in close agreement with the actual arrival times of peaks A, B and C in Figure 4.5 (ii). At a contact time of 0 hr with no introduction of foulant, the difference in arrival times for peaks B and C corresponds to the thickness of the unfouled membrane. When the foulant is added at a contact time > 0 hours, the difference in arrival times then corresponds to the combined thicknesses of the membrane and the foulant layer.

Figure 4.4 shows a schematic of the crossflow filtration module and the ultrasonic transducer. Figure 4.5 shows the plots of the amplitude of the acoustic wave response in volts for peaks A, B and C of interest as a function of the arrival time in microseconds for a contact time at 0 hours: (i) full reflected signals of the cell and (ii) enlarged region for peaks A, B and C.

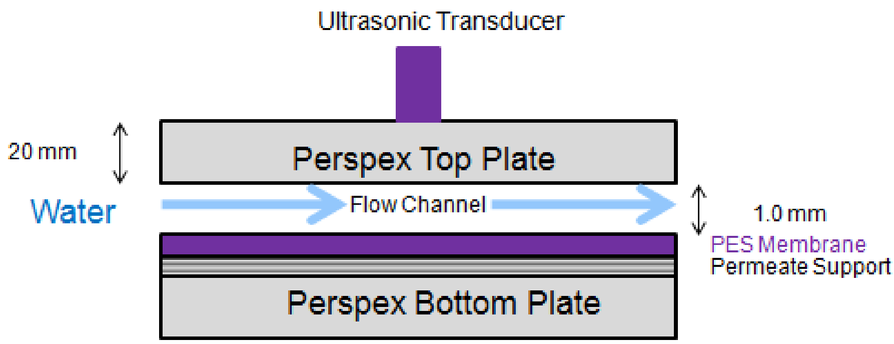

Figure 4.4: Schematic of low pressure crossflow filtration module with ultrasonic transducer.

(i)

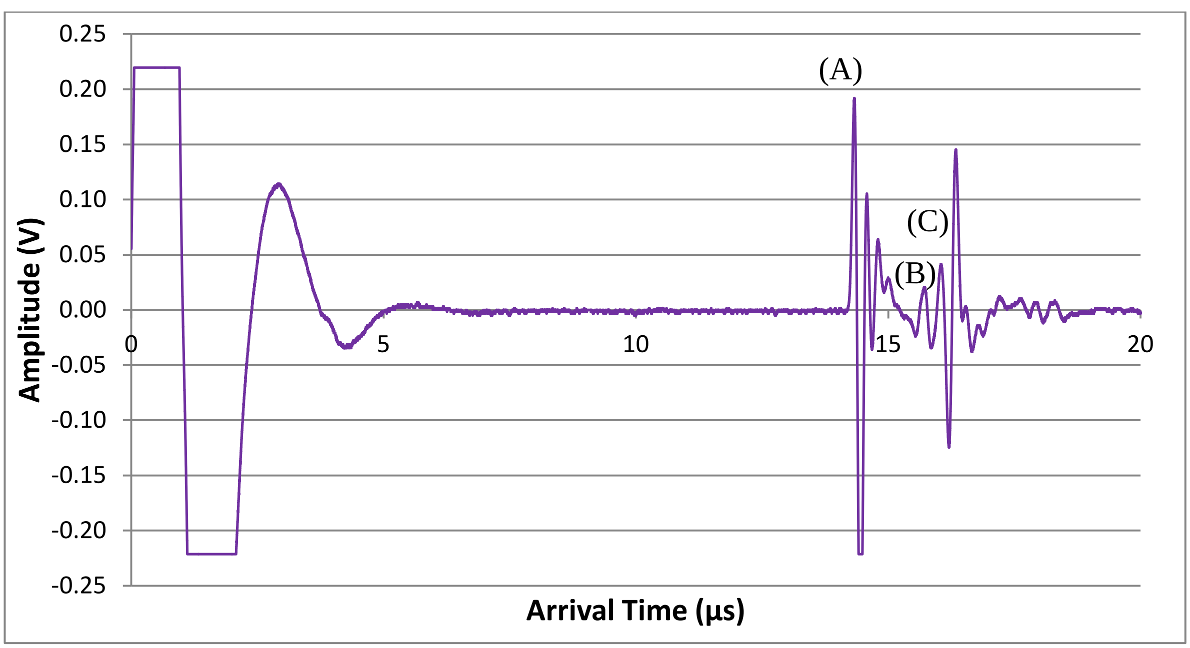

(ii)

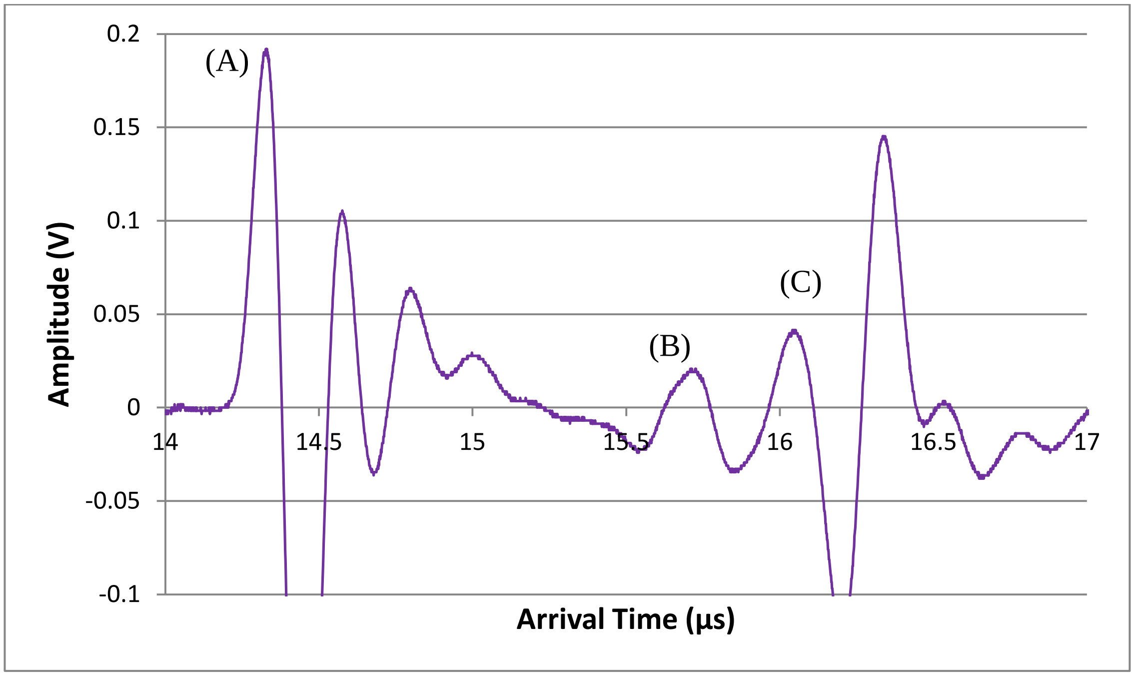

Figure 4.5: Peak Amplitude versus arrival time at various experiment run times for a crossflow velocity of 0.10 m/s , an aqueous sodium chloride solution of 2 g/L and a constant flux of 44.4 L/m^{2}h for a contact time at 0 hours: (i) full reflected signals of the cell and (ii) peaks A, B and C of interest. Peak (A) is the reflection from the fixed top plate/feed solution interface, Peak (B) is the reflection from the feed solution/membrane interface and Peak (C) is the reflection from the membrane/permeate support interface.

4.2.2 RO Membrane without Spacer

The peaks of interest are peaks A and B corresponding to the reflected acoustic wave generated from the following interfaces; (i) feed solution/membrane, and (ii) permeate support/fixed bottom plate, respectively. Therefore, the theoretical arrival time of peaks A and B are calculated to be 19.63 µs and 20.02 µs, respectively, which are in close agreement with the actual arrival times of peaks A and B in Figure 4.6 (ii). At a contact time of 0 hr with no introduction of foulant, the difference in arrival times for peaks A and B corresponds to the thickness of the unfouled membrane and permeate spacer. When the foulant is added at a contact time > 0 hours, the difference in arrival times then corresponds to the combined thicknesses of the membrane, product spacer and the foulant layer.

Figure 4.6 shows a schematic of the crossflow filtration module and the ultrasonic transducer. Figure 4.7 shows the plots of the amplitude of the acoustic wave response in volts for peaks A and B of interest as a function of the arrival time in microseconds: (i) full reflected signals of the cell and (ii) enlarged region for peaks A and B.

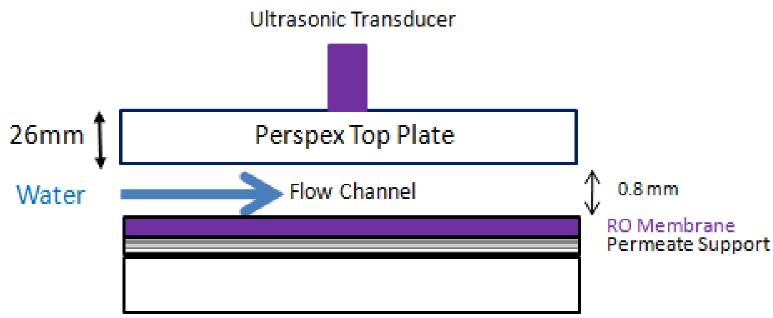

Figure 4.6: Schematic of high pressure crossflow filtration module with ultrasonic transducer.

(i)

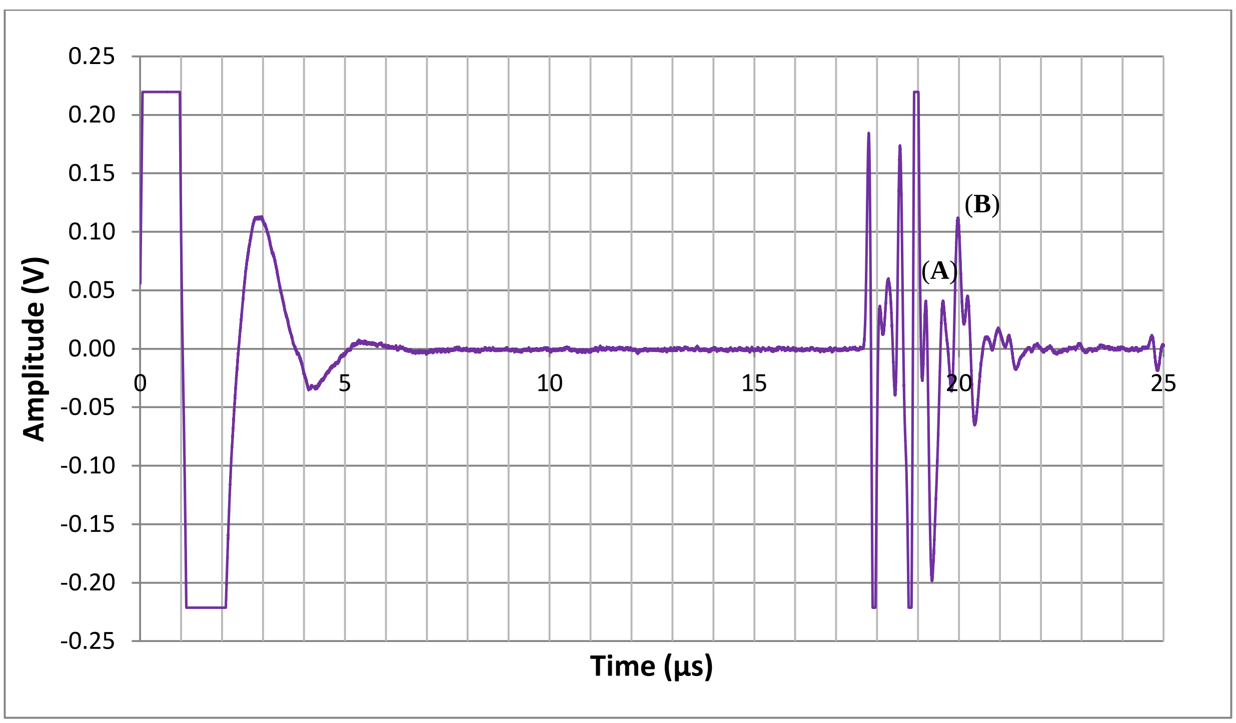

(ii)

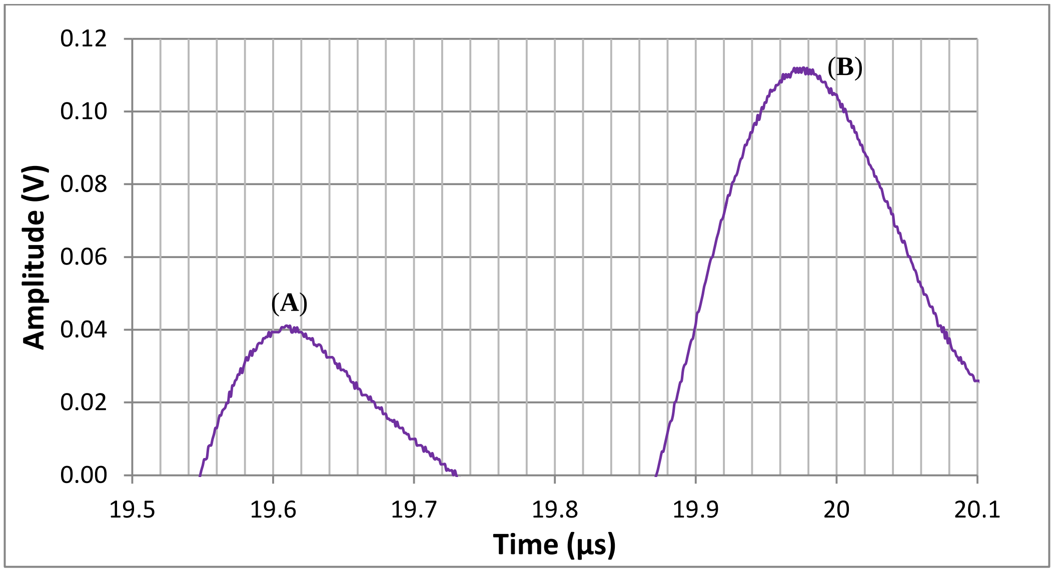

Figure 4.7: Peak Amplitude versus arrival time for a crossflow velocity of 0.10 m/s, an aqueous sodium chloride solution of 2 g/L and a constant flux of 48.1 L/m^{2}h: (i) full reflected signals of the cell and (ii) peaks A and B of interest. Peak (A) is the reflection from the membrane/feed solution interface, Peak (B) is the reflection from the permeate support/fixed bottom plate interface.

4.2.3 RO Membrane with Spacer

The peaks of interest are peaks A and B corresponding to the reflected acoustic wave generated from the following interfaces; (i) feed solution/membrane, and (ii) permeate support/fixed bottom plate, respectively. The same high pressure crossflow module in section 4.2.1 is used. Therefore, the theoretical arrival time of peaks A and B are estimated to be 19.63 μs and 20.02 μs, respectively. The theoretical time difference of peaks A and B at 0.39 μs is in close agreement with the actual time difference of 0.34 μs in the arrival times of peaks A and B in Figure 4.6 (ii).

Figure 4.8 shows the plots of the amplitude of the acoustic wave response in volts for peaks A and B of interest as a function of the arrival time in microseconds: (i) full reflected signals of the cell and (ii) enlarged region for peaks A and B for an aqueous solution containing 2 g/L of sodium chloride at a constant flux of 35 L/m^{2}h at a crossflow velocity of 0.17 m/s. Figure 4.9 shows the plots of the amplitude of the acoustic wave response in volts for peak A of interest as a function of the arrival time in microseconds using data from Figures 4.7 (without spacer) and 4.8 (with spacer). A 0.3 μs delay in the actual arrival times of peaks A and B relative to the theoretical estimate can be observed. This is likely due to the additional distance caused by the feed spacer pressing on the membrane surface.

(i)

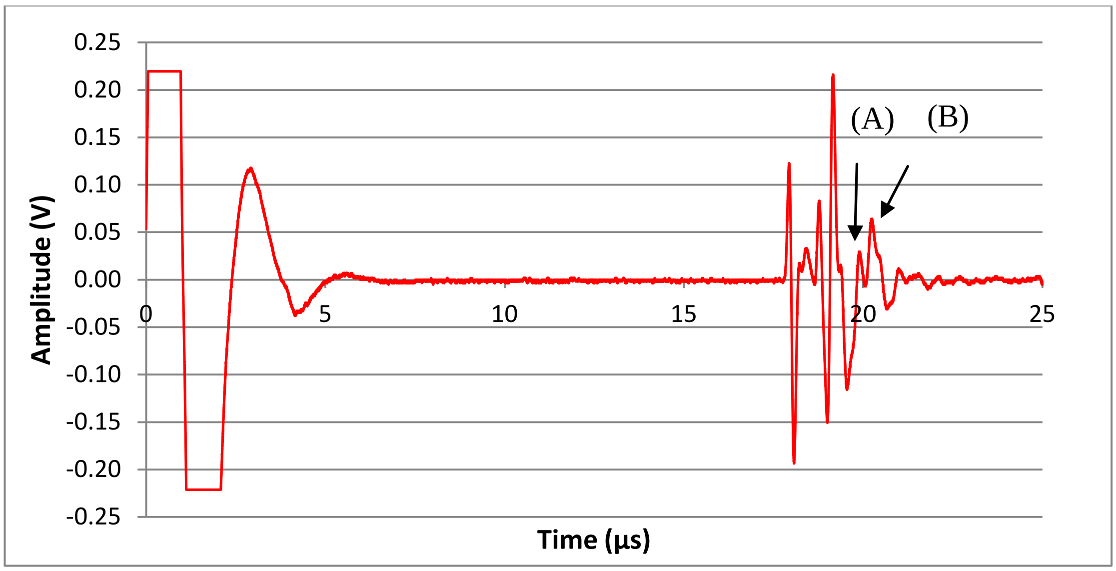

(ii)

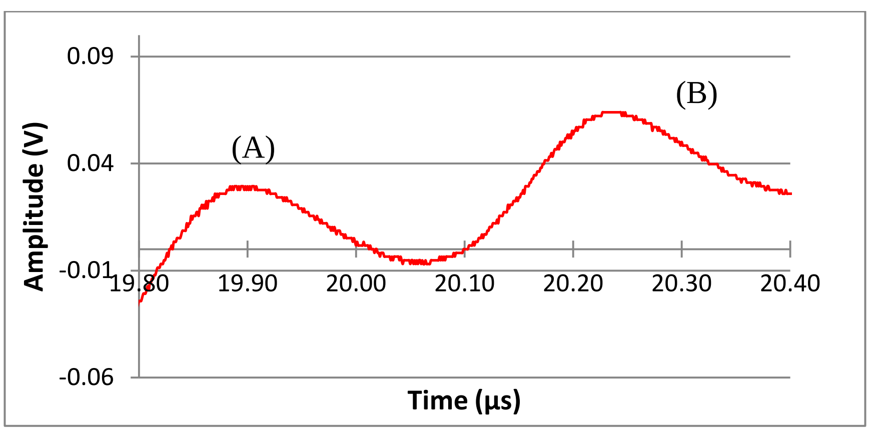

Figure 4.8: Peak Amplitude versus arrival time for an aqueous solution containing 2 g/L of sodium chloride at a constant flux of 35 L/m^{2}h under a crossflow velocity of 0.17 m/s: (i) full reflected signals of the canary cell and (ii) peaks A and B of interest. Peak A corresponds to the

membrane/feed solution interface and Peak B is the reflection from the permeate support/fixed bottom plate interface.

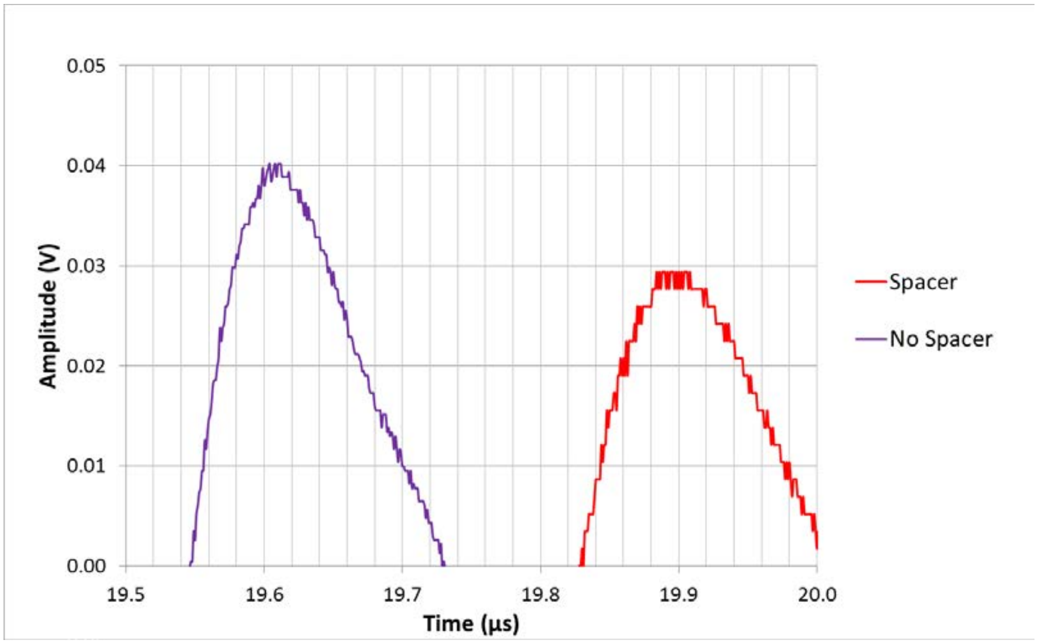

Figure 4.9: Peak Amplitude versus arrival time for the arrival times of peak A with and without spacer utilizing raw data from Figures 4.7 and 4.8. Peak A corresponds to the membrane/feed solution interface.

4.3 Concluding Remarks

This chapter provides the fundamental information on how the peaks of interest are located for the various experiments using UTDR. In summary, the arrival time for the peaks of interest is dependent on the dimensions of the module, materials and the sound velocities assumed. The use of a feed spacer does not constitute a new peak of interest but due to the pressing of the feed spacer on the membrane, it does slightly delay the arrival time for the peak of interest, which is the membrane/feed solution interface. The locating of the peaks of interest in subsequent chapters will be referenced back to the appropriate sections in this chapter.

CHAPTER 5 : COLLOIDAL FOULING AND ITS ASSOCIATED METASTABILITY [4]

5.1 Abstract

There are two foci of this chapter. The first focus provides experimental evidence based on various techniques including TMP, UTDR and SEM measurements to monitor the deposition and physicochemical nature of colloidal silica fouling on a polyethersulfone ultrafiltration membrane under crossflow and constant flux conditions. There are three characteristic stages of fouling based on the rate of TMP increase: (1) an initial rapid rate due to concentration polarization; (2) a slow constant rate; and (3) a nonconstant increasing rate associated with colloidal metastability. During stage 3, the destabilization of the colloidal particles in the foulant layer can be associated with an increase in the UTDR peak amplitude. On switching to a colloid-free feed, a residual tightly bound foulant layer is detected on the membrane by UTDR. The residual thickness by UTDR corroborates well with off-line scanning electron microscopy analysis.

For the second focus, the effects of crossflow velocity, flux, salinity and colloids concentration on the metastability are described. Both concentration polarization (surface concentration) and effective volume fraction (cake-average concentration) influence the occurrence of the metastability with the former being the more significant factor. Lower crossflow velocity and higher flux, salinity and colloids concentration decrease the time required for metastability to occur. There appears to be a 'metastable' (critical) flux that delays the occurrence of colloidal metastability considerably. The use of UTDR as an independent non-invasive detection technique allows the measurement of the foulant layer thickness that consists of a thin dense layer below a thick highly porous layer in-situ, in real-time and non-destructively.

---

[4] The first focus in this chapter has been published in: Sim S.T.V., Chong T.H., Krantz W.B., Fane A.G., J. Membr. Sci. 401-402 (2012) 241-253.

5.2 Introduction

At constant pressure, flux typically declines during the initial phase of crossflow filtration; thereafter it can become relatively stable for hours (Wang and Song, 1999). At constant flux, the TMP may show an initial rise followed by a slow increase over a sustained period. However, abnormal flux drifts or TMP jumps have been reported even for ‘model’ solutions of only one foulant dispersed in apppropriate buffer solutions (Su et al., 2000; Metsämuuronen *et al.*, 2002). These abnormalities have been associated with adsorption (Gekas *et al.*, 1993) and/or pore plugging (Aimar *et al.*, 1988) but are also thought to be due to the metastability of the foulant suspensions whereby destabilization causes formation of gels or aggregates (Aimar and Bacchin, 2010; Ye *et al.*, 2005). Although kinetic boundaries in the composition diagram of colloidal suspensions in drying processes can be asssociated with this type of metastability (Haw *et al.*, 2002), there are not many studies on the metastability of colloids for membrane processes. Some studies consider it to be solely thermodynamically driven (Bacchin *et al.*, 2002) but it could also be kinetically dependent (Aimar and Bacchin, 2010).

The kinetics of the metastability becomes faster as the volume fraction of the particles increases. Due to concentration polarization the membrane surface would be the most conducive to metastable occurrence of colloidal fouling (Aimar and Bacchin, 2010; Bacchin *et al.*, 2002). However, this metastability may be affected by changes in the effective volume fraction indicated by the average porosity within the foulant layer. Therefore, the first focus of this chapter is to apply UTDR to study colloidal fouling and its associated metastability. The UTDR is used to elucidate the physicochemical nature of the fouling and to provide data on cake height that is compared with off-line autopsy measurements. The second focus explores experimentally the effects of the flux, crossflow velocity, salinity, and foulant concentration on the effective volume fraction of the deposits and examines its relationship to metastability. Colloidal silica has been found to be metastable and experiences a glass transition region (Trompette *et* *al.,* 2005; Sim *et al.,* 2012a) and is a suitable model foulant to be used for a study of colloid metastability.

This chapter is organised into two main parts, Part 1 – Evidence for Metastability and Part 2 – Effects of Operational Parameters on Metastability, with separate experimental protocols. Section 5.3 introduces the experimental procedures. Section 5.4 presents the experimental results for the first focus followed by the discussion of the results in section 5.5. Section 5.6 presents the experimental results for the second focus and the discussion of the results is in section 5.7. Final conclusions are summarized in section 5.8 .

5.3 Experimental Procedure

For the crossflow experiments, the membranes were first compressed with Milli-Q water for 30 minutes to stabilise the clean membrane resistance, R_m. The flux was then dropped to the required value and allowed to stabilise before adding the filtered salt solution at the appropriate concentration. After an additional 10 minutes, the silica solution was then added and membrane fouling was allowed to proceed until the TMP was approximately 70 kPa. The TMP of 70 kPa was chosen to permit observing the different fouling stages for all conditions for crossflow experiments used in this chapter. For the dead-end experiments the filtered salt and silica solution were mixed at the appropriate concentration to obtain 50 ml of feed solution. The module then was pressurized to 210 kPa with nitrogen gas. The flux was increased in incremental steps of 20 L/m^2h to reach the target value. Fouling was continued until the target flux could not be maintained. Note that the dead-end experiments were only carried out to cross-check the porosities found from the TMP profile via an independent measurement without the interference of fractional deposition as highlighted earlier in section 3.2.4 of Chapter 3, i.e. carrying the filtration in the absence of shear.

5.3.1 Part 1 – Evidence for Metastability of Colloidal Fouling

There were two types of experiments, referred to as I and II. Type I experiments were allowed to foul till the TMP of 70 kPa was reached under different crossflow velocities. All crossflow experiments were replicated twice (i.e. three experiments) except for that at 0.08 m/s, to verify the overall trend caused by changes in crossflow velocity in the TMP profile and UTDR measurements. For Type II experiments, membrane fouling was allowed to proceed until the TMP was approximately 70 kPa after which the feed solution was replaced with a fresh solution of the same sodium chloride concentration but without the silica foulant, i.e., the introduction of a foulant-free solution,. The experiments were then run with the same initial conditions (flux and crossflow velocity) until the TMP stabilized. Type II experiments were performed to evaluate the reversibility of the foulant layer.

5.3.2 Part 2 – Effects of Operational Parameters on Metastability of Colloidal Fouling

There were five types of crossflow filtration experiments that involved varying conditions of salinity, foulant concentration, crossflow velocity, constant flux, and a doubling of either the salinity or foulant concentration. All crossflow experiments were replicated once (i.e., two experiments) except for the study on the crossflow velocity at different constant fluxes that were replicated twice.

1. For constant fluxes at 60, 70, 80, 90, and 100 L/m^{2}h, experiments were performed for an aqueous solution containing 2 g/L of sodium chloride and 0.4 g/L of silica at crossflow velocities of 0.13 m/s and 0.15 m/s except for constant fluxes of 70 and 90 L/m^{2}h that were also done for a crossflow velocity of 0.20 m/s. The additional crossflow velocity of 0.20 m/s was used to verify the overall trend in the TMP profile and porosities.

2. For salinities of 1, 2, 3, 4, 6 and 8 g/L of sodium chloride, experiments were performed for an aqueous solution containing 0.4 g/L of silica at a crossflow velocity of 0.1 m/s for a constant flux of 44.4 L/m^2h.
3. For a crossflow velocity of 0.13 m/s, experiments were performed for an aqueous solution containing 2 g/L of sodium chloride and 0.4 g/L of silica at constant fluxes at 50, 55, 60, 70, 80, 90, and 100 L/m^2h.
4. For foulant concentrations of 0.2, 0.4, 0.8, 1.2 and 1.6 g/L of silica, experiments were performed for an aqueous solution containing 2 g/L of sodium chloride at a crossflow velocity of 0.13 m/s at a constant flux of 80 L/m^2h.
5. The salinity and foulant concentration were doubled at constant fluxes of 60, 70, 80, and 90 L/m^2h experiments for a crossflow velocity of 0.13 m/s using a baseline condition of an aqueous solution containing 0.4 g/L of silica and 2 g/L of sodium chloride.

For the unstirred dead-end filtration experiments, there were two main experiments.

1. For constant fluxes at 60, 80 and 100 L/m^2h, dead-end experiments were performed with an aqueous solution of 0.4 g/L of silica and 2 g/L of sodium chloride.
2. For foulant concentrations at 0.4 g/L, 0.8 g/L and 1.2 g/L silica, dead-end experiments were performed with an aqueous solution containing 2 g/L of sodium chloride at a constant flux of 80 L/m^2h.

5.4 Experimental Results (Part 1 – Evidence for Metastability of Colloidal Fouling)

Representative results and observed trends are summarised in this section and detailed discussions are given in section 5.5. The fouling behaviour of colloidal silica can be described in three main stages with an interesting transition from a constant to an increasing rate of TMP rise during one of the stages. The growth of the foulant layer was successfully monitored using UTDR with the peak amplitude measurements correlated closely with the transition from a constant to an increasing rate of TMP rise. Large discrepancies existed between off-line SEM and UTDR measurements for Type I experiments where the off-line SEM measurements also appeared to increase with increased experiment run time. For Type II experiments, in-situ real time UTDR thickness measurement was found to match well with the off-line SEM measurements that confirmed the reliability of the UTDR technique. It also gave evidence of a residual foulant layer for every experiment.

5.4.1 TMP Profile

Figure 5.1 shows a plot of the TMP as a function of time for crossflow velocities of 0.08, 0.10, 0.13 and 0.15 m/s under a constant flux of 44.4 L/m^2h for an aqueous solution containing 2 g/L of sodium chloride and 0.4 g/L of silica. Three stages of foulant layer deposition are observed for each crossflow velocity. As shown by curve (d), stage 1 corresponded to concentration polarization caused by the retention of silica particles. Stage 2 corresponded to the silica foulant layer thickness build-up that had a constant relatively slow rate of TMP rise. A transition from a constant to an increasing rate of TMP rise was associated with stage 3, which varied for the different crossflow velocities. Beyond stage 3 towards the end of experiment is labeled as stage 3’ that corresponds to a return to a constant rate of TMP rise that is more rapid than that observed during stage 2, and occurs when the foulant thickness has reached a plateau (see below).

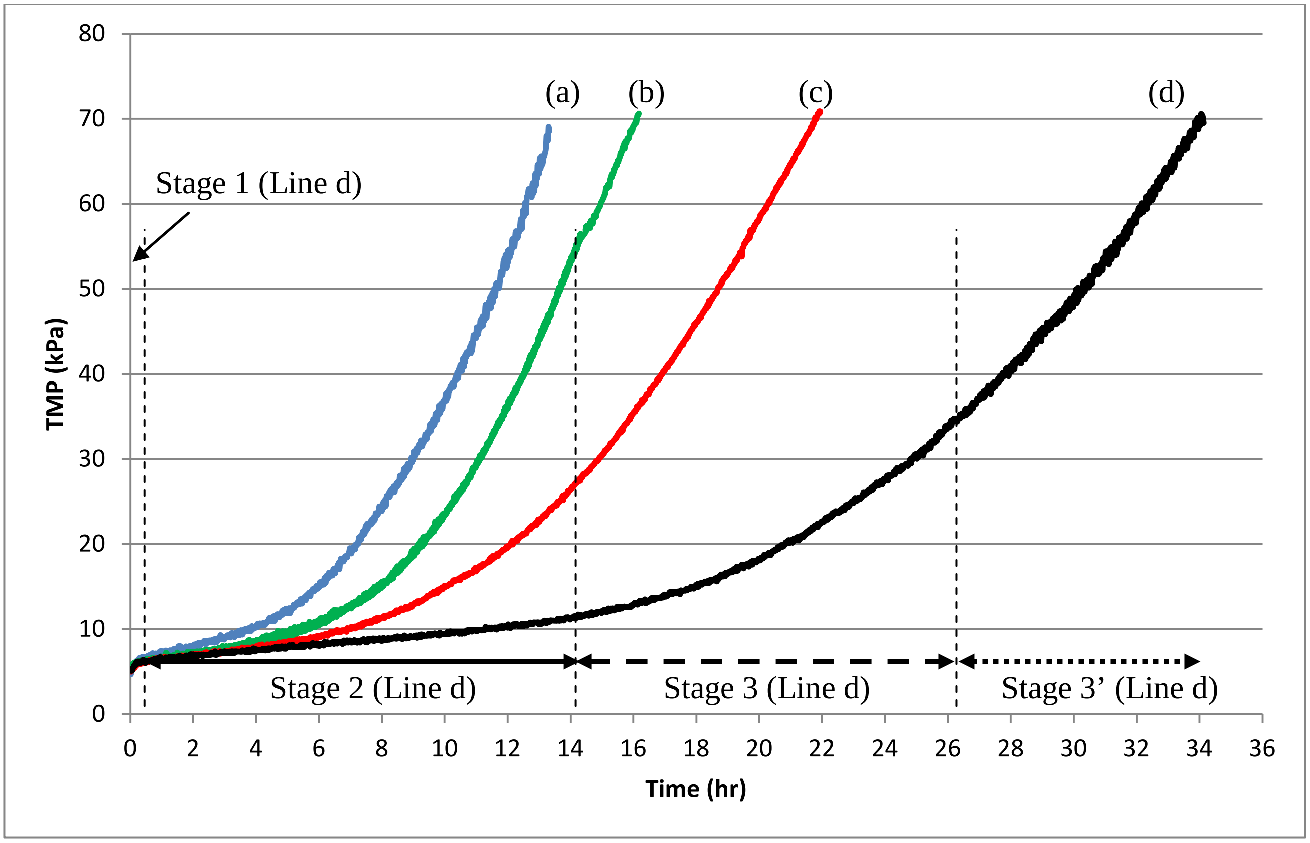

Figure 5.1: TMP versus time for different crossflow velocities, (a) 0.08 m/s, (b) 0.10 m/s, (c) 0.13 m/s, (d) 0.15 m/s under a constant flux of 44.4 L/m^{2}h for an aqueous solution containing 2 g/L of sodium chloride and 0.4 g/L of silica.

5.4.2 UTDR Measurements

Figure 5.2 shows a plot of the amplitude of the acoustic wave response in volts as a function of the arrival time in microseconds for contact times of 0, 5, 9 and 14 hours. The build-up of the foulant layer can be appreciated from the movement of peak B shifting towards the left that indicates a decrease in the arrival time of peak B or an increased difference in the arrival times of peaks B and C caused by the thickness of the silica foulant layer.

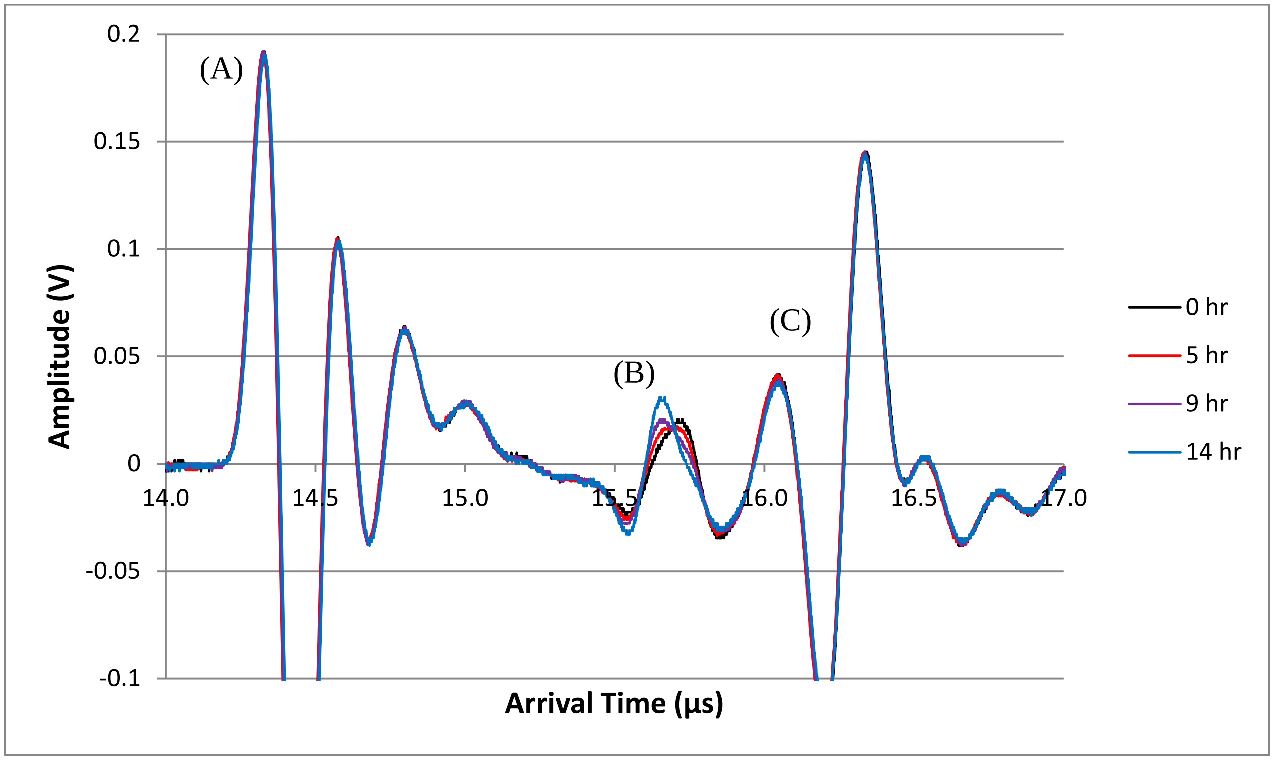

Figure 5.2: Peak Amplitude versus arrival time at various experiment run times of 0, 5, 9 and 14 hours for a crossflow velocity of 0.10 m/s, an aqueous sodium chloride solution of 2 g/L, a silica concentration of 0.4 g/L and a constant flux of 44.4 L/m^{2}h.

Figure 5.3 is a plot of the foulant layer thickness determined via UTDR as a function of contact time for crossflow velocities of 0.08, 0.10, 0.13 and 0.15 m/s. The foulant layer thickness decreased and the time taken to reach the required pressure of 70 kPa increased at higher crossflow velocities.

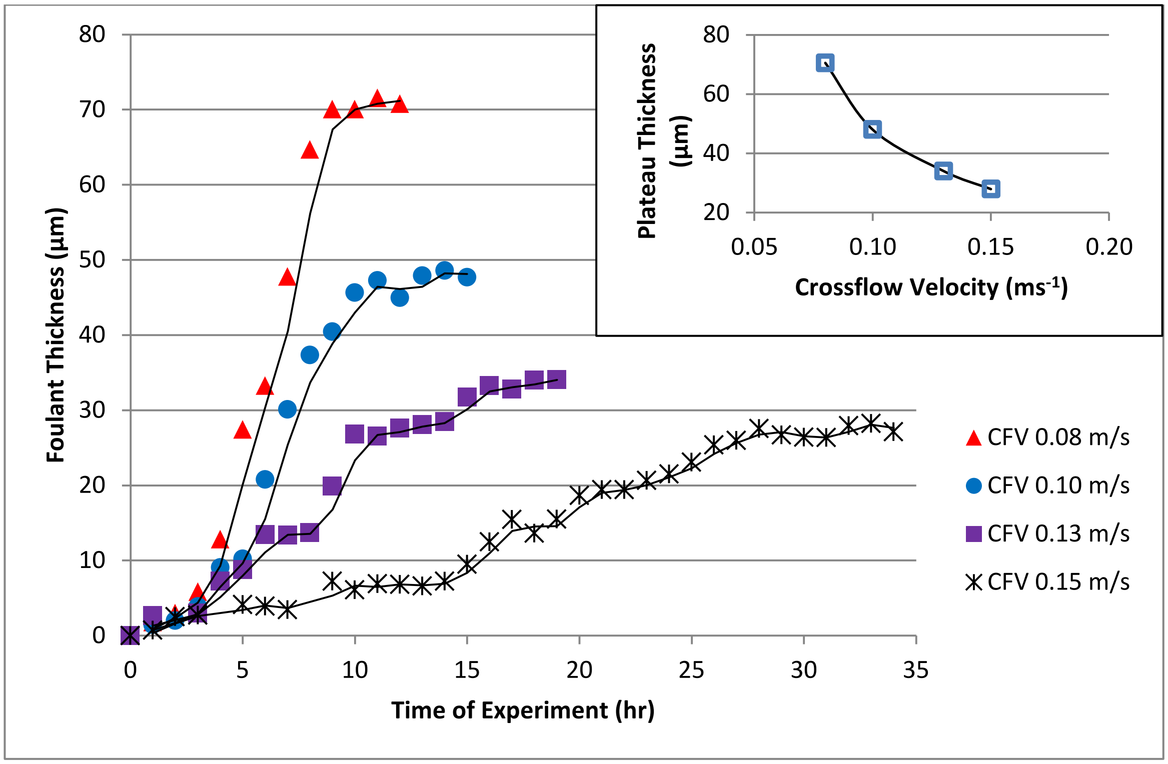

Figure 5.3: Foulant layer thickness determined via UTDR as a function of contact time for crossflow velocities of 0.08, 0.10, 0.13 and 0.15 m/s, an aqueous sodium chloride solution of 2 g/L, a silica concentration of 0.4 g/L and a constant flux of 44.4 L/m^{2}h.

Figures 5.4 and 5.5 show plots of the foulant thickness and peak amplitude, respectively, determined by UTDR along with the corresponding TMP as a function of contact time for the highest crossflow velocity of 0.15 m/s. Figure 5.4 shows a monotonic gradual increase in foulant thickness but a non-linear rapidly rising TMP profile. Figure 5.6 shows a corresponding increase in the peak amplitude that coincided with the occurrence of stage 3, which is described by the transition to an increasing rate of TMP rise. Similar increases in the peak amplitude were observed for all UTDR measurements during this stage of fouling. These trends are discussed in Section 5.5.

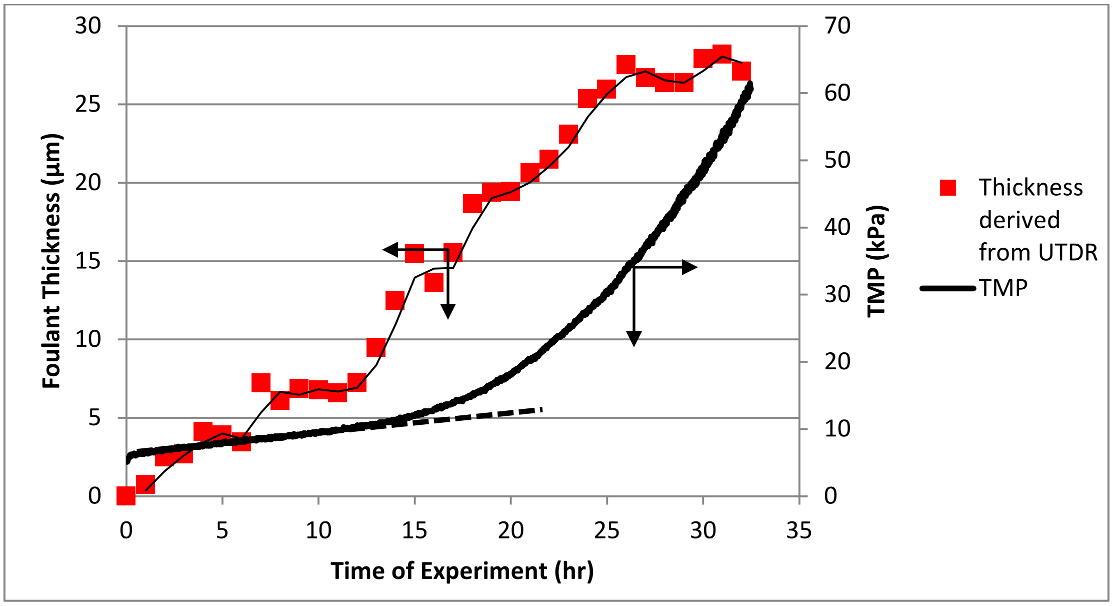

Figure 5.4: Foulant layer thickness determined via UTDR along with the corresponding TMP as a function of contact time for a crossflow velocity of 0.15 m/s, an aqueous sodium chloride solution of 2 g/L, a silica concentration of 0.4 g/L and a constant flux of 44.4 L/m^{2}h.

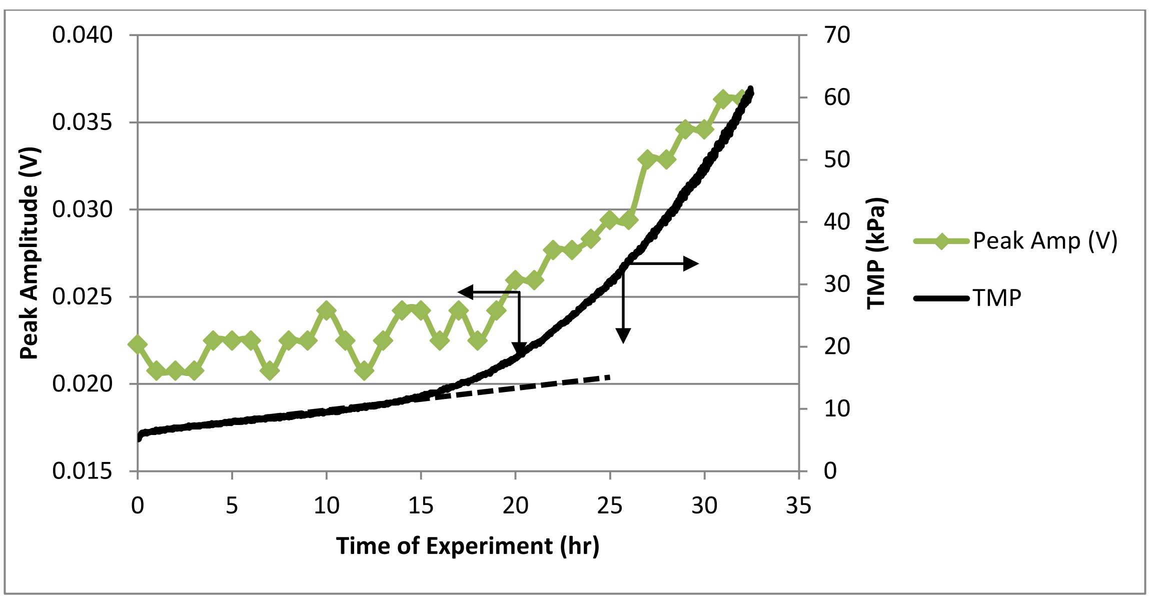

Figure 5.5: Peak amplitude determined via UTDR along with the corresponding TMP as a function of contact time for a crossflow velocity of 0.15 m/s, an aqueous sodium chloride solution of 2 g/L, a silica concentration of 0.4 g/L and a constant flux of 44.4 L/m^{2}h.

5.4.3 SEM Measurements

There were two sets of cross-sectional SEM pictures. The first set was to compare the foulant layer thickness at the end of experiments for different crossflow velocities corresponding to the UTDR data shown in Figure 5.4. The second set was taken for experiments stopped at different times within the stages of TMP rise observed in the TMP profile shown in Figure 5.1 under the same crossflow velocity of 0.13m/s, specifically at stage 2 – characterized by a slow constant rate of TMP rise, stage 3 – characterized by a transition from a constant to an increasing rate of TMP rise and at the end of the experiment.

Table 5.1 summarizes the foulant layer thickness measured by SEM for different crossflow velocities and a constant flux of 44.4 L/m^{2}h for an aqueous solution containing 2 g/L of sodium chloride and 0.4 g/L of silica for all four experiments for which the thickness determined by UTDR is shown in Figure 5.3.

Table 5.1: SEM Cross-sectional Thickness Measurements under different crossflow velocities.

Silica (g/L)	NaCl (g/L)	Flux (LMH)	**Crossflow Velocities (m/s)**	**Foulant Layer Thickness (µm)**	**Experimental Run Time (hr)**
0.4	2	44.4	**0.08**	**3.8**	**12**
0.4	2	44.4	**0.10**	**3.4**	**15**
0.4	2	44.4	**0.13**	**13.4**	**22**
0.4	2	44.4	**0.15**	**11.8**	**34**

There were two interesting observations. At relatively higher crossflow velocities, the foulant layer was thicker. Moreover, the absolute values of the residual foulant layer thickness were much lower than the UTDR measured thickness shown at the plateau in the film thickness determined by UTDR. The only observable trend was the relationship between experimental run time and the residual foulant layer thickness measured by SEM. Longer experimental run times resulted in somewhat larger residual foulant layer thicknesses measured by SEM. An explanation for the differences between the SEM and UTDR data is given in section 5.5.3.

Table 5.2 shows the foulant layer thickness values obtained from cross-sectional SEMs of membranes samples for experiments carried out at different time durations to characterize the different stages of TMP rise. The SEM characterization suggests that the growth of the foulant layer was minimal during stage 2, the slow constant rate of TMP rise, and grew progressively more rapidly beyond stage 2, the increasing rate and more rapid constant rate of TMP rises, respectively.

Table 5.2: SEM Cross-sectional Thickness Measurements under crossflow velocity of 0.13 m/s.

Stage of TMP rise	Silica (g/L)	NaCl (g/L)	Flux (LMH)	Crossflow Velocity (m/s)	**Residual Foulant Thickness (μm)**	dTMP/dt (kPa/h)
2 (*t* = 5 hrs)	0.4	2	44.4	0.13	**< 1.0**	0.644
3 (*t* = 13 hrs)	0.4	2	44.4	0.13	**4.1**	2.618
3’ (*t* = 22 hrs)	0.4	2	44.4	0.13	**13.4***	6.436

* Same experiment carried out at crossflow velocity of 0.13 m/s in Table 5.1.

5.4.4 Type II Experiments

Figure 5.6 shows a plot of the foulant layer thickness determined via UTDR and the corresponding TMP measurements as a function of contact time for a crossflow velocity of 0.13 m/s that was stopped at stage 3’. The feed was switched to a silica-free solution at a TMP of 70 kPa. Figure 5.7 shows a plot of the foulant layer thickness determined via UTDR and the corresponding TMP as a function of contact time for a crossflow velocity of 0.13 ms^{-1} that was purposely stopped halfway during stage 3, characterized by the transition from a constant to an increasing rate of TMP rise. These experiments were done to corroborate the SEM measurements shown in Table 5.2. It should be noted that in order to avoid compressing the data, the time, length and pressure scales in Figure 5.6 and 5.7 are not the same. The trend for the increase in residual foulant layer thickness determined by UTDR in Figures 5.6 and 5.7 follows that displayed by the off-line SEM measurements shown in Table 5.2.

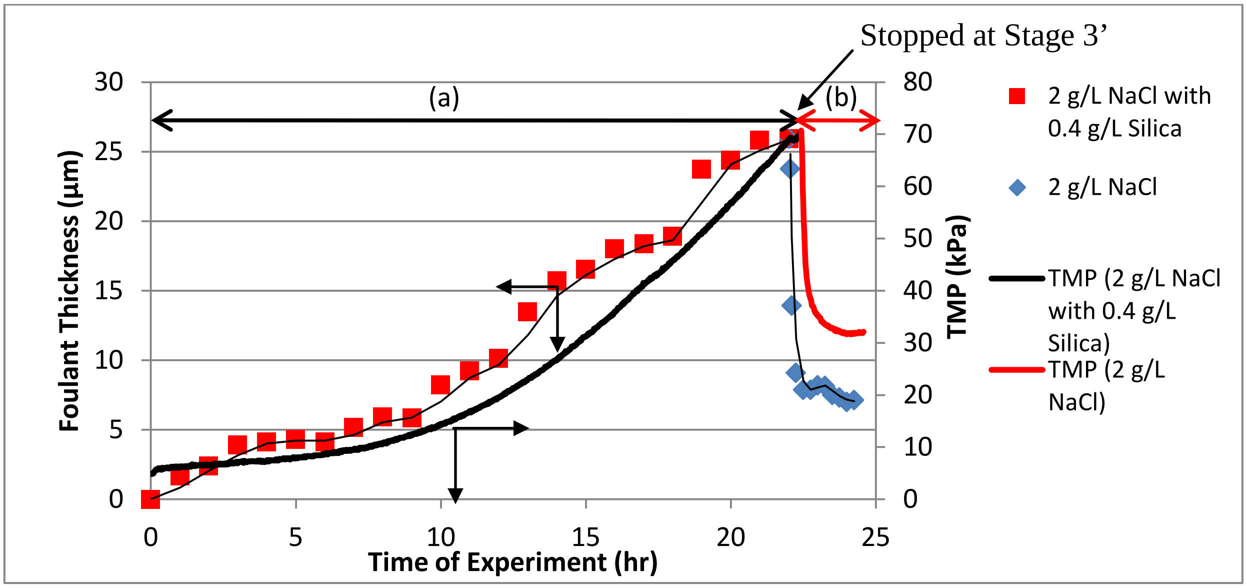

Figure 5.6: Foulant layer thickness determined via UTDR and corresponding TMP measurements for 0.13 m/s crossflow velocity and a constant flux of 44.4 L/m^{2}h under (a) an aqueous sodium chloride solution of 2 g/L, silica concentration of 0.4 g/L and (b) silica-free aqueous sodium chloride solution of 2 g/L.

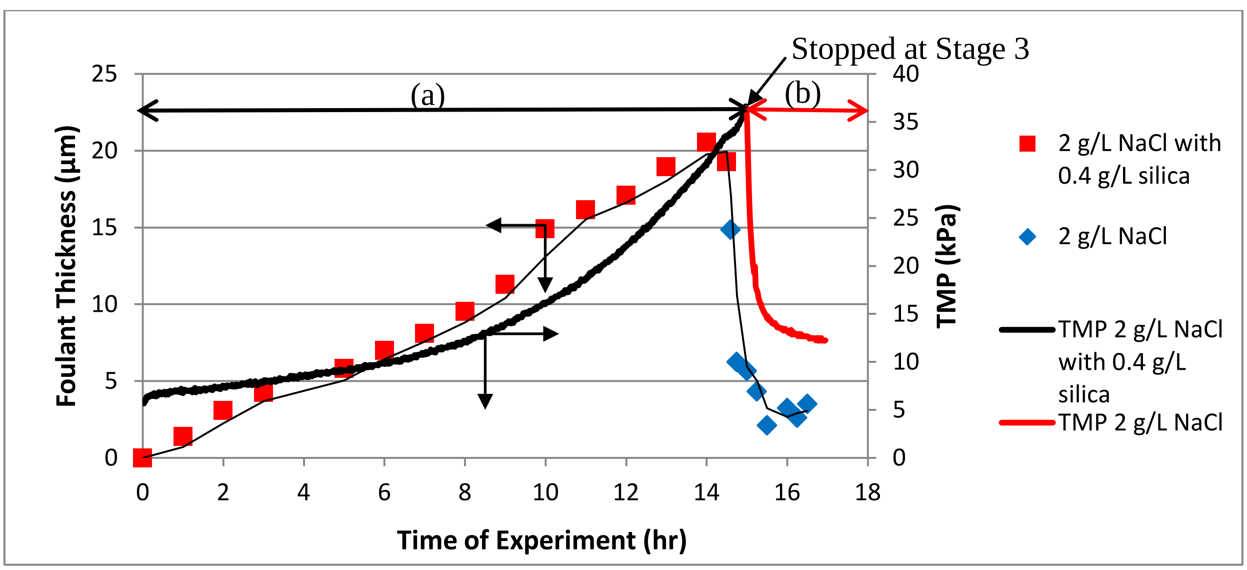

Figure 5.7: Foulant layer thickness determined via UTDR and corresponding TMP measurements for 0.13 m/s crossflow velocity (stopped halfway at 38 kPa) and a constant flux

of 44.4 L/m^2h under (a) an aqueous sodium chloride solution of 2 g/L, silica concentration of 0.4 g/L and (b) silica-free aqueous sodium chloride solution of 2 g/L.

5.5 Discussion

The transition from a constant to an increasing rate of TMP rise, the increasing UTDR peak amplitude, the presence of a residual foulant layer measured via SEM, and the detection of a residual foulant layer measured via UTDR in Type II experiments strongly suggests the occurrence of metastability in colloidal fouling. In addition, the destabilisation of the colloidal suspensions is rate-dependent as suggested by the positive correlation of the residual foulant layer thickness with experiment run time as measured by SEM. The irreversible foulant layer appears to begin growing from the membrane surface which is most prone to the occurrence of metastability in colloidal fouling.

5.5.1 TMP Profile

It is evident that the occurrence of stage 3, involving the transition from a constant to an increasing rate of TMP rise, appears later at higher crossflow velocities as shown in Figure 5.1. As noted above, possible explanation for this could be the metastability of the colloidal suspensions (Sim *et al.*, 2012a). If the volume fraction of the particles increases, the kinetics of this aggregation or gelation will be faster. This is particularly significant at the membrane surface due to concentration polarization (Aimar and Bacchin, 2010). A greater concentration of colloids or greater volume fraction at the surface would result from more severe concentration polarization with a lower crossflow velocity and cause the kinetics of aggregation or gelation to be faster. A variation in the average volume fraction within the foulant layer structure may also play a role as discussed in sections 5.6 and 5.7 in the second focus of this work.

5.5.2 UTDR Measurements

As seen in Figure 5.3, the foulant layer thicknesses decreased and the time taken to reach a TMP of 70 kPa increased at higher crossflow velocities. This is not surprising since at higher crossflow velocities, the increased shear force limits the layer thickness.

Comparing the UTDR measurements and the TMP profile reveals two interesting phenomena. There is a more rapid growth of foulant layer thickness determined via UTDR as stage 3 was reached, which indicates the transition from a constant to an increasing TMP rise. Secondly, the foulant layer thickness eventually plateaus to a constant value as measured by UTDR during stage 3' of the more rapid constant rate of TMP rise. It is apparent the foulant layer displays a yield stress below which it is immobile and above which the silica particles flow with the fluid thereby limiting increase in layer thickness. This phenomenon has been observed by other authors using Nuclear Magnetic Resolution (NMR) measurements of a flowing polarized layer within a foulant layer of colloidal silica (Airey *et al.*, 1998).

The fact that the foulant layer thickness did not increase during the final stage of the TMP rise implies that some other mechanism contributes to the continued increase in TMP. Two possible hypotheses are the following: a percolation phenomenon whereby destabilization of the colloidal particles forms an aggregated or gel layer that is able to trap more silica particles as the solution passes through the foulant layer; or further destabilization of the colloidal suspension within the foulant layer (Sim *et al.*, 2012a). Both mechanisms will have a greater effect when the foulant layer thickness is greater (Sim *et al.*, 2012a) as indicated by the increasing rates of TMP rise at lower crossflow velocities for the TMP profiles in Figure 5.1.

When the foulant layer thickness started to plateau at about 25 hours for the crossflow velocity of 0.15 m/s as shown in Figure 5.4, it was evident the UTDR peak amplitude was increasing in Figure 5.5. The latter could be due to an increase in the density of the foulant layer that would also cause a continuous increase in the foulant layer resistance

(Sim *et al.*, 2012a). This lends support to the aforementioned hypotheses of either percolation or further destabilization of the colloidal suspension within the foulant layer.

5.5.3 SEM Measurements

There is no quantitative agreement between UTDR and SEM measurements of the foulant layer thickness for experiments, such as in Figure 5.3 and Table 5.1. A possible explanation for the large difference between the UTDR and SEM foulant layer thicknesses is the fact that UTDR provides a dynamic measurement, whereas SEM is a static determination done as an autopsy after the fouled membrane is removed from the flow cell (Sim *et al.*, 2012a). UTDR measures a foulant layer thickness that includes the loosely bound outer layer, whereas SEM measures only the residual tightly bound portion of the foulant layer (Sim *et al.*, 2012a). The presence of two contiguous layers is further confirmed by the dead-end experiments carried out for the second focus in Section 5.6 utilizing UTDR. Hence for the SEM measurements, any loosely bound particles in the foulant layer will diffuse back into the bulk solution when the TMP is removed. NMR measurements have documented for such back diffusion of particles in the silica foulant layers (Airey *et al.*, 1998).

The trend where the monotonically decreasing plateau thicknesses measured by UTDR with increasing crossflow velocity shown in Figure 5.3 relative to the apparent increasing general trend with increasing crossflow velocity of the SEM measurements in Table 5.2, is unexpected. The most probable reason for this is that for higher crossflow velocities, the experiments required more time to reach the desired TMP rise, which in turn allowed for longer destabilization of the foulant layer (Sim *et al.*, 2012a). This would have resulted in the increase in the residual foulant layer thickness detected by SEM, which is not able to measure the total deposit thickness as noted above. Hence, the growth of the residual foulant layer is thought to experience a metastability that is rate-dependent. This is corroborated with both the SEM measurements as a function of time and the Type II experiments.

The SEM measurements also suggest that the destabilization of the colloidal particles is not likely to have taken place during stage 2 due to a negligible foulant layer thickness, characterized by a slow constant rate of TMP increase (Sim *et al.*, 2012a). Furthermore, the existence of a rate-dependent metastability of colloidal suspensions is supported by the relative rapid build-up of foulant layer thickness during stage 3.

5.5.4 Type II Experiments

As observed in Figures 5.6 and 5.7, the rapid decrease in the foulant layer thickness, on switching to silica-free feed, detected by UTDR corresponds with the quick drop of the TMP to a residual value. It explains the large discrepancies observed between the foulant layer thickness determined via UTDR and measured via SEM. The colloidal particles within the upper region of the foulant layer quickly back diffuse into the bulk solution as observed by other authors (Airey *et al.*, 1998). The thicknesses measured off-line using SEM that are reported in Table 5.2 agree reasonably well with the residual foulant layer thicknesses measured by UTDR (Figures 5.6 and 5.7). A smaller residual thickness was measured by UTDR when a shorter time was allowed for the destabilization of the colloidal particles to occur. This is strong evidence that the foulant layer observed on the membrane through SEM was the aggregrated or gelled foulant layer caused by the destabilization of the colloidal particles owing to the metastability of colloidal suspensions (Sim *et al.*, 2012a). The UTDR results suggest that the foulant layer consists of aggregated or gelled silica particles near the membrane and dispersed fluidized particles in the outer region and this is comfirmed by the dead-end experiments carried out for the second focus in section 5.6.

5.6 Experimental Results (Part 2 – Effects of Operational Parameters on Metastability of Colloidal Fouling)

The earlier focus of this chapter provides the evidence for the metastability of colloidal fouling, which is defined as stage 3 and is associated with a transition from a constant TMP rise to an increasing rate of TMP rise. In the second focus, the occurrence of stage

3 is found to be dependent on the operational parameters of flux, crossflow velocity, salinity and silica concentration under thr crossflow filtration mode. Increases in the flux, salinity, and silica concentration significantly reduced the time required for the metastability to occur but varied in their effects on the effective volume fraction within the silica foulant layer structure. It should be noted that the effective volume fraction is analogous to the cake-average porosities of crossflow filtration and dead-end filtration modes found using Equations 3.17 and 3.18, respectively, in section 3.4.1 of Chapter 3. There appears to be a 'metastable' (critical) flux below which the time required for the occurrence of metastability can be delayed significantly. Minimal variation of the cake-average porosities was observed when the crossflow velocity was varied. However, a slower crossflow velocity caused the metastability to occur more quickly. Doubling the salinity decreased the estimated porosity less than doubling the silica concentration. Interestingly, metastability occurred more slowly for a higher salinity leading to the conclusion that concentration polarization was the dominant factor influencing the occurrence of metastability.

For the dead-end experiments increasing the flux and silica concentration resulted in a faster TMP rise and foulant layer growth. The silica foulant layer was further confirmed to be composed of two contiguous layers, one at the bottom that was thin and dense and the other that was thick and loose.

5.6.1 Crossflow Velocity

Figure 5.8 shows a plot of the cake-average porosities for crossflow velocities of 0.13 m/s, 0.15 m/s, and 0.20 m/s at constant fluxes of 70 L/m^2h and 90 L/m^2h for an aqueous solution containing 2 g/L of sodium chloride and 0.4 g/L of silica. Figure 5.9 shows a plot of TMP/TMP_o as a function of time for crossflow velocities of 0.13 m/s and 0.15 m/s under constant fluxes of 70 and 90 L/m^2h for an aqueous solution containing 2 g/L of sodium chloride and 0.4 g/L of silica. These values were obtained by applying Equations 3.17 and 3.19 of Chapter 3 (with the assumption of $\theta = 0.10\beta$)

to the data obtained. Figure 5.10 shows a plot of the specific cake resistance and the cake-average porosity as a function of constant fluxes at 60, 70, 80, 90, and 100 L/m^{2}h for crossflow velocities of 0.13 m/s and 0.15 m/s for an aqueous solution containing 2 g/L of sodium chloride and 0.4 g/L of silica. It should be noted in Table 5.3 that as the flux increases, the metastability, characterized by the transition from a constant to an increasing rate of TMP rise, occurs earlier even though the cake-average porosity remains essentially constant for the different crossflow velocities.

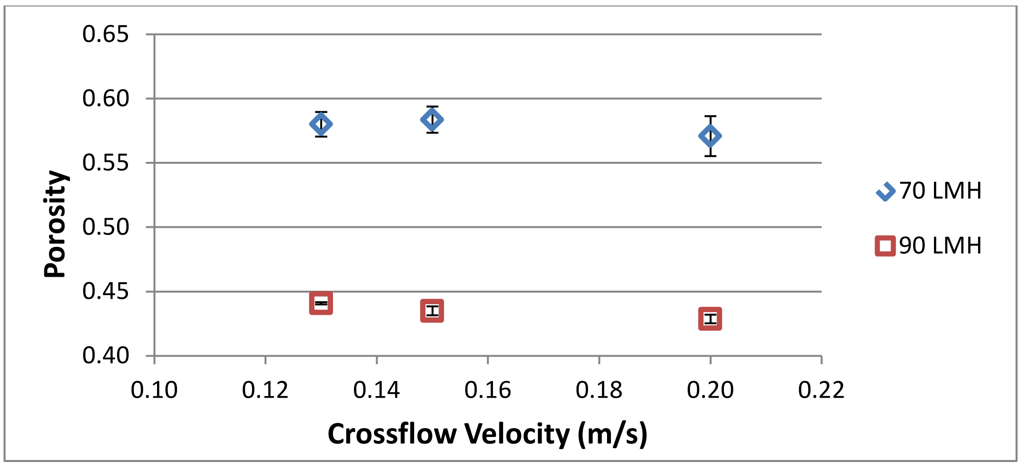

Figure 5.8: Estimated cake-average porosities of the foulant layer for crossflow velocities of 0.13 m/s, 0.15 m/s, 0.20 m/s under constant fluxes of 70 L/m^{2}h and 90 L/m^{2}h for an aqueous solution containing 2 g/L of sodium chloride and 0.4 g/L of silica.

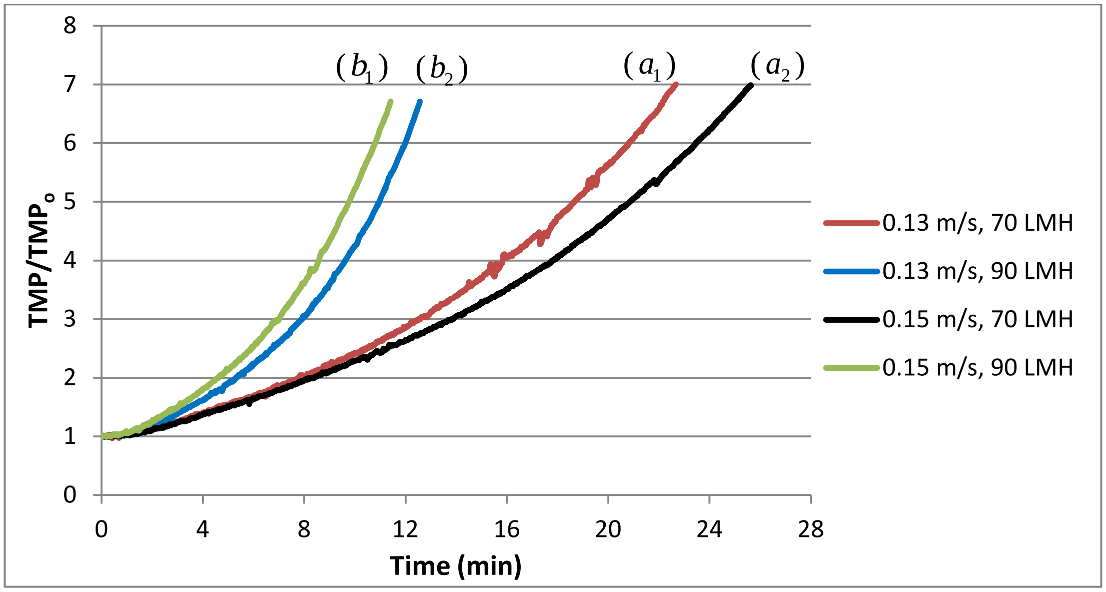

Figure 5.9: TMP/TMP$_o$ versus time for constant fluxes of (a) 70 L/m^{2}h and (b) 90 L/m^{2}h at crossflow velocities of 0.13 m/s and 0.15 m/s denoted by subscripts (1) and (2), respectively, for an aqueous solution containing 2 g/L of sodium chloride and 0.4 g/L of silica.

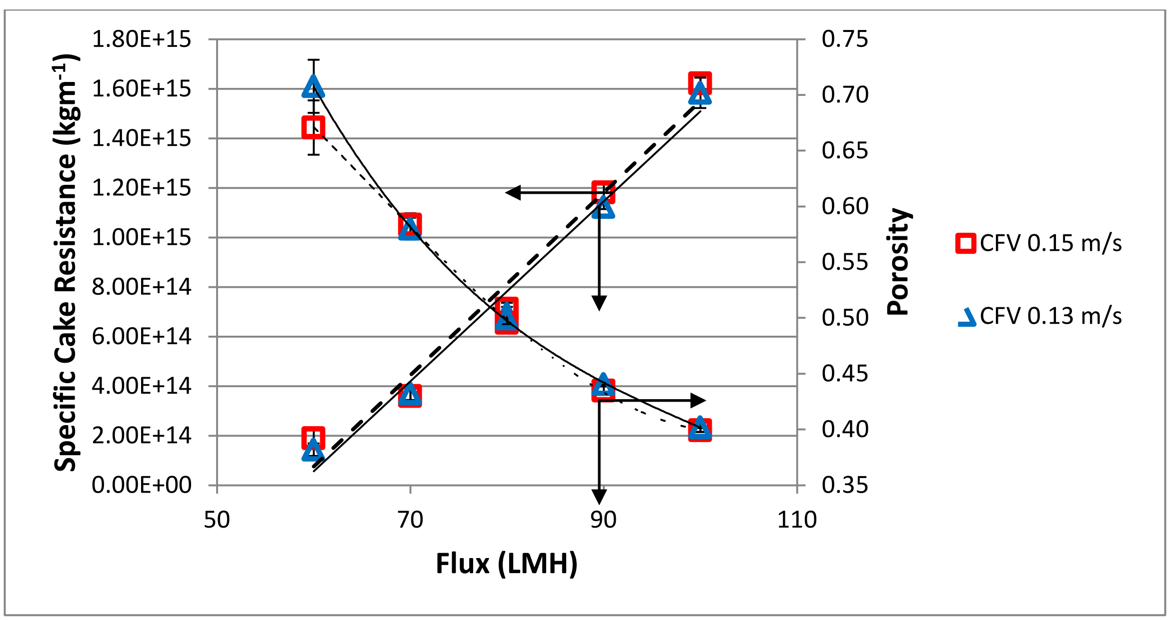

Figure 5.10: Specific cake resistance and cake-average porosity as a function of flux for crossflow velocities of 0.13 m/s and 0.15 m/s for an aqueous solution containing 2 g/L of sodium chloride and 0.4 g/L of silica.

Unlike in the first focus that observed the approximate time for metastability to occur, it is important here to determine accurately the time at which metastabiliy occurred for better comparision for the effects of the operational parameters. To do this, the equation of a trendline was first obtained from the TMP profile before the occurrence of metastabiliy. This is the same method used to obtain the slope of the plot of the TMP versus time in order to calculate the specific cake resistance as explained in section 3.4.1 of Chapter 3. A difference of 1.2 kPa (three times the standard deviation of the TMP profile) between the actual TMP and that predicted by the trendline equation was used as the criterion for establishing the time at which the transition between the constant and increasing rate of TMP rise occurs. Figure 5.11 shows how this was performed using a plot of TMP as a function of time for a crossflow velocity of 0.15 m/s at a constant flux of 70 L/m^2h for an aqueous solution containing 2 g/L of sodium chloride and 0.4 g/L of silica.

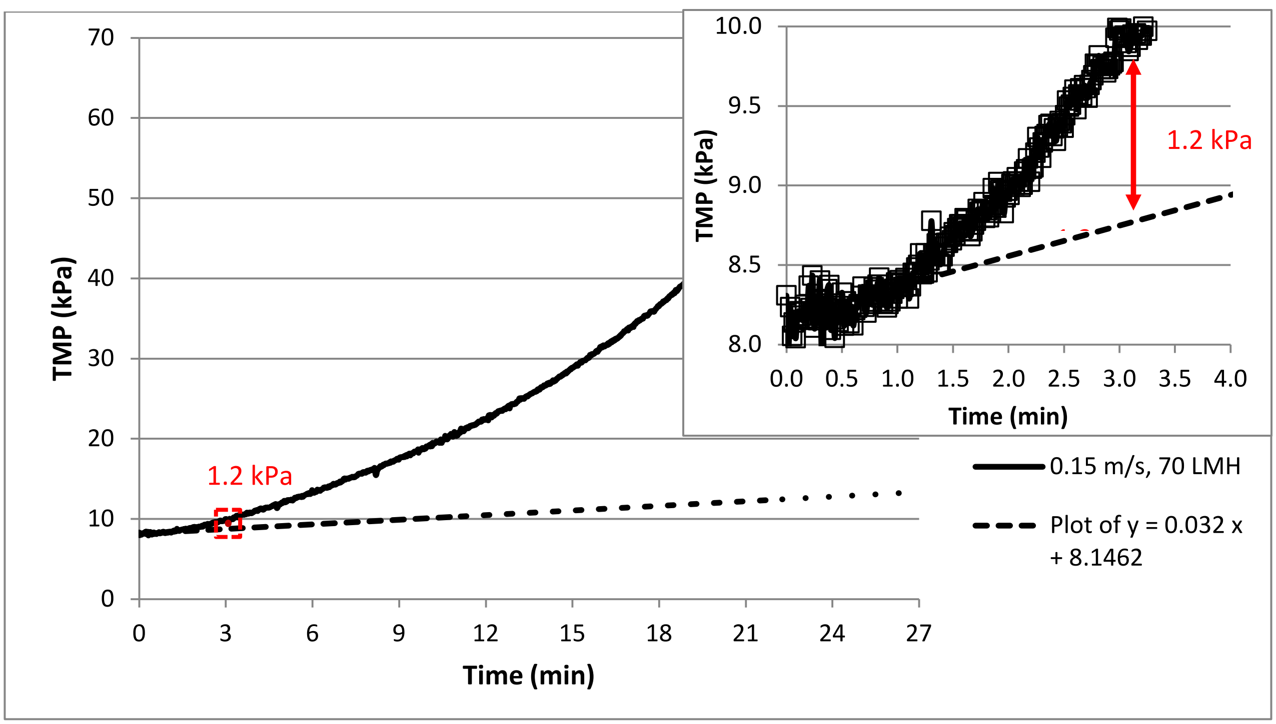

Figure 5.11: TMP versus time for a constant flux of 70 L/m^2h at a crossflow velocity of 0.15 m/s for an aqueous solution containing 2 g/L of sodium chloride and 0.4 g/L of silica (y = TMP in kPa, x = time in minutes).

Table 5.3 summarizes the times at which metastability occurred for the fluxes of 60, 70, 80, 90, and 100 L/m^2h for crossflow velocities of 0.13 m/s and 0.15 m/s for an aqueous solution containing 2 g/L of sodium chloride and 0.4 g/L of silica. Experiments carried out at higher fluxes resulted in denser packed foulant layers with increased specific cake resistances and lower cake-average porosities as shown in Figure 5.10. Since the kinetics of metastability increases with the effective volume fraction, this trend is expected. However, varying the flux affects both the concentration polarization (surface concentration) and the effective volume fraction (cake-average concentration).

Table 5.3 indicates that the metastability occurs sooner as the crossflow velocity decreases even though the cake-average porosity of the foulant layer remains essentially constant. A lower crossflow velocity will result in a greater concentration of colloids at the surface owning to more severe concentration polarization, thereby causing the kinetics of metastability to be faster. Unfortunately, there is insufficient information to conclude at this point whether the metastability is affected more severely by concentration polarization or the effective volume fraction. However, additional insight is obtained in section 5.6.5 that discusses the effects of doubling the silica concentration or the salinity on the occurrence of metastability. Moreover, there is an interesting significant delay in the metastability occurrence below the flux of 60 L/m^2h that will be further examined in section 5.6.3.

Table 5.3: Time for metastability to occur as a function of flux at crossflow velocities of 0.13 m/s and 0.15 m/s for an aqueous solution containing 2 g/L of sodium chloride and 0.4 g/L of silica.

Flux (LMH)	Time for metastability to occur (min)	
	CFV = 0.13 m/s	CFV = 0.15 m/s
100	2.42 (±0.02)	2.48 (±0.01)
90	2.68 (±0.17)	2.77 (±0.08)
80	2.88 (±0.06)	2.98 (±0.35)
70	2.96 (±0.06)	3.03 (±0.08)
60	3.62 (±0.25)	3.79 (±0.11)
44	495 (±9.00)	962 (±62.00)

5.6.2 Salinity

Table 5.4 summarizes the porosities and the times for metastability to occur at a crossflow velocity of 0.10 m/s under a constant flux of 44.4 L/m^{2}h for different aqueous solutions containing 1, 2, 3, 4, 6, and 8 g/L of sodium chloride and 0.4 g/L of silica. The average porosity within the silica foulant layer is significantly affected by changes in salinity; an increase in salinity causes a marked reduction in the porosity of the silica foulant layer. An increase in salinity results in a lower cake-average porosity and causes a marked decrease in the time required for the metastability to occur. Interestingly, there is a significant difference in terms of hundreds of minutes between the time required for the metastability to occur when the salinity was varied in comparison to section 5.6.1 when the crossflow velocity was varied. The significantly greater time required for metastability to occur when the salinity was varied was similar to section 5.4.1 when the crossflow velocity was also varied but at a significantly lower flux of 44.4 L/m^{2}h. It is thought to be related to the presence of a metastable flux, which could delay the occurrence of metastability significantly as discussed in greater detail in section 5.6.3.

Table 5.4: Cake-average porosity and time for metastability to occur as a function of salinity at a crossflow velocity of 0.10 m/s under a constant flux of 44.4 LMH for an aqueous solution containing 0.4 g/L of silica.

NaCl (g/L)	Time for metastability to occur (min)	Porosity, ε
8	63.59 (±1.42)	0.654 (±0.001)
6	114.50 (±62.50)	0.705 (±0.004)
4	210.50 (±46.50)	0.734 (±0.004)
3	257.09 (±87.08)	0.784 (±0.000)
2	367.34 (±1.33)	0.803 (±0.001)
1	426.00 (±41.00)	0.839 (±0.005)

In order to corroborate the effect of the changes in salinity on the cake-average porosity, a simple modification has been developed to account for the effect of the electrical double layer on the effective size of the silica particles. The Debye length, $1/\kappa$, representing the electrical double layer, can be obtained from the salinity by (Israelachvili, 1992):

$$1/\kappa = \frac{0.304}{\sqrt{[NaCl]}}\, nm \tag{5.1}$$

Figure 5.12 shows a plot of the experimentally determined cake-average porosity based on the 20 nm nominal diameter particle size and the revised particle size including the Debye length as a function of the Debye length determined for 1, 2, 3, 4, 6, and 8 g/L of sodium chloride under a crossflow velocity of 0.10 m/s for an aqueous solution containing 0.4 g/L of silica at a constant flux of 44.4 L/m^{2}h. The experimental cake-average porosities based on both the 20 nm particle size and the revised particle size including the Debye length have similar trends. However, at Debye lengths below 1.3 nm the experimental cake-average porosities decrease markedly. Van der Waals

(VDW) forces that become significant when the inter-particle distance decreases are thought to be responsible for this trend; that is, at higher salt concentrations the electrical double layer is compressed and decreases the Debye length, which allows the silica particles to come closer and thereby increases the relative importance of the VDW forces (Israelachvili, 1992).

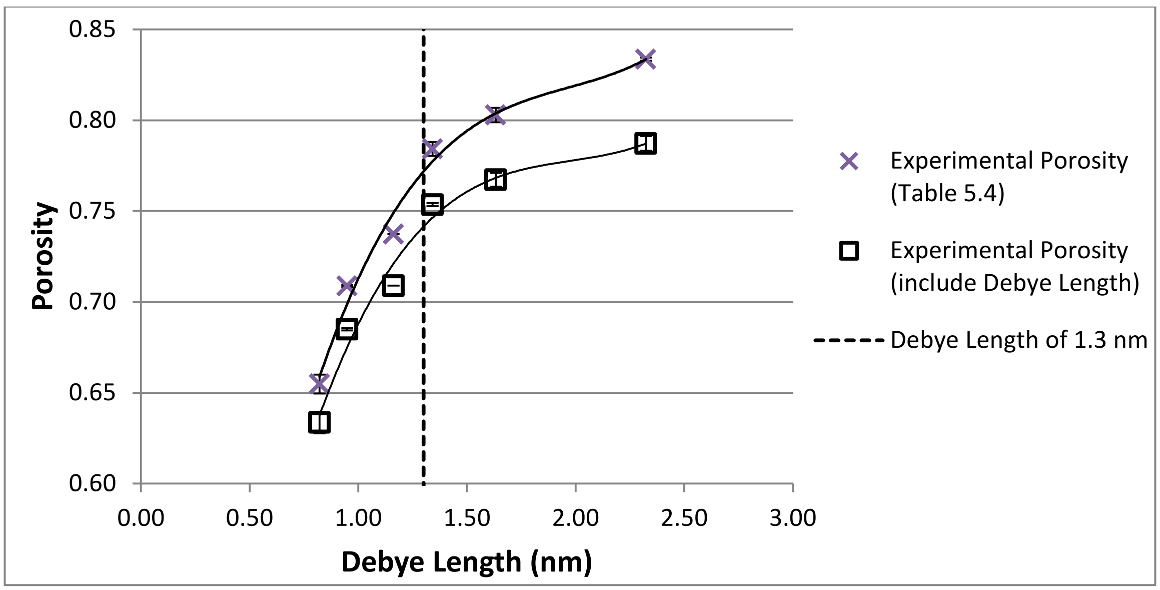

Figure 5.12: Experimentally determined cake-average porosity and the revised cake-average porosity as a function of the Debye length determined for 1, 2, 3, 4, 6, and 8 g/L of sodium chloride at a crossflow velocity of 0.10 m/s for an aqueous solution containing 0.4 g/L of silica at a constant flux of 44.4 L/m^{2}h.

The Debye length at which the long range VDW forces become significant can be estimated using Monte Carlo simulations employing the full Lennard-Jones potential. The simulated distance at which the inter-particle potential is zero is at 4.4 σ^* (Trokhymchuk and Alejandre, 1999); σ^* can be estimated using the Lorentz rule (Cuadros *et al.*, 1996):

$$\sigma^* = 0.5(\sigma_{Silica} + \sigma_{Water}) \qquad (5.2)$$

where σ_{Silica} = 0.27 nm (Coasne *et al.*, 2010) and σ_{Water} = 0.315 nm (Mahoney and Jorgensen, 2000). Hence, the distance at which the silica particles would be influenced by the VDW forces is estimated to be 1.29 nm [4.4 x 0.5 (0.27+0.315)]. This agrees well with the Debye length of 1.3 nm at which the experimental cake-average porosities decrease markedly in Figure 5.12.

5.6.3 Metastable Flux

As noted in sections 5.6.1 and 5.6.2, significantly more time is required for metastability to occur at a lower flux of 44.4 L/m^2h than at higher fluxes above 60 L/m^2h in Section 5.6.1. Hence, lower fluxes of 50 and 55 L/m^2h at the same crossflow velocity of 0.13 m/s were run to investigate this phenonmenon. Figure 5.13 shows a plot of the time for metastability to occur as a function of flux under a crossflow velocity of 0.13 m/s for an aqueous solution containing 2 g/L of sodium chloride and 0.4 g/L of silica. As suspected, there appears to be a metastable flux between 55 and 60 L/m^2h that signficantly delayed the onset of colloidal metastability. A possible explanation is a critical coagulation concentration (CCC) on the membrane surface as described by other authors (Trompette *et al.*, 2005). Unfortunately, it is beyond the scope of this thesis to predict the effect of these metastable fluxes on membrane performance. This remains an area for further study.

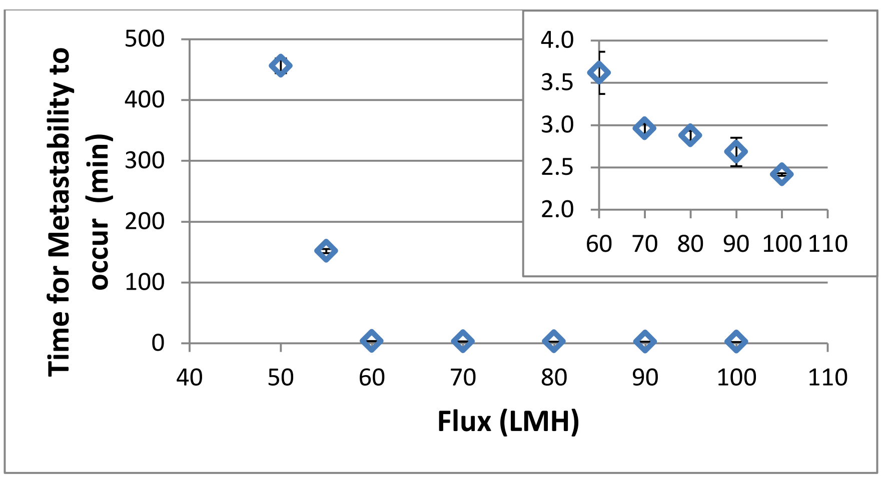

Figure 5.13: Time for metastability to occur as a function of flux determined at a crossflow velocity of 0.13 m/s for an aqueous solution containing 2 g/L of sodium chloride and 0.4 g/L of silica. Detailed values for fluxes from 60 L/m^2h shown as insert.

5.6.4 Silica Concentration

Table 5.5 summarizes the experimentally determined cake-average porosities and the times for metastability to occur under a crossflow velocity of 0.13 m/s under constant flux of 80 L/m^{2}h for an aqueous solution containing 0.2, 0.4, 0.8, 1.2, and 1.6 g/L of silica and 2 g/L of sodium chloride. The metastability occurs progressively earlier and the porosity decreases as the silica concentration increases.

Table 5.5: Cake-average porosity and time for metastability to occur as a function of silica concentration at a crossflow velocity of 0.13 m/s at a constant flux of 80 LMH using an aqueous solution containing 2 g/L of sodium chloride.

Silica (g/L)	Time for metastability to occur (min)	Porosity, ε
1.6	1.27 (±0.05)	0.414 (±0.001)
1.2	1.49 (±0.18)	0.426 (±0.001)
0.8	1.81 (±0.11)	0.461 (±0.002)
0.4	2.88 (±0.06)	0.499 (±0.005)
0.2	4.63 (±0.13)	0.533 (±0.003)

The decrease in the cake-average porosity caused by the silica concentration is believed to be due to a higher net volumetric flux, which is the operating flux minus the critical flux, $J_v - J_{Critical}$. As seen from the critical volumetric flux values in Section A.1 of the Appendix, the increases in silica concentration result in lower critical volumetric fluxes that cause gradual increases in the net volumetric flux experienced by the foulant layer. It is likely that the increase in silica concentration affects both the concentration polarization and the cake-average porosity, which affects the time for metastability to occur.

5.6.5 Doubling Silica Concentration or Salinity

Figure 5.14 and 5.15 show plots of the specific cake resistance and the cake-average porosity, respectively, as a function of constant fluxes at 60, 70, 80, 90, and 100 L/m^{2}h at a crossflow velocity of 0.13 m/s for an aqueous solution containing 2 g/L of sodium chloride and 0.4 g/L of silica, an aqueous solution containing 2 g/L of sodium chloride and 0.8 g/L of silica, and an aqueous solution containing 4 g/L of sodium chloride and 0.4 g/L of silica. Increases in the flux increased the specific cake resistance and decreased the cake-average porosity irrespective of whether the silica concentration or salinity was doubled. Doubling the salinity was found to be a less significant effect than doubling the silica concentration on increasing the specific cake resistance and decreasing the cake-average porosity.

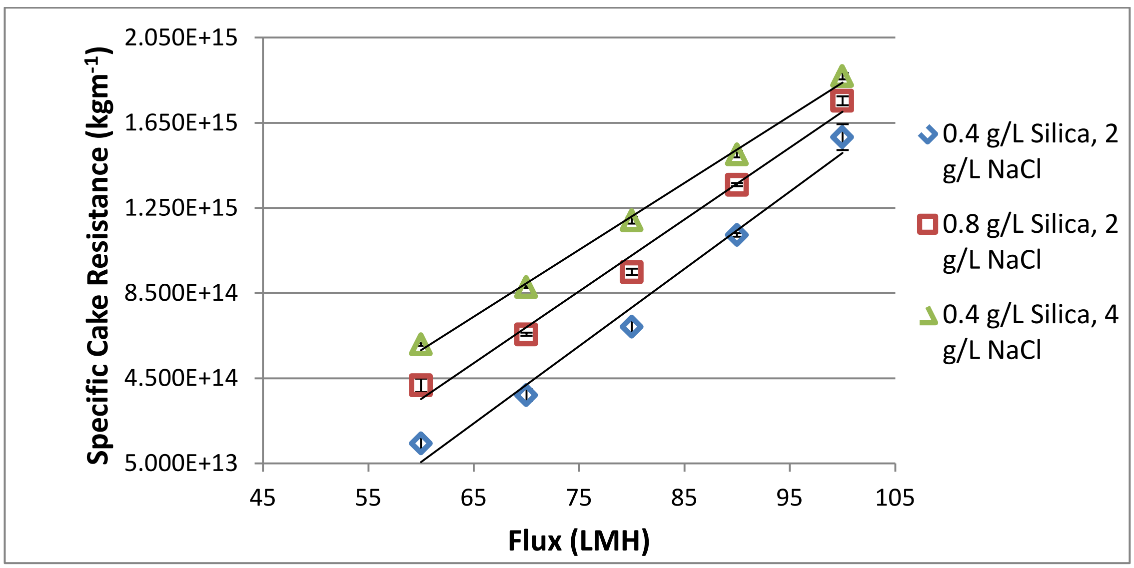

Figure 5.14: Specific cake resistance as a function of flux under a crossflow velocity of 0.13 m/s for an aqueous solution containing 2 g/L of sodium chloride and 0.4 g/L of silica, an aqueous solution containing 2 g/L of sodium chloride and 0.8 g/L of silica, and an aqueous solution containing 4 g/L of sodium chloride and 0.4 g/L of silica (y = specific cake resistance in kgm^{-1}, x = flux in L/m^{2}h).

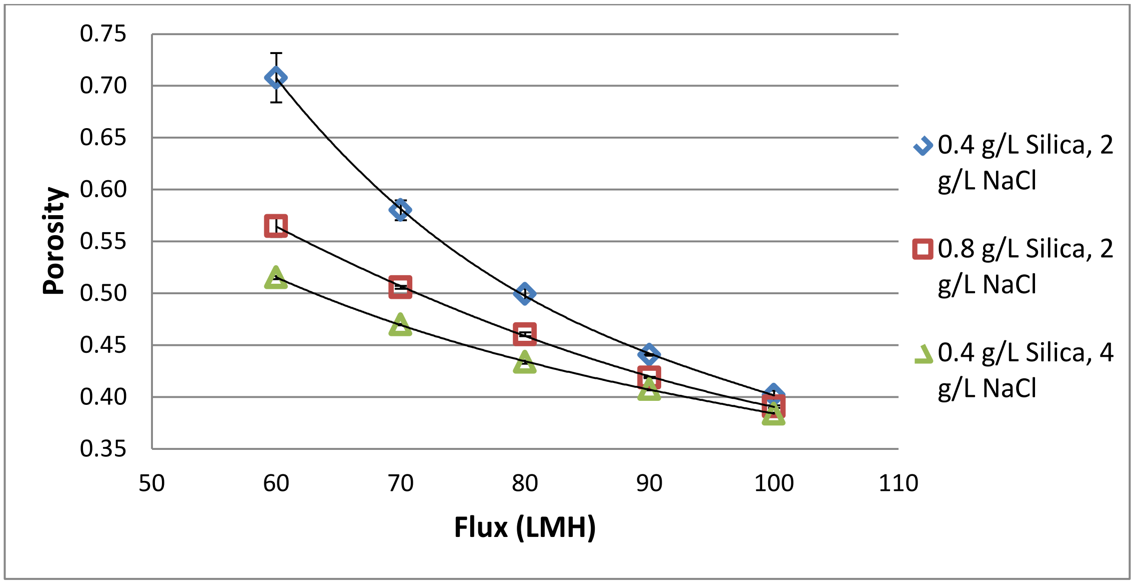

Figure 5.15: Cake-average porosity of the foulant layer as a function of flux under crossflow velocities of 0.13 m/s for an aqueous solution containing 2 g/L of sodium chloride and 0.4 g/L of silica, an aqueous solution containing 2 g/L of sodium chloride and 0.8 g/L of silica, and an aqueous solution containing 4 g/L of sodium chloride and 0.4 g/L of silica.

Table 5.6 summarizes the experimentally determined cake-average porosities and the times for metastability to occur for a crossflow velocity of 0.13 m/s and a constant flux of 80 L/m^{2}h for aqueous solutions containing 2 g/L of sodium chloride and 0.4 g/L of silica, 4 g/L of sodium chloride and 0.4 g/L of silica, and 2 g/L of sodium chloride and 0.8 g/L of silica. The time trend for metastability to occur does not correlate with the cake-average porosity values. A lower cake-average porosity value of the silica foulant layer is indicative of a higher effective volume fraction that should result in the kinetics of metastability being faster (Aimar and Bacchin, 2010). However, Table 5.6 shows when the silica concentration was doubled (Condition C) in comparison to doubling the salinity (Condition B), metastability occurred earlier even though the cake-average porosity was higher. A possible explanation is that the concentration polarization is a more significant factor influencing the time at which metastability occurs, as suggested in the discussion in section 5.6.1. The increased concentration polarization associated with a higher silica concentration could provide a ‘reservoir’ of particles that gradually form aggregates through perikinetic flocculation, layer-by-layer, as predicted in prior modeling studies of proteins causing the irreversible deposition of solutes on membranes (Suki *et al.*, 1986). Therefore, metastability appears to be affected by both the concentration polarization and the effective volume fraction; however, concentration polarization appears to play a more significant role since it drives the localized aggregation.

Table 5.6: Cake-average porosities and time for the occurrence of metastability for a constant flux of 80 LMH under a crossflow velocity of 0.13 m/s for an aqueous solution containing (A) 2 g/L of sodium chloride and 0.4 g/L of silica, (B) 4 g/L of sodium chloride and 0.4 g/L of silica, and (C) 2 g/L of sodium chloride and 0.8 g/L of silica.

Condition	Time for metastability to occur (min)	Porosity, ε
(A) 2 g/L NaCl and 0.4 g/L Silica	2.88 (±0.06)	0.499 (±0.005)
(B) 4 g/L NaCl and 0.4 g/L Silica	2.33 (±0.25)	0.434 (±0.002)
(C) 2 g/L NaCl and 0.8 g/L Silica	1.81 (±0.11)	0.461(±0.002)

5.6.6 Dead-end Filtration

Table 5.7 summarizes the values of the TMP rise, the UTDR measurements and the cake-average porosity under the dead-end filtration mode for an aqueous solution containing 2 g/L of sodium chloride and 0.4 g/L of silica at constant fluxes of 80 and 100 L/m^{2}h, and aqueous solutions containing 0.8 and 1.2 g/L of silica with 2 g/L of sodium chloride at a constant flux of 80 L/m^{2}h. These porosity values were obtained by applying Equations 3.18 and 3.19 of Chapter 3 (with the assumption of $\theta = 0.10\beta$) to the data. Figure 5.16 shows a plot of the TMP rise as a function of the UTDR measurements for the cake layer growth based on the values of Table 5.7. Figure 5.16 indicates the growth rate of cake thickness is a non-linear increasing function of the TMP rise, which is not expected since the cake-average porosity decreases with increasing flux. This meant that the growth rate of cake thickness should be a decreasing function of the TMP rise. However, this is likely due to the presence of an upper highly porous cake detectable by UTDR that is discussed in detail later in this section with Figure 5.18 and Table 5.8.

Table 5.7: Rate of TMP rise, rate of foulant layer thickness increase measured by UTDR, and cake-average porosity under the dead-end filtration mode for an aqueous solution containing 2 g/L of sodium chloride and 0.4 g/L of silica under constant fluxes of 60, 80 and 100 LMH, and for aqueous solutions containing 2 g/L of sodium chloride with 0.8 and 1.2 g/L of silica under a constant flux of 80 LMH.

Silica (g/L)	Flux (LMH)	Rate of TMP rise (Pa/s)	Rate of Foulant Layer Thickness increase measured by UTDR (μm/min)	Porosity, ε
0.4	60	26.25 (±0.36)	1.0503 (±0.0383)	0.640 (±0.002)
0.4	80	94.47 (±1.58)	1.4280 (±0.0199)	0.546 (±0.002)
0.4	100	209.51 (±14.79)	2.4958 (±0.0258)	0.502 (±0.009)
0.8	80	259.45 (±15.05)	3.2457 (±0.0888)	0.506 (±0.007)
1.2	80	622.08 (±34.52)	4.7348 (±0.3400)	0.449 (±0.007)

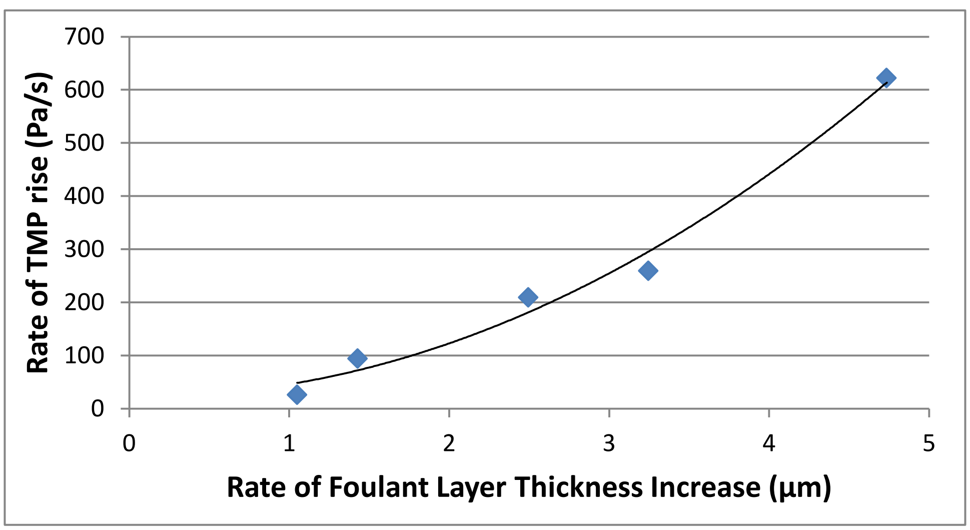

Figure 5.16: Rate of TMP rise as a function of the rate of UTDR measured foulant layer thickness increase for the dead-end filtration mode based on values of Table 5.7.

Figure 5.17 shows a plot of TMP/TMP_o and UTDR measured foulant layer thickness as a function of time under the dead-end filtration mode for an aqueous solution containing 2 g/L of sodium chloride and 0.4 g/L of silica at constant fluxes of 80 and 100 L/m^2h, and aqueous solutions containing 0.8 and 1.2 g/L of silica with 2 g/L of sodium chloride at a constant flux of 80 L/m^2h. Detailed analysis of the UTDR waveform has been described in section 4.1 of Chapter 4. The rate of TMP rise increases when the flux or silica concentration increases. The UTDR measured foulant layer thickness is a linear function with time and the slope increases with increasing flux or silica concentration.

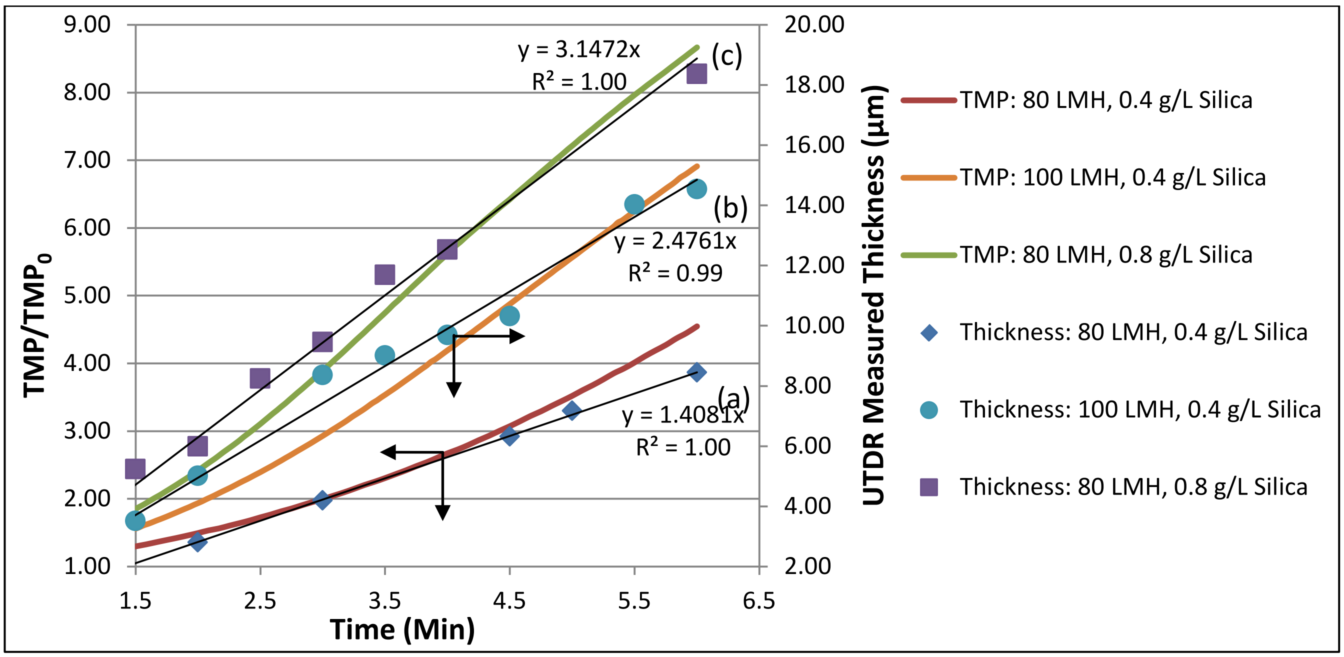

Figure 5.17: TMP/TMP_o and UTDR measured thickness versus time for the dead-end filtration mode under constant fluxes of (a) 80 and (b) 100 L/m^2h for an aqueous solution containing 2 g/L of sodium chloride and 0.4 g/L of silica, and (c) for an aqueous solution containing 2 g/L of sodium chloride and 0.8 g/L of silica at a constant flux of 80 L/m^2h (y = UTDR measured thickness in µm, x = time in minutes).

Figure 5.18 shows a plot of the UTDR determined and TMP derived thickness values for dead-end filtration as a function of (a) flux of an aqueous solution containing 2 g/L of sodium and 0.4 g/L of silica, and as a function of (b) silica concentration of an aqueous solution containing 2 g/L of sodium under a constant flux of 80 L/m^2h. The

TMP dervied foulant layer thicknesses were found using Equations 3.20 and 3.21 of Chapter 3. The UTDR measured and TMP derived foulant layer thicknesses display similar trends. However, Figure 5.18 indicates that there is a significant difference between the thicknesses of the foulant layer determined via UTDR measurements and from the TMP profile. This difference arises because of the inherently different manner in which the thicknesses are determined. In the TMP derived method a thin dense layer of low porosity will dominate the bulk of the TMP rise with a relatively high specific cake resistance in the presence of a thick loose layer of high porosity as inferred from Equation 3.18 in Section 3.4.1 and Equation 3.19 in section 3.4.1.1 of Chapter 3. However, in the UTDR determination the bulk of the foulant layer thickness will be dominated by the presence of the thick loose layer; UTDR detects the top of this layer. The term $(1-\varepsilon)$ in the denominator of Equation 3.20 in section 3.4.1.1 of Chapter 3 implies that a loose layer with ε > 0.90 will begin to dominate the thickness measurements when a layer of 90% porosity is approximately five times the thickness of a 50% porous layer.

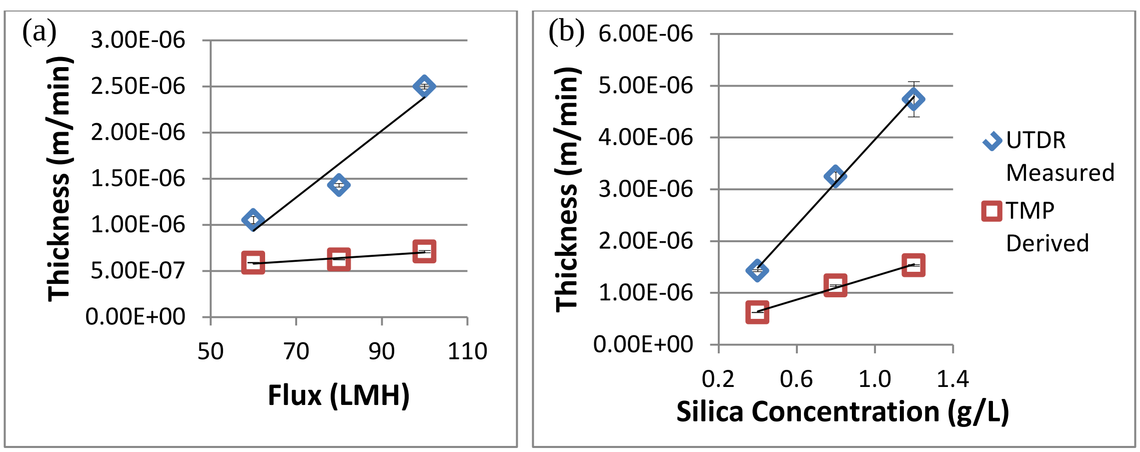

Figure 5.18: Thickness of the foulant layer under the dead-end filtration mode as a function of (a) flux for an aqueous solution containing 2 g/L of sodium chloride and 0.4 g/L of silica, and as a function of (b) silica concentration for an aqueous solution containing 2 g/L of sodium chloride at a constant flux of 80 L/m^{2}h.

Table 5.8 summarizes the apparent cake-average porosity, ε_{app}, back-calculated from Equation 3.20 using the UTDR measured foulant layer thickness and the cake-average porosity, ε, calculated from Equations 3.18 and 3.19 using the TMP profile. Table 5.8 indicates that the apparent cake-average porosity of the foulant layer back-calculated from the UTDR measured foulant layer thickness is significantly larger than the cake-average porosity determined from the TMP profile. This is not unexpected since other studies have shown that a highly porous foulant structure can be formed during the filtration of nanoparticles (Elmøe *et al.*, 2009) with a significant increase in the porosity towards the upper part of the foulant layer (Neese *et al.*, 2009).

Table 5.8: Apparent cake-average porosity and cake-average porosity of the silica foulant layer under different volumetric fluxes and silica concentrations for an aqueous solution containing 2 g/L of sodium chloride.

Silica (g/L)	Flux (LMH)	Apparent Porosity*, ε_{app}	Porosity**, ε
0.4	60	0.854	0.640
0.4	80	0.857	0.546
0.4	100	0.898	0.502
0.8	80	0.874	0.506
1.2	80	0.870	0.449

* based on the UTDR measured foulant layer thickness, ** based on TMP data using Equations 3.18 and 3.19.

To confirm the UTDR measured foulant layer thickness, the results of a study are reported in section A.3 of the Appendix that was done to determine the acoustic impedance for a range of silica suspensions chosen to simulate porous layers having porosities of more than 90% porosity. UTDR is shown to be capable of detecting the reflected acoustic signal from an interface between a silica foulant layer having a 99.5% porosity and an aqueous feed solution containing 0.48 g/L of silica. Therefore, it is believed that the foulant layer in dead-end filtration consists of two contiguous layers, a thin dense layer that dominates the TMP rise and a thick loose layer that dominates the thickness measured by UTDR. The differences between the UTDR cake thickness and porosity from the TMP derived data could imply that the UTDR has limitations for fouling monitoring. However, the actual cake thickness (identified by

UTDR) is important in estimating the effect of cake enhanced osmotic pressure (the hindered diffusion layer). In Chapter 7, it is shown that UTDR measured cake thicknesses combined with measurement of fouling resistance can provide reasonable prediction of TMP rise due to progressive fouling.

The dead-end filtration study supports the observation of fractional deposition as discussed in section 3.2.4 of Chapter 3 that indicates a need for further refinement of Equation 3.7 of Chapter 3 to account for the reduced rate of foulant accumulation under crossflow conditions, i.e. the fractional deposition phenomenon. A highly porous structure would be easily dislodged by tangential shear along the membrane surface. Studies at constant flux that utilize the same model colloidal silica under crossflow filtration mode by several authors (Chong *et al.*, 2008; Taheri *et al.*, 2013) found the empirical rate of deposition factor to be only 5% – 10% of what would have theoretically accumulated on the membrane based solely on Equation 3.7. The rate of accumulation in this chapter has been semi-empirically calculated using a conservative rate of accumulation of 10% and influenced by the fouling potential of foulant, β, as highlighted in Equation 3.16 of Chapter 3. The assumptions made in Equation 3.16 are valid as the porosities reported in this work are in relatively good agreement with reported values for colloidal silica having porosities of 0.3 - 0.7 (Faibish *et al.*, 1998). Importantly, the trends reported in this chapter for the metastability dependence on the cake average porosities are insensitive to the assumed values of the fractional deposition factor, θ. However, the values of specific cake resistance and estimated cake-average porosities do depend on the assumed value of θ. The value of 0.10 used here is based on both literature value (Chong *et al.*, 2008) and a best-fit value required for TMP prediction (Chapter 7).

5.7 Concluding Remarks

The first focus of this chapter shows that UTDR in combination with TMP measurements and SEM characterization provide considerable insight into the physicochemcial nature of colloidal fouling. SEM observations of a residual foulant layer together with the transtion to an increased rate of TMP rise along with the UTDR data are evidence of the metastability of the colloidal suspension that causes the destabilization of the foulant layer. A rate-dependent metastability can be assumed from the dependency of the thickness of the residual foulant layer with experimental run time. Interestingly, UTDR can detect both the immobile and mobile parts of the foulant layer, whereas SEM can measure only the residual tightly bound part of the foulant layer since more loosely bound silica particles will back diffuse into the bulk solution in the absence of any TMP. The tightly bound residual layer developed by colloidal materials such as silica cannot be removed by dissolution but requires a more aggressive type of remediation. As such, this residual layer can be problematic for membrane processes involving colloidal fouling agents. This led to the second focus of this chapter in trying to understand the effects of operational parameters on the metastability of colloidal fouling.

Systematic studies involving different fluxes, crossflow velocities, salinity, and foulant concentrations here provided considerable insight into the metastability of colloidal fouling. A lower crossflow velocity, higher flux, higher salinity, and higher foulant concentration decreased the time required for metastability to occur through a combined effect of more severe concentration polarization and a denser foulant layer. The effects of the aforementioned system parameters on the metastability of colloidal fouling are summarized as follows:

- A lower crossflow velocity causes more severe concentration polarization and an earlier occurrence of colloidal metastability even though the crossflow velocity appears to have no significant effect on the cake-average porosity.
- A higher volumetric flux causes more severe concentration polarization and a denser foulant layer that causes an earlier occurrence of colloidal metastability. There appears to be a metastable flux below which colloidal metastability can be delayed significantly.

- A higher salinity creates a denser foulant layer that causes an earlier occurrence of colloidal metastability. Significant VDW forces can affect the effective volume fraction of the foulant layer and influence the occurrence of colloidal metastability.
- A higher foulant concentration causes more severe concentration polarization and a denser foulant layer that causes an earlier occurrence of colloidal metastability.
- The experiments that involved doubling the salinity and the silica concentration indicated that increased concentration polarization has a greater effect on the earlier occurrence of metastability than forming a denser foulant layer.

A combination of TMP measurements and foulant layer thickness by UTDR in dead-end filtration sucessfully probed the difference foulant layer structures under conditions of different fluxes and silica concentrations. The use of UTDR as an independent non-invasive detection technique allowed the in-situ, real-time and non-destructive measurement of the foulant layer thickness that consists of a thin dense and a thick highly porous portion and confirmed the earlier obervation of UTDR being able to detect the two portions under crossflow conditions. On the other hand, TMP measurements respond to only the thin dense part of the foulant layer across which most of the pressure drop occurs.

This chapter provides an explanation for abnormal flux drifts or TMP jumps that have been observed in ultrafiltration. These can result from the onset of metastabilty of colloidal foulants. The relatively high salinity involved when ultrafiltration is used as a pretreatment for RO will accelerate the occurrence of colloidal metastabilty. However, this study indicates that the onset of metastability can be mitigated by a better management of the membrane surface foulant concentration through the control of concentration polarization. This can be achieved through operating at a higher crossflow velocity and/or by employing a lower permeation flux. The presence of a metastable flux also suggests appropriate risk management between the needs for productivity and fouling control.

CHAPTER 6 : ENHANCED ULTRASONIC MONITORING OF BIOFILMS IN MEMBRANE SYSTEMS[5]

6.1 Abstract

The formation and development of biofilms causing biofouling in UF and RO under crossflow and constant flux conditions can now be monitored in-situ, real-time and non-destructively with UTDR combined with a new patented enhanced acoustic method using colloidal silica as an 'acoustic enhancer'. Characterization of the biofouling includes measurements of the exponential TMP profile, the exponential biofilm thickness growth, and an increase in the amount of measurable EPS and number of colony forming units. The new technique utilizing UTDR corroborates reasonably well with the membrane performance and biofilm development. The use of colloidal silica does not affect biofilm development since its presence has no significant effects on the viability of the bacteria. Considerable insight into the inhomogeneous nature of the biofilm is also possible with the new technique.

6.2 Introduction

For both RO desalination and reclamation plants, the major fouling issue is frequently biofouling. For the sustainability of RO membrane technology, there is a need to have suitable sensitive techniques for studying and/or detecting membrane biofouling in order to develop appropriate strategies for its control. Conventional production parameters such as pressure drop or flux decline and product quality suffer from disadvantages such as long response time or low sensitivity to detect incipient fouling. Unfortunately, the application of UTDR in its current state is not capable of monitor biofouling without the use of immersion transducers. As highlighted in section 2.4.1 of Chapter 2, the magnitude of the reflected and transmitted waves is a function of the

---

[5] Findings in this chapter have been published in: Sim S.T.V., Suwarno S.R. Chong T.H., Krantz W.B., Fane A.G., J. Membr. Sci. 401-402 (2013) 241-253 and patented in Sim S.T.V., Suwarno S.R., Chong T.H., Krantz W.B., Fane A.G., Patent WO/2013/066268 filed on 31 October 2011.

difference between the acoustic impedances of the media. If the acoustic impedances are very similar, the interface of the media behaves as if it is totally transparent to the sound waves and does not result in any significant reflection or mode conversion. Given that the bulk 70% or more of biofilms are water medium, they have very similar acoustic impedances to water. Therefore UTDR, without very low attentuation of the waveform, as in the usage of immersion transducers, is limited in the detection of biofouling.

If the acoustic properties of the biofilm can be appropriately changed using ‘acoustic enhancers’, UTDR could be adapted to detect biofilms. However, it is essential that the acoustic enhancer does not affect the biofilm’s growth. Therefore, the focus of this chapter is to describe the adaptation of UTDR to monitor biofouling and to relate the changes in the UTDR to the membrane performance and biofilm development (Krantz and Greenberg, 2008).

This chapter is organized as follows. Section 6.3 summarizes the experimental procedure. Section 6.4 presents the results and these are subsequently discussed in section 6.5. Section 6.6 provides the concluding remarks.

6.3 Crossflow Filtration Experimental Procedure

Two types of experiments (Types I - Start/End Dosing and II - Daily Dosing) were conducted to correlate the UTDR measurements to changes in TMP profile and corroborate the UTDR measured biofilm thickness with CSLM measurements. Type I (Start/End Dosing) experiments were run as both low pressure applications of ultrafiltration and high pressure applications of reverse osmosis systems where the dosing procedure for the silica particles was done only at the start of the experiment and at the end of the experiment. Type II (Daily Dosing) experiments were only carried out under high pressure conditions where the dosing procedure for the silica particles was done at the start of the experiment and subsequently daily at the end of each day. To achieve a dosing procedure to enhance the biofilm’s acoustic impedance, a continuous dosing of 0.2 g/L concentration of silica was carried out for 30 minutes at the end of each experimental runs. Flushing for another 30 minutes was subsequently carried out after each dosing. As indicated in Figures 3.2 and 3.3 of Chapter 3, the dosing and flushing procedure for all crossflow experiments was done with V1 opened and V2 closed. V1 was closed and V2 was opened when not under the dosing and flushing procedure.

For CLSM measurements described in Section 3.3.1.3 of Chapter 3 used to compare with the UTDR measured biofilm thickness, all fouled membranes were analyzed at the end of each experiment. For membrane autopsies described in Section 3.3.1 of Chapter 3 for biofilm characterization, only fouled membranes from low pressure experiments were analyzed at the end of each experiment. All crossflow experiments were repeated once to verify the overall trend caused by changes in the biofilm development.

6.3.1 Low Pressure UF Experiments

Membranes were first compressed at a maximum flux with Milli-Q water for 30 minutes for the low pressure experiments carried out at the crossflow filtration mode. Flux was then reduced to the value required before adding the background electrolyte, sodium chloride, and Nutrient Broth (NB) solution (Beckton-Dickinson, Difco NB) to achieve 2 g/L of sodium chloride and 0.02 g/L of NB, which was equivalent to a Total Organic Carbon (TOC) value of 6.5 mg/L. After 30 minutes, continuous injection of the bacteria stock solution into the flow line was performed. Experiments were carried out at a constant crossflow velocity of 0.1 m/s and a constant flux of 25 L/m^{2}h. Low Pressure Type I experiments consisted of three individual runs of different durations; 1 day, 2 days and 3 days.

6.3.1 High Pressure RO Experiments

Membranes were first compacted at a maximum flux overnight with Milli-Q water until a stable flux was achieved for the high pressure experiments carried out under crossflow filtration mode. Flux was then reduced to the value required before adding the background electrolyte, sodium chloride to mix for 1.5 hours before adding in the NB solution (Beckton-Dickinson, Difco NB) to achieve 2 g/L of sodium chloride and 0.02 g/L of NB, which was equivalent to a Total Organic Carbon (TOC) value of 6.5 mg/L. After 30 minutes, continuous injection of the bacteria stock solution into the flow line was performed.

Two conditions, a crossflow velocity of 0.15 m/s at a constant flux of 35 L/m^{2}h, and a crossflow velocity of 0.13 m/s at a constant flux of 40 L/m^{2}h were carried out for the high pressure experiments. Both conditions had the same duration of 4 days but different procedures for the dosing and flushing of silica particles were carried out. The experiments are labeled as High Pressure Type I (Start/End Dosing) and Type II (Daily Dosing).

6.4 Experimental Results

This section summarizes observed trends and representative results for the UTDR and CSLM measurements, TMP profile, silica toxity test and the membrane autopsies. Detailed discussion of the results is given in section 6.5. The fouling behaviour of biofilm can be described as an exponential phenomenon in terms of TMP rise that correlates well with the exponential growth of the biofilm found in both low pressure and high pressure Type I (Start/End Dosing) and II (Daily Dosing) experiments. The more severe the biofouling, the greater the thickness of the biofilm with a corresponding increase in the number of bacteria counts and the amount of EPS. The UTDR measured biofilm thickness for all experiments corresponded relatively well to the thickness measured by CLSM. Biofilm thicknesses were only detectable after the first introduction of silica particles. Bacteria that were exposed longer and to more concentrated amounts of silica particles were found to have no significant responses in terms of the number of bacteria colony forming units.

6.4.1 UTDR Measurements

Figure 6.1 shows an enlarged plot of the amplitude of the acoustic wave response in volts as a function of $t - t_b$, the difference in the arrival time, t, with respect to the arrival time of peak B, t_b, for the high pressure filtration apparatus at a crossflow velocity of 0.15 m/s at a constant flux of 35 L/m^{2}h with an aqueous solution containing 0.02 g/L of NB and 2 g/L of sodium chloride solution as a result of the dosing and flushing procedure. Peak B in Figure 6.1 is the reflection initially from the fouled membrane without the ‘acoustic enhancers’. It later represents the reflection from the biofilm surface with the introduction of the ‘acoustic enhancers’ during the dosing procedure, which resumes the initial higher arrival time of the membrane surface when the ‘acoustic enhancers’ are removed during the flushing procedure. Peak C is the reflection from the bottom of the membrane.

The thickness of the unfouled membrane was derived from the difference in arrival times for peaks B and C when no silica particles were introduced. During the dosing procedure where the silica particles were added to enhance the biofilm’s acoustic impedance, the difference in arrival times then corresponded to the combined thicknesses of the membrane and the biofilm. This is represented by the decrease in arrival time and the increase in amplitude of peak B as observed in Figure 6.1. The silica particles were removed during the flushing procedure, which shows peak B approximately resuming the initial arrival time with a higher value and lower amplitude prior to the dosing procedure as shown in Figure 6.1.

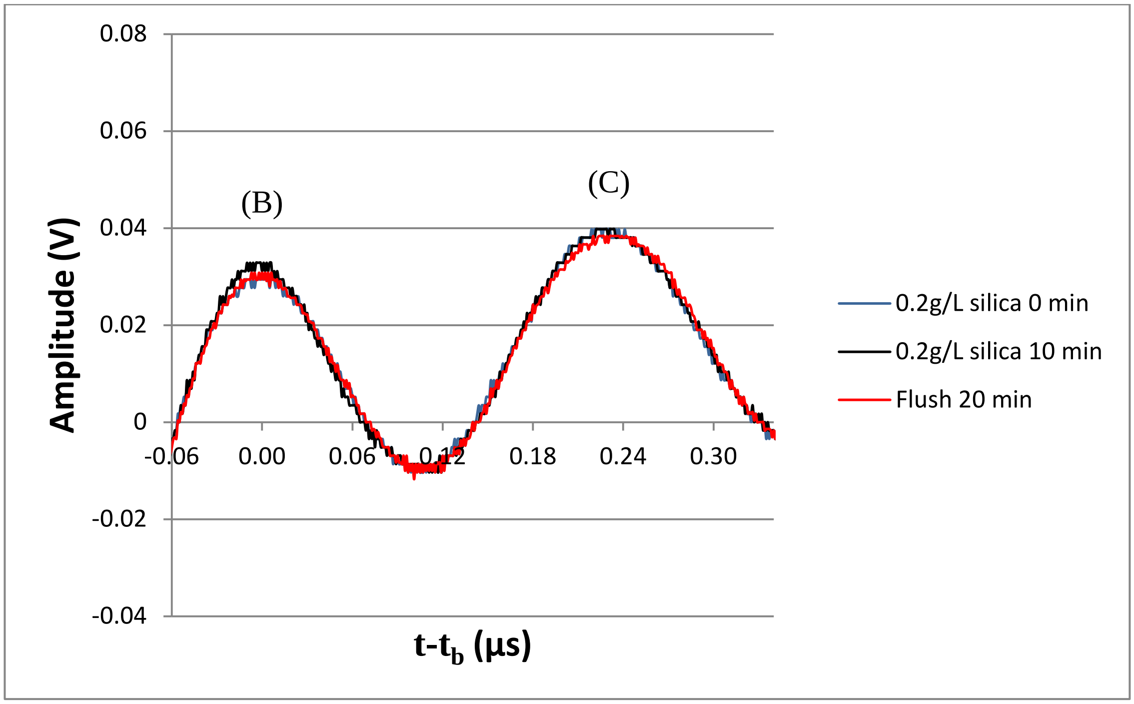

Figure 6.1: Peak Amplitude versus $t - t_b$, the difference in the arrival time, t, with respect to the arrival time of Peak B, t_b, for High Pressure Type I (Start/End Dosing) experiment for an aqueous solution containing 0.02 g/L of NB and 2 g/L of sodium chloride solution at a crossflow velocity of 0.15 m/s at a constant flux of 35 L/m^{2}h: peaks B and C of interest. Peak B corresponds to the reflection from the feed solution/membrane interface while peak C corresponds to the reflection from the membrane/permeate support interface.

6.4.2 Low Pressure Experiments (Type I – Start/End Dosing)

Figure 6.2 shows the plot of the TMP/TMP$_o$ as a function of time for different Low Pressure Type I (Start/End Dosing) experiments with time durations of 1 day, 2 days, and 3 days at a constant flux of 25 L/m^{2}h at a crossflow velocity of 0.10 m/s for an aqueous solution containing 0.02 g/L of NB and 2 g/L of sodium chloride with the dosing procedure done at the end of each experiment. The fouling behavior of biofilm formation caused an exponential rise in TMP where the effects of biofouling were reproducible in terms of the TMP profile. There was an associated TMP jump at the end of each experiment especially for the duration of 2 days and 3 days experiments with the dosing and flushing procedure for the silica particles. This is illustrated more clearly in Figures 6.3 and 6.4. This TMP jump is evident only in low pressure experiments and it is interesting to note that this TMP rise is absent in the TMP/TMP_o profile for the High Pressure Type I (Start/End Dosing) and II (Daily Dosing) experiments shown in section 6.4.3.

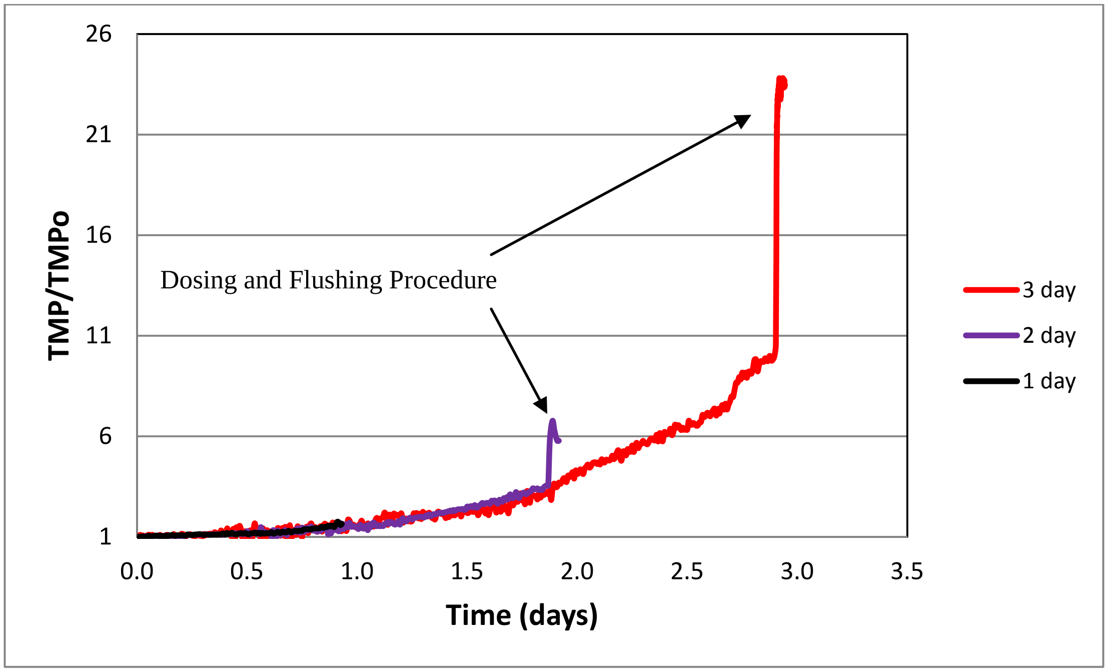

Figure 6.2: TMP/TMPo versus time for different Low Pressure Type I (Start/End Dosing) experiments with time durations of 1 day, 2 days, and 3 days at a constant flux of 25 L/m^2h at crossflow velocity of 0.10 m/s for an aqueous solution containing 0.02 g/L of NB and 2 g/L of sodium chloride.

Figures 6.3 to 6.5 show (i) the plot of the TMP/TMP_o and the corresponding UTDR measured biofilm thickness as a function of time, (ii) the enlarged plot of the corresponding UTDR measured biofilm thickness, and (iii) the biofilm thickness measured by CSLM, for different Low Pressure Type I (Start/End Dosing) experiments with time durations of 1 day, 2 days, and 3 days at a constant flux of 25 L/m^2h at a crossflow velocity of 0.10 m/s for an aqueous solution containing 0.02 g/L of NB and 2 g/L of sodium chloride with the dosing procedure done at the end of each experiments. Figure 6.6 shows the plot of biofilm thicknesses measured by both UTDR and CSLM for the different Low Pressure Type I (Start/End Dosing) experiments with time durations of 1 day, 2 days, and 3 days at a constant flux of 25 L/m^{2}h at a crossflow velocity of 0.10 m/s for an aqueous solution containing 0.02 g/L of NB and 2 g/L of sodium chloride at the end of each experiments. Figure 6.7 shows a plot of (i) the bacterial count and (ii) the EPS measurements for the same conditions as in Figures 6.3 to 6.5 as a function of the experimental time duration. As the biofilm becomes thicker with the increased duration of the experiments, there is an increase in both the bacterial count and EPS concentration.

Figure 6.6 shows that the UTDR measured biofilm thicknesses from Figures 6.3 to 6.5 are in good agreement with the CSLM measured biofilm thicknesses. As TMP rise became steeper due to more severe biofouling, the biofilm thicknesses were found to be thicker with corresponding increases in bacteria counts and EPS measurements as illustrated in Figures 6.6 and 6.7 respectively. There is lack of significant UTDR measured biofilm thicknesses in the absence of silica as seen in Figures 6.3 to 6.5. The intended removal of the dosed silica during the flushing procedure does not show complete recover of the changes in ultrasonic signal caused by the introduction of silica particles as ‘acoustic enhancers’. This results in the detectable biofilm thicknesses increasing with each subsequent dosing and flushing procedure, especially in subsequent flushing procedures of increasing time duration. This is further discussed in section 6.5.1. The trend of the detectable biofilm thicknesses compares well with the trend of exponential TMP rise. Interestingly, the UTDR measured biofilm thickness also seems to level off towards the end of the dosing procedure as observed in Figures 6.3 to 6.5.

(i)

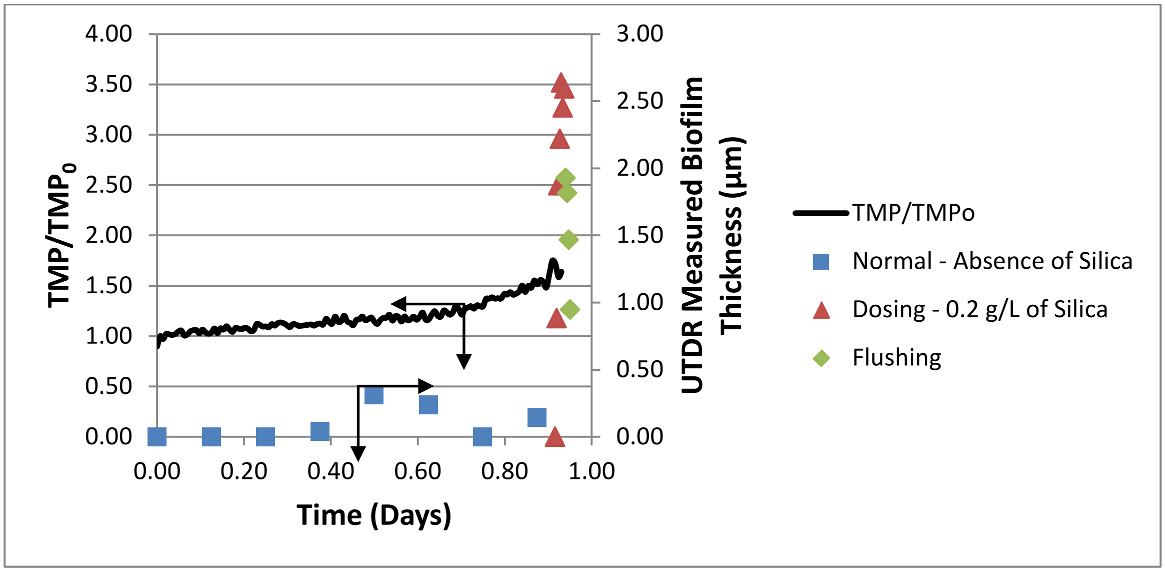

(ii)

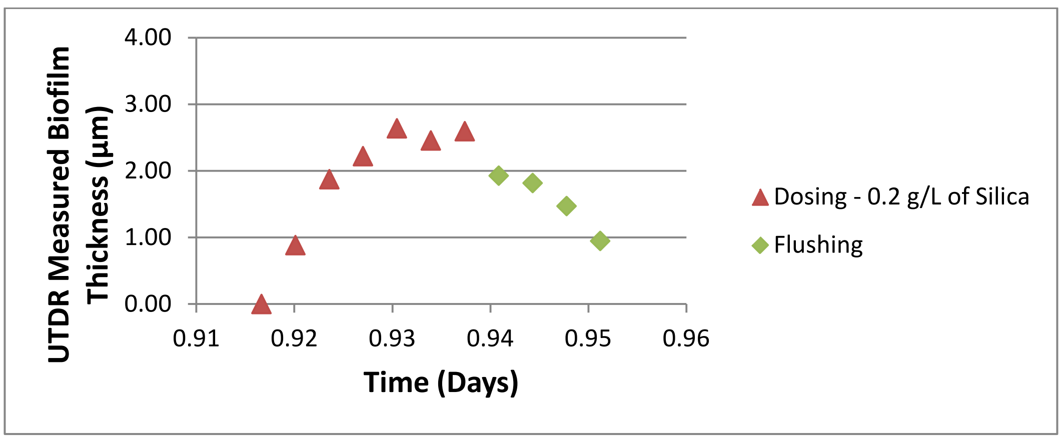

(iii)

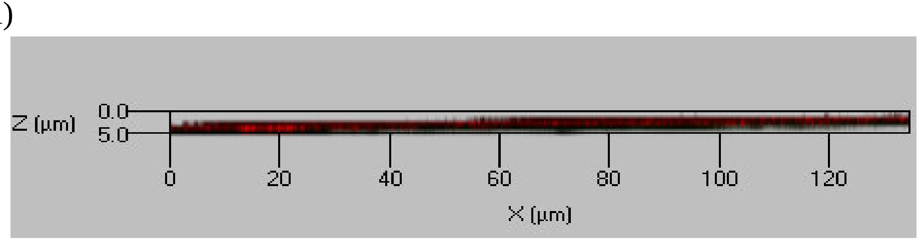

Figure 6.3: (i) TMP/TMPo and the corresponding UTDR measured biofilm thickness as a function of time, (ii) the enlarged plot of the corresponding UTDR measured biofilm thickness at the end of experiment, and (iii) the biofilm thickness of approximately 3 μm measured by CSLM, for Low Pressure Type I (Start/End Dosing) experiment with time duration of 1 day at a constant flux of 25 L/m^{2}h at a crossflow velocity of 0.10 m/s for an aqueous solution containing 0.02 g/L of NB and 2 g/L of sodium chloride.

(i)

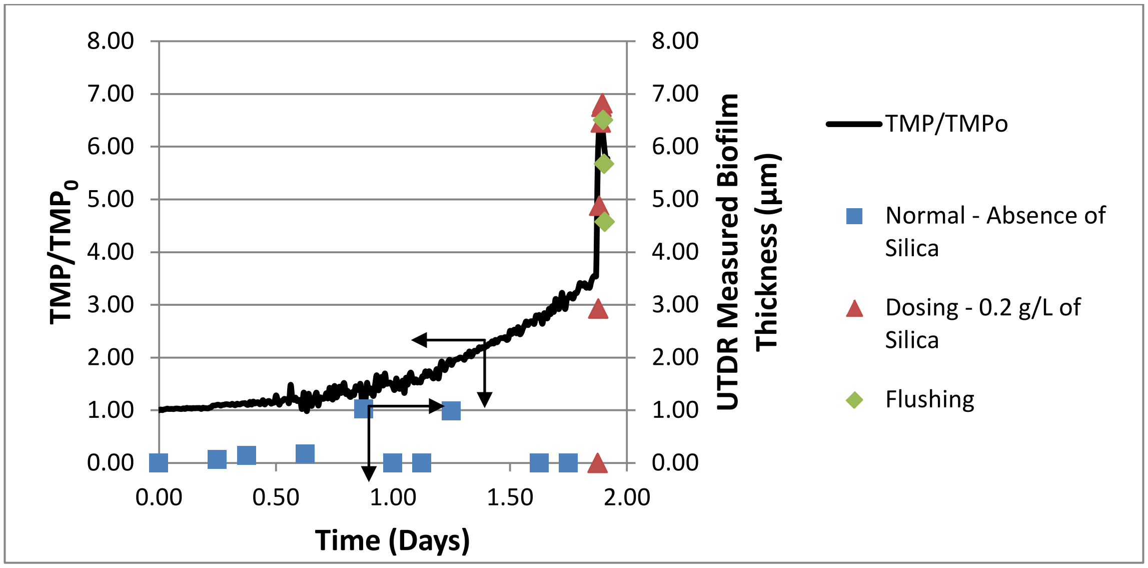

(ii)

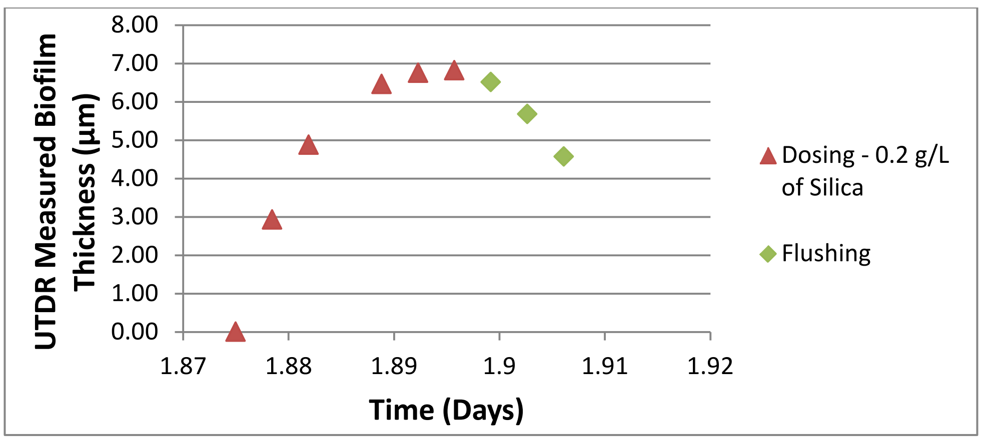

(iii)

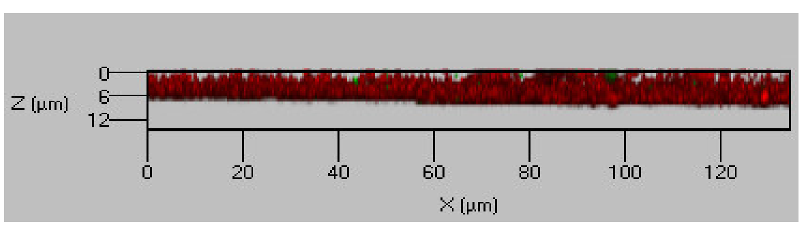

Figure 6.4: (i) TMP/TMPo and the corresponding UTDR measured biofilm thickness as a function of time, (ii) the enlarged plot of the corresponding UTDR measured biofilm thickness at the end of experiment, and (iii) the biofilm thickness of approximately 7 µm measured by CSLM, for Low Pressure Type I (Start/End Dosing) experiment with time duration of 2 days at a constant flux of 25 L/m^{2}h at a crossflow velocity of 0.10 m/s for an aqueous solution containing 0.02 g/L of NB and 2 g/L of sodium chloride.

(i)

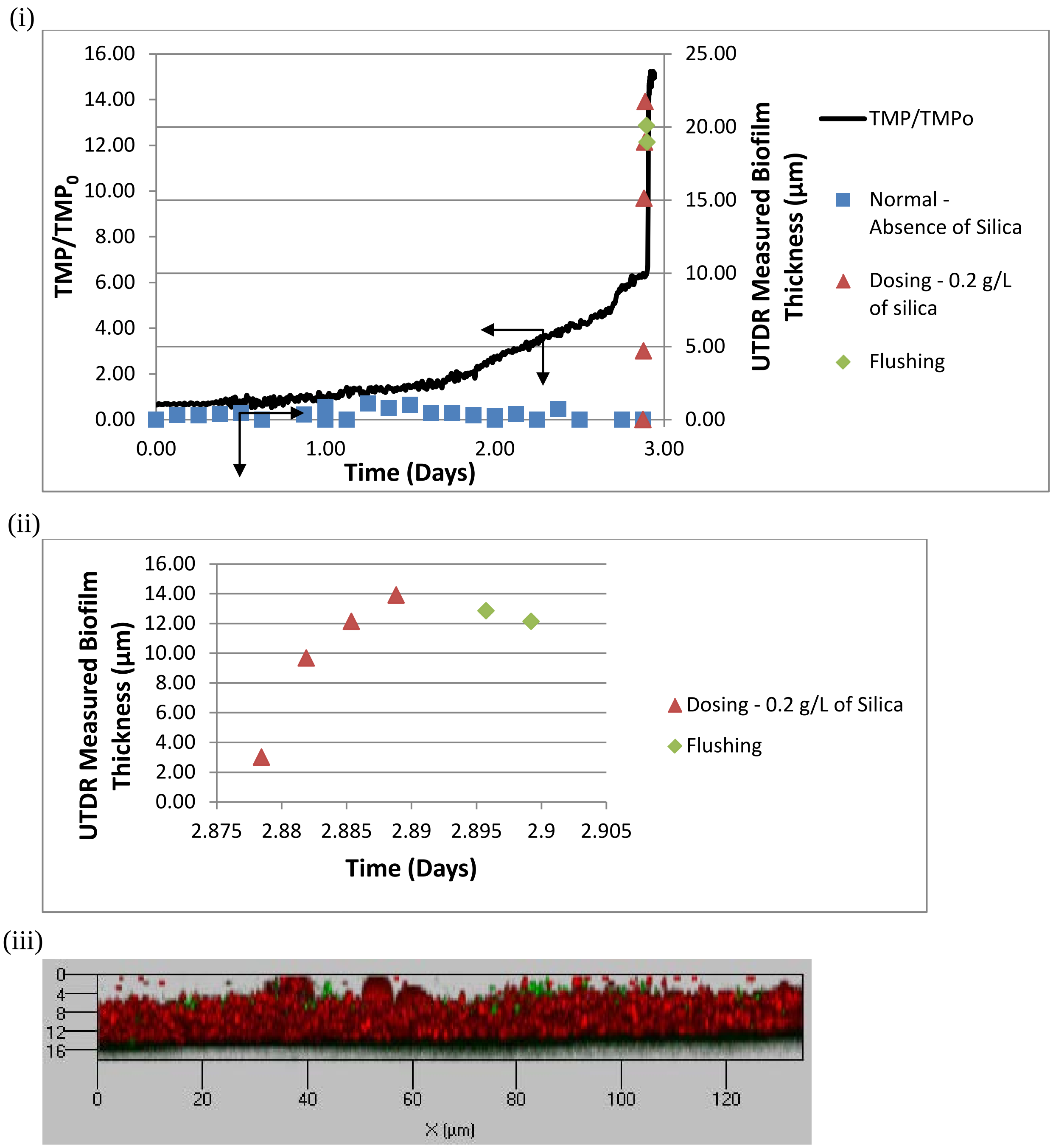

Figure 6.5: (i) TMP/TMPo and the corresponding UTDR measured biofilm thickness as a function of time, (ii) the enlarged plot of the corresponding UTDR measured biofilm thickness at the end of experiment, and (iii) the biofilm thickness of approximately 12 µm measured by CSLM, for Low Pressure Type I (Start/End Dosing) experiment with time duration of 3 days at a constant flux of 25 L/m^{2}h at a crossflow velocity of 0.10 m/s for an aqueous solution containing 0.02 g/L of NB and 2 g/L of sodium chloride.

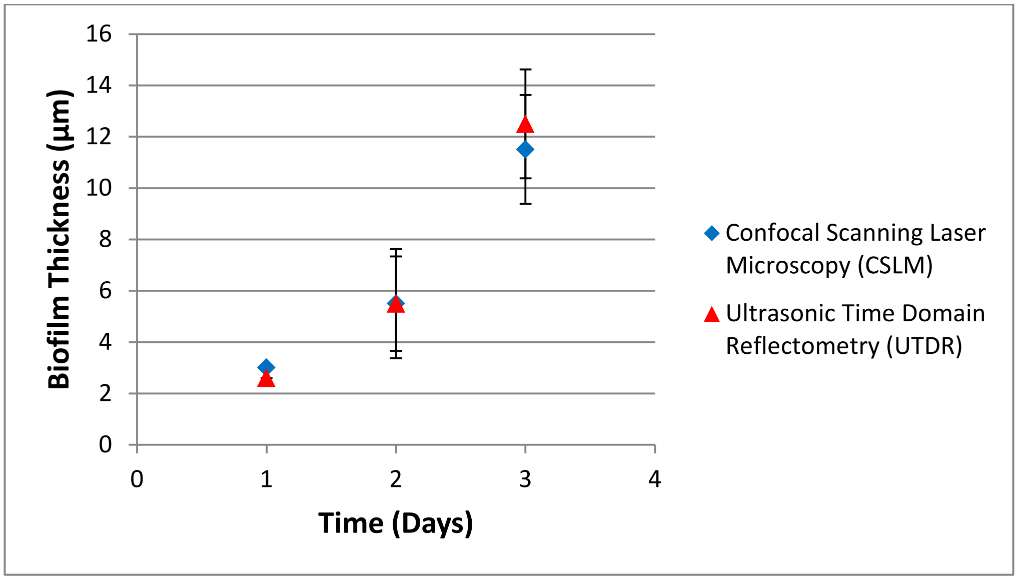

Figure 6.6: Comparison of the biofilm thicknesses measured by both CSLM and UTDR for the different Low Pressure Type I (Start/End Dosing) experiments with time duration of 1 day, 2 days, and 3 days at a constant flux of 25 L/m^2h at a crossflow velocity of 0.10 m/s for an aqueous solution containing 0.02 g/L of NB and 2 g/L of sodium chloride with the dosing procedure done at the end of each experiments.

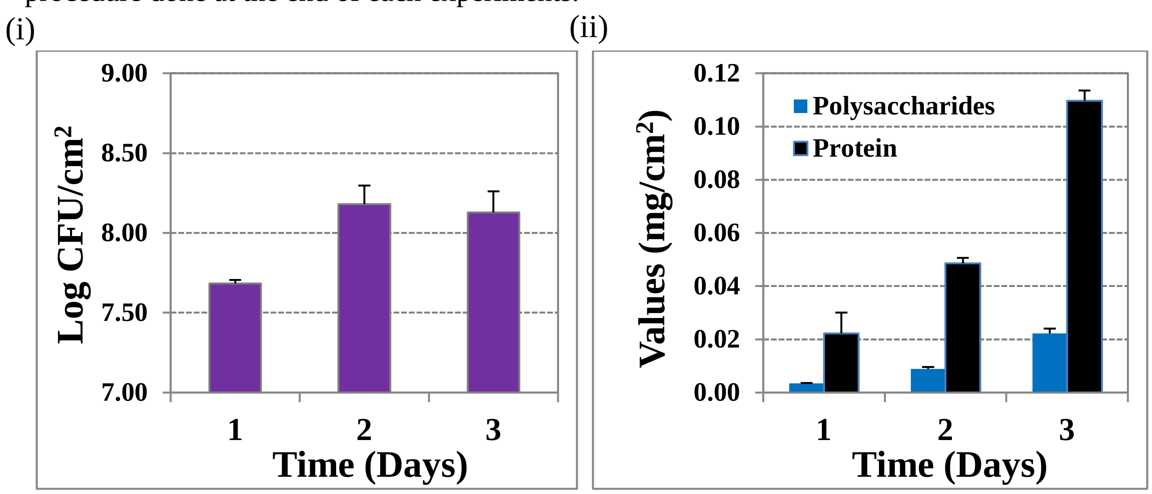

Figure 6.7: (i) Bacteria counts and (ii) EPS measurements for the different Low Pressure Type I (Start/End Dosing) experiments with time duration of 1 day, 2 days, and 3 days at a constant flux of 25 L/m^2h at a crossflow velocity of 0.10 m/s for an aqueous solution containing 0.02 g/L of NB and 2 g/L of sodium chloride with the dosing procedure done at the end of each experiments.

6.4.3 High Pressure Experiments (Type I – Start/End Dosing and II – Daily Dosing)

Figure 6.8 shows (i) the plot of the TMP/TMP_o and the corresponding UTDR measured biofilm thickness as a function of time, (ii) the biofilm thickness measured by CSLM, for High Pressure Type I (Start/End Dosing) experiment with time duration of 4 days at a constant flux of 35 L/m^2h and a crossflow velocity of 0.15 m/s for an aqueous solution containing 0.02 g/L of NB and 2 g/L of sodium chloride with the dosing procedure done only at the start of the experiment and at the end of the experiment. Figure 6.9 shows (i) the plot of the TMP/TMP_o and the corresponding UTDR measured biofilm thickness as a function of time, (ii) the biofilm thickness measured by CSLM, for High Pressure Type II (Daily Dosing) experiment with time duration of 4 days at a constant flux of 40 L/m^2h at a crossflow velocity of 0.15 m/s for an aqueous solution containing 0.02 g/L of NB and 2 g/L of sodium chloride with the dosing procedure done at the start of the experiment and at the end of each day.

The UTDR measured biofilm thicknesses from Figures 6.8 and 6.9 are in good agreement with the CSLM measured biofilm thicknesses at the end of the experiment. The daily UTDR measured biofilm thicknesses corresponds quite well to the TMP rise from Figure 6.9. Similar to the low pressure experiments in Sections 6.4.2, there is a lack of significant UTDR measured biofilm thicknesses in the absence of silica. This is seen in Figure 6.8 as well as within the first day of UTDR measurements of Type II (Daily Dosing) experiment in Figure 6.9. Complete removal of the dosed silica during the flushing procedure can be observed at the start of the Type II (Daily Dosing) experiment. However, subsequent flushing procedures are not able to completely recover the changes in ultrasonic signal due to the introduction of silica particles as ‘acoustic enhancers’. This results in detectable biofilm thicknesses increasing with each dosing and flushing procedure. Similar to section 6.4.2, the presence of detectable biofilm thicknesses is further discussed in section 6.5.1.

(i)

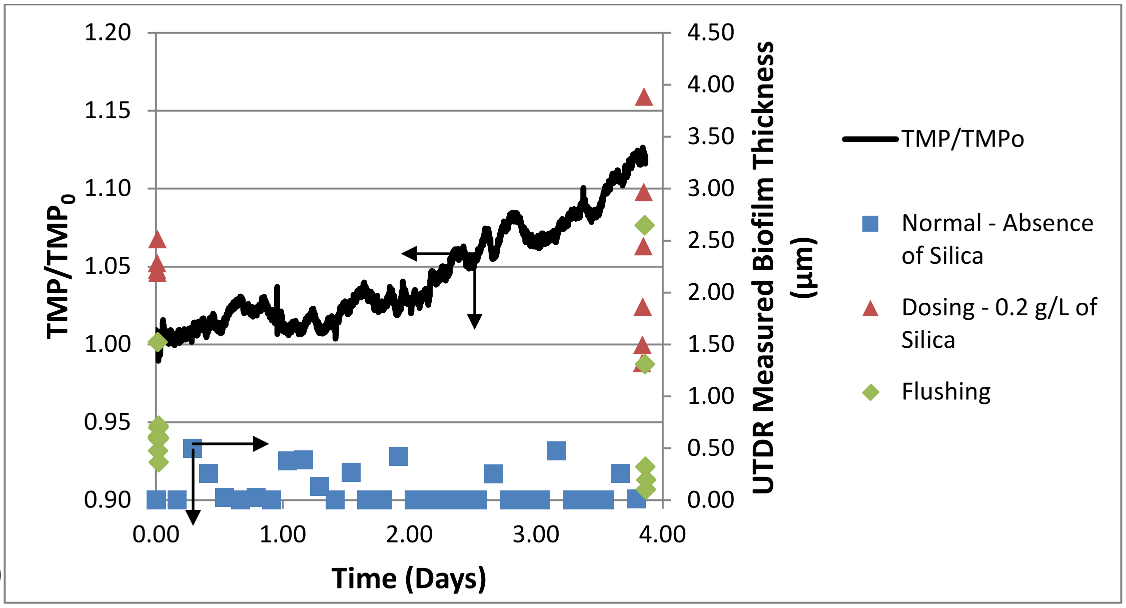

(ii)

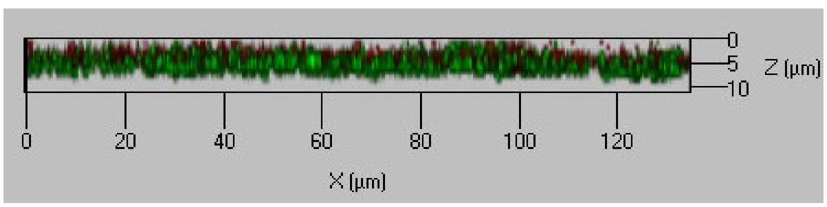

Figure 6.8: (i) TMP/TMPo and the corresponding UTDR measured biofilm thickness as a function of time, and (ii) the biofilm thickness of approximately 4 µm measured by CSLM, for High Pressure Type I (Start/End Dosing) experiment with time duration of 4 days at a constant flux of 35 L/m^{2}h at a crossflow velocity of 0.15 m/s for an aqueous solution of 0.02 g/L of NB and 2 g/L of sodium chloride solution, and the dosing procedure at the start and the end of the experiment.

(i)

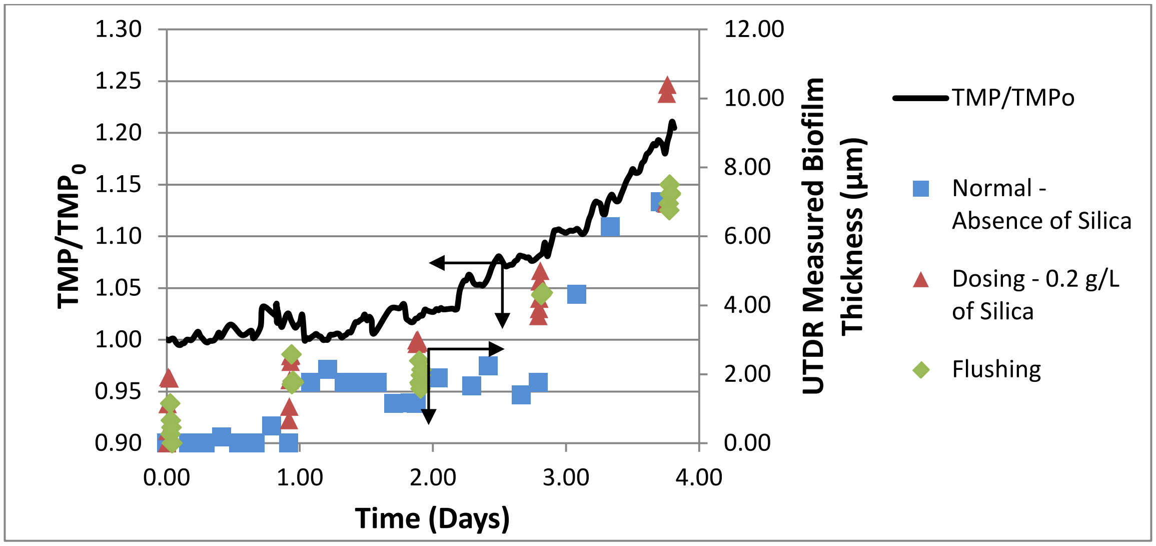

(ii)

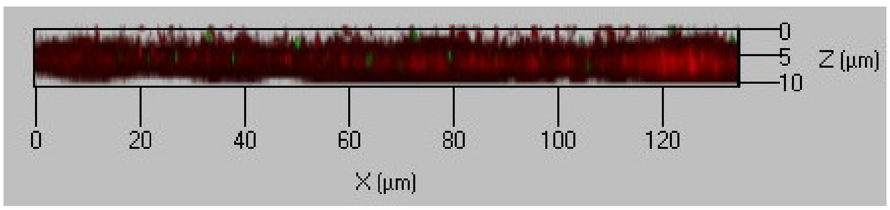

Figure 6.9: (i) TMP/TMPo and the corresponding UTDR measured biofilm thickness as a function of time, and (ii) the biofilm thickness of approximately 10 µm measured by CSLM , for High Pressure Type II (Daily Dosing) experiment of 4 days duration at a crossflowlz velocity of 0.13 m/s at a constant flux of 40 L/m^{2}h for an aqueous solution 0.02 g/L of NB, 2 g/L of sodium chloride, and the dosing procedure at the start of the experiment and daily at the end of each day.

6.4.4 Silica Toxicity Test

Figure 6.10 shows a plot of the logarithm of bacteria counts as the number of colony forming units (CFU) per ml as a function of concentration of silica for aqueous solutions containing 0, 0.2, 1.0, 6.0 g/L of silica, 5 g/L of NB, and 2 g/L of sodium chloride used to incubate the bacteria after 24 hours. No significant difference in the number of colony forming units was observed whether or not silica was present up to a concentration of 6.0 g/L of silica. This is 30 times more concentrated than the amount of silica used in the dosing procedure. The 24 hours exposure time of the bacteria to silica is also up to 48 times longer than the 30 minutes during the dosing procedure.

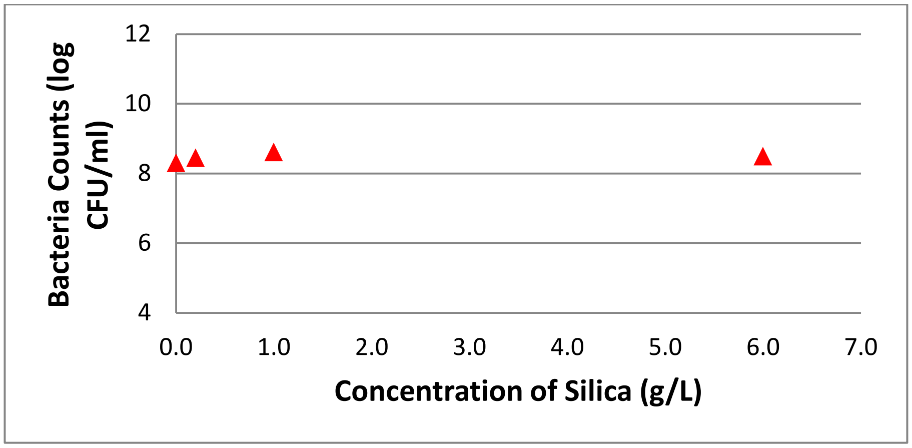

Figure 6.10: Bacteria counts (Logarithm CFU/ml) versus concentration of silica for different aqueous solutions containing 0 g/L, 0.2 g/L, 1.0 g/L, and 6.0 g/L of silica, 2 g/L of sodium chloride, and 5 g/L of NB.

6.5 Discussion

The use of silica particles as 'acoustic enhancers' has been shown to be able to enhance the acoustic impedances difference of the biofilm/feed solution and biofilm/membrane interfaces. This allowed UTDR to detect and measure the biofilm growth in real-time, in-situ and non-destructively. The detectable biofilm thicknesses after each dosing procedure was due to the residual silica embedded within the biofilm. For low pressure (UF) experiments, the added silica produced some detectable fouling. However, this was not observed for high pressure (RO) membranes due to the magnitude of the membrane resistance and cake enhanced osmotic pressure effects. At 30 times more concentration and with an exposure time 48 times longer than the conditions used in this new method, silica is believed to be non-toxic.

6.5.1 Low and High Pressure Experiments

Without the presence of a biofilm, silica particles were able to be removed with crossflow alone due to tangential shear and critical flux effects. This was evident from the introduction of silica particles at the start of the experiments. However, residual silica was left behind in subsequent dosing procedures because the colloids were held in the biofilms. This resulted in detectable biofilm thicknesses. Previous studies have shown that particles do not get removed completely and can get embedded within biofilms (Battin *et al.*, 2003; Vieira and Melo, 1995) so the entrapment of silica particles was not unexpected. Without a biofilm, there was no residual silica and there was no detection by UTDR as observed in Figures 6.8 and 6.9 within the first day in the high pressure experiments. Silica particles start to get entrapped within the biofilm during the dosing procedure once the biofilm was formed. However, only those silica particles near the surface of the biofilm were able to be removed during the flushing procedure due to the effect of crossflow. As the biofilm grew thicker, it would result in greater sinuosity [6] and higher fragmentation [7] towards the top layers in order for enhanced transport of particles and substrate to assure the appropriate mass transfer of substrates essential to satisfy microbial demand (Battin *et al.*, 2003). This explains why the entrapped silica particles, not removed by the flushing procedure, were only within the bottom layers of the biofilm nearer to the membrane. Energy-dispersive x-ray spectroscopy (EDX) performed on biofilms for a Low Pressure Type I (Start/End Dosing) experiment with time duration of 2 days also detected a small but significant amount of silicon relative to other elements such as carbon, oxygen and sulphur present, which supports the suggestion that residual silica was entrapped within the biofilm. However, examination on the likely mechanisms for the dispersion of the silica particles within the biofilm was beyond the scope of this study and could be explored in future work.

It is assumed that during dosing, the silica locates mainly in the upper part of the biofilm. This would lead to the UTDR measured biofilm thicknesses being the detection of the top of the biofilm/feed solution interface. However, comparing the high

---

[6] As the sinuosity of the biofilm is thought to affect mass transport, it is analogous to surface enlargement (Picioreanu *et al.*, 1998).

[7] As a measure suggested over which a substrate molecule must diffuse from the void to bacterial cells within a cluster, the fragmentation of the biofilm is analogous to the average diffusion distance (Yang *et al.*, 2000).

pressure and low pressure experiments, there is a distinct difference in the nature of the TMP profile during the dosing procedure. For low pressure experiments, a sudden TMP rise can be associated with the introduction of the silica particles and this gets progressively more significant from longer durations of experimental run-time as the biofilm gets thicker. If this is caused by the entrapment of silica particles within the biofilm, this phenomenon of rapid TMP rise bares resemblance to that observed during the blocking filtration mechanism (Boerlage *et al.*, 2003). However, this was not clearly observed during the high pressure experiments as seen in Figures 6.8 and 6.9. A plausible reason is due to the different hydraulic resistances of the low and high pressure experiments. Depending on the severity of the biofouling and the amount of osmotic pressure to overcome, the pressure required for the hydraulic resistance of the RO membrane plus the osmotic pressure resulting from the accumulation of ions and the biofilm is around 12 to 16 bars while the pressure required for the increment of the hydraulic resistance caused by the entrapment of silica within the biofilm is only of the order of 1 bar or less as evident from the low pressure experiments.

6.4.2 Silica Toxicity Test

Exposure of bacteria to 30 times more concentration and for 48 times as long as the dosing procedure was found to have no adverse effects on their viability to proliferate and grow. This provides evidence that silica should have no effect on the formation of the biofilm at the current conditions of the dosing procedure since it is non-toxic to the bacteria.

6.6 Concluding Remarks

Without the colloidal silica as an ‘acoustic enhancer’, ultrasonic reflectometry using an external transducer is not able to detect the interfaces of biofilm/feed solution and biofilm/membrane without any additional modifications. This chapter indicates that considerable insights into the nature of biofouling can be obtained from UTDR with the use of silica particles as appropriate acoustic enhancers. Further information is provided by TMP measurements and CSLM characterization. Monitoring the growth of biofilms quantitatively in real-time, in-situ and non-destructively is now possible with this new UTDR method. The detectable biofilm thicknesses also indicate inhomogeneity within the biofilm; a tightly packed region nearer the membrane with increasing sinuoisty and fragmentation across the biofilm.

Significant membrane fouling does occur for low pressure systems when colloidal silica is introduced as acoustic enhancers and pose a problem for monitoring of biofouling in ultrafiltration or microfiltration membrane processes. However, the marked change in membrane fouling could offer insight to the inhomogeneity of the biofilm and its structure. Fortunately for high pressure systems, the increment of the hydraulic resistance caused by the presence of entrapped silica particles within the biofilm is insignificant in comparison to the much larger hydraulic resistance of the RO membrane, the osmotic pressure resulting from the accumulation of ions and the biofilm. Therefore, this method is adaptable for use in high pressure systems. In addition, it has been shown that silica particles are non-toxic to the viability of bacteria even at 30 times more concentration and when exposed for 48 times as long as the conditions used for the dosing procedure.

CHAPTER 7 : UTDR COMBINED WITH FFM FOR RO FOULING PREDICTION[8]

7.1 Abstract

Ultrasonic time domain reflectometry (UTDR) was combined with an on-line feed fouling monitor (FFM) under constant flux filtration to predict RO colloidal fouling. The FFM was used to simulate similar hydrodynamics and net flux conditions as the RO crossflow filtration module. The FFM utilized the same type and concentration of colloidal silica foulant as the RO feed that is continuously passed over a small ultrafiltration (UF) membrane. The UF membrane with a lower hydraulic resistance than a RO membrane allowed greater sensitivity to fouling resistance that decreased monitoring time and increased accuracy. The rate of cake thickness increase was monitored by UTDR coupled to a RO crossflow filtration module and utilized to estimate the cake-enhanced osmotic pressure (CEOP). Increased fouling rate and rate of cake thickness increase were observed under higher fluxes with the estimated CEOP effect dominating the fouling rate (as TMP rise) under all flux conditions.

7.2 Introduction

As highlighted in section 2.1.3.1 of Chapter 2, the back transport of solute is hindered in the presence of a foulant cake layer. Based on Equations 2.9 and 2.10 in section 2.1.3.1, two important parameters, the cake layer thickness and cake porosity, are required to be measured in order to estimate the CEOP effect. The height of the developing cake layer in the RO system was measured by UTDR while the cake porosity was estimated using the TMP profile by running the FFM under similar hydrodynamics and flux conditions as the RO experiments. The FFM is an adaptation of the integrity sensor that is described in the section SA.3 of the Special Appendix. It

---

[8] The main findings in this chapter has been published in: Taheri A.H., Sim S.T.V., Sim L.N., Chong T.H., Krantz W.B., Fane A.G., J. Membr. Sci. 448 (2013) 12-22.

is assumed that the structure of the cake layer is similar under similar hydrodynamics and net flux conditions regardless of whether a UF or RO membrane is used. In addition, a best fit value of 0.05 was assumed for the value of the fractional deposition factor in Equation 3.17 (Taheri *et al.*, 2013). This chapter describes the use of these two monitors to measure the data required to predict the transmembrane pressure (TMP) rise over the RO membrane fouled by colloidal silica.

However, the uses of UTDR and FFM have their own key concerns that need to be addressed before being assured of the accuracy for the fouling prediction. Under the high pressure conditions of the RO fouling experiments, the accuracy in measuring the growth of the cake layer thickness can be compromised by the compressibility of the RO membrane. Unlike a RO membrane, the UF membrane used in the FFM does not retain the salt used as the background electrolyte. As the higher concentration of salinity near the RO membrane surface can affect the packing density of the silica foulant cake layer, it is necessary to account for the difference in the salinities. Therefore, the focus of this chapter is to provide experimental evidence for RO fouling prediction using the combination of UTDR and FFM after accounting for the key concerns mentioned above; compressibility of the RO membrane and the difference in salinities of the FFM and RO experiments.

This chapter is organized as follows. Section 7.3 summarizes the experimental procedure. Section 7.4 presents and discusses the results. Section 7.5 provides the concluding remarks.

7.3 Experimental Procedure

Three types of experiments were run. The first two types consist of accounting for the compressibility of the RO membrane and the difference in salinities encountered by the UF membrane used in the FFM relative to the RO membrane. The last type involved running experiments using both the FFM and the RO crossflow filtration under the same hydrodynamics and net flux conditions to predict the TMP rise on the RO membrane caused by colloidal silica fouling. Refer to sections 3.2.3 and 3.2.4 for description of the crossflow and dead-end filtration equipments.

7.3.1 Compressibility of the RO membrane

RO membranes were first compacted at a maximum flux overnight with Milli-Q water until a stable flux was achieved. Flux was then reduced to the value required of 30.1 L/m^{2}h before adding the background electrolyte, sodium chloride to mix for 1.5 hours. The flux was then increased to subsequent values of 36.1, 42.1, 48.2 and 54.2 L/m^{2}h with each flux increase allowed to stabilize for 1 hour before UTDR measurements were taken.

7.3.2 Salinity effects on cake structure

Dead-end filtration tests under a constant flux and various salt concentrations of 2 to 16 g/L NaCl were done to investigate the effects of salinity on the specific cake resistance and cake porosity of the colloidal silica. Using the TMP profile and Equations 3.18 and 3.19 of sections 3.4.1 and 3.4.1.1 of Chapter 3 allowed the determination of the changes in the specific cake resistance and cake porosity due to the different salt concentrations. These results allowed the estimation of the cake porosity in the FFM in relationship to the changes in salinity experienced in the RO fouling experiments.

7.3.3 RO prediction experiments

UTDR was coupled with a RO crossflow filtration module as described in section 3.2.3 and fouling experiments were carried out with an aqueous solution containing 0.2 g/L of silica and 2 g/L of NaCl for a range of constant fluxes at 30, 36.1, 42.1 and 48.1 L/m^{2}h. Both the TMP profiles and the cake layer thicknesses were measured for these experiments. Under the same hydrodynamic conditions as the RO experiments, the FFM experiments were carried out at different net fluxes to obtain the specific cake resistances and cake porosities for RO using Equations 3.17 and 3.19 of sections 3.4.1 and 3.4.1.1. The critical flux of the colloidal silica for the RO membrane was measured using the flux stepping method and found to be 20 ± 2 L/m^{2}h. Therefore, the FFM experiments covered the same net fluxes of 10 L/m^{2}h to 28 L/m^{2}h that applied in the RO experiments.

Combining the results of the UTDR and FFM, the TMP for the RO scenario was predicted and compared with experimental results for the actual RO module. Figure 7.1 is a flow diagram that shows how the FFM results of the specific cake resistance and cake porosity are utilized together with the UTDR measured growth of the cake layer thicknesses to estimate CEOP and foulant cake resistance to predict the TMP profile of the fouled RO membrane. For the UTDR measurement, the initial trends (5 to 10 hrs) in cake height and specific cake resistance were used to predict RO fouling up to 45 hours. Based on regular updates of new data from the FFM and UTDR, longer term operation of predicted TMP could be further obtained.

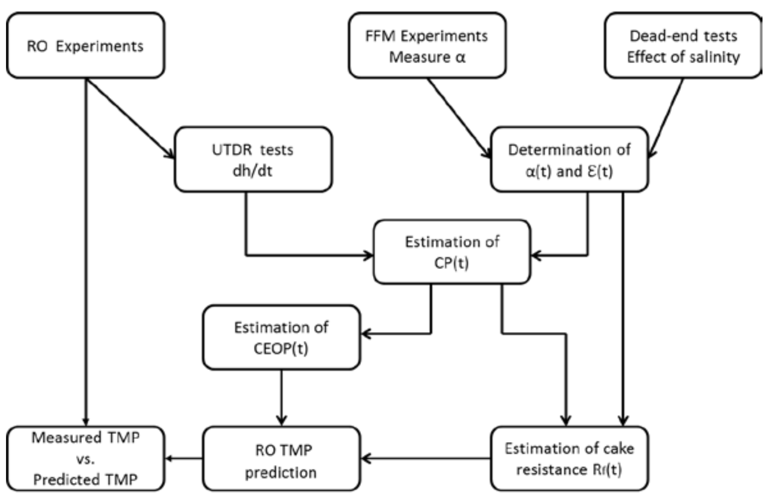

Figure 7.1: Flow diagram on the procedure for predicting TMP profile of fouled RO membranes.

7.4 Experimental Results

7.4.1 Compressibility of the RO membrane

Figure 7.2 shows the plot of the TMP and the UTDR measured membrane compaction for the RO membrane run at different constant fluxes under a crossflow velocity of 0.1

m/s for an aqueous solution containing 2 g/L of sodium chloride. The detailed analysis of the UTDR waveform has been described in section 4.2.2 of Chapter 4.

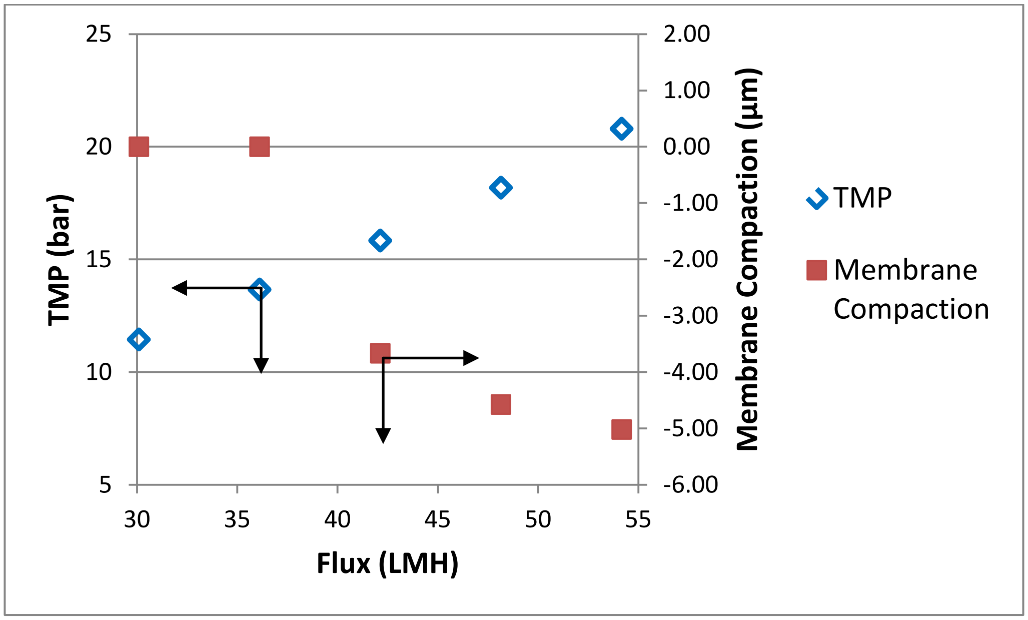

Figure 7.2: UTDR measured membrane compaction and TMP of RO membrane under different constant fluxes at a crossflow velocity of 0.1 m/s for an aqueous solution containing 2 g/L of sodium chloride.

The membrane compaction due to increase in transmembrane pressure (TMP) of approximately 7 bar when the flux increases from 42.1 L/m^{2}h to 54.2 L/m^{2}h resulted in the compaction of membrane thickness of only approximately 1.5 µm. This was expected since the RO membrane had already been compressed overnight prior to the experiments. In the subsequent RO fouling experiments, the increases in TMP were only of the order of 1 - 2.5 bar over a long period and that would result in the inaccuracy of the UTDR measured cake thicknesses to be less than 0.014 µm/h. Therefore, it is reasonable to assume the initial UTDR measured cake thickness growth rate of 0.375 µm/h – 0.513 µm/h as shown in section 7.4.3 to be relatively unaffected by possible membrane compaction under the experimental conditions.

7.4.2 Salinity effects on cake structure

Figure 7.3 presents the experimentally determined specific cake resistance and cake porosity as a function of the NaCl concentration in dead-end filtration mode under a constant flux for an aqueous solution containing 0.2 g/L of silica and 2 g/L of sodium chloride. As the salt concentration increases, the specific cake resistance increases with a corresponding decrease in the cake-average porosity. Similar results has been observed by other authors (Chong *et al.*, 2008) for colloidal silica fouling, where they account the observation due to a suppression of the electrostatic double layer repulsion at higher ionic strength.

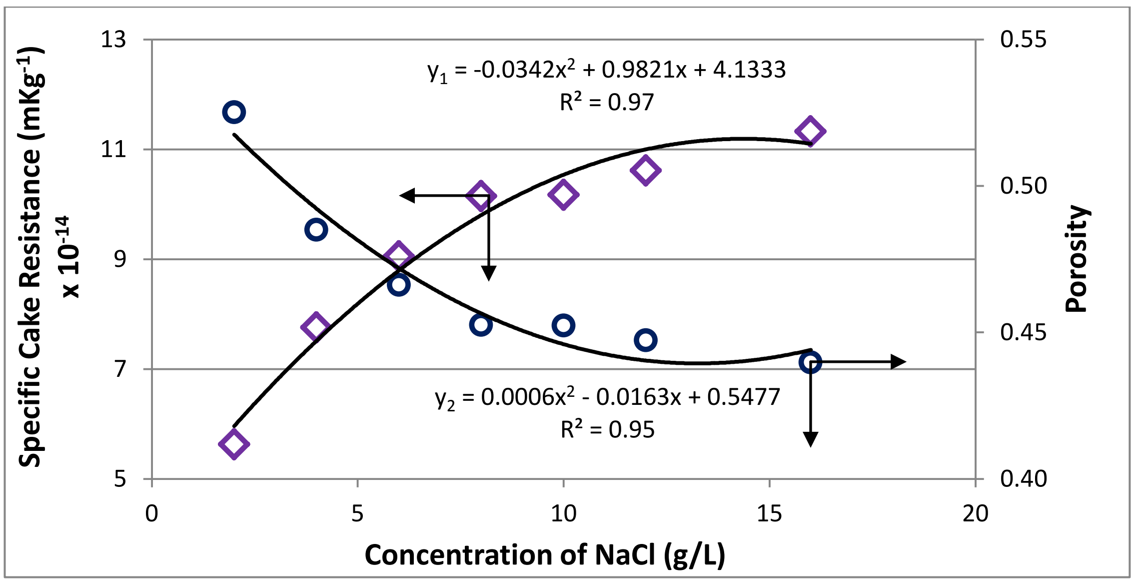

Figure 7.3: Specific cake resistance and cake porosity for an aqueous solution containing different concentrations of sodium chloride and 0.2 g/L of silica for a constant flux in dead-end filtration mode (where y_1 = specific cake resistance, y_2 = porosity, and x = concentration of sodium chloride).

The formation of a cake layer on the membrane surface can hinder the back diffusion of the salt to the bulk solution as highlighted in the cake enhanced osmotic pressure (CEOP) phenomenon described in section 2.1.3.1 of Chapter 2. In the operation of high pressure RO systems, this can cause the TMP to increase dramatically. On the other hand, low pressure UF systems do not retain salts where the salinity difference between the operation of UF and RO systems needs to be accounted for during fouling prediction. Therefore, the specific cake resistance at different salinities needs to be normalized with the specific cake resistance at the reference salinity of 2 g/L of sodium chloride, α_0. Figure 7.4 plots the trend of the normalized specific cake resistance as a function of concentration polarization in dead-end filtration mode under a constant flux for an aqueous solution containing 0.2 g/L of silica and 2 g/L of sodium chloride. Equation 8.1, which is the fitted trendline of the normalized specific cake resistance as a function of concentration polarization, can then be used to estimate the specific cake resistance in RO, α_{RO}, at any value of concentration polarization after obtaining the specific cake resistance determined from FFM measurements done using UF membranes.

$$\alpha_{RO} = \alpha_0 \times (-0.0243\mathrm{CP}^2 + 0.3446\mathrm{CP} + 0.7336) \tag{8.1}$$

The estimated cake-average porosity for RO can then be estimated from equation 3.19 from section 3.4.1.1 of Chapter 3. These results are used in section 7.4.3 to convert the FFM results to predict the RO fouling in terms of TMP profile.

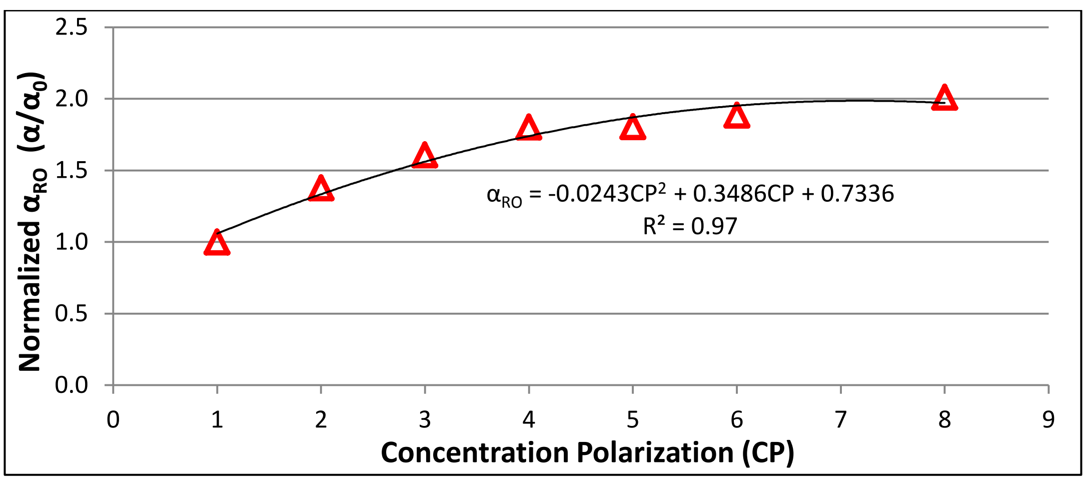

Figure 7.4: Correction factor for the specific cake resistance as a function of concentration polarization for an aqueous solution containing different concentrations of sodium chloride and 0.2 g/L of silica for a constant flux in dead-end filtration mode (Normalization uses α_0 at 2 g/L NaCl).

7.4.3 RO prediction experiments

Figure 7.5 shows the experimentally determined specific cake resistance and cake porosity as a function of constant net flux for the FFM experiments run at a crossflow velocity of 0.1 m/s for an aqueous solution containing 0.2 g/L of silica and 2 g/L of sodium chloride to investigate the effect of applied flux on the cake properties. It can be noted that the cake-average porosities of the FFM experiments are found using Equations 3.17 and 3.19, respectively, in section 3.4.1 and Section 3.4.1.1 of Chapter 3. Figure 7.5 indicates that with increasing net flux, the specific cake resistance increases while the cake-average porosity decrease. These trends are expected as earlier observed in sections 5.6.1 and 5.6.3 of Chapter 5 where higher fluxes can produce denser cake structures. The specific cake resistances found using the FFM results are then modified by Equation 8.1 that accounts for the changes in salinity on cake structures for RO membranes before being used to predict RO fouling potential performance later in this section.

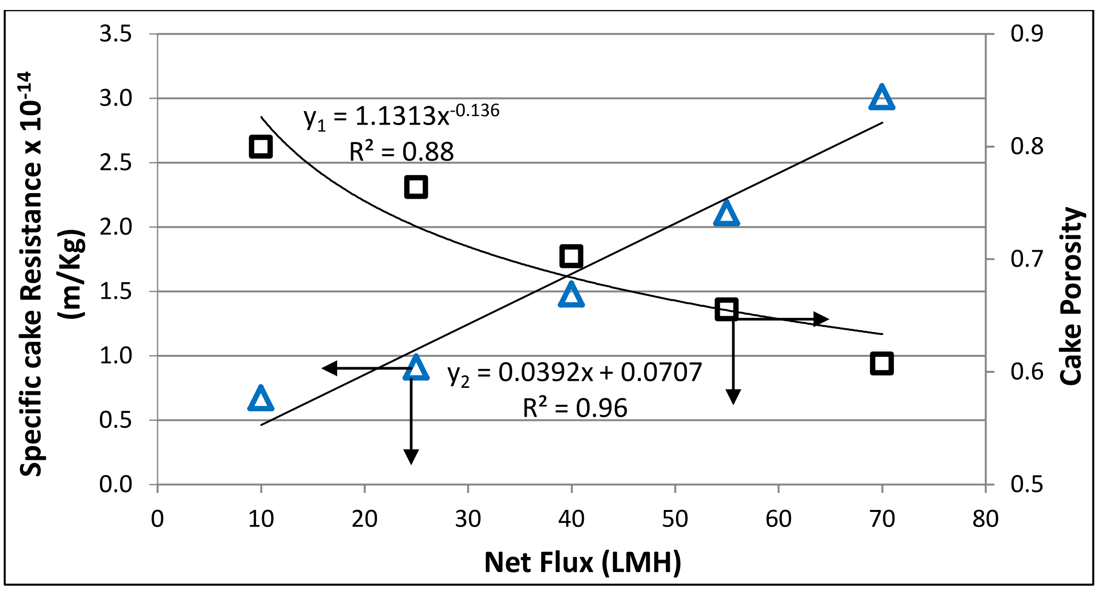

Figure 7.5: Specific cake resistances and porosities as a function of constant net flux for the FFM experiments ran at a crossflow velocity of 0.1 m/s for an aqueous solution containing 0.2 g/L of silica and 2 g/L of sodium chloride (where y_1 = porosity, y_2 = specific cake resistance, and x = net flux).

The other important parameter to predict the CEOP phenomenon other than the porosity of the cake is the cake thickness. Figure 7.6 is a plot of the cake layer thickness measured by UTDR as a function of time during the RO experiments run at different constant fluxes under a crossflow velocity of 0.1m/s for an aqueous solution containing 0.2 g/L of silica and 2 g/L of sodium chloride. Figure 7.6 shows the increasing constant rate of cake layer growth as flux increases. This trend is expected as there will be more deposition of particles under higher drag forces when the flux increases from 30 L/m^{2}h to 48.1 L/m^{2}h that corresponds to net fluxes of 10 L/m^{2}h to 28 L/m^{2}h, respectively, based on the critical flux of 20 L/m^{2}h for RO experiments. These rates of cake layer growth are then used with the revised specific cake resistances and porosities found using the FFM and dead-end experiments to predict the TMP profile trend from the silica fouling of the RO membranes as illustrated by Figure 7.1.

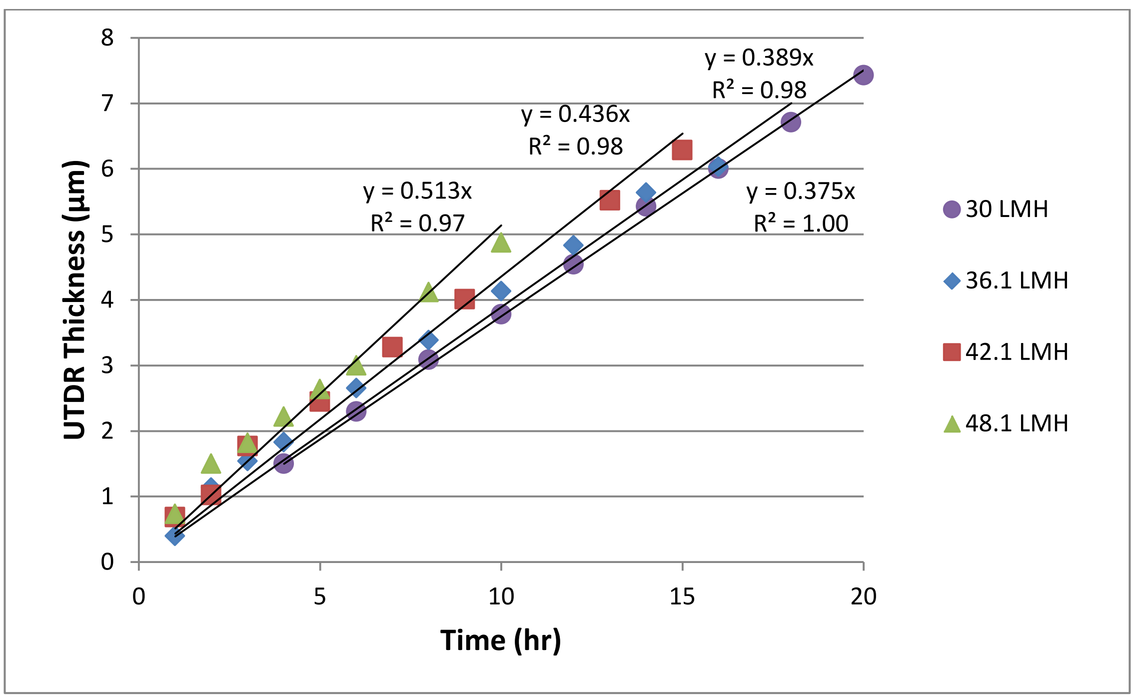

Figure 7.6: UTDR measured thickness as a function of time for the RO experiments ran at different constant fluxes at a crossflow velocity of 0.1 m/s for an aqueous solution containing 0.2 g/L of silica and 2 g/L of sodium chloride (where y = cake layer growth and x = time).

Figure 7.7 shows both the actual experimental and predicted TMP as a function of time for the RO experiments run under different constant fluxes at a crossflow velocity of 0.1 m/s for an aqueous solution containing 0.2 g/L of silica and 2 g/L of sodium chloride. It is clear from Figure 7.7 that the prediction from the combination of results from the FFM and UTDR measurements provides a good estimate of the actual experimental TMP profile for the colloidal fouling of the RO membrane over the range of constant fluxes used. The more rapid fouling rate as indicated by the faster increase in TMP profile for higher fluxes is consistent with observations reported in Chapter 5 for silica fouling due to the increase in particle deposition rate and denser cake structure.

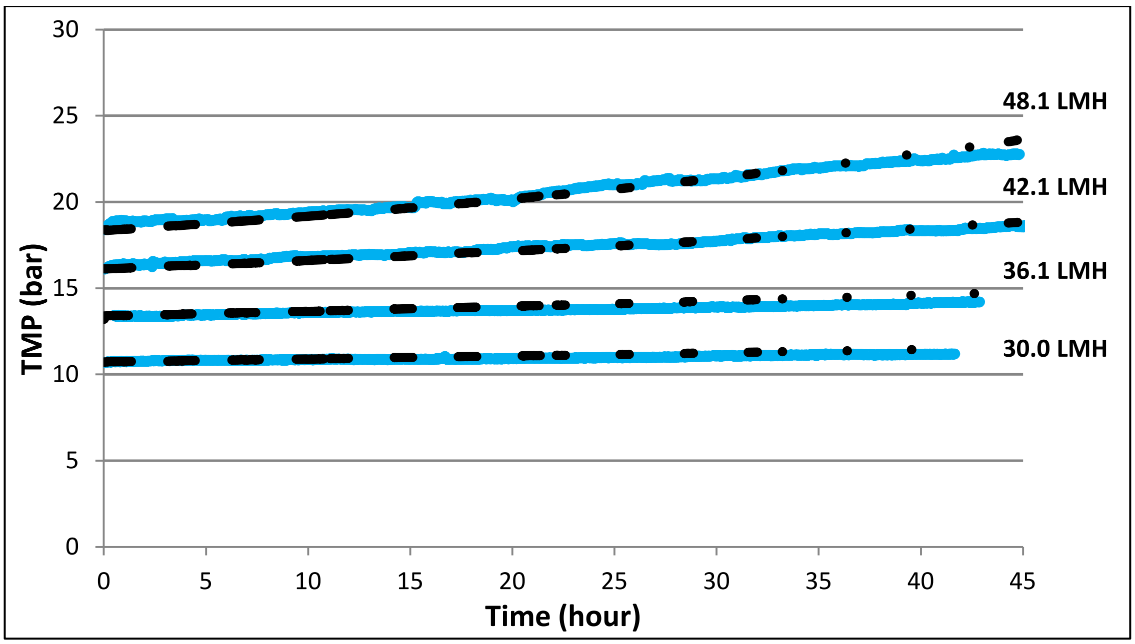

Figure 7.7: Actual experimental (continuous lines) and predicted (dotted lines) TMP profile as a function of time for the RO experiments ran at different constant fluxes at a crossflow velocity of 0.1 m/s for an aqueous solution containing 0.2 g/L of silica and 2 g/L of sodium chloride.

Figure 7.8 shows the estimated relative contribution of the CEOP effect and hydraulic resistance of the cake layer to the overall increase in the TMP profile for the RO experiments run under different constant fluxes at a crossflow velocity of 0.1 m/s for an aqueous solution containing 0.2 g/L of silica and 2 g/L of sodium chloride. It can be observed that the contribution of the hydraulic resistance of the cake layer to the overall TMP profile is relatively small with increasing flux as compared to the CEOP effect. It can also be observed that the CEOP exponentially increases with increasing flux. The trend of the CEOP exponential dependence on flux as agrees with studies by others (Chong *et al.*, 2008). The exponential dependence on flux can be anticipated from Equation 2.7 that describes the CEOP in section 2.1.3.1,

$$CP = \exp(\frac{J_v}{k_{eff}}) \tag{2.7}$$

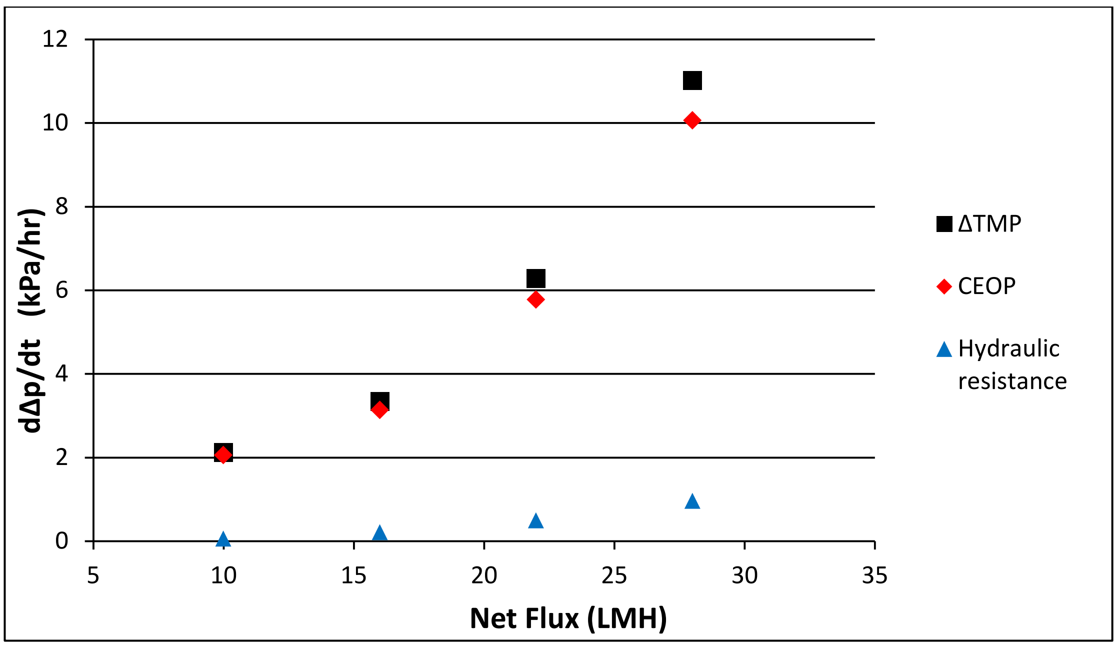

Figure 7.8: The estimated contributions of the hydraulic resistance of the cake layer and CEOP effect on the TMP rise for the predicted TMP profiles of the RO experiments run at different constant net fluxes at a crossflow velocity of 0.1 m/s for an aqueous solution containing 0.2 g/L of silica and 2 g/L of sodium chloride.

7.5 Concluding Remarks

To predict accurately the RO fouling phenomenon, both the CEOP effect and the hydraulic resistance from the cake layer needs to be estimated. In this study, they have been measured using a combination of FFM and UTDR that measures the specific cake resistance and cake layer thickness, respectively. Moreover, the difference in salinity environment between the FFM and RO experiments caused by the retention of the salt by the RO membranes has been accounted for where higher salinity increases the specific cake resistance and decreases the cake-average porosity. This has been done using the dead-end experiments to adjust the specific cake resistances measured directly from the FFM experiments so that they can be used to estimate the specific cake resistances for the RO experiments.

In addition, this chapter has shown that the CEOP effect is more significant than the hydraulic resistance of the cake layer in the overall TMP rise of the RO membranes fouled by colloidal silica. It is noted that such a monitoring and prediction approach to real world applications may be challenging due to the inherent mixtures and sizes of real world foulants. However, this could be overcome by using a modified model that assumes an effective foulant size, which remains an area of further study.

CHAPTER 8 : CANARY CELL VERSUS SWM

8.1 Abstract

Development of a side-stream cell to simulate a spiral wound module (SWM) called the 'canary cell' has been performed using a thin film polyamide composite reverse osmosis membrane. Representative fouling rate and ex-situ membrane autopsies have shown the capability of the canary cell to simulate the SWM under controlled hydrodynamics and flux conditions. The development of a dimensionless calibration curve allows the canary cell to act as an early warning system with respect to the SWM. The rate of cake thickness increase was also monitored by UTDR coupled to the canary cell and used to monitor membrane fouling and cleaning.

8.2 Introduction

Once the RO process is in operation, there are two avenues to pre-empt fouling problems. Firstly, the fouling propensity of the water can be measured and allowed for. The most commonly used technique for this, Silt Density Index (SDI), is empirical and potentially unreliable (Schippers and Verdouw, 1980, Lipp *et al.*, 1990; Yiantsios and Karabelas, 2002; Boerlage *et al.*, 2003). The other approach is through more sensitive monitoring of the 'state of the process' using fouling monitor(s) on a side-stream cell simulating the RO elements in the main plant. This could have benefits compared to measurements of pressures and flows on the main plant that may fail to detect incipient fouling (Moody, 1983) since they are integral measurements over the whole system. Typically, production parameters such as overall pressure drop or flux decline and product quality are used as indicators of fouling. Together with destructive membrane autopsies, these indicators are used as diagnostic tools for fouling (Vrouwenvelder *et al.*, 2006b). Using biofouling as an illustration, this is the most expensive way to monitor fouling (Flemming *et al.*, 1996) as by the time, (bio)fouling is detected, it is in a very late phase (Flemming *et al.*, 1998). It would save much time, material and money to know much earlier the development and extent of (bio)fouling and to design anti-fouling measures (Flemming, 2003). There is a need for better tools and measurements for an early warning system where microscopic observations of the fouling affecting membrane processes can be monitored in-situ, in real-time and non-destructively that can subsequently allow specific countermeasures (Flemming *et al.*, 1998; Flemming, 2003). It is estimated that the global overall costs for biofilms caused by downtime in desalination is significantly high (Flemming, 2011a). For example, the potential annual savings for an early warning of biofouling on an average 10,000 m^3/d seawater RO plant are estimated to be about 2 million dollars (Vrouwenvelder *et al.*, 2011).

The focus of this chapter is to monitor the stages of the fouling process on a side stream using a 'canary cell' to act as a fouling monitor that incorporates non-invasive detection. The term 'canary' is derived from the canaries taken by miners into coal mines to warn of dangerous gases. The canary cell needs to be representative of a spiral wound RO module in terms of materials, spatial dimensions, and hydraulics. It should be further characterized in terms of its accuracy and reproducibility under different conditions that simulate the operating conditions at different locations of the spiral wound RO elements in a train in order to function as an early warning system. With the integration of non-invasive ultrasonic time domain reflectometry (UTDR), the canary cell also has the capability to monitor fouling in-situ, real-time and non-destructively.

This chapter is organized as follows. Section 8.2 provides the experimental procedure for the experiments. The results are presented and discussed in section 8.3. The conclusions are summarized in section 8.4.

8.2 Experimental Procedure

For all experiments, the membranes in the canary cell and the SWM were first compressed at a minimum flux of approximately 50 L/m^2h overnight with Milli-Q water until a stable flux was achieved. The flux then was set to the desired value and allowed to stabilize before adding the filtered salt solution. 200 g/L of sodium chloride solution was added into the feed tank to reach 2 g/L of sodium chloride and the system was mixed for 2 hours. There were three main types of experiments; calibration, correlation and flushing experiments. The calibration experiments were done to obtain a calibration curve based on the normalized fouling rate of the TMP rise in order to predict how the canary cell would respond relative to the SWM at different hydrodynamic conditions, i.e., the amount of TMP rise of the canary cell relative to the SWM at different Reynolds Number. The Reynolds Number (Re) for the canary cell and the SWM can be calculated using Equations 3.30 and 3.31, respectively, in section 3.4.1.2 of Chapter 3. The correlation experiments were performed by running the canary cell and the SWM under the same hydrodynamic conditions to obtain similar fouling rate and state through the TMP rise and the ex-situ membrane autopsies, respectively. Moreover, monitoring of the fouling state was complemented with the non-invasive UTDR for in-situ, real-time and non-destructive observations for some of the conditions.

Equally important is the capability of the canary cell to correlate to the SWM in terms of fouling state to indicate the removal of the foulant layer during membrane cleaning. In this study, this is known as the flushing procedure since it only removes the liable upper foulant layer and leaves behind the aggregated foulant layer affected by colloidal metastability (see Chapter 5). Similar to the correlation experiments, monitoring of the fouling state during the flushing procedure was also be complemented with the non-invasive UTDR and ex-situ membrane autopsies to indicate the final fouling state of the canary cell and the SWM. Although prior studies have shown the capability of a crossflow filtration model coupled with the non-invasive UTDR technique to monitor a similar flushing procedure (Sim *et al.*, 2012a; Sim *et al.*, 2013b), they were performed without the presence of a feed spacer. Unfortunately, it is beyond the scope of the thesis to optimize the cleaning frequency and method(s). This could be developed in future studies to evaluate the positive impact(s) of an optimized membrane cleaning method(s) on the life of the installed membranes, the reduction of chemical, electrical and membrane-replacement costs (Poppe, 2012).

8.2.1 Calibration Experiments

To test the robustness of the calibration experiments, three sets of experiments at various average crossflow velocities were performed using only the canary cell to obtain the normalized dimensionless calibration curve, dTMP/dt*. The normalization is performed with respect to the fouling rate, dTMP/dt, at the lowest average crossflow velocity of 0.10 m/s (Re=81.2) for the three different conditions. The three different sets of experiments were:

(i) Experiments were performed for an aqueous solution containing 2 g/L of sodium chloride and 0.8 g/L of silica at a constant flux of 35 L/m^2h under average crossflow velocities of 0.10, 0.13, 0.17, 0.20 and 0.22 m/s that corresponded to Reynolds Number of 81.2, 105.6, 138.0, 162.4, and 178.7, respectively.

(ii) Experiments were performed for an aqueous solution containing 2 g/L of sodium chloride and 0.8 g/L of silica at a constant flux of 30 L/m^2h under average crossflow velocities of 0.10, 0.13, and 0.17 m/s that corresponded to Reynolds Number of 81.2, 105.6, and 138.0, respectively.

(iii) Experiments were performed for an aqueous solution containing 2 g/L of sodium chloride and 0.4 g/L of silica at a constant flux of 35 L/m^2h under average crossflow velocities of 0.10, 0.13, and 0.20 m/s that corresponded to Reynolds Number of 81.2, 105.6, and 162.4, respectively.

8.2.2 Correlation Experiments

Two different experiments were performed for an aqueous solution containing 2 g/L of sodium chloride and 0.4 g/L of silica with both the canary cell and the SWM at the same constant flux of 35 L/m^2h under average crossflow velocities of 0.13, 0.17 and 0.20 m/s that corresponded to Reynolds Number of 105.6, 138.0, and 162.4, respectively. The ex-situ membrane autopsies were done for the experiment run under the average crossflow velocity of 0.20 m/s (Re=162.4) while UTDR monitoring was done for the experiments run under average crossflow velocities of 0.17 (Re=138.0) and 0.20 m/s (Re=162.4). A separate experiment was intentionally performed with both the canary cell and the SWM under different average crossflow velocities for an aqueous solution containing 2 g/L of sodium chloride and 0.4 g/L of silica to observe the accuracy of the calibration curve obtained in section 8.3.1 to predict how the canary cell would respond relative to the SWM at different hydrodynamic conditions, i.e., amount of TMP rise of the canary cell relative to the SWM at various time durations.

8.2.3 Flushing Experiments

The flushing procedure was carried by first fouling both the canary cell and the SWM with an aqueous solution containing 2 g/L of sodium chloride and 0.4 g/L of silica under an average crossflow velocity of 0.17 m/s (Re=138.0) followed by the introduction of a foulant-free solution. Membrane fouling was allowed to proceed for 4 hours after which the feed solution was replaced with a fresh solution of the same sodium chloride concentration but without the silica foulant for another 2 hours under the same initial conditions of flux and average crossflow velocity. The duration of the fouling and flushing procedure were selected based on prior studies done on colloidal silica metastability in Chapter 5. The consideration was to have sufficient aggregated silica foulant on the membrane for ex-situ membrane autopies while allowing appropriate removal of the liable upper foulant layer detectable by UTDR.

8.3 Experimental Results

This section summarizes and discusses representative results and observed trends for the calibration, correlation and flushing experiments with UTDR measurements, and the ex-situ membrane autopies.

8.3.1 Calibration Experiments

Figures 8.1 and 8.2 show plots of the fouling rate, dTMP/dt, and the noramlized dimensionless calibration curve, dTMP/dt*, respectively, as a function of Reynolds Number for the canary cell at a constant flux of 35 L/m^2h for an aqueous solution containing 2 g/L of sodium chloride and 0.8 g/L of silica, an aqueous solution containing 2 g/L of sodium chloride and 0.4 g/L of silica, and at a constant flux of 30 L/m^2h for an aqueous solution containing 2 g/L of sodium chloride and 0.8 g/L of silica. Increases in the Reynolds Number decreased both the dTMP/dt and dTMP/dt* as the greater hydrodynamic effect increases the mass transfer coefficient and reduces fouling. dTMP/dt decreased at lower flux and silica concentration as such conditions reduce fouling. Interestingly, the normalization for each different sets of conditions collapsed to form the same calibration curve, dTMP/dt*. This suggests that over the range of feed conditions the fouling mechanisms are similar that resulted in similar trends of fouling rate.

Prior works have found the main bulk (90% and greater) of the fouling rate has been attributed to the cake enhanced osmotic pressure phenomenon (Taheri *et al.*, 2013). As the average porosity of the silica foulant layer is also found to be relatively independent of crossflow velocities as found in section 5.6.1 of Chapter 5, it is expected the Schmidt Numbers for the ionic solutes (sodium and chloride ions) should remain the same under different average crossflow velocities for each set of experiments. Therefore, the feasibility of the dTMP/dt* calibration curve can be expected at least for a specified mono-dispersed foulant.

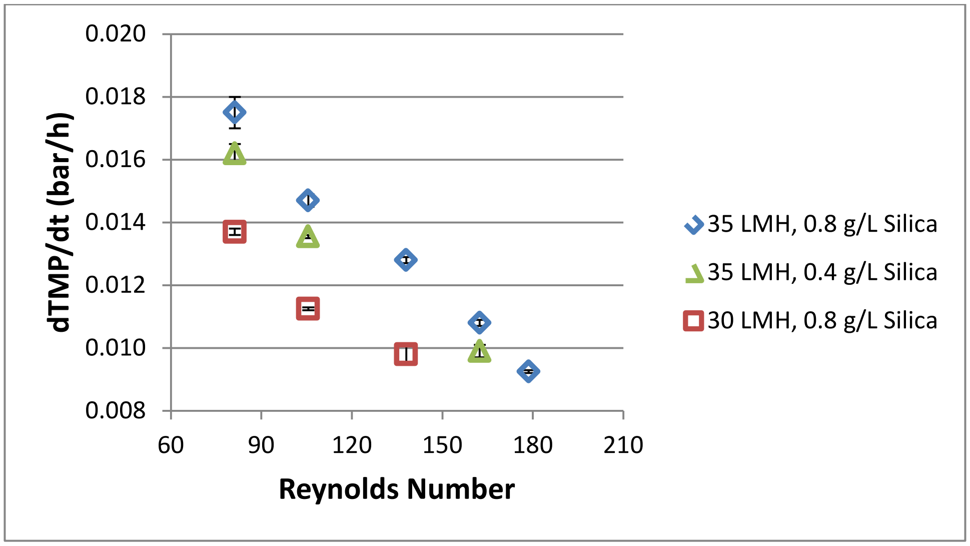

Figure 8.1: Fouling rate, dTMP/dt, of the canary cell as a function of Reynolds Number at a constant flux of 35 L/m^{2}h for an aqueous solution containing 2 g/L of sodium chloride and 0.8 g/L of silica, an aqueous solution containing 2 g/L of sodium chloride and 0.4 g/L of silica, and at a constant flux of 30 L/m^{2}h for an aqueous solution containing 2 g/L of sodium chloride and 0.8 g/L of silica.

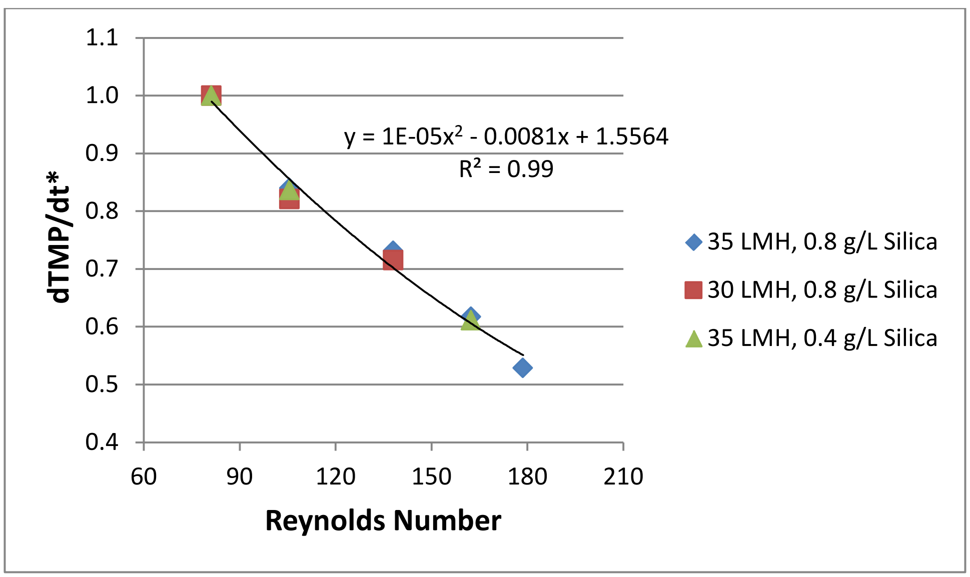

Figure 8.2: Normalized dimensionless calibration curve, dTMP/dt, as a function of Reynolds Number for the canary cell at a constant flux of 35 L/m^{2}h for an aqueous solution containing 2 g/L of sodium chloride and 0.8 g/L of silica, an aqueous solution containing 2 g/L of sodium chloride and 0.4 g/L of silica, and at a constant flux of 30 L/m^{2}h for an aqueous solution containing 2 g/L of sodium chloride and 0.8 g/L of silica (y = dTMP/dt*, x = Reynolds Number). Normalizatin relative to the dTMP/dt at the lowest Re number for each flux and feed combination.

8.3.2 Correlation Experiments

Figure 8.3 show plots of the TMP rise, TMP-TMP_0, as a function of time for the canary cell and the SWM run at a constant flux of 35 L/m^2h under average crossflow velocitites of 0.13 and 0.20 m/s that corresponded to Reynolds Number of 105.6 and 162.4, respectively, for an aqueous solution containing 2 g/L of sodium chloride and 0.4 g/L of silica. Figure 8.4 shows similar plots for average crossflow velocitites of 0.13 and 0.17 m/s that corresponded to Reynolds Number of 105.6 and 138.0, respectively. Figures 8.3 and 8.4 showed that the canary cell is representative of the SWM in terms of fouling rate when run at similar hydrodynamic conditions. Running under lower average crossflow velocities would result in lower mass transfer and faster rate of TMP rise due to higher fouling rates. The similar deposited foulant concentration in both the canary cell and the SWM complements the representative fouling rate in terms of fouling state. Non-invasive monitoring of the fouling state in-situ, real-time and non-destructively was also performed with UTDR with the canary cell run at similar Reynolds Number. The foulant layer growth rates were 1.10 μm/h (R^2=0.98) and 0.45 μm/h (R^2=0.99) for the canary cell run at a constant flux of 35 L/m^2h under average crossflow velocitites of 0.17 and 0.20 m/s, corresponding to Reynolds Number of 138.0 and 162.4, respectively, for an aqueous solution containing 2 g/L of sodium chloride and 0.4 g/L of silica. A detailed analysis of the UTDR waveform in response to the canary cell's dimensions can be found in Section 4.2.3 of Chapter 4.

Table 8.1 summarizes the experimental ratio of the canary cell TMP rise and the SWM TMP rise taken at different time durations and the predicted ratio of the dTMP/dt* obtained from the calibration curve in Figure 8.2 based on the representative Reynolds Number for the various experiments; the canary cell and the SWM were run under average crossflow velocities of 0.13, 0.17 and 0.20 m/s at a constant flux of 35 L/m^2h for an aqueous solution containing 2 g/L of sodium chloride and 0.4 g/L of silica as represented by Figures 8.3 and 8.4. It is clear from the experimental and predicted ratios, that the calibration curve can be used to predict reasonably accurately how the canary cell would respond relative to the SWM at different hydrodynamic conditions, i.e., the amount of TMP rise of the canary cell relative to the SWM at various time durations. It is clear from Table 8.1 and Figure 8.4, that the calibration curve could be used even when the canary cell and SWM were ran at different hydrodynamic conditions.

Table 8.2 shows the distribution of the deposited foulant concentration in the SWM, and the canary cell when both were run under an average crossflow velocity of 0.20 m/s (Re=162.4) at a constant flux of 35 L/m^2h for an aqueous solution containing 2 g/L of sodium chloride and 0.4 g/L of silica. Figure 8.5 shows graphical representative of (a) the distribution of the deposited foulant concentration in the SWM, and (b) the deposited foulant concentration in the canary cell obtained from Table 8.2. From Figure 8.5, the foulant maldistribution in the SWM along the membrane length and width was also anticipated as studies have shown such a distribution to be typical of the SWM due to flux and crossflow velocity distributions along the membrane length and width (Schwinge *et al.*, 2002; Schwinge *et al.*, 2004; Alexandis *et al.*, 2007). As depicted in Figure 8.5, the foulant deposition would tend to decrease from the inlet as depicted by Region 1 to the outlet as depicted by Region 9 and from the side close to the permeate collector tube to the closed end of the permeate channel as depicted by Regions 1 to 3, 4 to 6, and 7 to 9. It should be noted that this concept is different from the fouling creep phenomenon described by other authors (Chen *et al.*, 2004a; Hoek *et al.*, 2008) where the first few SWM elements of a RO train or stage initially fouls followed by a shift to the relatively less fouled regions along the length of the train or stage to compensate for the loss of upstream permeability. Similarly if a single SWM element is fouled sufficiently long, the distribution on the leaf can also shift over time as the flux goes to the least fouled regions. The focus is to get the canary cell to simulate the same fouling rate as the SWM, and this has been shown in Figure 8.3. Moreover, the similar amount of foulant deposition in both the canary cell and the SWM as depicted in Figure 8.5

futher supports the capability of the canary cell to simulate the SWM at similar hydrodynamics and flux conditions.

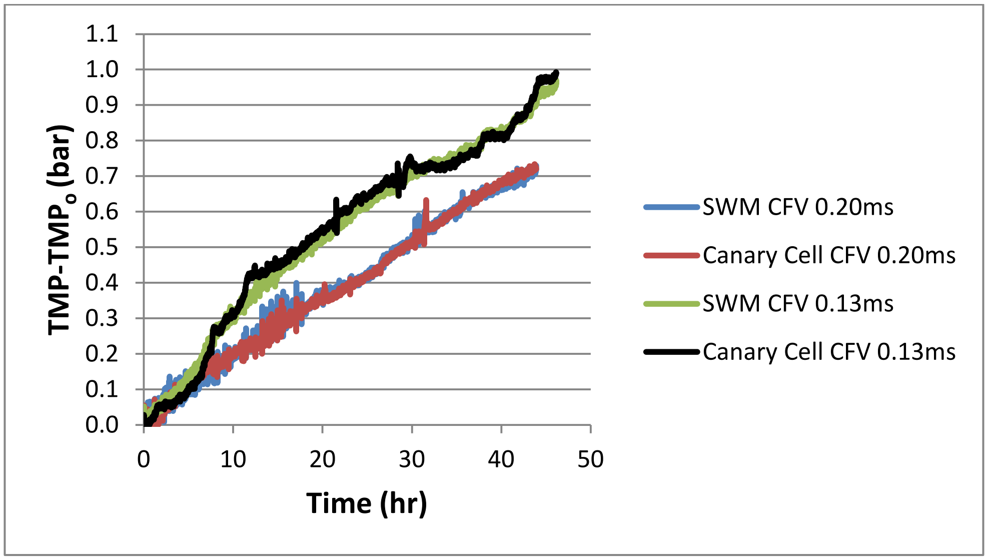

Figure 8.3: TMP-TMP$_0$ as a function of time for both the canary cell and SWM ran at a constant flux of 35 L/m^{2}h under average crossflow velocities 0.13 and 0.20 m/s that corresponds to Reynolds Number of 105.6 and 162.4, respectively, for an aqueous solution containing 2 g/L of sodium chloride and 0.4 g/L of silica.

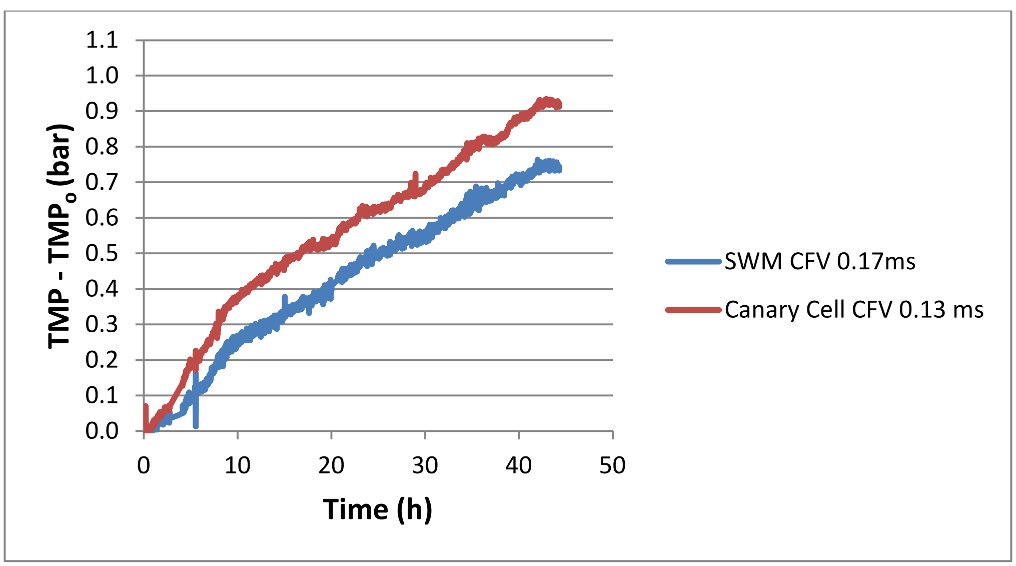

Figure 8.4: TMP-TMP$_0$ as a function of time for the canary cell and SWM ran at a constant flux of 35 L/m^{2}h under average crossflow velocities 0.13 and 0.17 m/s, that corresponds to Reynolds Number of 105.6 and 138.0, respectively, for an aqueous solution containing 2 g/L of sodium chloride and 0.4 g/L of silica.

Table 8.1: Experimental and Predicted Ratios of the TMP rise of the canary cell relative to the SWM based on different time durations and the calibration curve in Section 4.1, ran at a constant flux of 35 LMH under average crossflow velocities of 0.13, 0.17 and 0.20 m/s that corresponds to Reynolds Number of 105.6, 138.0, 162.4, respectively, for an aqueous solution containing 2 g/L of sodium chloride and 0.4 g/L of silica.

			Experimental				Predicted	
		Reynolds Number	$TMP-TMP_o$ at t= 20 h	$TMP-TMP_o$ at t= 30 h	$TMP-TMP_o$ at t= 40 h	Ratio (Canary Cell/SWM)	dTMP/dt*	Ratio
Figure 8.3	**Canary Cell**	105.6	0.55	0.71	0.81	1.40 (±0.14)	0.86	1.41
	SWM	162.4	0.35	0.51	0.66		0.61	
Figure 8.4	**Canary Cell**	105.6	0.53	0.68	0.88	1.26 (±0.03)	0.86	1.22
	SWM	138.0	0.41	0.56	0.70		0.70	

Table 8.2: Distribution of the foulant concentration in the SWM, and in the canary cell when both were run under an average crossflow velocity of 0.20 m/s (Re=162.4) at a constant flux of 35 L/m^2h for an aqueous solution containing 2 g/L of sodium chloride and 0.4 g/L of silica.

	Foulant Concentration ($\mu g/cm^2$)		Foulant Concentration ($\mu g/cm^2$)
Region 1	46.577 (±3.931)	**Region 6**	43.261 (±1.701)
Region 2	45.324 (±5.756)	**Region 7**	43.472 (±5.294)
Region 3	44.461 (±3.566)	**Region 8**	42.997 (±2.204)
Region 4	45.321 (±1.617)	**Region 9**	42.501 (±3.951)
Region 5	44.410 (±1.050)	**Canary Cell**	44.258 (±2.464)

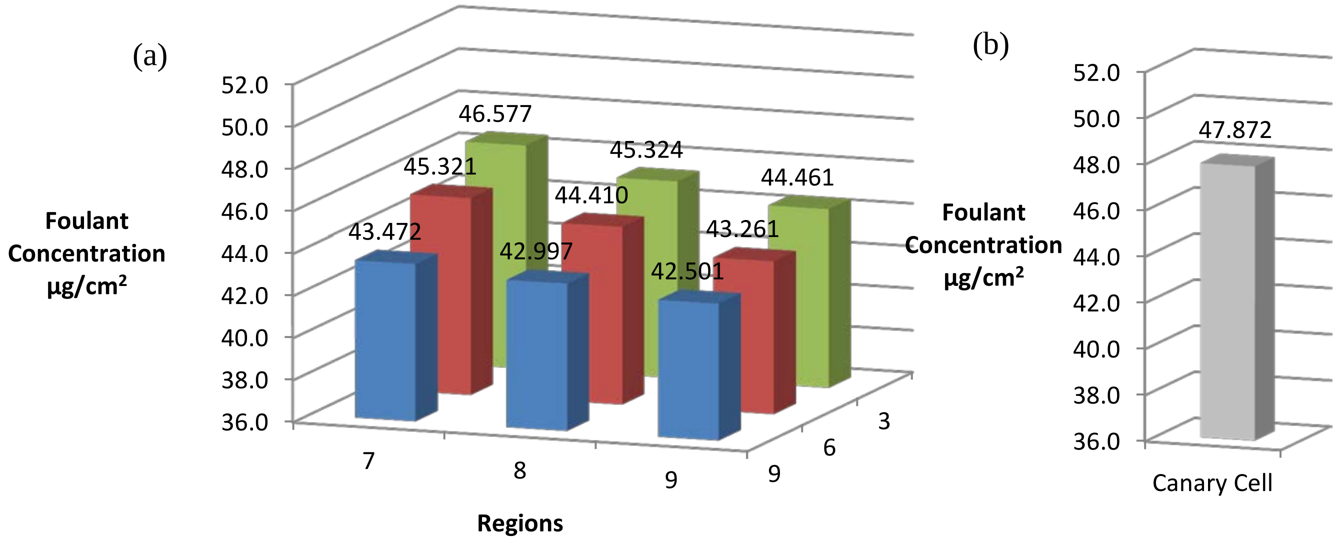

Figure 8.5 (a) Distribution of the foulant concentration in the SWM, and (b) the foulant concentration in the canary cell when both were run under an average crossflow velocity of 0.20 m/s (Re=162.4) at a constant flux of 35 L/m^{2}h for an aqueous solution containing 2 g/L of sodium chloride and 0.4 g/L of silica.

8.3.3 Flushing Experiments

Figure 8.6 shows the plots of the amplitude of the acoustic wave response in volts for peaks A and B of interest as a function of the arrival time in microseconds: (i) peaks A and B of interest and (ii) enlarged region for peak A for the canary cell ran at a constant flux of 35 L/m^{2}h under an average crossflow velocity of 0.17 m/s (Re=138.0) for an aqueous solution containing 2 g/L of sodium chloride and 0.4 g/L of silica for 4 hours. The feed was then replaced with a silica-free solution under the same condition of flux and average crossflow velocity for a further 2 hours. Table 8.3 shows the distribution of the deposited foulant concentration in the SWM, and the canary cell for the conditions of Figure 8.6. Figure 8.7 shows graphical representative of (a) the distribution of the deposited foulant concentration in the SWM, and (b) the deposited foulant concentration in the canary cell obtained from Table 8.3. It is clear from Figure 8.6 that the non-invasive technique of UTDR can observe both the growth and removal of the foulant layer. The decrement of 7 ns in the arrival time of Peak A corresponds to a foulant layer thickness of 5.25 μm ($\pm$0.38 μm) after 4 hours of fouling that is close to the growth rate of 1.10 μm/h as reported earlier in section 8.3.2 when both the canary cell and SWM were run under the same conditions. During the flushing procedure, there is an increment of 4 ns in the arrival time of Peak A that corresponds to a removal of around 3.00 μm (± 0.38 μm) and a remaining foulant layer thickness of 2.25 μm (± 0.38 μm). The remaining foulant layer thickness is consistent with the results in Section 5.4.3 of Chapter 5 that showed a minimal foulant layer thickness of approximately 4 μm or less during the onset of metastability (Sim *et al.*, 2012a). In this experiment, the onset of metastability was estimated for the given salinity, flux and crossflow velocity conditions to be around 4 hours or greater based on the work done in sections 5.6.1 to 5.6.3. In addition, the similar deposited foulant concentration in both the canary cell and the SWM in Figure 8.7 illustrates the representative fouling state of the canary cell relative to the SWM. It should be noted that the foulant maldistribution of the SWM in Figure 8.7 is less distinct than in Figure 8.5, which is expected since the fouling time duration was much shorter and lessen the influence of the hydrodynamic factors affecting the onset of metastability across the module length and width. The lower crossflow velocity (0.17 m/s versus 0.20 m/s) would also tend to have less foulant distribution.

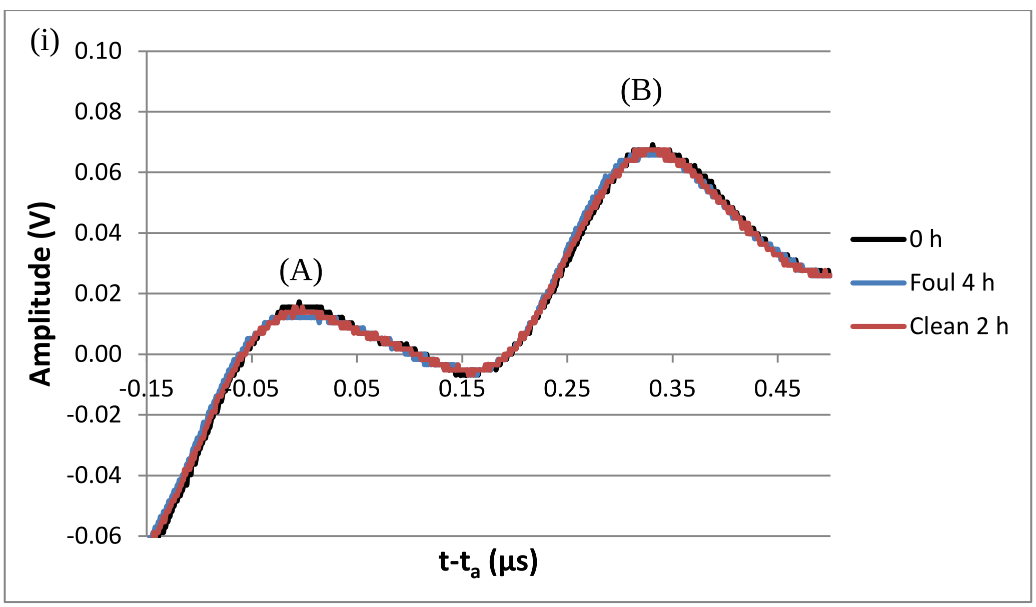

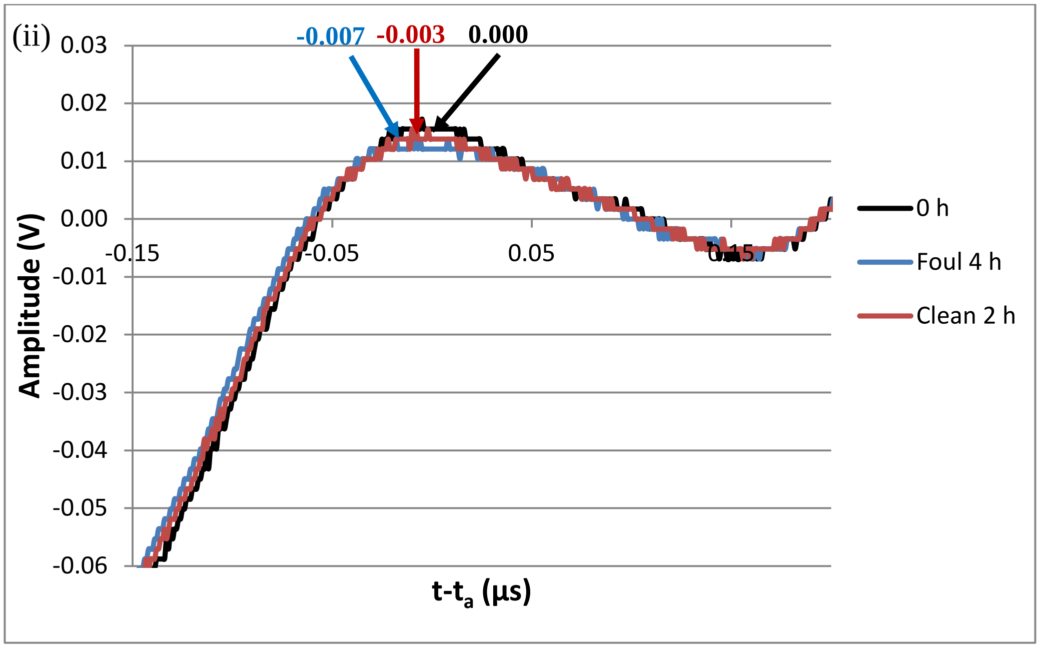

Figure 8.6: Peak Amplitude versus $t-t_a$, the difference in the arrival time, t, with respect to the arrival time of peak A, t_a, for an aqueous solution containing 2 g/L of sodium chloride and 0.4 g/L of silica at a constant flux of 35 L/m^{2}h under an average crossflow velocity of 0.17 m/s (Re=138.0) for contact times of 0 hour, fouling = 4 hour and flushing = 2 hour: (i) peaks A and B of interest and (ii) enlarged region of peak A. Peak A corresponds to the membrane (time = 0 hr) of the difference in the arrival time = 0.000 µs, and foulant layer surface/feed solution interfaces (fouling = 4 hrs and flushing = 2 hrs) of the difference in the arrival time = -0.003 and -0.007 µs.

Table 8.3: Distribution of the foulant concentration in the SWM, and in the canary cell after the flushing experiment ran under an average crossflow velocities 0.17 m/s (Re=138.0) at a constant flux of 35 L/m^{2}h for an aqueous solution containing 2 g/L of sodium chloride.

	Foulant Concentration (µg/cm^2)		Foulant Concentration (µg/cm^2)
Region 1	18.154 (±1.938)	**Region 6**	17.765 (±1.311)
Region 2	17.986 (±1.745)	**Region 7**	17.649 (±1.287)
Region 3	17.790 (±0.334)	**Region 8**	17.540 (±1.103)
Region 4	17.788 (±0.020)	**Region 9**	17.313 (±1.054)
Region 5	17.777 (±1.883)	**Canary Cell**	17.751 (±0.476)

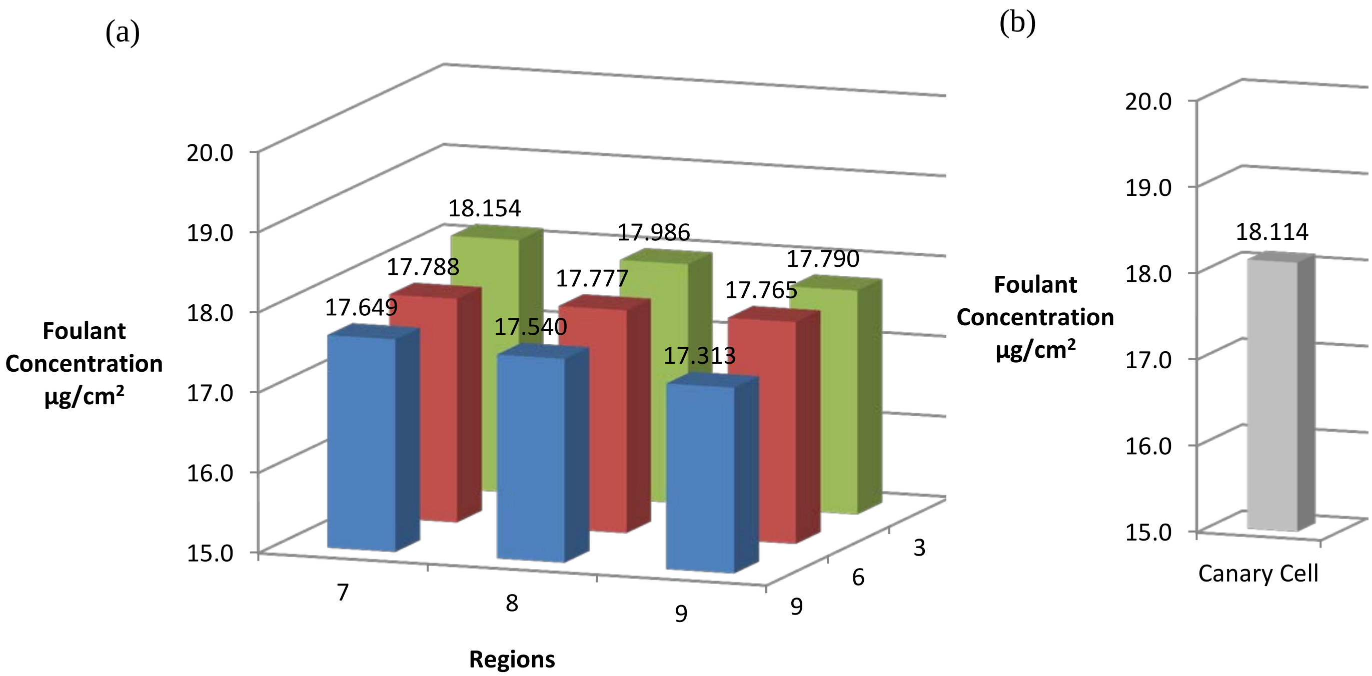

Figure 8.7: (a) Distribution of the foulant concentration in the SWM, and (b) the foulant concentration in the canary cell after the flushing experiment ran under an average crossflow velocities 0.17 m/s (Re=138.0) at a constant flux of 35 L/m^2h for an aqueous solution containing 2 g/L of sodium chloride.

8.4 Concluding Remarks

This study establishes that the canary cell can be representative of a spiral-wound RO module in terms of materials, spatial dimensions and hydraulics. This is characterized in terms of its accuracy and reproducibility under simulated conditions that represent operating conditions influenced by different locations of spiral-wound RO elements in a RO train or stage. The establishment of a calibration curve gives the operator flexibility in determining the canary cell's response relative to the SWM at different hydrodynamic conditions and provides a controllable early warning system. When the canary cell is integrated with UTDR it is capable of monitoring the state of fouling quantitatively and allows in-situ, real-time, nondestructive observations.

CHAPTER 9 : FUTURE WORK

Before elaborating on what kind of future work could be done from this thesis, it would be useful to recap the objective of this thesis and summarize the work done in this thesis. The main objective was to utilize and optimize a UTDR sensor for monitoring the fouling state of the membrane process that provides signals for process control to reduce fouling in RO systems. The emphasis is on colloidal and biofouling monitoring. The UTDR sensor would be integrated into a ‘canary cell’, a side-stream cell simulating the flow within a spiral wound RO module, and act as an early detection fouling monitor system for incipient fouling.

Chapters 2 to 4 had shown what are required to understand the systematic steps in using the UTDR sensor to monitor the fouling state of the membrane process. Chapter 5 gave a fundamental study for the process control parameters behind the onset of metastability for colloidal silica. Chapter 6 resolved the limitation of UTDR to detect biofouling, which is a prevalent issue in RO plants. Chapter 7 extended the use of the UTDR sensor by combining it with the FFM monitor for the development of a new technique to predict progressive RO fouling through real-time estimation of the cake enhanced osmotic pressure effect and the hydraulic resistance of the foulant cake layer. Chapter 8 demonstrated the representative character of the canary cell for the SWM, the ability to provide as an early warning system, and the integration of the UTDR sensor with the canary cell to monitor RO fouling on a potential commercial scale. It is clear that the main objectives have been met but there are still further improvements for the technology developed in this thesis.

This chapter has two foci. Section 9.1 focuses on the potential improvement of the UTDR sensor while section 9.2 focuses on future work already highlighted on Chapters 5 to 7.

9.1 Future Development of Ultrasound Reflectometry

UTDR has been a useful technology for the study of membrane processes for more than a decade as highlighted in Section 2.4.2 of Chapter 2 but there is the ability to further analyze it in terms of other parameters such as looking at the changes in amplitudes or in the frequency domain, using Fourier transformation and wavelet decomposition. As shown in Section 5.4.2 of Chapter 5, the amplitude measurements can be an indication of the density of the media and that was used as one of the pieces of evidence for the onset of metastability. Studies by other authors have shown the capability of ultrasonic reflectometry to characterize the physical properties of various media from analyzing changes in the sound waves (Gómez Álvarez-Arenas et al., 2002; Guidarelli et al., 1998; Richter et al., 2006). Such studies have not been extended to membrane processes. Moreover, UTDR could be further applied to the field of measuring flow rates of gas or liquids using the technique of transit-time ultrasonic flowmeters, which works on the principle that the transit times for two parallel but contra-propagating sound waves to pass through the media are influenced by the flow rate of the media (Buess, 2004; Hemp, 1982).

9.2 Future Work on Metastability, Biofouling and RO Prediction

In Section 5.6.3 of Chapter 5, it was observed that the presence of metastable fluxes delayed significantly the onset of the metastability. The effect of these metastable fluxes suggests appropriate risk management between the needs for productivity and fouling control that has to be further studied. In Chapter 6, the residual silica detected in the biofilm indicates inhomogeneity of the biofilm that can be further used to study the morphology of the biofilm. However, this would also require future work in decyphering the mechanisms for the dispersion of the silica particles within the biofilm to understand how to utilize the residual silica entrapped within the biofilm in relationship to the biofilm's morphology. For the RO prediction using the combined sensors of UTDR and FFM in Chapter 7, it was highlighted that real world applications would be challenged by the mixtures of real world foulants of different sizes.

Therefore, a future model has to be developed that assumes an effective foulant size and its effectiveness evaluated when being applied to RO plants with real feeds. Resolving this model would likewise allow a similar prediction of biofouling and organic fouling in membrane processes. As plants typically run for months at a time, it would be useful to extend the RO prediction for a similar time frame. In addition, using a focused transducer with higher frequency would equip operators with sufficient sensitivity to resolve different fouling layers resulting from heterogeneous feeds. The ability to increased lateral resolution of transducers would also allow detection of fouling around membrane pores that would be important for early detection of fouling.

In summary, the findings in this dissertation showcased how non-invasive, in-situ and rigorous quantification of processes affecting membrane performance can lead to significant new findings. Combination of different sensors could lead to even more accurate predictions and better understanding of membrane performance as seen in the combination of UTDR and FFM in Chapter 7. The study of optical methods such as OptiQuad highlighted in the Special Appendix could further complement the usage of UTDR and FFM, leading to a greater understanding of fouling, which will continue to be the Achilles' heel of membrane performance.

APPENDIX

A.1 Critical Fluxes of Colloidal Silica under crossflow filtration

The critical flux was measured using the time-step method using 10-minute increments of 5 L/m^2h starting from 10 L/m^2h for a MWCO 30 kDa membrane (Pall, Omega). The flow channel dimensions were 0.18 m x 0.03 m x 1 mm. The conditions were (I) crossflow velocities of 0.08, 0.10, 0.13, 0.14, 0.15, and 0.20 m/s for an aqueous solution containing 2 g/L of sodium chloride and 0.4 g/L of silica, (II) 1, 2, 3, 4, 6, and 8 g/L of sodium chloride at a crossflow velocity of 0.10 m/s for an aqueous solution containing 0.4 g/L of silica, and (III) 0.2, 0.4, 0.8, 1.2, and 1.6 g/L of silica at a crossflow velocity of 0.13 m/s for an aqueous solution containing 2 g/L of sodium chloride.

Table A.1 summarizes the equations describing the correlation between the experimentally determined critical volumetric flux, J_{crit}, and x, the parameter varied, where x denotes either the crossflow velocity, sodium chloride (NaCl) concentration, or silica concentration. The critical fluxes decrease with increasing sodium chloride and silica concentrations but increase with increasing crossflow velocity. The exponent of 0.31 on the crossflow velocity is expected for laminar flow conditions.

Table A.1: Experimentally determined critical volumetric fluxes as a function of crossflow velocity, sodium chloride concentration, and silica concentration.

Conditions	**Varying Parameter, x**	Experimentally Determined Critical Flux (LMH), J_{crit}	Correlation
I	**Crossflow Velocity (m/s)**	$J_{crit} = 51.06x^{0.31}$	$R^2 = 1.00$
II	**NaCl Concentration (g/L)**	$J_{crit} = 27.632 - 1.2206x$	$R^2 = 1.00$
III	**Silica Concentration (g/L)**	$J_{crit} = 23.184 - 4.57\ln(x)$	$R^2 = 1.00$

To verify the trends in Table A.1, the critical volumetric flux, $J_{critical}$, can be estimated using Equation A.1 (Field *et al.*, 1995) to find the steady state volumetric flux, J_{SS}, based on the convective-diffusion phenomenon through the concentration polarization boundary layer (Porter, 1972; Suki *et al.*, 1986) and is given by

$$J_{SS} = k \ln \frac{C_g}{C_b} \tag{A.1}$$

where the mass-transfer coefficient, k, can be obtained from the Graetz-Lévêque equation for flat rectangular channels (Porter, 1972) and is defined by Equation A.2:

$$k = 0.816 \left(\frac{6QD_{eff}{}^{2}}{h^2 wL} \right)^{1/3} \tag{A.2}$$

The experimentally determined critical flux of 25 L/m^{2}h for an aqueous solution containing 2 g/L of sodium chloride, 0.4 g/L of silica at a crossflow velocity of 0.10 m/s was used as a reference value to determine the solute concentration of the cake or gel layer, C_g.

The trends of the experimentally determined critical volumetric flux with increasing crossflow velocities and silica concentration were expected based on the effects of these parameters on the mass transfer coefficient, k and the steady state volumetric flux, J_{ss} as shown by Equation A.2. A higher crossflow velocity increases the mass transfer coefficient that in turn increases the critical flux as has been reported in prior studies (Kim and Park, 2002; Li *et al.*, 1998; Li *et al.*, 2000). A higher silica concentration causes the critical flux to decrease as indicated by Equation A.1 and in Table A.1. The correlation between the critical volumetric flux, $J_{critical}$ and the crossflow velocity, v, found here, namely $J_{crit} \propto v^{0.31}$, differs from same prior studies for which a linear correlation was observed (Kim and Park, 2002; Li *et al.*, 1998). However, these were for supramicron particles that are not governed by Brownian diffusion. Other authors (Li *et al.*, 2003; Chong *et al.*, 2008) report that the critical flux for the sub-micron bacteria *Pseudomonas* SW8 and colloidal silica for a high pressure RO system was proportional to $v^{0.66}$ and $v^{0.4}$, respectively. It has been highlighted in a review paper that no common exponent for the power law can be deduced from the many studies dealing with the effect of crossflow velocity on the critical volumetric flux (Bacchin *et al.*, 2006). However, the trend of the experimentally determined critical volumetric flux with sodium chloride concentration was not expected. Since the concentration of the solute at the cake or gel layer, C_g, is assumed to be constant in the gel layer model (Wijmans *et al.*, 1984), the estimated critical volumetric fluxes using Equation A.1 should be independent of any change in the sodium chloride concentration. However, the decrease in the experimentally determined critical volumetric flux with increasing sodium chloride concentration is similar to that observed in a study of clay particles by other authors (Bacchin *et al.*, 1996), who reported that the critical flux decreases as the salinity increases due to an observed effect of particle charge on its diffusivity. They attributed this to surface interactions of the colloids (Bacchin *et al.*, 1996). As evident from the decrease in surface zeta potential in Table A.2 of section A.2, the increase in salinity decreases the repulsive interactions of the colloidal silica. Therefore, it is believed that the decrease in the surface repulsive interactions is the reason for the decrease in the experimentally determined critical flux with increasing sodium chloride concentration.

A.2 Surface Zeta Potential of Colloidal Silica

The surface zeta potential of colloidal silica (Sigma Aldrich, Ludox TMA) supplied in the form of a 34 wt% suspension in deionised water at pH 7.0 was measured using the Laser Doppler Velocimetry (LDV) technique (Malvern ZetaSizer Nano ZS). All suspensions were prepared in Milli-Q water; the samples were gently injected into the zeta potential cell to avoid any possible interference by bubbles during measurement. To ensure reproducibility of the results, each condition was independently measured three times.

Table A.2 shows the values of surface zeta potential of the colloidal silica as a function of sodium chloride concentration at 1, 2, 3, 4, 6, and 8 g/L for an aqueous solution containing 0.4 g/L of silica.

Table A.2: Zeta potential versus 1, 2, 3, 4, 6, and 8 g/L of sodium chloride for an aqueous solution containing 0.4 g/L of silica.

Silica (g/L)	NaCl (g/L)	Zeta Potential, ζ (mv)
0.4	0	- 59.05 ($\pm$ 1.25)
0.4	1	- 49.60 ($\pm$ 2.70)
0.4	2	- 42.10 ($\pm$ 1.10)
0.4	3	- 28.15 ($\pm$ 0.65)
0.4	4	- 25.27 ($\pm$ 1.26)
0.4	6	- 21.50 ($\pm$ 0.59)
0.4	8	- 21.75 ($\pm$ 1.55)

A.3 Acoustic Impedance of the Silica Suspensions

Aqueous solutions containing a range of silica concentrations were used to simulate porosities that included 87.0%, 90.3%, 93.5%, 96.8%, 98.7% and 99.99% (which is a silica suspension containing 0.48 g/L of silica). The acoustic impedance was calculated using $Z_i \equiv \rho_i c_i$ from the density and sound velocity of the media. The amplitude reflection coefficient, A, of the reflected wave relative to the incident wave perpendicular to an interface then is given by equation 2.13 in Section 2.4.1 of Chapter 2 where Z_1 is the acoustic impedance of the silica suspension containing 0.48 g/L of silica simulating a porosity value of 99.99%. The sound velocity of the medium is calculated using Equation 2.12 in section 2.4.1 of Chapter 2, after measuring the arrival time for the reflected sound wave corresponding to the aqueous silica suspension/air interface for an aqueous silica suspension of known thickness.

Figure A.1 shows a plot of the speed of sound and the corresponding density of the medium as a function of the porosity determined for the different silica suspensions. Figure A.2 shows a plot of the acoustic impedance and the corresponding amplitude reflection coefficient as a function of the porosity determined for the different silica suspensions.

Interestingly, the sound velocity decreases as the silica concentration increases because sound travels faster through water than through the absorbing colloidal silica particles. It is the increase in density that causes an increase in the amplitude reflection coefficient that allows the reflection of the sound wave to be detected during UTDR applications for colloidal fouling. An amplitude reflection coefficient of 0 means that no reflection can occur and no detection by UTDR is possible. In medical ultrasonic diagnostics the boundary between "soft tissues" such as that between blood and the kidney usually results in an amplitude reflection coefficient of approximately 0.01 (Levitov, 2009; Lee *et al.*, 2009; Martin and Ramnarine, 2010). Based on this value UTDR should be capable of detecting the reflected acoustic signal of an interface between a 99.5% porous silica foulant layer and an aqueous feed solution containing 0.48 g/L of silica.

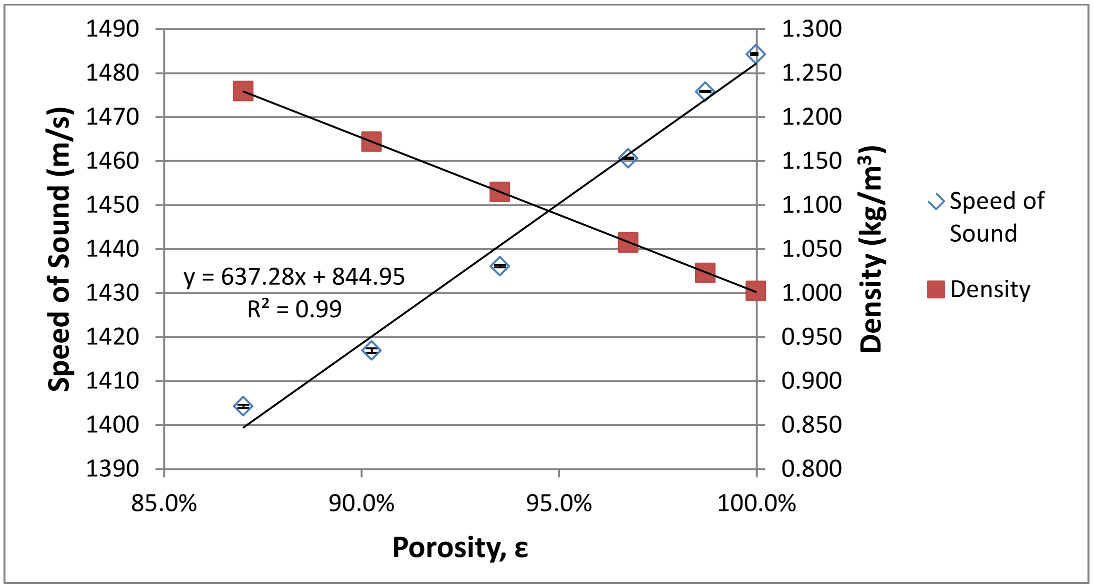

Figure A.1: Speed of sound and the corresponding density of the medium as a function of the porosity determined for the different silica suspensions.

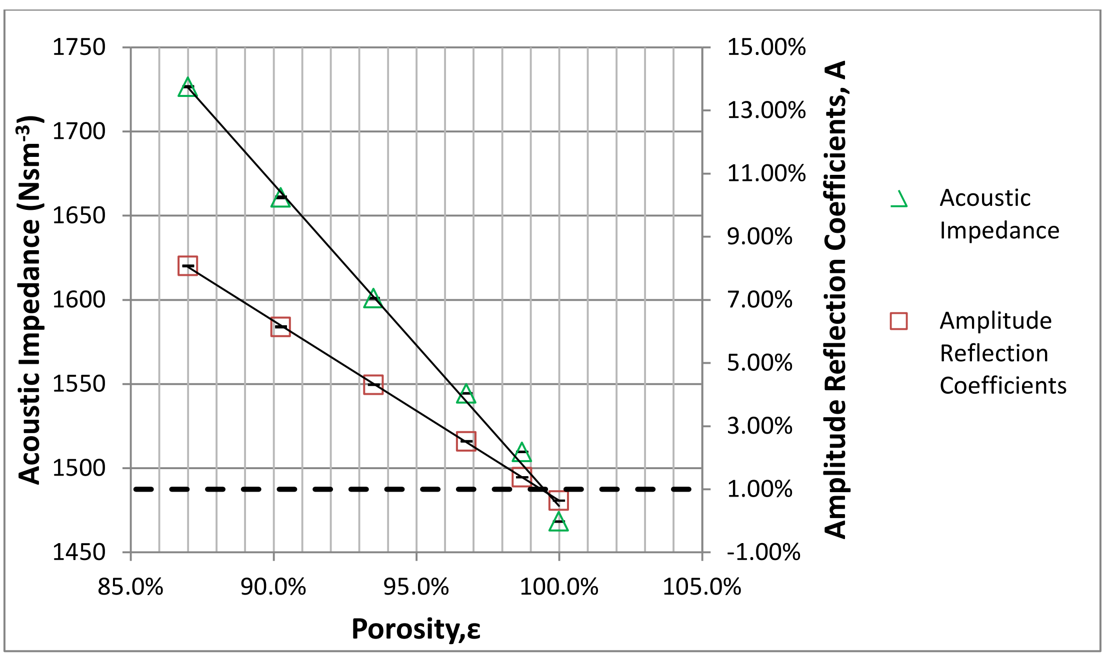

Figure A.2: Acoustic impedance and the corresponding amplitude reflection coefficient as a function of the porosity determined for the different silica suspensions.

SPECIAL APPENDIX

During the course of this thesis a number of ‘membrane related’ subprojects were carried out. This Special Appendix provides a record of these subprojects.

SA1 Pressure Retarded Osmosis (PRO)

This section first covers the state-of-the-art of PRO before discussing a recent invention of a robust PRO membrane and the utilization of PRO in a hybrid process involving desalination based on the concept of strategic co-locations.

SA1.1 PRO State-of-the-Art[9]

Pressure retarded osmosis (PRO) is an intermediate osmotic process between the natural phenomenon of forward osmosis (FO) and the non-spontaneous thermodynamic process of RO. The basic principle behind the functionality of PRO is the same as FO, where a osmotic pressure difference draws water spontaneously towards the saline water from the fresh water when both solutions are placed on the opposite sides of a semi-permeable membrane. PRO has only a slight difference where the saline water is pressurized unlike in FO, where there is a lack of operating pressure. The presence of pressure in the saline water retards the movement of water molecules but as long as the difference in applied pressure of the water of different salinities is less than the osmotic pressure difference, there will be continuous transport of water molecules towards the pressurized saline water. Mechanical recovery of the potential chemical energy obtained from the difference in osmotic pressure can be done using the increased volume of pressurized water to power electrical generators or in energy recovery

[9] The main findings have been published in: Sim S.T.V., Wang R., Fane A.G., Encyclopedia of Membranes (2013) and Sim S.T.V., Wang R., Miao T., Fane A.G. Encyclopedia of Membrane Science and Technology (2013).

devices for hybrid processes (Thorsen and Holt, 2009; Sim *et al.*, 2013a). Figure SA.1 shows a schematic of the PRO process.

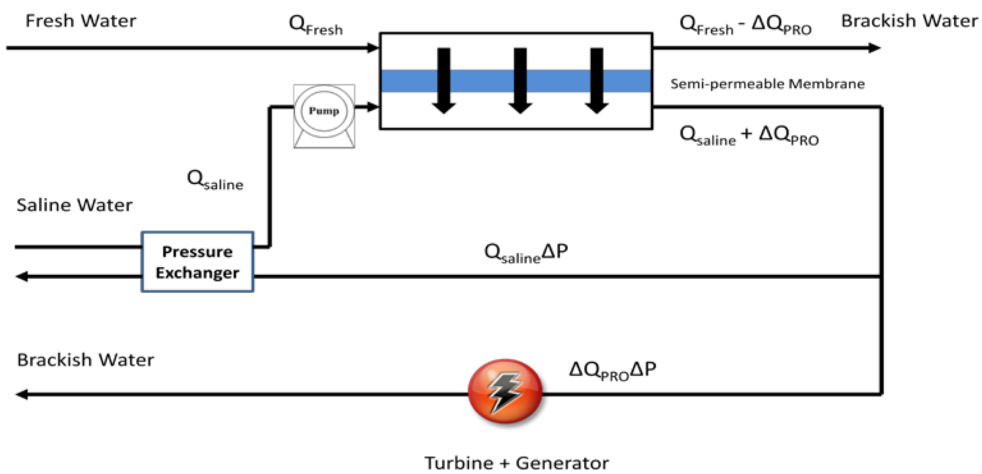

Figure SA.1: Conceptual representation of a PRO scheme (adapted from Skilhagen *et al.*, 2008); ΔQ_{PRO} is the amount of transported water per unit time through the membrane, ΔP is the difference in applied pressure between the fresh water (Q_{Fresh}) and the saline water (Q_{saline}). The amount of osmotic power recoverable is $\Delta Q_{PRO}\ \Delta P$.

Before utilizing PRO, it is necessary to acknowledge PRO is still not commercialized due to the drawbacks of a suitable membrane. Moreover, the way PRO is used in the conventional way of water treatment needs to be properly engineered. Therefore, there are two foci in this section; the development of a suitable PRO membrane in Section SA1.2, and the hybrid process involving PRO and desalination using the concept of strategic co-locations in Section SA1.3.

SA1.2 Development of a suitable PRO membrane[10]

To make PRO commercially viable, a minimum power density of 5 W/m^2 is required (Nijmeijer and Metz, 2010). Otherwise, a large amount of membrane area will be

[10] The main findings have been patented in: Tang C.-Y., She Q., Ma N., Wei J., Sim S.T.V., Fane A.G., Patent Application PCT/SG2013/000350 filed on 15 August 2013.

needed under low water fluxes and low power densities. When PRO was initially developed, the best reported PRO membranes had a power density of only 5.64 W/m^2 (Loeb, 1998) that barely meets the target 5 W/m^2. Conventional RO membranes have been evaluated but failed with low power densities due to the membranes' thick support layers (Loeb *et al.*, 1976; Ramon *et al.*, 2011). This is compounded by the fact that current membranes used for PRO applications lack the robustness and observe a 'spacer shadow' effect that adversely affects the achievable power density by impeding the water transport through the membranes. This eventually leads to severe membrane deformation as observed by a number of researchers (Yip *et al.*, 2011; She *et al.*, 2012; Kim and Elimelech, 2012). Therefore, the desired characteristics of PRO membranes would be to have a high water permeability supported by a relatively thin and highly porous substrate but be able to withstand the operating pressure required.

A recent invention involves a mechanical reinforcement with high porosity and strong mechanical strength being inserted into the multiple layers of the membrane. This transfers the desired property of mechanical stability to the membrane and reduces the extent of deformation at high applied hydraulic pressures under PRO operation while at the same time not compromising the water permeability. This invention is thus far the most robust membrane that withstands a hydraulic pressure above 28 bar and can achieve a peak power density of 7.1 W/m^2 when tested with 1 M NaCl draw solution and 10 mM NaCl feed solution. This new membrane offers the potential to bring PRO a step closer to commercialization.

SA1.2 Hybrid Process involving desalination and PRO[11]

Recovery for seawater desalination is typically within 35-55% (Desalination Committee, 2011), which implies that a significant amount of pre-treated seawater feed

---

[11] The main findings have been published in: Sim S.T.V., She Q., Chong T.H., Tang C.-Y., Fane A.G., Krantz W.B., Membranes 3 (2013) 98-125.

and the chemicals used are discarded wastefully during brine disposal. An attempt to identify the possible synergies of the seawater desalination and water reuse processes was evaluated using the concept of strategic co-location. Focus was placed on a design as depicted in Figure 1 that simultaneously dilutes the feed solution with impaired water and produce renewable energy via options of PRO, Forward Osmosis (FO) or direct mixing. A second PRO process is then employed to harness the energy from salinity gradients between the brine streams of impaired water and seawater brine that are otherwise perceived as waste and require proper disposal. In summary, a higher recovery results relative to the independent operations of the water reuse and seawater desalination plants. Such integrated Hybrid Processes of RO and FO have gained traction recently (Bamaga *et al.*, 2011; Cath, 2010; Shaffer *et al.*, 2012) but no attempts has been made to quantitatively calculate the potential savings. Therefore, the focus of this section is to showcase an engineering perspective for a conservative estimate of the cost/benefit analysis for the Hybrid Process. Minimal disruption of conventional processes and equipment is considered when calculating the potential reductions in energy consumption and capital costs from the synergistic coupling of processes.

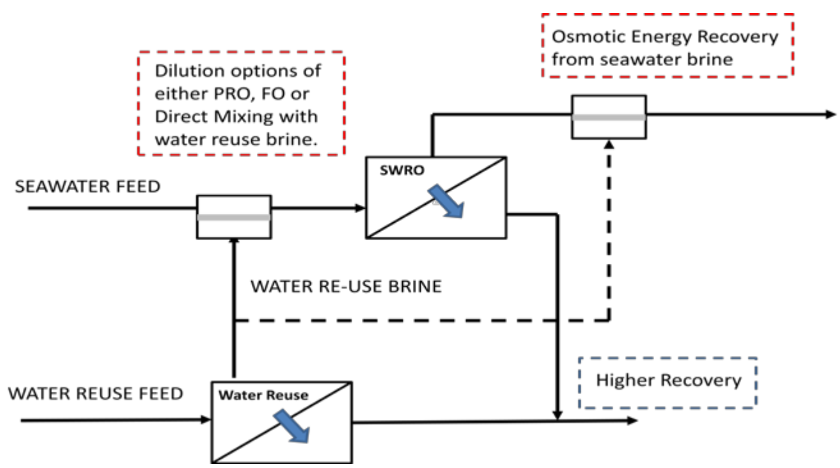

Figure SA.2: Proposed configuration of Hybrid Process (Sim *et al.*, 2013a).

Through the use of an impaired water source, it is observed that the Hybrid Process increased the recovery of water from the assumed 66.7% for conventional seawater desalination and water reuse processes to a potential 80% (Sim *et al.*, 2013a). This can be complemented by a projected reduction up to 23% in energy consumption and 8.7%–20% potential capital cost savings when compared to conventional seawater desalination plants. Considerable merit and insights are gained in several areas of the study that include the following: (1) the use of osmotic pressure via different forms of energy recovery devices (ERDs); (2) the advantages of energy production versus other forms of energy reduction resulting from the reduction in seawater feed flow rate and reduced requirements of brine disposal; (3) the counter-intuitive reduction in capital costs even when taking into account the increased number of ERDs and membrane area. However, it is noted that this is a conservative method since a hypothetical scenario based on average process values was assumed as outlined in the design considerations that can be potentially affected by other considerations such as the type of feed source for both the water reuse and SWRO plants. The feed source could affect the operating pressure, fouling and scaling behavior, pre-treatment and brine disposal methods.

A key concern is that the principal savings come from the seawater desalination process so the implementation of the Hybrid Process is critically dependent on the amount of impaired water available for the dilution of the seawater feed. The possible reduction in the seawater feed pre-treatment and brine disposal is what makes the Hybrid Process a potentially successful technology. The availability of sufficient impaired water could be an issue since water stressed areas usually rely on seawater desalination to make up for the shortfall in the water supply. As such, for these areas there is a real probability of not having sufficient impaired water sources. The main concern in this design analysis is for the water reuse plant to have a capacity that is three times that of the SWRO plant. In response to this concern of the reviewer, a sensitivity analysis on the capacity of the water reuse plant has been done whereby it was reduced to 1/3 and 2/3 of the original capacity. As might be anticipated in the absence of a sufficient amount of impaired water, both the specific energy consumption and capital costs increase significantly.

SA.2 Optical Sensor – OptiQuad®

SA2.1 Introduction

A short internship was carried out at IWW Water Centre (Mulheim, Germany), an institute under the University of Duisburg-Essen, supported by the German Minstry of Education and Research (BMBF) under the Green Talents Programme 2011. The project was on the evaluation of OptiQuad®, an optical sensor that allows the detection of biotic materials. The OptiQuad® is an optical sensor that allows the identification of a biological material and the ability to detect signs of viability so as to assess the efficiency of disinfections. Using a test system available in the IWW Water Centre (Mulheim, Germany), the response of the sensor was compared to independent determination of biofilm cell density on a surface. Due to the limited time frame for the internship, both cleaning and detection of abiotic materials were not done although there were already proven experimental results that illustrated the success of the OptiQuad® in differentiating both abiotic and biotic materials and the ability to assess the efficiency of cleaning protocols for the removal of biofilms.

This section is organized into the following parts. Section SA2.2 consists of the optical sensors state-of-the-art in particular the improvements made from the Fibre Optical Sensors (FOS) to the OptiQuad®. This will be followed by Section SA2.3 for the experimental procedure. Section SA2.4 gives the results for the evaluation of the OptiQuad®. Final conclusions are summarized in Section SA2.5.

SA2.2 Optical Sensors State-of-the-Art

Originally designed to monitor biofouling in water systems such as piping systems, fiber optical sensors (FOS) are small, flexible, electrically as well as chemically passive and can be placed in suitable sites. The attachment of microorganisms and the growth of biofilm on the FOS is understood to be similar to biofilm formation in water systems. The main point of measurement is the tip of the fiber that is integrated into the probe head. It has to be able to transmit light of a chosen wavelength to the biofilm within a well defined measurement area, be able to collect the reflected light while eliminating the effects of background ambient light and transmit to a photodetector without changing its intensity (Flemming *et al.*, 1998). Figure SA.3 shows a schematic view of the sensor's operating principle.

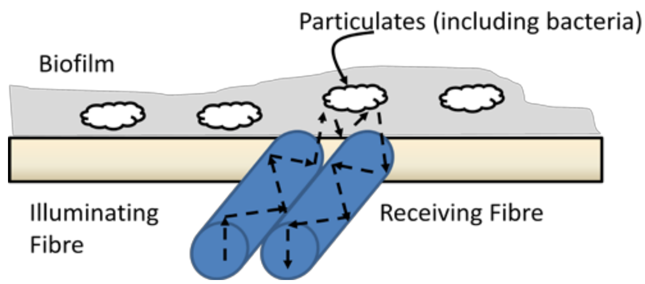

Figure SA.3: Schematic view of the FOS's operating principle. Adapted from (Tamachkiarowa and Flemming, 2003).

Effectiveness of FOS has been shown in a couple of studies where cleaning efficiency and different rates of biofilm growth have been investigated (Tamachkiarowa and Flemming, 2003; Schaule *et al.*, 2007). FOS has been further improved through the usage of a UV-LED illuminating light source and used the intrinsic fluorescence of biomolecules that is the detection of light emitted by molecules after excitation (Fischer *et al.*, 2012). Some of the intrinsic fluorescence of biomolecules is suitable for quantitative detection of biomass through the detection of tryptophan, or the presence of biofilm through the detection of extracellular polymeric substances (EPS) (Saxena *et al.*, 2002a; Saxena *et al.*, 2002b). The observation of biomass activity is done through the detection of NADPH and cell growth such as pyridoxine (Wolf *et al.*, 2002).

Unfortunately, the FOS was limited in a couple of ways, such as allowing the usage of only a single wavelength and the inability to resolve the commonly encountered but complex combination of biotic and abiotic components in biofouling layers. An advanced approach combining the four optical measurements principles of florescence, scattering, transmission and refraction is thus proposed and can be simultaneously performed by a single sensor system called the OptiQuad® (Krohne Optosens GmbH, Neuss, Germany).

Schematic depictions of the all-in-one system of the OptiQuad® are shown in Figures SA.4 and SA.5. The OptiQuad® is already commercially available and has previously been used successfully for the detection of sewage water parameters, oil deposits and oil films in water, protein deposits in milk industry etc (Mittenzwey et al., 2008). It has been successfully attempted to detect biofilms and deposits in drinking water systems that was financed during the "Biosens" project (Berlin Centre of Competence for Water, Germany).

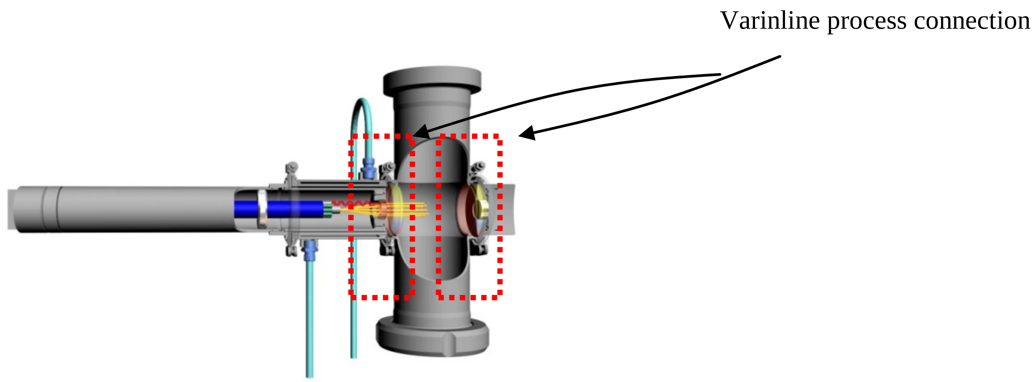

Figure SA.4: Schematic depiction of the OptiQuad® sensor system adapted to a Varinline® process connection (http://www.krohne-optosens.com/)

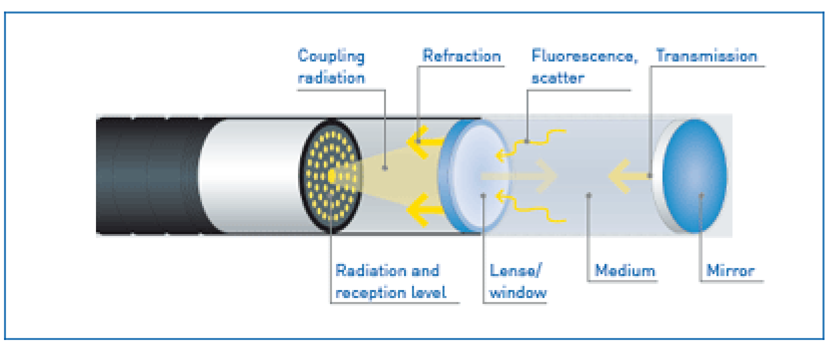

Figure SA.5: Details of sensor head (http://www.krohne-optosens.com/)

There are four wavelengths exploited by OptiQuad® namely 290, 340, 663 and 810 nm. Table SA.1 shows the breakdown for the purpose of each wavelength.

Table SA.1: Wavelengths used for the OptiQuad ®.

Wavelength (nm)	Measuring Principle	Type of Deposit
290[a,b]	Fluorescence of Tryptophan	Biotic: Biofilm (Excitation @ 290 nm, Detection @ 340 nm)
340[a,b]	Fluorescence of NADH	Biotic: Biological Activity (Excitation @ 340 nm, Detection @ 460 nm)
663[a]	Refraction	Inorganic particles in deposit
810[b]	Transmission	Deposit characterization and quantification

[a] Can also be used for transmission to characterize and quantify inorganic deposits.
[b] Can also be used for dispersion to characterize inorganic deposits at surface.

SA2.3 Material and methods

SA2.3.1 Generation of biofilms

Natural drinking water microbial population of the laboratory drinking water supply was used as inoculum to generate biofilms on the surfaces of the coupons and the sensor in the test rig. The storage tank was filled with 250 litres of fresh drinking tap water for the experiment and carried out at room temperature (varying between 20 and 25 °C). To provide and maintain a sufficient nutrient concentration a constant dosing of R2A medium (Reasoner and Geldreich, 1985) by a dosing pump was done with a rate of 3.25 ml/h of R2A solution and doubled the rate to 6.5 ml/h after 7 days. The flow velocity in the system was adjusted to 0.67 m/s (1.0 m^3/h) by means of the flow meter and a regulation valve. The pressure was held constant at 2 bars by the booster station and operated in circulation mode.

SA2.3.2 Test Coupons

For independent determination of deposit composition, removable test surfaces known also as ‘test coupons’ were made from polyethylene high density pipes (PEHD 100) and integrated in the test rig as shown in Figure SA.6. PEHD 100 is actually a common material for new drinking water distribution pipes and installations in Germany. The cells were quantified by fluorescence microscopy using DAPI staining of the bacteria followed by either direct counting on the coupon surface (if surface coverage was low) or detachment of the biofilm with a Teflon scraper, suspended in a defined volume of sterile deionized water and subsequent microscopic counting. Cell counts were accounted for the sampled surface area. A detailed view of the coupon system is depicted by Figure SA.7.

DAPI staining was performed using a stock solution containing 10 µg/ml DAPI and 2 % (v/v) formaldehyde in deionized water. Samples of suspended bacteria were filtered on 0.2 µm black polycarbonate membrane filters and stained subsequently by applying 1 ml of the DAPI stock solution onto the filter and incubated 15 min in the dark at room temperature. For the utilization of the biofilm samples directly on coupon surfaces, they were stained directly by covering the surface with 0.5 ml of the DAPI stock solution and subsequent incubation for 15 min in the dark at room temperature. Samples were investigated using fluorescence microscopy (Nikon, 90i) and applying a filter set (band pass 340-380 nm, long pass 425 nm).

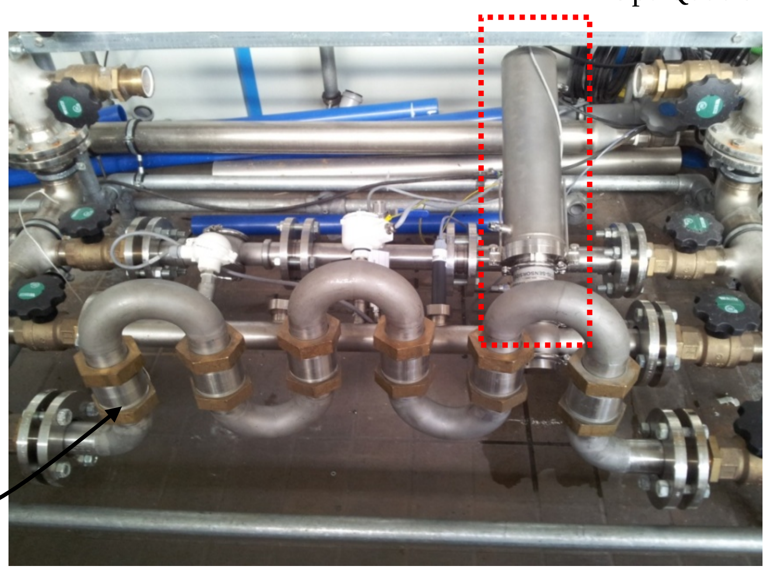

Figure SA.6: Test Rig with Optiquad® (Location: IWW Water Centre, Techniqum)

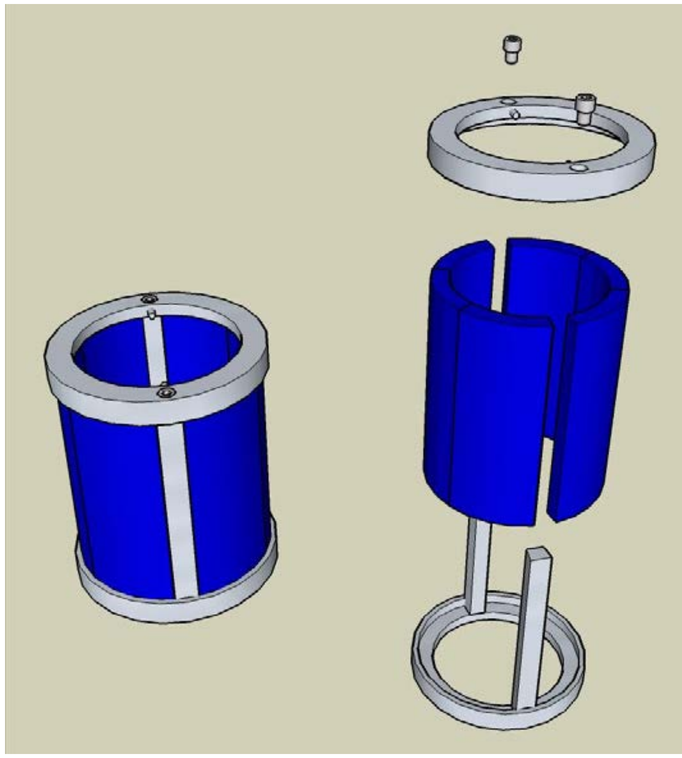

Figure SA.7: Detailed view of test coupon device (SecurEau; http://www.secureau.eu/)

SA2.4 Results

Figure SA.8 shows the experimental results of the OptiQuad® and the Total Cell Numbers (TCN) measured. It is clear the fluorescence signal of both the trypotan and NAPH clearly indicated good biofilm growth and increased in biological activity that correlated well with the increase in TCN measurement. The lack of significant scattering measurements of the OptiQuad® was expected as there was no deposition of the inorganic particles expected.

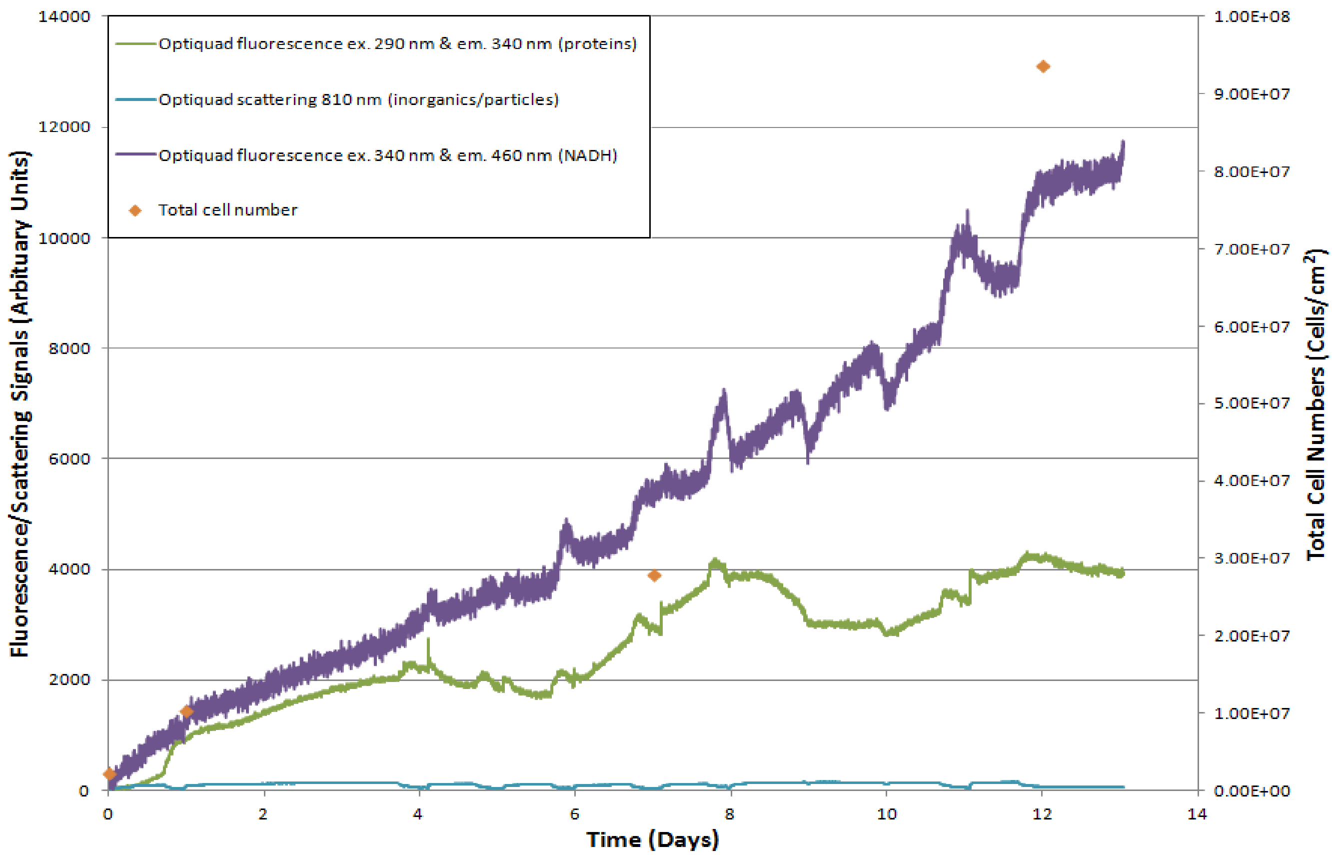

Figure SA.8: OptiQuad® scattering, fluorescence and TCN measurements.

SA2.5 Concluding Remarks

The experiments done with the OptiQuad®, it showed that was a useful sensor for detecting biotic materials and able to serve as a desirable non-invasive, in-situ and real-time detection of biofilms on surfaces such as heat exchangers. However, employing it directly to monitor biofilm formation on membrane systems may not be as straight forward as the intrinsic fluorescence of biomolecules needs the biofilm to be formed on the sensor's head in order for the Optiquad to utilize total internal reflection for detection. Moreover, the biofilm formation through the attachment to the sensor's head experiences mainly diffusion controlled transport of nutrients associated with an impermeable surface. This is fundamentally different from the biofilm formation on a membrane surface where the transport of nutrients is dominated mainly through flux-driven concentration polarization where the nutrients are retained by the membrane. Therefore, the ability for the OptiQuad® to monitor directly on the membrane surface is currently not possible with the existing configuration. In a visit to Optosens GmbH in Berlin, the inventors of the OptiQuad®, Dr. Mittenzway and Dr. Sinn, highlighted that it was possible to measure on the membrane surface that is typically an additional 700 – 900 µm away from the sensor. If the OptiQuad® can be adapted for monitoring on membrane surfaces, there is great potential for the membrane industry.

Another potentially interesting method of using the OptiQuad® for membrane system could be done through the concept of photoacoustics that has been proven to work for biofilms (Schmid *et al.*, 2003). This is based on the absorption of non-ionising radiation inside a sample and the relxation process that converts the absorbed energy into thermal vibrations through a non-radiative process. The vibrations then create a pressure wave that can be detected by piezoelectirc tranducers. There may be a need for contrasting agents such as nanospheres if the non-radiative relaxation is found to be challenged by low signal to noise ratio as shown by other authors (Lu *et al.*, 2010).

SA3. Development of the Improved Integrity Sensor (IS)[12]

Once the RO process is in operation, there are two avenues to pre-empt fouling problems. Other than a more sensitive monitoring of the 'state of the process' using novel monitors on a side-stream cell, which is the canary cell as developed in this thesis, the other way is to measure the fouling propensity of the water and allowed for. However, the commonly used technique for this, Silt Density Index (SDI), is empirical and potentially unreliable (Schippers and Verdouw, 1980, Lipp *et al.*, 1990; Yiantsios and Karabelas, 2002; Boerlage *et al.*, 2003). A novel method to measure the fouling propensity called the Integrity Sensor (IS) was developed recently (Phattaranawik *et al.*, 2008) that allowed continuous online real time measurements unlike the SDI, which is essentially an offline measurement. The IS operates by measuring the transmembrane pressure (TMP) across a membrane of low hydraulic resistance such as a ultrafiltration (UF) or microfiltration (MF) membrane relative to a reference pressure differential (Krantz *et al.*, 2011). The measurement is then converted into a dimensionless metric referred to as the π-factor (ratio of the transmembrane pressure to the reference pressure differential) and is define as follows:

$$\pi = \frac{P_1 - P_2}{P_2 - P_3} = \frac{JR_1}{JR_2} = \frac{R_1}{R_2} \qquad \text{(SA.1)}$$

Where R_1 = membrane resistance of the upper membrane and R_2 = membrane resistance of the lower membrane (old design) or the valve resistance (improved design) as depicted in Figure SA.9.

When the feed water is sampled, the π-factor has an initial value that corresponds to the unfouled membrane in the IS. As the feed water is continuously sampled, the π-factor

[12] The main findings of the MIS have been patented in: Maung N.W., Tan E.K., Wong F.-S., Yeo P.S.A., Krantz W.B., Fane A.G., Sim S.T.V. (2010), "A Membrane Sensor and Method of Detecting Fouling in a Fluid", Patent WO/2012/060778 filed on 1 November 2010.

will increase if there is progressive fouling of the membrane in the IS (Phattaranawik *et al.*, 2008). However, there is an issue with the long term operation of the IS as particulates that pass through the upper membrane deposit on the lower membrane. In comparison, it is relatively easy to clean the upper membrane but the deposited foulants are not easily removed from the lower membrane. In addition, the sensitivity of the IS decreases as the upper membrane becomes progressively fouled. Therefore, the IS has been patented with an improved design to have a reference resistance that is tunable and allows an easy operating back-wash mechanism. Figure SA.9 shows the schematic of both set-ups where the improved design has been patented.

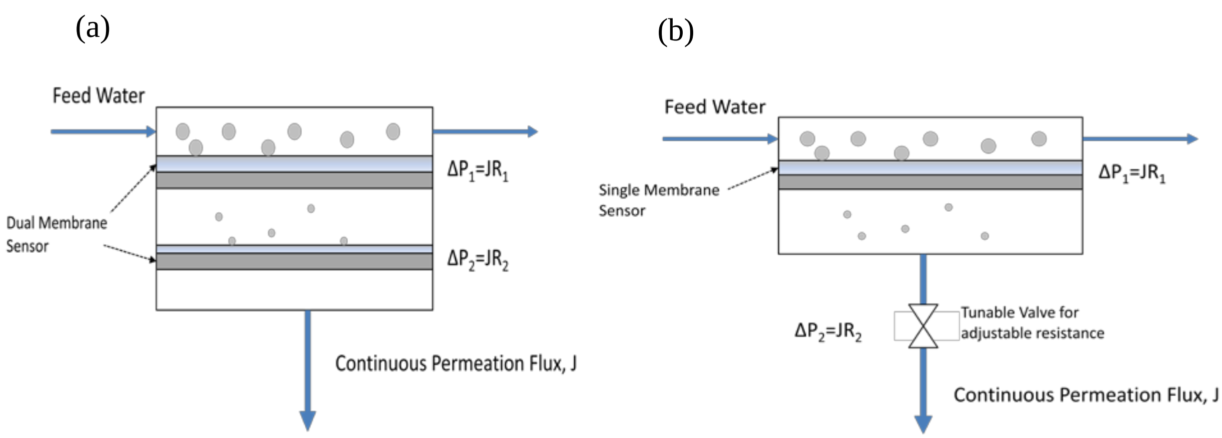

Figure SA.9: (a) Schematic of old Integrity Sensor (Phattaranawik *et al.*, 2008) and (b) Schematic of the improved Integrity Sensor.

REFERENCES

Aerts P., Greenberg A.R., Leysen R., Krantz W.B., Reinsch V.E., Jacobs P.A. (2001), "The influence of filler concentration on the compaction and filtration properties of Zirfon composite ultrafiltration membranes", Separation and Purification Technology, **22-23**: 663-669.

Airey D., Yao S., Wu J., Chen V., Fane A.G., Pope J.M. (1998), "An investigation of concentration polarization phenomena in membrane filtration of colloidal silica suspensions by NMR micro-imaging", Journal of Membrane Science, **145**: 145-158.

Aimar P., Bacchin P. (2010), "Slow colloidal aggregation and membrane fouling", Journal of Membrane Science, **360**: 70-76.

Aimar P., Taddei C., Laifille J.P., Sanchez V. (1988), "Mass transfer limitations during ultrafiltration of cheese whey with inorganic membranes", Journal of Membrane Science, **38**: 203-221.

Alexandis A., Wiley D.E., Vishnoi A., Lee R.H.K., Fletcher D.F., Bao J. (2007), "CFD modelling of reverse osmosis membrane flow and validation with experimental results", Desalination, **217**: 242-250.

Bacchin P., Aimar P., Field R.W. (2006), "Critical and sustainable fluxes: theory, experiments and applications", Journal of Membrane Science, **281**: 42-69.

Bacchin P., Aimar P., Sanchez V. (1996), "Influence of surface interaction on transfer during colloid ultrafiltration", Journal of Membrane Science, **115**: 49-63.

Bacchin P., Si-Hassen D., Starov V., Clifton M.J., Aimar P. (2002), "A unifying model for concentration polarization, gel-layer formation and particle deposition in crossflow membrane filtration of colloidal suspensions", Chemical Engineering Science, **57**: 77-91.

Baker R.W. (2004), Membrane Technology and Application, Wiley, New York, United States.

Baker J.S., Dudley L.Y. (1998), "Biofouling in membrane systems – a review", Desalination, **118**: 81-89.

Bartman A.R., Lyster E., Rallo R., Christofides P.D., Cohen Y. (2011), "Mineral scale monitoring for reverse osmosis desalination via real-time membrane surface image analysis", Desalination, **273**: 64-71

Bartels C., Bergman R., Hallan M., Henthorne L., Knappe P., Lozier J., Metcalfe P., Peery M., Shelby I. (2005), "Industry Consortium Analysis of Large Reverse Osmosis and Nanofiltration Element Diameters", in: Desalination and Water Purification Research and Development Report No. 114, Bureau of Reclamation, Department of Interior, United States.

Bamaga O.A., Yokochi A., Zabara B., Babaqi A.S (2011), "Hybrid FO/RO desalination system: Preliminary assessment of osmotic energy recovery and designs of new FO membrane module configurations", Desalination, **258**: 153–159.

Battin T.J., Kaplan L.A., Newbold J.D., Cheng X., Hansen C. (2003), "Effects of Current Velocity on the Nascent Architecture of Stream Microbial Biofilms", Applied and Environmental Microbiology, **69**: 5443-5452.

Bird R.B., Stewart W.B., Lightfoot E.N., Transport Phenomena, First Ed., John Wiley & Sons, Inc., New York, 1960.

Boerlage S.F.E., Kennedy M.D., Aniye M.P., Abogrean E.M., Galjarrd G., Shippers J.C. (1998), "Monitoring particulate fouling in membrane systems", Desalination, **118**: 131-142.

Boerlage S.F.E., Kennedy M.D., Aniye M.P., Abogrean E., Tarawneh Z.S., Schippers J.C. (2003), "The MFI-UF as a water quality test and monitor", Journal of Membrane Science, **211**: 271-289.

Boudreau B.P. (1996), "The diffusive tortuosity of fine-grained unlithified sediments", Geochimica et Cosmochimica Acta, **60**: 3139–3142.

Brodkey R.S., Hershey H.C. (1988), "Methods of Analysis", in: Brodkey R.S., Hershey H.C. (Eds.) Transport Phenomena A Unified Approach – Part 1, McGraw-Hill, United States.

Buess C. (2004), "Transit-time Ultrasonic Flowmeters for Medical Applications", in: ndd Medizintecknik AG (http://www.ndd.ch/), Zurich, Switerland.

Buffle J., Leppard G.G. (1995), "Characterization of aquatic colloids and macromolecules: 1. Structure and behaviour of colloidal material", Environmental Science & Technology, **29**: 2169-2175.

Carman P.C. (1937), "Fluid flow through granular beds", Chemical Engineering Research and Design, **15**: 150-166.

Carpineti M., Giglio M. (1992), "Spinodal-type dynamics in fractal aggregation of colloidal clusters", Physical Review Letter, **68**: 3327-3330.

Cath T.Y (2010), "Osmotically and thermally driven membrane processes for enhancement of water recovery in desalination process", Desalination and Water Treatment, **15**: 279–286.

Chai G.-Y., Cao B., Zhao G.Y., Greenberg A.R., Krantz W.B. (2012), "Effects of concentration polarization, temperature and pressure on ultrasound detection of inorganic fouling and cleaning in a spiral-wound membrane module", Desalination and Water Treatment, **50**: 411-422.

Chai G.-Y., Greenberg A.R., Krantz W.B. (2007), "Ultrasound, gravimetric , and SEM studies of inorganic fouling in spiral-wound membrane modules", Desalination, **208**: 277-293.

Chen K.L., Song L., Ong S.L., Ng W.J. (2004a), "The development of membrane fouling in full-scale RO processes", Journal of Membrane Science, 232: 63-72.

Chen J.C., Li Q., Elimelech M. (2004b), "In situ monitoring techniques for concentration polarization and fouling phenomena in membrane filtration", Advances in Colloid and Interface Science, **107**: 83-108.

Chen M., Russel W.B. (1991), "Characteristics of flocculated silica dispersions", Journal of Colloid and Interface Science, **141**: 564-577.

Chen V., Li H., Fane A.G. (2004c), "Non-invasive observation of synthetic membrane processes – a review of methods", Journal of Membrane Science, **241**: 23-44.

Chen X., Suwarno S.R., Chong T.H., McDougald D., Kjelleberg S., Cohen Y., Fane A.G., Rice S.A. (2013), "Dynamics of biofilm formation under different nutrient levels and the effect on fouling in a reverse osmosis membrane system", Biofouling, **29**: 319-330.

Chong T.H., Wong F.S., Fane A.G. (2007), "Fouling in reverse osmosis: Detection by non-invasive techniques", Desalination, **204**: 148-154.

Chong T.H., Wong F.S., Fane A.G. (2008), "Implications of critical flux and cake enhanced osmotic pressure (CEOP) on colloidal fouling in reverse osmosis: Experimental observations", Journal of Membrane Science, **314**: 101-111.

Chong T.H. (2008), "Reverse Osmosis Desalination and Reclamation – Control of Colloidal and Biofouling", Ph.D. Dissertation, Nanyang Technological Univeristy, Singapore.

Chudacek M.W., Fane A.G. (1984), “The dynamics of polarization in unstirred and stirred Ultrafiltration”, Journal of Membrane Science, **21**: 145-160.

Coasne B., Galarneau A., Renzo F.D., Pellenq R.J.M. (2010), “Molecular Simulation of Nitrogen Adsorption in Nanoporous Silica”, Langmuir, **26**: 10872-10881.

Cuadros F., Cachadina I., Ahumada W. (1996), “Determination of Lennard-Jones Interaction Parameters Using a New Procedure”, Molecular Engineering, **6**: 319-325.

Da Costa A.R., Fane A.G., Wiley D.E. (1994), “Spacer characterization and pressure drop modelling in spacer-filled channels for ultrafiltration”, Journal of Membrane Science, **87**: 79-98.

Desalination Committee (2011), “Seawater Desalination Power Consumption, White Paper”, WaterReuse Association, Alexandra, VA, USA, 2011.

Dore M.H.I. (2005), “Forecasting the economic costs of desalination technology”, Desalination, **172**: 207-217.

Dubois M., Gilles K.A., Hamilton J.K., Rebers P.A., Smith, F. (1956), "Colorimetric method for determination of sugars and related substances", Analytical Chemistry, **28**: 350-356.

Elimelech M., Philip W.A. (2011), “The Future of Seawater Desalination: Energy, Technology, and the Environment”, Science, **333**: 712-717.

Elmøe T.D., Tricoli A., Grunwaldt J.-D., Pratsinis S.E. (2009), “Filtration of nanoparticles: Evolution of cake structure and pressure-drop”, Journal of Aerosol Science, **40**: 965-981.

Faibish R.S., Elimelech M., Cohen Y. (1998), “Effect of interparticle electrostatic double layer interactions on permeate flux decline in crossflow membrane filtration of colloidal suspensions: An experimental investigation", Journal of Colloid and Interface Science, **204**: 77-86.

Fane A.G., Chong T.H., Le-Clech P. (2009), "Fouling in Membrane Processes", in: Drioli E., Giorno L. (Eds.), Membrane Operations – Innovative Separations and Transformations, Wiley-VCH, Germany.

Flemming H.-C. (2003), "Role and levels of real-time monitoring for successful anti-fouling strategies – an overview", Water Science & Technology, **47**: 1-8.

Flemming H.-C. (2011a), "Microbial Biofouling - Unsolved Problems, Insufficient Approaches, and Possible Solutions", in: Flemming H.-C., Wingender J., Szewzyk U. (Eds.), Biofilm Highlights, Springer-Verlag, Berlin, Germany.

Flemming H.-C. (2011b), "The perfect slime", Colloids and Surfaces B: BioInterfaces, **86**: 251-259.

Flemming H.-C., Griebe T., Schaule G. (1996), "Antifouling strategies in technical systems – a short review", Water Science & Technology, **34**: 517-524.

Flemming H.-C., Schaule G., McDonogh R., Ridgway H.F. (1994), "Mechanism and extent of membrane biofouling", in: Geesey G.G., Lewandowski Z., Flemming H.-C. (Eds.) Biofouling and biocorrosion in industrial water systems, Lewis, Chelsea, United States.

Flemming H.-C., Tamachkiarowa A., Klahre J., Schmitt J. (1998), "Monitoring of fouling and biofouling in technical systems", Water Science & Technology, **38**: 291-298.

Flemming H.-C., Wingender J. (2010), "The biofilm matrix", Nature Reviews Microbiology, **8**: 623-633.

Field R.W. (2010), “Fundamentals of Fouling” in: Peinemann K.-V., Nunes S.P. (Eds.), Membranes for Water Treatment, Wiley-VCH, Great Britain.

Field R.W., Wu D., Howell J.A., Gupta B.B. (1995), “Critical flux concept for microfiltration fouling”, Journal of Membrane Science, **100**: 259-272.

Fischer M., Wahl M., Friedrichs G. (2012), “Design and field application of a UV-LED based optical fiber biofilm sensor”, Biosensors and Bioelectronics, **33**: 172-178.

Fonseca A.C. (2002), “Biofouling of nanofiltration membranes and in-situ biofilm detection”, Ph.D. Dissertation, Univeristy of Colorado, Boulder, United States.

Gekas V., Aimar P., Lafaille J.P., Sanchez V. (1993), “A simulation study of the adsorption-concentration polarisation interplay in protein ultrafiltration”, Chemical Engineering Science, **48**: 2753-2765.

Geise G.M., Park H.B., Sagle A.C., Freeman B.D., McGrath J.E. (2011), “Water permeability and water/salt selectivity tradeoff in polymers for desalination”, Journal of Membrane Science, **369**: 130-138.

Gleick P.H. (1996), “Water Resources”, in: Schneider S.H. (Ed.), Encyclopedia of Climate and Weather Vol. 2, University Press. New York, United States.

Gleick P.H., Cooley H. (2009), “Data Table 1: Total Renewable Freshwater Supply, by Country”, in: Gleick P.H., Cooley H., Cohen M., Morikawa M., Morrison J., M. Palaniappan M. (Eds.), The World’s Water 2008-2009, Island Press, Washington, DC, United States, pp. 195-201.

Gómez Álvarez-Arenas T.E., Segura L.E., Sarabia E.R.F.D. (2002), “Characterization of suspensions of particles in water by an ultrasonic resonant cell”, Ultrasonics, **39**: 715-727.

Greenlee L.F., Lawler D.F., Freeman B.D., Marrot B., Moulin P. (2009), "Reverse osmosis desalination: Water sources, technology and today's challenges", Water Research, **43**: 2317-2348

Gu H., Bartman A.R., Uchymiak M., Chrsitofides P.D., Cohen Y. (2013), "Self-adaptive feed flow reversal operation of reverse osmosis desalination", Desalination, **308**: 63-72.

Guidarella G., Craciun F., Galassi C., Roncari E. (1998), "Ultrasonic characterisation of solid-liquid suspensions", Ultrasonics, **36**: 467-470.

GWI – Global Water Intelligence (2007), "Desalination Markets", in: A Global Industry Forecast (www.globalwaterintel.com), Media Analytics Ltd., Oxford, United Kingdom.

GWI – Global Water Intelligence (2009), "New Revenue Stream Springs Up: Water Reuse Market set for Explosive Growth", in: Municipal Water Reuse Markets 2010 (www.globalwaterintel.com), Media Analytics Ltd., Oxford, United Kingdom.

Haw M.D., Gillie M., Poon W.C.K. (2002), "Effects of phase behavior on the drying of colloidal suspensions", Langmuir, **18**: 1626-1633.

Hentzer M., Riedel K., Rasmussen T.B., Heydorn A., Andersen J.B., Parsek M.R., Rice S.A., Givskov M. (2002), "Inhibition of quorum sensing in Pseudomonas aeruginosa biofilm bacteria by a halogenated furanone compound", Microbiology, **148**: 87-102.

Hemp J. (1982), "Theory of Transit-Time Ultrasonic Flowmeters", Journal of Sound and Vibration, **84**: 133-147.

Her N., Amy G., Plottu-Pecheux A., Yoon Y. (2007), "Identification of nanofiltration membrane foulants", Water Research, **41**: 3936-3947.

Hoek E.M.V., Allred J., Knoell T., Jeong B.-H. (2008), "Modelling the effects of fouling on full-scale reverse osmosis processes", Journal of Membrane Science, **314**: 33-49.

Hoek E.M.V., Kim A.S., Elimelech M. (2002), "Influence of crossflow membrane filter geometry and shear rate on colloidal fouling in reverse osmosis and nanofiltration separations", Environmental Engineering Science, **19**: 357–372.

Huang X., Guillen G.R., Hoek E.M.V. (2010), "A new high-pressure optical membrane module for direct observation of seawater RO membrane fouling and cleaning", Journal of Membrane Science, **364**: 149-156.

IDA – International Desalination Association (2012), "25th DesalData IDA Worldwide Desalting Plant Inventory", in: IDA Desalination Yearbook 2012-2013 (www.desalyearbook.com), Media Analytics Ltd., Oxford, United Kingdom.

Ivnitsky H., Katz I., Minz D., Shimoni E., Chen Y., Tarchitzky J., Semiat R., Dosoretz C.G. (2005), "Characterization of membrane biofouling in nanofiltration processes of wastewater treatment", Desalination, **185**: 255-268.

Israelachvili J.N. (1992), Intermolecular and Surface Forces, Academic Press Limited, London, United Kingdom.

Kolodziejski J., Gasson C. (2005), "Water Reuse Markets 2005-2015" in: A Global Assessment and Forecast, Global Water Intelligence.

Kools W.F.C., Konagurthu S., Greenberg A.R., Bond L.J., Krantz W.B., Van Den Boomgard T., Strathmann H. (1998), "Use of ultrasonic time-domain reflectometry for real-time measurement of thickness changes during evaporative casting of polymeric films", Journal of Applied Polymer Science, **69**: 2013-2019.

Koutsou C.P., Yiantsios S.G., Karabelas A.J. (2009), "A numerical and experimental study of mass transfer in spacer-filled channels: Effects of spacer geometrical characteristics and Schmidt Number", Journal of Membrane Science, **326**: 234-251.

Kim S., Park H. (2002), "Applicability assessment of subcritical flux operation in crossflow microfiltration with a concentration polarization model", Journal of Environmental Engineering, **128**: 335-340.

Kim Y.C., Elimelech M. (2012), "Adverse impact of feed channel spacers on the performance of pressure retarded osmosis", Environment Science and Technology, **46**: 4673–4681.

Kimura K., Yamato N., Yamamura H., Watanabe Y. (2005), "Membrane fouling in pilot-scale membrane bioreactors (MBRs) treating municipal wastewater", Environmental Science & Technology, **39**: 6293-6299.

Krantz W.B., Greenberg A.R. (2008), "Membrane characterization by ultrasonic time-domain reflectometry", in: Li N.N., Fane A.G., Ho W.S.W., Matsuura T. (Eds.), Advanced Membrane Technology and Applications, John Wiley & Sons, Inc., New York, United States.

Krantz W.B., Lin C.S., Sin P.C.Y., Yeo A., Fane A.G. (2011), "An Integrity Sensor for assessing the performance of low pressure membrane modules in the water industry", Desalination, **283**: 117-122.

Krauskopf K.B. (1956), "Dissolution and precipitation of silica at low temperatures", Geochimica et Cosmochimica Acta, **10**: 1-26.

Kujundzic E., Fonseca A.C., Evans E.A., Peterson M., Greenberg A.R., Hernandez M. (2007), "Ultrasonic monitoring of early-stage biofilm growth on polymeric surfaces", Journal of Microbiological Methods, **68**: 458-467.

Latteman S., Kennedy M.D., Schippers J.C., Amy G. (2010), "Global Desalination Situation", in: Escobar I., Schӑfer A. (Eds.), Sustainable Water for the Future – Water Recycling versus Desalination, Elseiveir B.V. Amsterdam, Netherlands and Oxford, United Kingdom.

Lee K.P., Arnot T.C., Mattia D. (2011), "A review of reverse osmosis membrane materials for desalination – Development to date and future potential", Journal of Membrane Science, **370**: 1-22.

Lee N., Amy G., Croué J.P., Buisson H. (2004), "Identification and understanding of fouling in low-pressure membrane (MF/UF) filtration by natural organic matter (NOM)", Water Research, **38**: 4511-4523.

Lee Y., Clark M.M. (1998), "Modeling of flux decline during crossflow ultrafiltration of colloidal suspensions", Journal of Membrane Science, **149**: 181-202.

Lee Y.Z., McGregor J., Chong W.K. (2009), "Ultrasonic-Guided Kidney Biopsies", Ultrasonic Clinics, **4**: 45-55.

Levitov A. (2009), "Physics of Sound, Ultrasound, and Doppler Effect and its Diagnostic Utility", in: Levitov A., Mayo P.H., Slonim A.D. (Eds.), Critical Care Ultrasonography, The McGraw-Hill Companies, Inc., China.

Li H., Fane A.G., Coster H.G.L., Vigneswaran S. (1998), "Direct observation of particle deposition on the membrane surface during crossflow microfiltration", Journal of Membrane Science, **149**: 83-97.

Li H., Fane A.G., Coster H.G.L., Vigneswaran S. (2000), "An assessment of depolarisation models of crossflow microfiltration by direct observation through the membrane", Journal of Membrane Science, **172**: 135-147.

Li H., Fane A.G., Coster H.G.L., Vigneswaran S. (2003), "Observation of deposition and removal behaviour of submicron bacteria on the membrane surface during crossflow microfiltration", Journal of Membrane Science, **217**: 29-41.

Li J., Hallbauer D.K., Sanderson R.D. (2005a), "The challenge of detecting the very initial onset of biofouling on membranes by novel ultrasonic wavelet technique", in: The International Congress on Membranes and Membrane Processes (ICOM2005), Seoul, Korea.

Li J., Liu J., Yang T., Xiao C. (2007), "Quantitative study of the effect of electromagnetic field on scale deposition on nanofiltration membranes via UTDR", Water Research, **41**: 4595-4610.

Li J., Sanderson R.D. (2002), "In situ measurement of particle deposition and its removal in microfiltration by ultrasonic time-domain reflectometry", Desalination, **146**: 169-175.

Li J., Sanderson R.D., Hallbauer D.K., Hallbauer-Zadorozhnaya V.Y. (2002a), "Measurement and modelling of organic fouling deposition in ultrafiltration by ultrasonic transfer signals and reflections", Desalination, **146**: 177-185.

Li J., Sanderson R.D., Jacobs E.P. (2002b), "Non-invasive visualization of the fouling of microfiltration membranes by ultrasonic time-domain reflectometry", Journal of Membrane Science, **201**: 17-29.

Li J., Sanderson R.D., Chai G.-Y., Hallbuer D.K. (2005b), "Development of an ultrasonic technique for insitu investigating the properties of deposited protein during crossflow ultrafiltration", Journal of Colloid and Interface Science, **284**: 228-238.

Li X., Li J., Wang J., Zhang H., Pan Y. (2012), "In situ investigation of fouling behavior in submerged hollow fiber membrane module under sub-critical flux operation via ultrasonic time domain reflectometry”, Journal of Membrane Science, **411-412**: 137-145.

Lipp B., Gorge B., Gimbel R. (1990), “A comparative study of fouling-index and fouling-potential of waters to be treated by reverse osmosis”, Desalination, **79**: 203-216.

Loeb S. (1998), “Energy production at the Dead Sea by pressure-retarded osmosis: Challenge or chimera?”, Desalination, **120**: 247–262.

Loeb S., Hessen F.V., Shahaf D. (1976), “Production of energy from concentrated brines by pressure-retarded osmosis: I. Preliminary technical and economic correlations”, Journal of Membrane Science, **1**: 249–269.

Lu W., Huang Q., Ku G., Wen X., Zhou M., Guzatov D., Brecht P., Su R., Oraevsky A., Wang L.V., Li C. (2010), "Photoacoustic imaging of living mouse brain vasculature using hollow gold nanospheres“, Biomaterials, **31**: 2617-2626.

Lu X., Kujundzic E., Mizrahi G., Wang J., Cobry K., Peterson M., Gilron J., Greenbery A.R. (2012), “Ultrasonic sensor control of flow reversal in RO desalination – Part 1: Mitigation of calcium sulfate scaling”, Journal of Membrane Science, **419-420**: 20-32.

Mahoney M.W., Jorgensen W.L. (2000), “A five-site model for liquid water and the reproduction of the density anomaly by rigid, nonpolarizable potential functions”, Journal of Chemical Physics, **112**: 8910-8922.

Mairal A.P., Greenberg A.R., Krantz W.B. (2000), “Investigation of membrane fouling and cleaning using ultrasonic time-domain reflectometry”, Desalination, **130**: 45-60.

Mairal A.P., Greenberg A.R., Krantz W.B., Bond L.J. (1999), “Real-time measurement of inorganic fouling of RO desalination membranes using ultrasonic time-domain reflectometry”, Journal of Membrane Science, **159**: 185-196.

Martin K., Ramnarine K. (2010), “Physics”, in: Hoskins P., Martin K., Thrush A. (Eds.), Diagnostic Ultrasound – Physics and Equipment, Cambridge University Press, Cambridge, United Kingdom.

Matthiasson E., Sivik B. (1980), “Concentration polarization and fouling”, Desalination, **35**: 59-103.

Maung N.W., Tan E.K., Wong F.-S., Yeo P.S.A., Krantz W.B., Fane A.G., Sim S.T.V. (2010), “A Membrane Sensor and Method of Detecting Fouling in a Fluid”, Patent WO/2012/060778 filed on 1 November 2010.

Megen W.V., Underwood S.M. (1994), “Glass transitions in colloidal hard spheres: Measurement and mode-coupling-theory analysis of the coherent intermediate scattering function”, Physical Review E, **49**: 4206-4220.

Metsämuuronen S., Howell J.A., Nyström M. (2002), “Critical flux in ultrafiltration of myoglobin and baker’s yeast”, Journal of Membrane Science, **196**: 13-25.

Mittenzwey K.-H., Sinn G. (2008), "Vorrichtung zur Messung der Streuung und/oder Absorption und/oder Refraktion einer Probe", Germany Patent DE 10 2008 017 433 B4, 8.4.2010.

Mizrahi G., Wong K., Lu X., Kujundzic E., Greenberg A.R., Gilron J. (2012), “Ultrasonic sensor control of flow reversal in RO desalination – Part 2: Mitigation of calcium carbonate scaling”, Journal of Membrane Science, **419-420**: 9-19.

Moody C.D., Kaakinen J.W., Lozier J.C., Laverty P.E. (1983), “Yuma desalting test facility: Foulant component study”, Desalination, **47**: 239-253.

Neese T.H., Dueck J., Djatchenko E. (2009), “Simulation of filter cake porosity in solid/liquid separation”, Powder Technology, **193**: 332-336.

Nickel J.C., Ruseska I., Wright J.B., Costerton J.W. (1985), "Tobramycin resistance of Pseudomonas aeruginosa cells growing as a biofilm on urinary catheter material", Antimicrobial Agents and Chemotherapy, **27**: 619-624.

Nijmeijer K., Metz, S. (2010), "Salinity Gradient Energy", in: Sustainable Water for the Future: Water Recycling versus Desalination, Escobar I.C., Schäfer A.I., (Eds.), Elsevier: Amsterdam, the Netherlands and Oxford, UK.

Ning R.Y., Troyer T.L., Tominello R.S. (2005), "Chemical control of colloidal fouling of reverse osmosis systems", Desalination, **172**: 1-6.

Nishimura M., Koyama K. (1992), "Reverse Osmosis", in: Osada Y., Nakagawa T. (Eds.), Membrane Science and Technology, Marcel Dekker, Inc., New York, United States.

O'Toole G.A., Kolter R. (1998), "Flagellar and twitching motility are necessary for Pseudomonas aeruginosa biofilm development", Molecular Microbiology, **30**: 295-304.

Pearce G.K. (2008), "UF/MF pre-treatment to RO in seawater and wastewater reuse applications: a comparison of energy costs", Desalination, **222**: 66-73.

Peterson R.A., Greenberg A.R., Bond L.J., Krantz W.B. (1998), "Use of ultrasonic TDR for real-time noninvasive measurement of compressive strain during membrane compaction", Desalination, **116**: 115-122.

Petersen R.J. (1993), "Composite reverse osmosis and nanofiltration membranes", Journal of membrane science, **83**: 81-150.

Peterson R.J., Cadotte J.E. (1990), "Thin film composite reverse osmosis membrane", in: M.C. Porter (Ed.), Handbook of Industrial Membrane Technology, Noyes Publication, New Jersey, United States.

Phattaranawik J., Fane A.G., Wong F.S., “Novel membrane-based sensor for online membrane integrity monitoring”, Journal of Membrane Science, **323**: 113-124.

Picioreanu C., Loosdrecht M.C.M.V., Heijnen J.J. (1998), “Mathematical Modeling of Biofilm Structure with a Hybrid Differential-Discrete Cellular Automation Approach”, Biotechnology & Bioengineering, **58**: 101-116.

Poppe G. (2012), “Make the Most of RO Membranes”, Chemical Processing (http://www.chemicalprocessing.com/articles/2012/make-the-most-of-ro-membranes/)

Porter M.C. (1972), “Concentration polarization with membrane ultrafiltration”, Industrial and Engineering Chemistry Product Research and Development, **11**: 234-248.

Pusey P.N., Megen W.V. (1987), “Observations of a glass transition in suspensions of spherical colloidal particles”, Physical Review Letter, **59**: 2083-2086.

Ramon G.Z., Feinberg B.J., Hoek E.M.V. (2011), “Membrane-based production of salinity-gradient power”, Energy and Environmental Science, **4**: 4423–4434.

Reasoner D.J., Geldreich E.E. (1985), “A new medium for the enumeration and subculture of bacteria from potable water”, Applied and Environmental Microbiology, **49**: 1-7.

Richter A., Babick F., Stintz M. (2006), “Polydisperse particle size characterization by ultrasonic attentuation spectroscopy in the micrometer range”, Ultrasonics, **44**: e483-e490.

Sanderson R.D., Li J.X., Koen L.J., Lorenzen L. (2002), “Ultrasonic time-domain reflectometry as a non-destructive visualization technique to monitor fouling and cleaning on reverse osmosis membranes”, Journal of Membrane Science, **207**: 105-117.

Sandiford B.R., Wooldridge W.R. (1931), “Resting Bacteria”, Biochemical Journal, **25**: 2172-2180.

Saxena I., Sturman P.J., Costerton J.W. (2002a), “Development and testing of a fiber-optic probe for biofilm detection and quantification”, in: Proceedings of the International Specialized Conference on Biofilm Monitoring, Porto, March 17–20.

Saxena I., Files D., Rao S., Costerton W.J. (2002b), “Autofluorescence-based bacteria detection using an optical fiber”, Proceedings of SPIE – The International Society for Optical Engineering, **4622**: 106–111.

Schaule G., Moschnitschka D., Schulte S., Tamachkiarowa A., Flemming H.C. (2007), “Biofilm growth in response to various concentrations of biodegradable material in drinking water”, Water Science and Technology, **55**: 191-195.

Schippers J.C., Verdouw J. (1980), “The modified fouling index, a method of determining the fouling characteristics of water”, Desalination, **32**: 137-148.

Schmid T., Panne U., Haisch C., Neiβner R. (2003), “Biofilm monitoring by photoacoustic spectroscopy (PAS)“, Water Science and Technology, **47**: 25-29.

Schwinge J., Neal P.R., Wiley D.E., Fane A.G. (2002), “Estimation of foulant deposition across the leaf of a spiral-wound module”, Desalination, **146**: 203-208.

Schwinge J., Neal P.R., Wiley D.E., Fletcher D.F., Fane A.G. (2004), “Spiral wound modules and spacers: Review and Analysis, Journal of Membrane Science, **242**: 129-153.

Segrè P.N., Prasad V., Schofield A.B., Weitz D.A. (2001), “Glasslike kinetic arrest at the colloidal-gelation transition”, Physical Review Letter, **86**: 6042-6045.

Semiat R., Hasson D. (2009), “Seawater and Brackish-Water Desalination with Membrane Operations”, in: Drioli E., Giorno L. (Eds.), Membrane Operations – Innovative Separations and Transformation, Wiley-VCH, Germany.

Shaffer D.L., Yip N.Y., Gilron J., Elimelech M. (2012), “Seawater desalination for agriculture by integrated forward and reverse osmosis: Improved product water quality for potentially less energy”, Journal of Membrane Science, **415–416**: 1–8.

She Q., Jin X., Tang C.-Y. (2012), “Osmotic power production from salinity gradient resource by pressure retarded osmosis: Effects of operating conditions and reverse solute diffusion”, Journal of Membrane Science, **401-402**: 262-273.

Silalahi S.H.D., Leiknes T., Ali J., Sanderson R. (2009), “Ultrasonic time domain reflectometry for investigation of particle size effect in oil emulsion seperation with crossflow microfiltration”, Desalination, **236**: 143-151.

Sim L.N., Ye Y., Chen V., Fane A.G. (2011), “Comparison of MFI-UF constant pressure, MFI-UF constant flux and crossflow sampler-modified fouling index ultrafiltration (CFS-MFI_{UF})”, Water Research, **45**: 1639-1650.

Sim S.T.V., Chong T.H., Krantz W.B., Fane A.G. (2012a), “Monitoring of colloidal fouling and its associated metastability using Ultrasonic Time Domain Reflectometry”, Journal of Membrane Science, **401-402**: 241-253.

Sim S.T.V., Jie C., Chong T.H., Yeo P.S.A., Krantz W.B., Coster H.G.L., Fane A.G. (2012b), “Development of Novel Monitors for Early Detection of Fouling in Reverse-Osmosis Systems”, in: International Desalination Association (IDA) Journal, Vol. 4, Numb. 3, pp. 36-48.

Sim S.T.V., She Q., Chong T.H., Tang C.-Y., Fane A.G., Krantz W.B. (2013a), “Strategic co-locations in a Hybrid Process involving desalination and Pressure Retarded Osmosis (PRO)”, Membranes, **3**: 98-125.

Sim S.T.V., Suwarno S.R., Chong T.H., Krantz W.B., Fane A.G. (2013b), “Monitoring membrane biofouling via ultrasonic time-domain reflectometry enhanced by silica dosing”, Journal of Membrane Science, **428**: 24-37.

Skilhagen S.E., Dugstad J.E., Aaberg R.J. (2008), “Osmotic power – power production based on the osmotic pressure difference between waters with varying salt gradients”, Desalination, **220**, 476–482.

Song L., Elimelech M. (1995), “Theory of concentration polarization in crossflow filtration”, Journal of the Chemical Society, Faraday Transactions, **91**: 3389-3398.

Stumm W. (1993), “Aquatic colloids as chemical reactants: Surface structure and reactivity”, Colloids Surface A, **73**: 1-18.

Su T.J., Lu J.R., Cui Z.F., Thomas R.K., (2000), “Fouling of ceramic membranes by albumins under dynamic filtration conditions”, Journal of Membrane Science, **173**: 167-178.

Subramani A., Hoek E.M.V. (2008), “Direct observation of initial microbial deposition onto reverse osmosis and nanofiltration membranes”, Journal of Membrane Science, **319**: 111-125.

Suki A., Fane A.G., Fell C.J.D. (1986), “Modeling Fouling Mechanisms in Protein Ultrafiltration”, Journal of Membrane Science, **27**: 181-193.

Suwarno S.R., Chen X., Chong T.H., Puspitasarim V.L., McDougald D., Cohen Y., Rice S.A., Fane A.G. (2012), “The impact of flux and spacers on biofilm development on reverse osmosis membranes”, Journal of Membrane Science, **405-406**: 219-232.

Taheri A.H., Sim S.T.V., Sim L.N., Chong T.H., Krantz W.B., Fane A.G. (2013), “Development of a new technique to predict reverse osmosis fouling”, Journal of Membrane Science, **448**: 12-22.

Tamachkiarowa A., Flemming H.C. (2003), “On-line monitoring of biofilm formation in a brewery water pipeline system with a fibre optical device”, Water Science and Technology, **47**: 19-24.

Tang C.Y., Chong T.H., Fane A.G. (2010), “Colloidal interactions and fouling of NF and RO membranes: A review”, Advances in Colloid Interface Science, **164**: 126-143.

Thorsen T., Holt T. (2009), “The potential for power production from salinity gradients by pressure retarded osmosis”, Journal of Membrane Science, **335**: 103–110.

Tran T., Bolto B., Gray S., Hoang M., Ostarcevic E. (2007), “An autopsy study of a fouled reverse osmosis membrane element used in a brackish water treatment plant”, Water Research, **41**: 3915-3923.

Trettin D.R., Doshi M.R. (1980), “Limiting flux in ultrafiltration of macromolecular solutions”, Chemical Engineering Communications, **4**: 507-522.

Trokhymchuk A., Alejandre J. (1999), “Computer simulations of liquid/vapor interface in Lennard-Jones fluids: Some questions and answers”, Journal of Chemical Physics, **111**: 8510-8523.

Trompette J.L., Clifton M.J., Bacchin P. (2005), “Ion-specific repulsive interactions in colloidal silica dispersions evidenced through osmotic compression measurements and implication in frontal ultrafiltration experiments”, Journal of Colloid and Interface Science, **290**: 445-461.

Uchymiak M., Rahardianto A., Lyster E., Glater J., Cohen Y. (2007), “A novel ex situ scale observation detector (EXSOD) for mineral scale characterisation and early detection”, Journal of Membrane Science, **291**: 86-95.

Uemura T., Henmi M. (2008), “Thin-Film Composite Membranes for Reverse Osmosis” in: Li. N.N., Fane A.G., Ho W.S.W., Matsuura T. (Eds.), Advanced

Membrane Technology and Applications, John Wiley & Sons, Inc., New Jersey, United States.

Vieira M.J., Melo L.F. (1995), "Effect of clay particles on the behaviour of biofilms formed by Pseudomonas Fluorescens", Water Science & Technology, **32**: 45-52.

Vrouwenvelder J.S., Bakker S.M., Cauchard M., Grand R.L., Apacandie M., Idrissi M., Lagrave S., Wessels L.P., Paassen J.A.M.V., Kruithof J.C., Loosdrecht M.C.M.V. (2007), "The membrane fouling simulator: a suitable tool for prediction and characterization of membrane fouling", Water Science & Technology, **55**: 197-205.

Vrouwenvelder J.S., Bakker S.M., Wessels L.P., Paassen J.A.M.V. (2006a), "The Membrane Fouling Simulator as a new tool for biofouling control of spiral-wound membranes", Desalination, **204**: 170-174.

Vrouwenvelder J.S., Hinrichs C., Meers W.G.J.V.D., Loosdrecht M.C.M.V.D., Kruithof J.C. (2009), "Pressure drop increase by biofilm accumulation in spiral wound RO and NF membrane systems: role of substrate concentration, flow velocity, substrate load and flow direction", Biofouling, **25**: 543-555

Vrouwenvelder J.S., Loosdrecht M.C.M.V., Kruithof J.C. (2011), "Early warning of biofouling in spiral wound nanofiltration and reverse osmosis membanes", Desalination, **265**: 206-212.

Vrouwenvelder J.S., Paassen J.A.M.V., Wessels L.P., Dam A.F.V., Bakker S.M. (2006b), "The Membrane Fouling Simulator: A practical tool for fouling prediction and control", Journal of Membrane Science, **281**: 316-324.

Vrouwenvelder J.S., Picioreanu C., Kruithof J.C., Loosdrecht M.C.M.V. (2010), "Biofouling in spiral wound membrane systems: Three-dimensional CFD model based evaluation of experimental data", Journal of Membrane Science, **346**: 71-85.

Wada Y., Beek L.P.H.V., Kempen C.M.V., Reckman J.W.T.M., Vasak S., Bierkens M.F.P. (2010), “Global depletion of groundwater resources”, Geophysical Research Letter, **37**: L20402.

Wagner J. (2001), Membrane filtration handbook – Practical tips and hints, Osmonics Inc.

Wang L., Song L. (1999), “Flux decline in crossflow microfiltration and ultrafiltration: experimental verification of fouling dynamics”, Journal of Membrane Science, **160**: 41-50.

Wang Y.-N., Tang C. (2011a), “ Fouling of Nanofiltration, Reverse Osmosis, and Ultrafiltration Membranes by Protein Mixtures: The Role of Inter-Foulant-Species Interaction”, Environmental Science & Technology, **45**: 6373-6379.

Wang Y.-N., Tang C. (2011b), “ Nanofiltration Membrane Fouling by Oppositely Charged Macromolecules: Investigation on Flux Behaviour, Foulant Mass Deposition, and Solute Rejection”, Environmental Science & Technology, **45**: 8941-8947.

Weitz D.A., Oliveria M. (1984), “Fractal structures formed by kinetic aggregation of aqueous gold colloids”, Physical Review Letter, **52:** 1433-1436.

Wijmans J.G., Nakao S., Smolders C.A. (1984), “Flux Limitation in Ultrafiltration: Osmotic Pressure Model and Gel Layer Model”, Journal of Membrane Science, **20**: 115-124.

Wilf M., Klinko K. (2001), “Optimization of seawater RO systems design”, Desalination, **138**: 299-306.

Wolf G., Crespo J.G., Reis M.A.M (2002), “Optical and spectroscopic methods for biofilm examination and monitoring”, Reviews in Environmental Science and Biotechnology, **1**: 227-251.

Xiu X., Li J., Li H., Cai Y., Cao Y., He B., Zhang Y. (2002), Non-invasive monitoring of fouling in hollow fiber membrane via UTDR, Journal of Membrane Science, **201**: 17-29.

Yang X., Beyenal H., Harkin G., Lewandowski Z. (2000), "Quantifying biofilm structure using image analysis", Journal of Microbiological Methods, **39**: 109-119.

Ye Y., Clech P.L., Chen V., Fane A.G. (2005), "Evolution of fouling during crossflow filtration of model EPS solutions", Journal of Membrane Science, **264**: 190-199.

Yiantsios S.G., Karabelas A.J. (2002). An assessment of the Silt Density Index based on RO membrane colloidal fouling experiments with iron oxide particles. Desalination. **151**: 229-238.

Yiantsios S.G., Sioutopoulos D., Karabelas A.J. (2005), "Colloidal fouling of RO membranes: an overview of key issues and efforts to develop improved prediction techniques", Desalination, **183**: 257-272.

Yip N.Y., Tiraferri A., Phillip W.A., Schiffman J.D., Hoover L.A., Kim Y.C., Elimelech M. (2011), "Thin-film composite pressure retarded osmosis membranes for sustainable power generation from salinity gradients", Environment Science and Technology, **45**: 4360–4369.

Zhang Y.P., Law A.W.K., Fane A.G. (2010), "Determination of critical flux by mass balance technique combined with direct observation image analysis", Journal of Membrane Science, **365**: 106-113.

Zhu A., Christofides P. D., Cohen Y. (2009), "On RO membrane and energy costs and associated incentives for future enhancements of membrane permeability", Journal of Membrane Science, **344**: 1-5.